

DOTTORATO DI RICERCA IN

CHIMICA

Ciclo XXX

Settore concorsuale: 03/B1

Settore scientifico-disciplinare di afferenza: CHIM/03

Property tuning and supramolecular organization of oligo-
and polythiophenes for applications in biology and organic
electronics

Presentata da: Mattia Zangoli

Coordinatore Dottorato

Prof. Aldo Roda

Supervisore

Prof. Giacomo Bergamini

Co-supervisori

Dr. Francesca Di Maria

Prof. Paola Ceroni

Esame finale anno 2018

My research activity was focused on the synthesis and characterization of novel thiophene-based oligomers and polymers for the preparation via self-assembly of nanoparticles (0D supramolecular structures) and fibers (1D supramolecular structures) aimed to application in organic electronics and biophotonics.

Numerous synthetic steps, in particular cross-coupling and bromination reactions, were carried out by taking advantage of enabling technologies such as microwave and ultrasound irradiation, which led to marked improvements in reaction yields, purity, rapidity and environment-friendly conditions.

In the first chapter I give an overview of the most recent developments in synthesis and application of oligo- and polythiophenes as organic materials, highlighting the state of the art in synthetic procedures, performances in devices and application in biology as fluorescent probes.

The second chapter reports the synthesis of novel classes of selectively sulphur-oxidized oligo- and polythiophenes. Oligomers and polymers containing thiophene-S,S-dioxide and thiophene-S-oxide units in the desired number and position are described. Examples of their application in devices and supramolecular organization inside live cells are given.

The third chapter is dedicated to the preparation and characterization of polythiophene based nanoparticles for biophotonics, in sterile conditions and in the absence of surfactants. It is demonstrated that live cells easily uptake poly(3-hexylthiophene) nanoparticles (P3HT-NPs) without toxic effects while preserving their physiological functions. In addition, it is reported that P3HT-NPs can act as “photosensitizers” after internalization in live animals, *Hydra vulgaris*, modifying their behaviour and genic expression upon white light irradiation. Finally, the preparation of amino-reactive NPs, obtained from a properly functionalized polythiophene, is reported. The ability of the nanoparticles to remain docked on cell membrane and to act as phototransducers under illumination is demonstrated.

In the fourth chapter I report the synthesis and the supramolecular organization in crystalline, fluorescent and electro-active fibers of oligothiophenes possessing the same quaterthiophene core functionalized with an alkylthio group per ring and characterized by head to head regiochemistry. Further functionalization of the quaterthiophene with different electron withdrawing aromatic terminal units causes the variation of the electronic distribution without altering the growth modalities of the fibers. In this way a wide tuning of the optical and redox properties of the fibers is obtained. Studies on the effects of the terminal substituents on charge transport properties are currently under way.

La mia attività di ricerca è stata incentrata sulla sintesi e caratterizzazione di nuovi oligomeri e polimeri a base tiofenica per la preparazione *via* self-assembly di nanoparticelle (strutture supramolecolari 0D) e fibre (strutture supramolecolari 1D) finalizzate ad applicazioni in organica elettronica e biofotonica.

Numerosi passaggi sintetici, in particolare le reazioni di cross-coupling e bromurazione, sono stati effettuati con l'uso di tecnologie abilitanti, quali irradiazione con microonde e ultrasuoni che hanno portato a notevoli miglioramenti in rese di reazione, purezza, rapidità e condizioni eco-sostenibili.

Nel primo capitolo riporto una panoramica dei più recenti sviluppi nella sintesi e applicazione di oligo- e politiofeni come materiali organici, mettendo in luce lo stato dell'arte delle procedure sintetiche, delle prestazioni in dispositivi e della loro applicazione in campo biologico come marcatori fluorescenti.

Il secondo capitolo riporta la sintesi di nuove classi di oligo- e politiofeni selettivamente ossidati allo zolfo. Sono descritti oligomeri e polimeri contenenti unità tiofene-S,S-diossido e tiofene-S-ossido in numero e posizione predeterminati. Vengono inoltre riportati esempi della loro applicazione in dispositivi e della loro organizzazione supramolecolare in cellule viventi.

Il terzo capitolo è dedicato alla preparazione e caratterizzazione di nanoparticelle politiofeniche per la biofotonica, in condizioni sterili e assenza di surfattanti. Si dimostra che cellule viventi internalizzano facilmente nanoparticelle di poli(3-esiltiofene), P3HT-NPs, senza che si producano effetti tossici e preservando le loro funzioni fisiologiche. Inoltre, si riporta che le nanoparticelle NPs-P3HT agiscono come 'photosensitizers' dopo internalizzazione in sistemi viventi quali *Hydra vulgaris*, modificando il loro comportamento e espressione genica in seguito a irradiazione con luce bianca. Infine, si riporta la preparazione di nanoparticelle ammino reattive, ottenute da un politiofene opportunamente funzionalizzato, e si dimostra che rimangono localizzate sulla membrana cellulare, polarizzandola sotto illuminazione.

Nel quarto capitolo riporto la sintesi e l'organizzazione supramolecolare in fibre cristalline, fluorescenti e elettro-attive di oligotiofeni aventi lo stesso cuore centrale quatertiofenico funzionalizzato con un gruppo tioalchile per anello e caratterizzato da regiochimica testa-testa. Ulteriore funzionalizzazione del quatertiofene con gruppi aromatici elettron-attrattori terminali comporta la variazione della distribuzione elettronica senza alterare le modalità di crescita delle fibre. In questo modo si ottiene un'ampia modulazione delle proprietà ottiche e ossidoriduttive delle fibre. Studi sugli effetti dei sostituenti terminali sulle proprietà di trasporto di carica sono attualmente in corso.

CHAPTER I	INTRODUCTION: THIOPHENE DERIVATIVES AS ORGANIC MATERIALS	5
CHAPTER II	PROPERTY-FUNCTION CONTROL IN THIOPHENE MATERIALS BY STEPWISE OXIDATION OF THIOPHENE SULPHUR	55
CHAPTER III	POLYTHIOPHENE NANOPARTICLES FOR BIOPHOTONICS	139
<i>Part I</i>	<i>Sterile poly(3-hexylthiophene) nanoparticles for biophotonics in living cells</i>	140
<i>Part II</i>	<i>Semiconducting polymer are light nanotrasducers in eyeless animals</i>	160
<i>Part III</i>	<i>Engineering thiophene-based nanoparticles to induce phototransduction in live cells under illumination</i>	183
CHAPTER IV	RATIONAL PROPERTY TUNING OF CRYSTALLINE 1D OLIGOTHIOPHENE FIBERS HIERARCHICALLY ASSEMBLED FROM NANO- TO MICROSACLE	215
SUMMARY		281

CHAPTER I INTRODUCTION: THIOPHENE DERIVATIVES AS ORGANIC MATERIALS

This chapter is an overview of synthesis, characterization and application of thiophene-based compounds as organic materials. It describes advances in synthesis and characterization methodologies as well as in performance attained as active materials in devices such as field-effect transistors and photovoltaic devices. The developments in application of thiophene-based fluorophores in biological systems are also described. The last part looks at the relationship between the solid state morphology and the properties of thiophene materials discussing some common solid structure.

Published as:

G. Barbarella, **M. Zangoli** and F. Di Maria.

Book Series: Advances in Heterocyclic Chemistry; Volume: 123; Scriven E. F. V., Ramsden C. A. Eds.; 105-167; 2017.

I. INTRODUCTION

This chapter covers a few aspects of the most recent developments in synthesis and application of thiophene oligomers and polymers for use in a wide range of fields, from very efficient organic solar cells ^[1] to fluorophores specifically binding amyloid fibrils formed inside neural cells in Alzheimer's and other neurodegenerative diseases ^[2]. Thiophene-based oligomers and polymers are organic semiconductors with a wealth of properties spanning from charge conduction in the oxidized or reduced states ('doped' states) to light emission upon irradiation at appropriate wavelength. Researches involving these compounds are highly interdisciplinary ^[3]. Owing to their multiple functional properties, chemical robustness and versatility, thiophene-based materials play a preminent role in nanoscience and nanotechnology, which largely rely on the production of new materials both from a scientific and a technological point of view. They exhibit a great amount of structural diversity and their synthesis is mainly oriented towards molecular structures useful to elucidate property-structure relationships for the optimization of specific properties. The impressive versatility of thiophene-based materials relies on the numerous possibilities of ring functionalization and chain elongation from a few rings forming monodisperse oligomers to a large number rings forming polydisperse polymers. Sulfur is a medium-sized atom located at the intersection of the 16th group (column) and the 3rd period (row) of the periodic table. It has diffuse orbitals, easily polarizable electrons and formal oxidation states 2, 4 and 6. In the oxidation states 4 and 6, it is hypervalent, i.e. it is surrounded by more than the eight electrons associated with filled s and p shells ^[4]. Thiophene sulfur has a formal oxidation state 2 and two lone pair electrons one of which participates in ring aromatization. To time most synthetic effort has focused on aromatic backbone functionalisation and relatively few investigations have taken into account the numerous possibilities related to the functionalization of thiophene sulfur ^[5].

Thiophene oligomers and polymers are described by their conformation generated by the rotations around the single bonds linking two adjacent thienyl rings. Rotation angles (ω) between α,α' -linked thienyl units may differ in magnitude and in sign, giving rise to different conformational isomers. Conformational isomers have slightly different energies and very low energy barriers for conversion from syn to anti forms, so that in solution interconversion between different conformers is rapid and the presence of even bulky substituents is not sufficiently high to hinder conformational mobility ^[6]. Variations in the inter-ring angle ω bring about variations in the overlap between the p orbitals of the α -linked carbons of two adjacent thienyls. The overlap is maximum for the planar syn ($\omega = 0^\circ$) and anti ($\omega = 180^\circ$) forms. The larger the distortion from planarity, the weaker the extent of π -conjugation and electron delocalisation. The electronic properties of oligomers and polymers depend on the degree of π -conjugation, which affects HOMO-LUMO orbitals energies, energy gaps, optical, electrochemical and electrical properties. Rotational distortions decreasing π -conjugation may deeply affect the molar absorption coefficient in the solid state ^[7]. The torsion angle between thiophene rings is also relevant to the question of chirality observed in the solid state for achiral thiophene oligomers. In this case, the optical activity observed in the solid state is the effect of hindered rotations about the thienyl-

thienyl inter-ring bonds caused by the freezing of the molecule on the solid support in conformations lacking any symmetry element. Thiophene rings are characterized by easy bond and angle deformability due to the high polarisability of sulphur bound and unbound electrons and the long C-S bonds. As a consequence, the aromatic backbone of oligo and polythiophenes is capable to adapt its geometry to surrounding molecules by means of small bond and angle deformations extended over the entire system ^[8]. This capability, well-illustrated by X-ray diffraction data of single crystals of thiophene oligomers showing that thiophene has always slightly different bond angles and lengths and is never a regular pentagon, together with the very low energy barriers to rotation around the inter-ring carbon-carbon bonds confer extreme flexibility to the aromatic backbone of oligo and polythiophenes. The great flexibility of the aromatic backbone of thiophene oligomers can give rise in the solid state to polymorphism, i.e. the possibility to pack with different modalities and different conformations causing variations in the electronic properties which depend on the degree of electron delocalization between adjacent rings. Most applications of thiophene-based materials concern organic (opto)electronics expected to replace in the near future the current technology based on inorganic semiconductors ^[9]. However, in recent years a few families of brightly fluorescent thiophene oligomers have been developed for a variety of possible medical applications ^[10], as fluorophores for proteins and DNA labeling ^[11] and for differential staining of various cell types, including cancer cells, by cytofluorimetry ^[12]. Fluorescent quinquethiophenes with precise regiochemistry of substitution have been exploited for the detection of the manifestations of protein misfolding diseases such as prion and Alzheimer's diseases ^[13]. These quinquethiophenes are amyloid proteins specific ligands showing fine variations in absorption and emission spectra upon binding to aggregates of misfolded proteins thus allowing to associate molecular structure modifications, conformational variations and consequent optical changes of the probes to the manifestation of pathogenesis. More generally, these studies have disclosed the possibility of using thiophene-based fluorophores, some of which show efficient crossing over the blood-brain barrier, as tools for pathological and prognostic evaluation of neurological diseases ^[14].

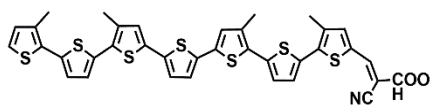
II. SYNTHESIS OF OLIGO- AND POLYTHIOPHENES

The synthesis of oligo and polythiophenes is aimed at creating new molecular structures with enhanced functional properties. The attention is oriented towards obtaining the most pure products and the easier to separate from side products. Purity and reproducibility are very crucial requirements in conjugated materials chemistry since even parts per million of *contaminants* can deeply affect properties such as charge transport or light emission.

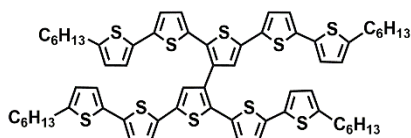
The synthesis of π -conjugated oligo and polythiophene, whether linear, bent or branched, requires the formation of thienyl-thienyl C-C bonds. Aryl-aryl C-C bond formation is one of the most important reactions in organic synthesis since many biological molecules, drugs, dyes, organic semiconductors and so on contain two or more aromatic rings linked together. The developments in synthetic strategies for aryl-aryl C-C bond formation are described in detail in several important reviews ^[15]. Concerning thiophene-based materials, in Section 2.1 we show

how over the past few years the most exploited reactions have been the palladium catalyzed cross-couplings between halogenated and metalated thienyl moieties, which allow the step-by-step regioregular formation of aromatic backbones with the most various substitution patterns, sizes, shapes and functionalization types. Of course many specific synthetic problems of thienyl-thienyl bond formation have also been solved by using other methods chosen case by case and are not discussed here. In Section 2.2 we show how in the last decade a transition metal catalyzed direct arylation method has emerged as an attractive alternative to traditional cross-coupling reactions although its application is still limited in comparison to conventional cross-coupling methods.

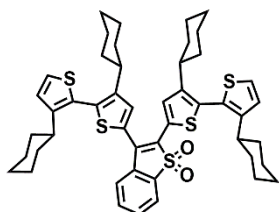
Chart 1



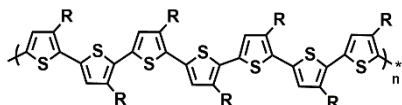
Rod-like ^[16]



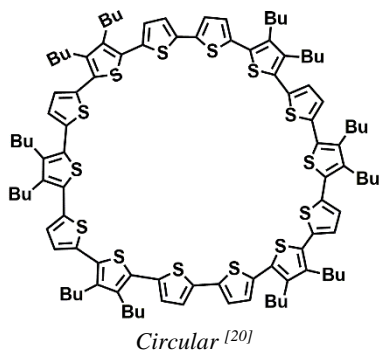
Swivel-cruciform ^[17]



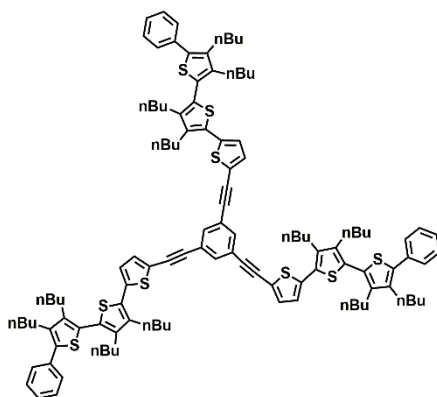
V-shaped ^[18]



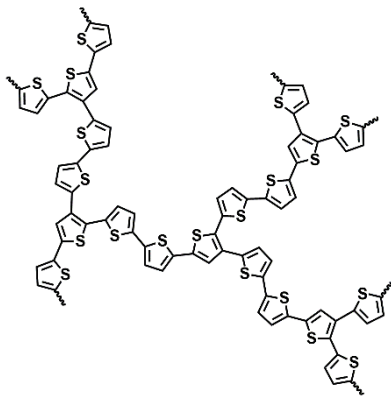
Alkyl substituted regioregular polythiophene ^[19]



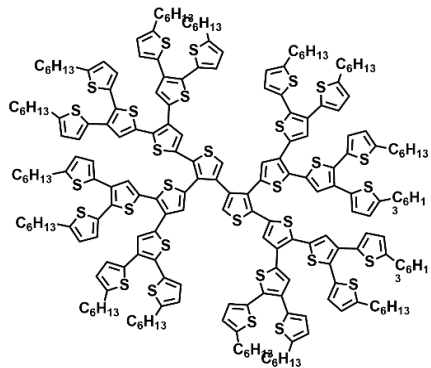
Circular ^[20]



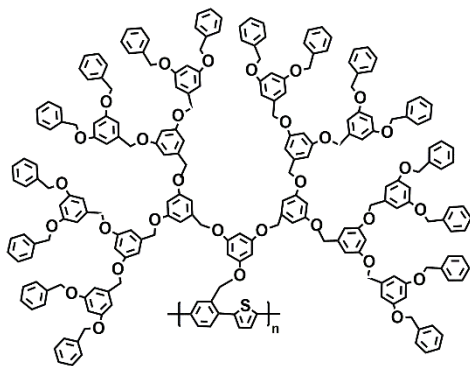
Star-shaped ^[21]



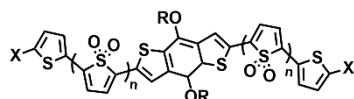
Hyperbranched polythiophene [22]



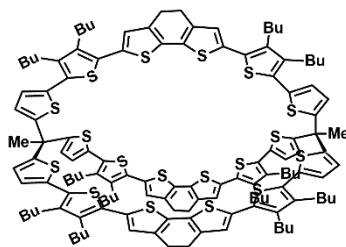
Dendrimer [23]



Dendritic polythiophene [24]



Donor-acceptor polythiophene [5b]



Three-dimensionally expanded sexithiophene [25]

Most of the numerous papers published so far on thiophene materials for application in nano science and technology concern compounds where the tuning of optical, electrical, self-assembly and other properties is obtained either by changing molecular size and shape or by grafting various substituents at the carbons α , β to sulfur. Owing to synthetic difficulties, thiophene sulfur functionalization has been scarcely explored in thiophene materials, although it is expected to deeply affect the aromatic character of the ring hence the functional properties of oligomers and polymers. In Section 1.3 we show how it is possible to synthesize new classes of functional thiophene-based oligomers and polymers whose molecular structures contain one or more thienyl-S,S-dioxide or thienyl-S-oxide moiety and the strong impact of this functionalization type on properties tunability. Finally, Section 1.4 briefly illustrates how the synthesis of oligo and polythiophenes can be facilitated by the assistance of the so-called enabling technologies.

2.1 Cross coupling reactions. In cross coupling reactions an arene substituted with a leaving group (-Cl, -Br, -I, -OTf, etc.) is reacted with an arene substituted with an organometallic moiety such as -SnR₃, -B(OR)₃, -ZnR or -MgX in the presence of a transition metal catalyst such as palladium or nickel (Figure 3).

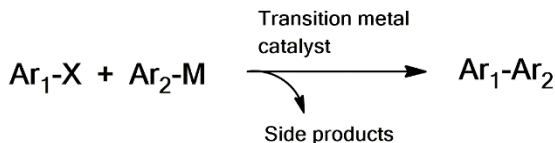
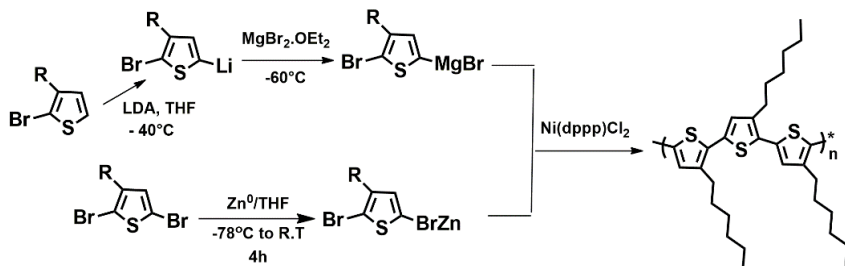


Figure 3

In early studies these reactions have been widely tested in the preparation of regioregular poly(3-hexylthiophene), P3HT, one of the most investigated and performant thiophene polymers in organic electronics. Scheme A shows the synthetic pattern for the preparation of highly regioregular P3HT by use of Nickel-catalyzed cross-coupling reactions of Grignard reagents^[26] and zinc reagents^[27] with alkyl bromides (R = *n*-hexyl). Over the last two decades the most employed cross coupling reactions for the preparation of thiophene-based oligomers and polymers have been the palladium-catalyzed Stille and Suzuki-Miyaura reactions described in sections 2.1.1 and 2.1.2, respectively.



Scheme 1

2.1.1 Stille reaction. For the formation of the thienyl-thienyl bond (Th₁-Th₂) the Stille reaction^[28] consists in the coupling of weakly nucleophilic thienyl stannanes with thienyl halogenides (Cl, Br, I), generally in the presence of palladium (zero) complexes (Figure 4).

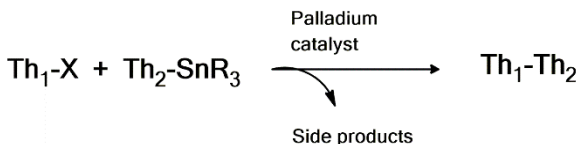
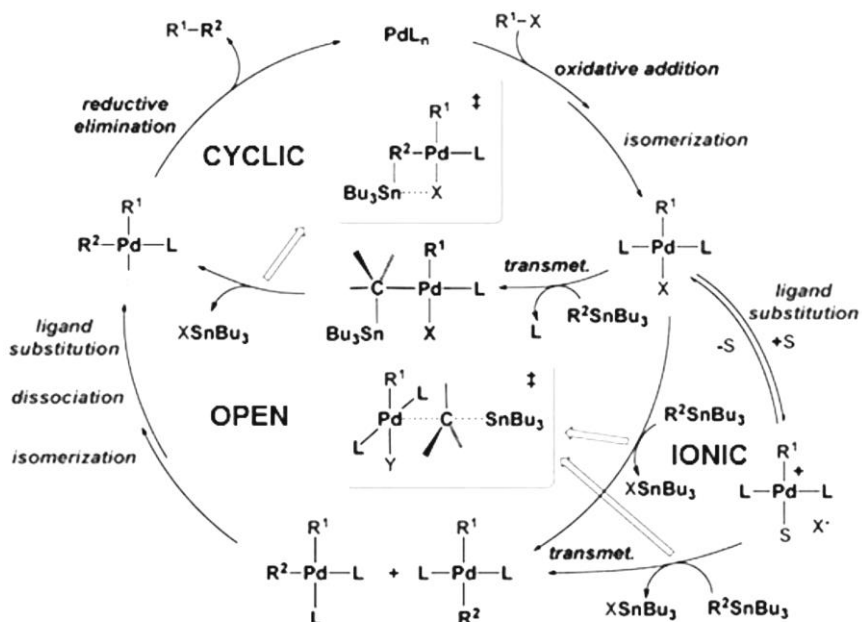


Figure 4

This reaction is a mild process compatible with a wide variety of functional groups and the aryltin derivatives can be prepared without protecting the functionalities present in the monomers.

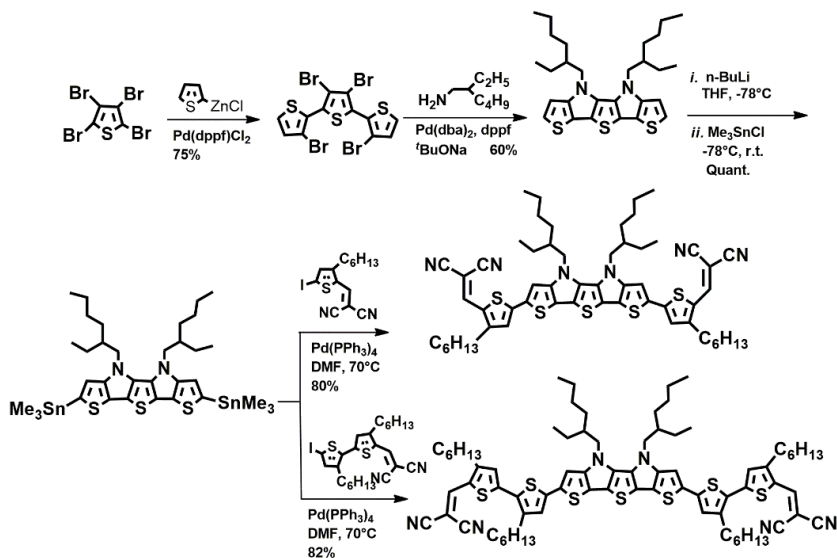
Moreover, they are far less moisture and oxygen sensitive than other organometallic counterparts such as Grignard or organolithium reagents. The reaction is regioselective and generally gives good yields although in few cases parallel reactions (for example the metal-halogen exchange) can cause the formation of undesired products difficult to separate from the target compound. Compared with boron or zinc thienyl derivatives, the lower basicity of stannanes makes them less nucleophilic and their higher steric requirements (in particular for tributyl stannyl derivatives much less toxic than the corresponding trimethyl counterparts) much less reactive although more selective. The Stille cross-coupling is an efficient way to various symmetrically and unsymmetrically substituted compounds and it has been in the past and still is extensively used for the preparation of semiconducting thiophene oligomers and polymers ^[29].



Scheme 2. Reprinted with permission from reference [30]. Copyright 2016 American Chemical Society.

The catalytic cycle of the reaction first hypothesized by Stille - oxidative addition of the aryl halogenide to the catalyst, trans-metalation from the metalated aryl to the intermediate arylpalladium halide, reductive elimination - is rather complex and has recently been deeply reviewed ^[30]. Scheme 2 reports the complete Stille catalytic cycle showing three different possible pathways, namely ionic, open or cyclic. According to the authors, the complex cycle shown in Scheme 2 "... is still a poor representation of reality but at least showing three important concepts sometimes forgotten: (i) it is the transition metal catalyst that does the job, obeying the rules of coordination chemistry. Ignoring coordination chemistry is like walking in a desert without a compass; (ii) a fourth type of process, isomerization, has to be considered where appropriate, as highlighted in the scheme, and also others, such as ligand dissociation and ligand

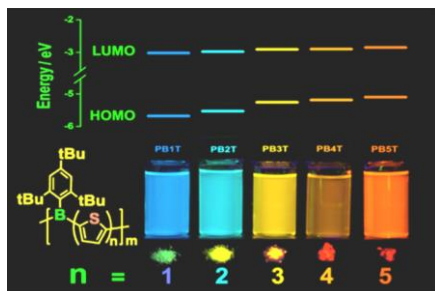
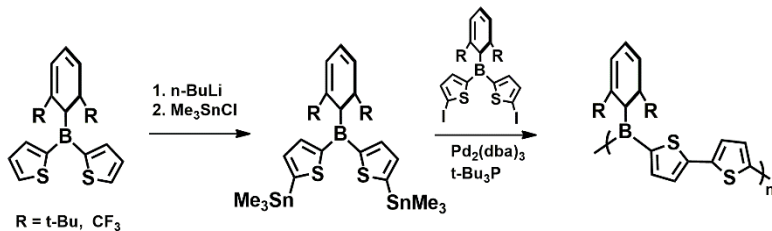
substitution; (iii) although not shown in the scheme, some steps in the cycle are easily reversible, which can give rise to undesired byproducts, particularly when the irreversible C–C coupling step closing the cycle is too slow, allowing generation of new species via undesired (mistaken) reversible transmetalations ...”. These authors^[30] also discuss the use of chiral stannanes in Stille reaction and the stereoselectivity - inversion vs retention - of the transmetalation step. Scheme 3 shows the synthesis via Stille coupling of two thiophene oligomers characterized by strong absorption in the low energy region and employed as donor materials in highly efficient organic-inorganic hybrid perovskite-based solar cells^[31]. These oligomers act simultaneously as good hole (positive charge) transporters and strongly light absorbing systems in the visible and near-infrared region. After preparation of the inner building block 3,3',3'',4'-tetrabromo-2,2':5',2''-terthiophene (5) according to already reported modalities^[32], the corresponding bis-stannylated derivative (7) was obtained by lithiation with n-BuLi followed by quenching with trimethyltin chloride.



Scheme 3. Reprinted with permission from reference [31]. Copyright 2014 Royal Society of Chemistry.

The target oligomers were obtained in yields 80 and 82%, by Pd-catalyzed Stille-type coupling of the distannane with dicyanovinylene iodothiophene and iodo-bithiophene.

Scheme 4 shows the synthesis of brightly fluorescent thiophene-based polymers with boron atoms incorporated into the conjugated polythiophene main chain prepared via Pd-catalyzed coupling of stannylated thienylborane monomers with the corresponding iodo thienyl borane derivatives^[33].



Scheme 4. Adapted with permission from reference [33]. Copyright 2016 American Chemical Society.

2.1.2 Suzuki reaction. For the formation of the thienyl-thienyl bond (Th₁-Th₂) the palladium catalyzed Suzuki-Miyaura reaction^[34] uses thienyl boronic acids or esters as nucleophiles in the presence of electrophilic thienyl halides: X = Cl, Br, I (Figure 5).

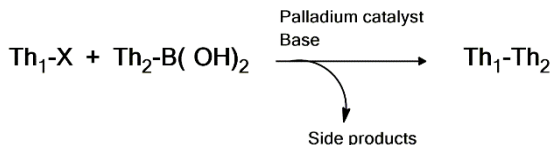
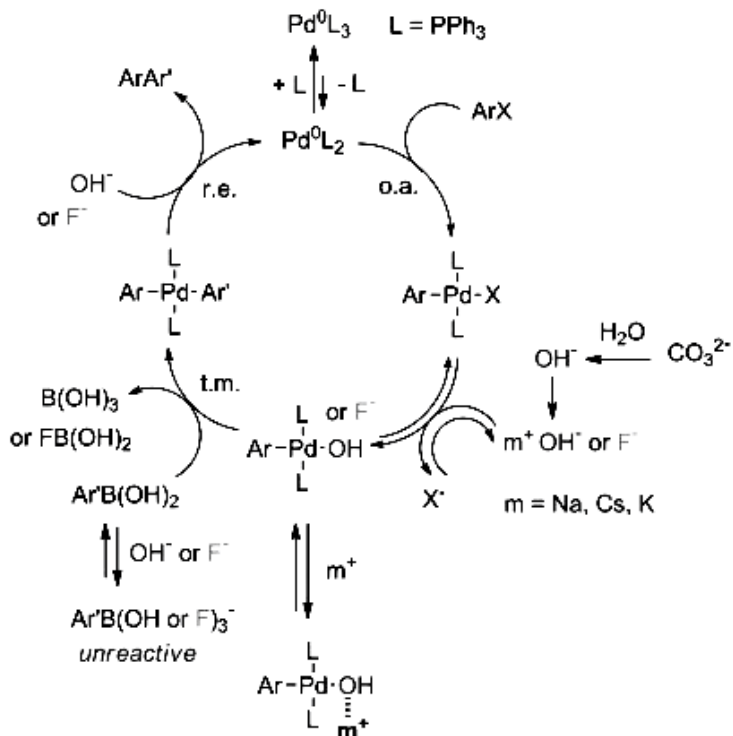


Figure 5

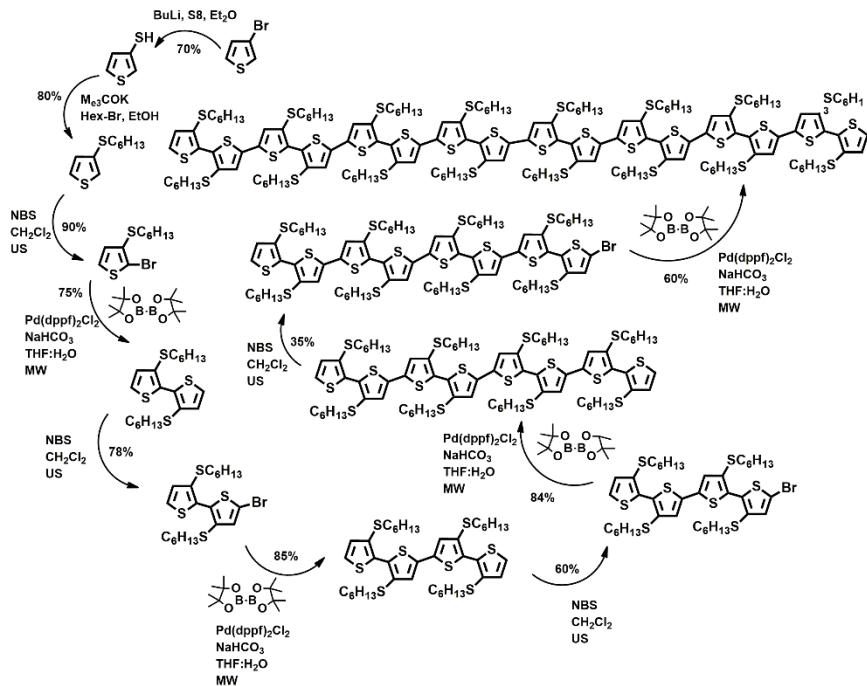
Boron derivatives are less toxic than tin derivatives and the reaction is also compatible with a great variety of functional groups and reaction conditions. As pointed out by Professor Akira Suzuki in his Nobel lecture^[34e], compared to other organometallic compounds, the C-B bond is perfectly covalent since boron and carbon have very similar electronegativities and the C-B distance is almost the same as that of the C-C bond. Moreover, the boron atom having an open p-electron structure is susceptible to nucleophilic attack. The Suzuki reaction requires the presence of a base. Various bases have been tested in particular OH⁻, MeO⁻, CO₃²⁻, F⁻, the role of which has been widely debated. Recently, an extensive mechanistic study based on kinetic data, has established that the anionic bases “.. do not play the role of a base but serve as a ligand for aryl-palladium(II) complexes...”^[35]. The bases play positive roles in formation of the reactive

species in the transmetalation rate determining step and as catalysts in the reductive elimination step. However, they also play negative roles, in particular the formation of unreactive aryl borates.



Scheme 5. Reprinted with permission from reference [35]. Copyright 2013 Wiley-VCH Verlag GmbH.

The different roles are clearly illustrated in Scheme 5 showing the entire cycle of the Suzuki reaction in the presence of different bases and the corresponding counteractions. As in the case of the Stille reaction, the complexity of the mechanism requires an accurate choice of the experimental conditions in order to achieve good reaction yields. It is worth noting that despite the numerous studies reported on the mechanism of the Suzuki-Miyaura reaction, only in 2016 [36] has the actual composition and structure of the intermediates, in particular those of the transmetalation precursors, have been unambiguously defined only very recently. By the combination of spectroscopic analysis (in particular rapid injection NMR), independent synthesis and kinetic measurements, three pre-transmetalation species containing Pd-O-B linkages that undergo the Suzuki-Miyaura cross coupling reaction have been identified and characterized.

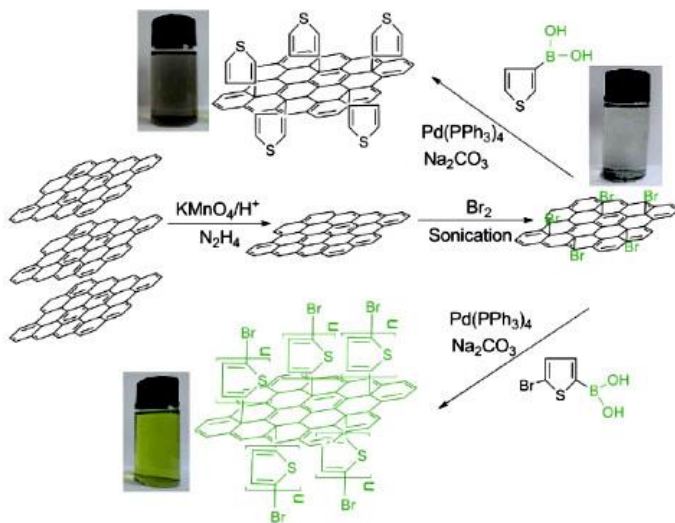


Scheme 6

Scheme 6 reports the synthesis of large size thiophene oligomers obtained by successive cycles of selective, ultrasound assisted, α -bromination and microwave-assisted Suzuki cross coupling starting from 3-S-alkylthiophene to the corresponding hexadecamer [37]. The notable feature of this preparation is that the dimer, tetramer, octamer and hexadecamer were all obtained by doubling the oligomer size by means of the reaction of the appropriate bromo-derivative with 4,4,5,5-tetramethyl-1,3,2-dioxaborolane. Contrary to what happens when bromoaryls react with the dioxaborolane, which lead to the replacement of bromo with boron [38], with thienyl bromo derivatives in the conditions employed the cross coupling of the bromo derivative with the just formed thiophene boron derivatives is rapid and leads to the double-sized oligomers.

An interesting recent application of the Suzuki reaction is the preparation of covalently bonded graphene-polythiophene hybrid materials [39] shown in Scheme 7. Graphene-based hybrid materials with conjugated oligomers and polymers are of great interest in various research areas such as nanohybrid (opto)electronic devices, energy storage, biotechnologies, and so on. In the case of the covalent grafting of polythiophene on graphene via Suzuki coupling the objective of the authors was to realize a strong electronic interaction and a good bandgap matching between the chemically bonded polythiophene and graphene in order to enhance charge transport. Scheme 7 illustrates the procedure for the synthesis of hybrid graphene-thiophene and graphene polythiophene starting from brominated graphene dispersion in water and 3-thienyl boronic acid

and 5-bromo-2-thienylboronic acid, respectively, with Pd(PPh₃)₄ as the catalyst and aqueous sodium carbonate as the base. The chemical composition of the surface after the reaction was investigated with a variety of techniques, including XPS, FT-IR and UV-vis spectroscopy.



Scheme 7. Reprinted with permission from reference [39]. Copyright 2015 Royal Society of Chemistry.

2.2 Direct arylation. Contrary to conventional cross coupling reactions, the so-called direct arylation method does not involve the preparation of metalated aryl derivatives, since the reaction takes place between aryl-halogen (Cl, Br, I) bonds and transition metal activated C-H bonds (Figure 6).

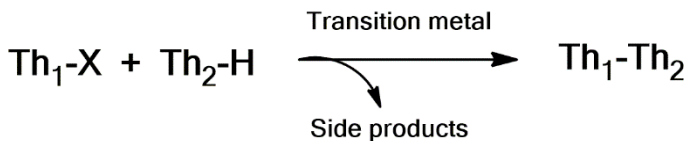
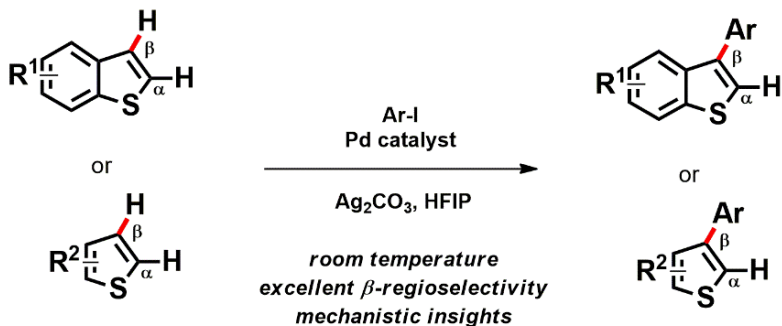


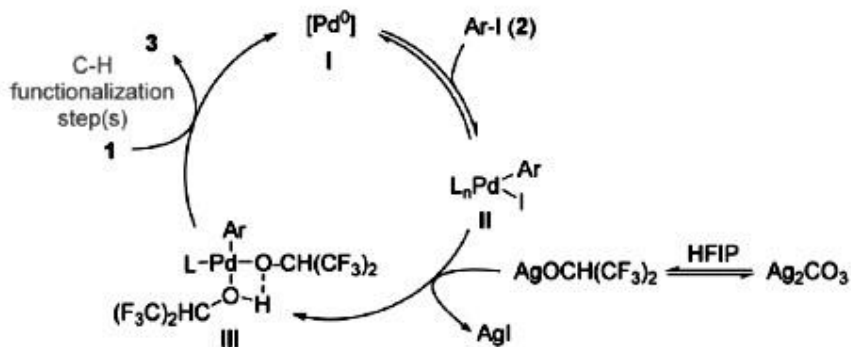
Figure 6

The reaction requires careful optimization of experimental conditions, which depend on the arene and the catalytic system employed^[40]. There are several possible mechanisms invoked for the aryl C-H bond activation^[41]. Very recently, the first experimental kinetic evidence supporting a Heck-type reaction pathway has been obtained in the regioselective, room temperature, β -arylation of thiophenes and benzo[b]thiophenes in the absence of directing groups^[42], see Scheme 8.



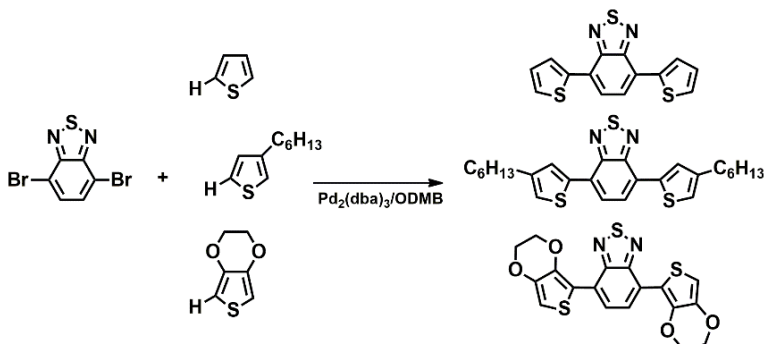
Scheme 8. Reprinted with permission from reference [42]. Copyright 2016 American Chemical Society.

A possible mechanism for this reaction is reported in Scheme 9. According to the authors, oxidative addition of Ar to Pd(0) leads first to PdArI species II. AgOCH-(CF₃)₂ results from the reaction of the mildly acidic hexafluoro-2-propanol (HFIP) and Ag₂CO₃ and transmetalates to Pd alkoxide III. In turn, this species undergoes the C-H arylation step(s) on the benzo-[b]thiophene [42].



Scheme 9. Reprinted with permission from reference [42]. Copyright 2016 American Chemical Society.

Most direct arylation studies on thiophene and thiophene derivatives concern the activation of the most acidic α -C-H bonds. Scheme 10 shows the arylation of commonly used building blocks for the preparation of thiophene-based polymers for use in high performance solar cells, namely 3-hexylthiophene and 3,4-ethylenedioxythiophene (EDOT) reacted with 4,7-Dibromobenzo[c]-1,2,5-thiadiazole [43]. According to the authors, the reaction proceeds through a concerted metalation-deprotonation pathway.



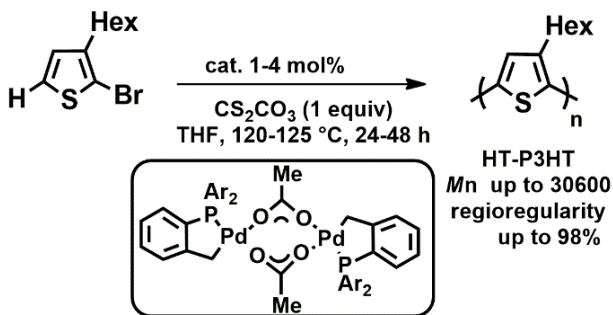
Scheme 10. Reprinted with permission from reference [43]. Copyright 2015 Royal Society of Chemistry.

Scheme 11 shows a high molecular weight polymer employed in solar cells obtained from EDOT and 2,7-dibromo-9,9-dioctylfluorene^[44].



Scheme 11. Reprinted with permission from reference [44]. Copyright 2013 Wiley-VCH Verlag GmbH.

Scheme 12 shows the synthesis of P3HT obtained by use of a highly efficient palladium catalyst capable to convert 2-bromo-3-hexylthiophene into linear, defect-free, regioregular head-to-tail poly(3-hexylthiophene), P3HT, with high molecular weight and regioregularity up to 98%^[45].

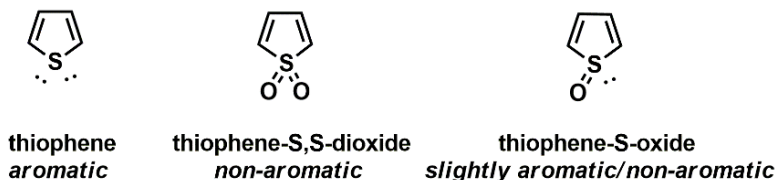


Scheme 12. Reprinted with permission from reference [45]. Copyright 2010 American Chemical Society.

Herrmann's catalyst (inset) acted as palladium source. This complex, obtained from Pd(OAc)₂ and P(*o*-tolyl)₃, was an efficient catalyst precursor with high thermal stability in the dehydrohalogenative polycondensation of 2-bromo-3-hexylthiophene. From the few examples reported above it is seen that the success of the direct arylation reactions largely depends on the

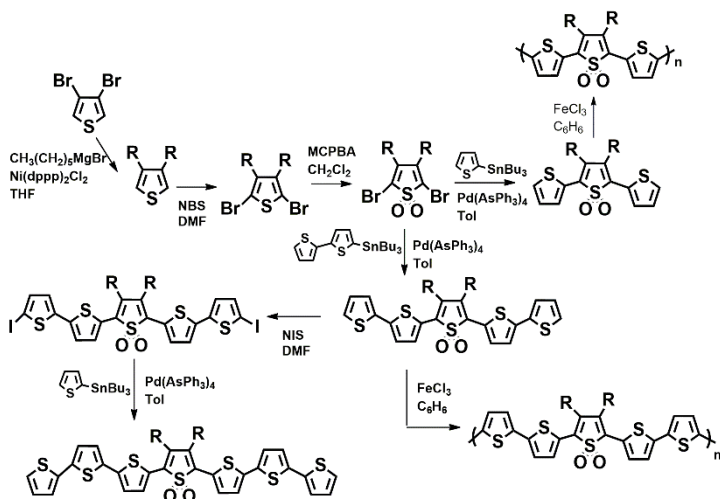
catalyst system employed. A recent paper outlines the perspectives of the method in the synthesis of π -conjugated polymers ^[46]. Many aspects, particularly in polymers synthesis, have to be addressed before the direct arylation can replace conventional cross-coupling reactions. In authors own words: "... Although advances in direct arylation have shown promise for applications in the field of conjugated polymer materials, we do not expect traditional coupling of aryl halides to be abandoned at this stage ...".

2.3 Sulfur functionalization. The formal oxidation state of sulfur in thiophene is 2. However, sulfur can be hypervalent, i.e. it can accommodate more than the eight electrons pertaining to filled *s* and *p* shells and acquire formal oxidation state 4 or 6 ^[47]. In consequence, thiophene sulfur can be functionalized with a variety of functional groups, in particular with oxygen to form thiophene-S,S-dioxide and thiophene-S-oxide, as shown in Scheme 13.



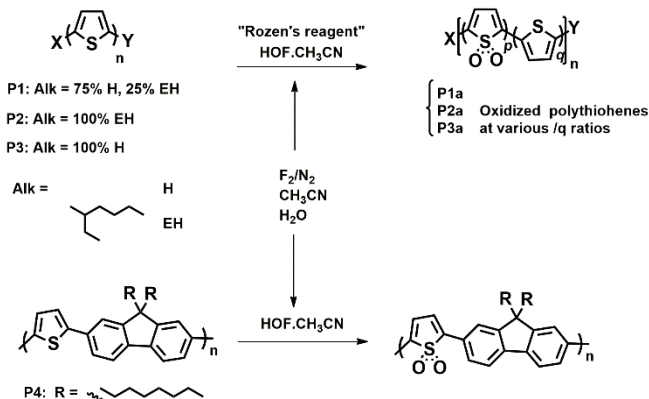
Scheme 13

The thienyl-S,S-dioxide moiety is non aromatic while the thienyl-S-oxide one having one residual lone pair on sulfur displays a borderline non-aromatic/slightly aromatic behavior ^[48]. Extensive developments in the direction of thiophene sulfur oxidation have been hampered by the low reactivity of thiophene sulfur requiring use of strong oxidants, such as *m*-chloroperoxybenzoic acid, MCPBA. More recently, a new strong oxidant, Rozen's reagent, namely the HOF·CH₃CN complex generated by flowing fluorine through an aqueous solution of acetonitrile has been described ^[49]. Oxidation with Rozen's reagent, leads to di-oxidation of all the thiophene rings of a preformed oligomer and up to 60% of a preformed polymer ^[50]. Oxidation with strong oxidants such as MCPBA and Rozen's reagent cannot be stopped at the single oxygen stage, i.e. to the S-oxide formation. In consequence, until recently only the synthesis of oligo and polythiophene-S,S-dioxides has been developed while only sparse data had been reported on oligothiophene-S-oxides. Regioregular oligo and polythiophene-S,S-dioxides were obtained by oxidation of variously substituted brominated thiophenes with MCPBA and subsequent Stille coupling with appropriate thienyl stannanes ^[51] as illustrated in Scheme 14.



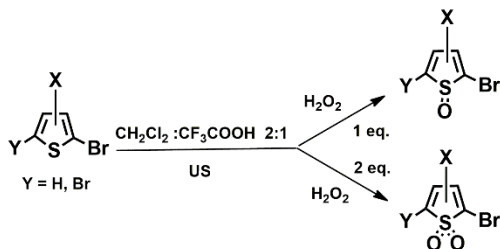
Scheme 14. Adapted with permission from reference [51]. Copyright 1999 American Chemical Society

The synthesis of a regiorandomly S,S-dioxidized polythiophene and poly(9,9-dioctyl-9H-fluorene-*co*-thiophene) was carried out as shown in scheme 15. The oxidation reaction required less than an hour at room temperature. It was demonstrated that the electronic properties of the polymers can be tuned over a wide range varying the degree of oxidation ^[50b].



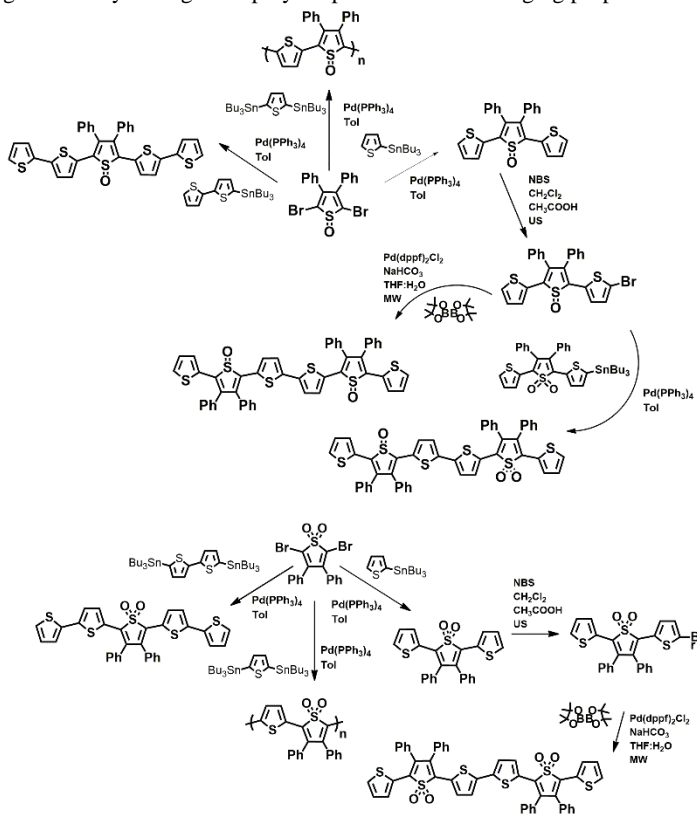
Scheme 15. Adapted with permission from reference [50b]. Copyright 2014 Wiley-VCH Verlag GmbH.

It has been reported that variously functionalized thiophene rings and their mono- and dibromo derivatives can be chemoselectively oxidized in very mild conditions to thiophene-S-oxides or thiophene-S,S-dioxides in high yields employing ultrasound irradiation (US) in organic or aqueous solvents (Scheme 16).



Scheme 16

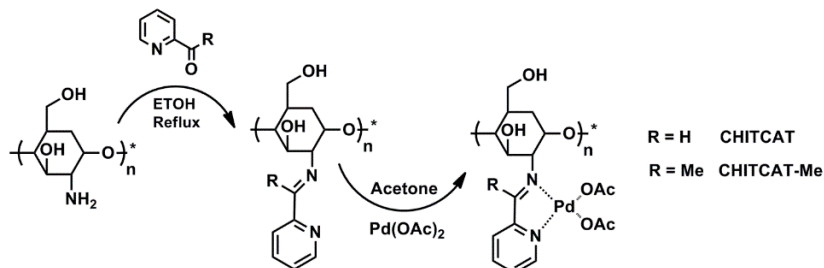
The use of sonication for the selective preparation of mono and dibromo thiophene-S-oxides or thiophene-S,S-dioxides coupled to the use of metalated thiophene rings in sequential microwave assisted Stille or Suzuki reactions for C-C bond formation allows the facile insertion of these units into a great variety of oligo and polythiophenes with challenging properties [5d].



Scheme 17. Adapted with permission from reference [5d]. Copyright 2016 Wiley-VCH Verlag GmbH.

Scheme 17 illustrates the synthesis by microwave-assisted Suzuki and Stille coupling of three thiophene hexamers containing either two thienyl-S,S-dioxide or two thienyl-S-oxide units or one thienyl-S,S-dioxide and one thienyl-S-oxide. The scheme also shows the synthesis of the first polythiophene-S-oxide reported so far. This polymer displays high electron affinity, similar to the corresponding polymer bearing thiophene-S,S-dioxide units. However, the charge transport properties of the two polymers are very different, the former being an ambipolar charge carrier and the latter being an electron charge carrier ^[54].

2.4 Enabling technologies. Post-synthesis purification to the degree needed for application in electronics (ppm of impurities) often requires huge amounts of organic solvents to carry out synthetic methodologies have been developed to obtain the materials free from byproducts and contaminants. The development of new synthetic platforms integrating the use of two or more so-called ‘enabling technologies’ - such as microwave and/or ultrasound irradiation, solid-phase assistance, non-conventional solvents, supported catalysts, flow chemistry techniques and the design of new reactors - are of great interest in all fields of organic synthesis, including machine-assisted processes in research laboratories and industries. The aim is to speed up synthetic transformations in a rapid and clean manner, improving workup and products isolation ^[52]. In view of industrial applications of organic semiconductors and taking into account the fact that today’s priorities of chemical industry are not only processes and products safety but also environment protection, the development of increasingly efficient and eco-sustainable platforms for the synthesis of highly pure conjugated materials becomes a priority. Note that purity and batch-to-batch reproducibility are very stringent requirements in the synthesis of conjugated materials since even the presence of parts per million of contaminants can deeply alter important properties such as electrical charge transport or light emission. The most employed enabling technologies in the synthesis of oligo- and polythiophenes are microwave (MW) and ultrasound (US) assistance. The first microwave-enhanced organic synthesis were reported in 1986 ^[53].

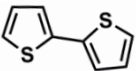
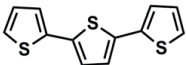
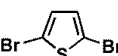
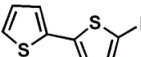
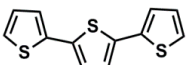
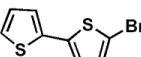
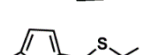
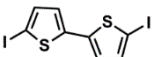
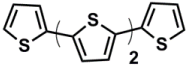
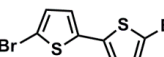
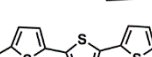
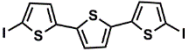


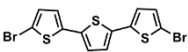
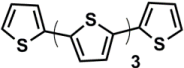
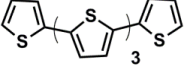
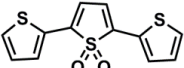
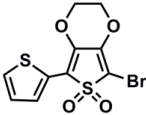
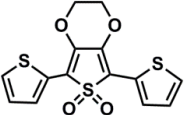
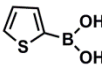
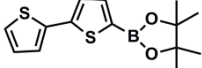
Scheme 18. Reprinted with permission from reference [55]. Copyright 2008 Royal Society of Chemistry.

Major improvements in equipment quality and temperature/pressure control have been achieved so that MW irradiation has now become a valuable tool in organic synthesis ^[54]. Replacing conventional heating with microwave heating leads to more homogeneous and higher temperatures, faster reaction rates, higher yields and cleaner products. Microwave assistance has

been often successfully employed in the synthesis of oligo and polythiophenes (see Scheme 17 and reference [11, 44]). Nice results have been obtained in coupling the microwaves with use of stable chitosan supported palladium catalysts in aqueous media [55]. Chitosan is a commercially available water tolerant linear polysaccharide derived from the shells of sea crustaceans. Scheme 18 shows the molecular structure and synthetic pattern for the preparation of chitosan-supported catalysts CHICAT-Me and CHITCAT used for the synthesis of various oligothiophenes in aqueous media by Suzuki-Miyaura reaction (Table 1). Chitosan was functionalized with 2-acetyl pyridine (or 2-pyridin carboxyaldehyde) and subsequently complexed with palladium acetate. Table 1 shows that the coupling of thienyl iodides or bromides with thienyl boron derivatives in the presence of potassium fluoride (KF) as the base takes place in aqueous ethanol in high yield and very short times. The heterogeneous catalyst was easily removed by filtration from the reaction mixture and reused in consecutive reactions. Very pure products were obtained compared to the reaction using conventional catalysts. Table 1 shows experimental conditions and yields of the reaction of thienyl halogenides with boronic acid/ester in the presence of CHITCAT-Me [55].

Table 1 Products, reagents, and experimental conditions of the reaction of thienyl halogenides boronic acid/ester in the presence of CHITCAT-Me.

Entry	Starting Material	Product	Solvent 1:1 (v/v)	Microwave Irradiation time (min)	Yield (%)
1			EtOH/H ₂ O	2	100
			DMF/H ₂ O	2	100
			EtOH/H ₂ O	6	23
			DMF/H ₂ O	6	30
2			EtOH/H ₂ O	3	100
			DMF/H ₂ O	3	100
			EtOH/H ₂ O	6	23
3			EtOH/H ₂ O	3	80
			DMF/H ₂ O	3	90
			EtOH/H ₂ O	6	68
			DMF/H ₂ O	6	88
4			EtOH/H ₂ O	3	78
			DMF/H ₂ O	3	85
			EtOH/H ₂ O	2	30
			DMF/H ₂ O	2	35
5			EtOH/H ₂ O	8	72
			DMF/H ₂ O	3	86

			EtOH/H ₂ O	12	24
			DMF/H ₂ O	8	72
6			EtOH/H ₂ O	5	22
			DMF/H ₂ O	5	80
7			EtOH/H ₂ O	4	71
			DMF/H ₂ O	4	81
8			EtOH/H ₂ O	4	60
			DMF/H ₂ O	4	80
		Items 1-5, 7-8 CHITCAT-Me			
			Item 6; halide 1.0 eq.; boronic acid /ester 3 eq. for monohalide; 4 eq. for dihalide; 3.5 mol%, KF 3 eq. per halide		

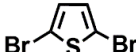
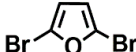
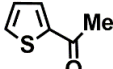
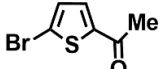
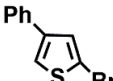
^b Fixed T = 140°C (power 300W).

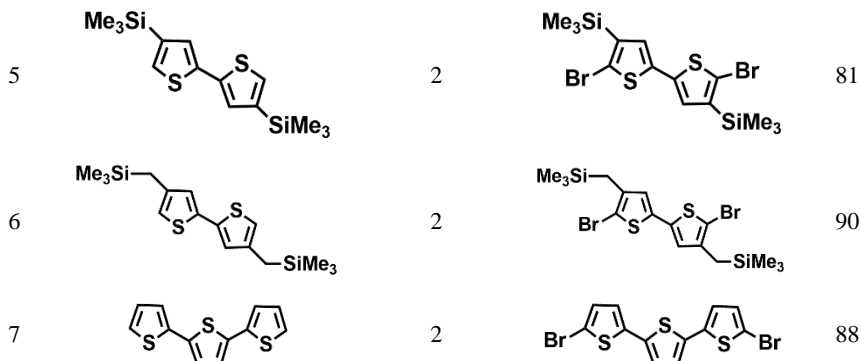
^c GC conversion with respect to *n*-dodecane as internal standard.

Adapted with permission from reference [55]. Copyright 2008 Royal Society of Chemistry.

Ultrasound assistance allows bromination of thiophenes to occur in very mild conditions, in minutes time and with very good to excellent yields depending on substrate structure and on solvent [56]. Table 2 shows a few examples illustrating the importance of ultrasound assistance in selective thiophene bromination. In our experience ultrasound assistance is of invaluable help to achieve selective bromination of large size oligothiophenes rapidly and in good yield (see Scheme 6).

Table 2. Ultrasonic bromination of various thiophenes using N-bromosuccinimide (NBS)

Entry	Substrate	NBS equivalents	Product	Yield (%)
1		2		98
2		2		86
3		1		99
4		1		88



Adapted with permission from reference [56].

III. OLIGO- AND POLYTHIOPHENES IN ORGANIC (OPTO)ELECTRONICS

The thiophene ring is one of the most widely used building blocks in the synthesis of semiconducting conjugated oligomers and polymers to be incorporated into devices for organic electronics. Organic electronics ^[9] is expected to replace in a near future inorganic solid state electronics owing to its advantages in terms of flexibility, low costs, easy deposition of materials on large-area substrates, environmentally benign manufacturing and tunability of electrical properties *via* chemical synthesis. However, organic electronics still needs extensive research to become competitive with the technology based on inorganic materials and only a few commodities - displays for smartphones, portable solar cells, curved television screens and so on - are already available on the market. Organic semiconductors are compatible with biopolymers hence enabling applications that are not achievable, for example, by crystalline silicon technology. One can also speculate that all-organic devices might be integrated with living organisms for therapeutic applications, sensing, or drug delivery ^[57]. Thiophene oligomers and polymers have been employed as active elements in a variety of devices such as light emitting transistors ^[58], lasers ^[59], electrochromic devices ^[60], chemo and biosensors ^[61]. The best results in terms of possible industrial applications are thin film field-effect transistors (FETs) and photovoltaic devices (PVDs). Numerous conjugated oligomers and polymers have been described and investigated in FETs and PVDs with regard to structure-property relationship, fundamental chemical and physical processes, materials optimization, fabrication approaches, materials behaviour at interfaces and elucidation of molecular-scale processes in relation to device working principles.

3.1 Organic Field-effect Transistors (OFETs). All electronic devices are based on charge transport properties of semiconducting materials. OFETs are basic elements for organic electronic circuits and provide information on charge transport properties of π -conjugated oligomers and polymers ^[62]. The first report on the electrical conduction of π -conjugated systems

dates back to 1977 ^[63]. For that discovery Alan Heeger, Alan MacDiarmid, and Hideki Shirakawa were awarded the Nobel Prize in Chemistry in 2000. In contrast to band transport in inorganic semiconductors, charge transport in conjugated materials takes place via several different mechanisms largely dependent on their aggregation state, i.e. whether they are single crystals, liquid crystals, polycrystalline or amorphous compounds. Organic field-effect transistors consist of a layer made of a film of organic semiconductor, a layer acting as gate insulator and three electrodes: drain, source, and gate electrodes.

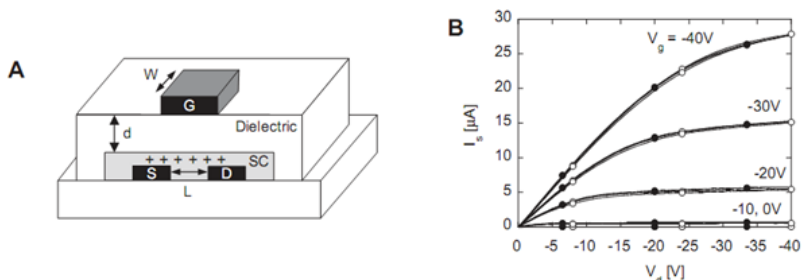


Figure 7. (A) Schematic representation of a standard field-effect transistor device (top-gate architecture) and (B) plot of the corresponding current/voltage output. Adapted with permission from reference [64]. Copyright 2005 Wiley-VCH Verlag GmbH.

Figure 7 shows a schematic representation of a standard FET device (top-gate architecture) and the plot of the corresponding current/voltage output (drain voltage, V_d vs. source current I_s measured in air and light; closed circles: after manufacture, open circles: two weeks later). By means of a FET device it is possible to distinguish positive and negative charge carriers. Theoretical calculations reveal that the intrinsic mobility of holes (positive charges) and electrons in π -conjugated materials should be quite comparable ^[65]. Nevertheless, experimentally measured electron charge mobilities are generally much lower than hole mobilities. The observation of low electron mobilities is the consequence of extrinsic effects, such as the instability of radical-anions with respect to water, oxygen or hydroxyl groups. The charge carriers mobility depends on many inter-correlated factors such as molecular structure and the HOMO-LUMO energy gap, molecular ordering in the organic semiconductor film and orientation of the molecules with respect to the electrodes, intermolecular orbital overlap and film morphology ^[66]. Based on FET measurements, most thiophene-based semiconductors have been characterized as *p*-type materials, i. e. having holes as the majority charge carriers ^[67]. However, several *n*-type thiophene-based materials, i. e. having electrons as the majority charge carriers, have also been demonstrated ^[68]. A detailed description of OFET devices and of charge transport properties of organic semiconductors is given in a recent comprehensive review covering over 700 π -conjugated systems including thiophene oligomers and polymers ^[69]. Figure 8 shows the molecular structure of some of the most investigated *p*-type oligo and polythiophenes and the corresponding FET charge mobilities (μ_h).

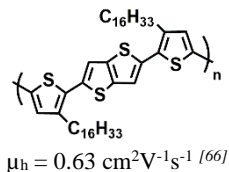
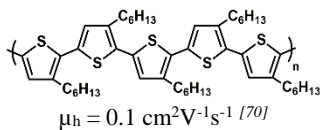
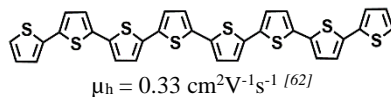
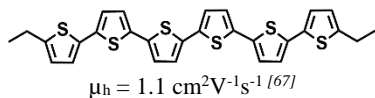


Figure 8 Molecular structures and hole charge mobilities (μ_h) of selected thiophene materials.

To develop functional complementary organic circuitry, both hole-transporting (p-type) and electron transporting (n-type) conjugated materials are required. Introduction of appropriate strong electron-withdrawing substituents into the backbone of π -conjugated compounds [68, 69] allows to achieve n-type charge conduction. Figure 9 shows examples of substituted oligo and polythiophenes displaying good electron mobilities (μ_e) measured employing thin film field-effect transistors.

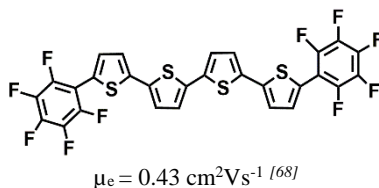
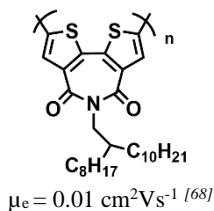
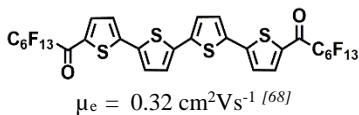


Figure 9 Molecular structures and electron charge mobilities (μ_e) of selected thiophene materials.

In the last few years several ambipolar thiophene copolymers with balanced electron and hole transport have been described [71]. Examples are reported in Figure 10.

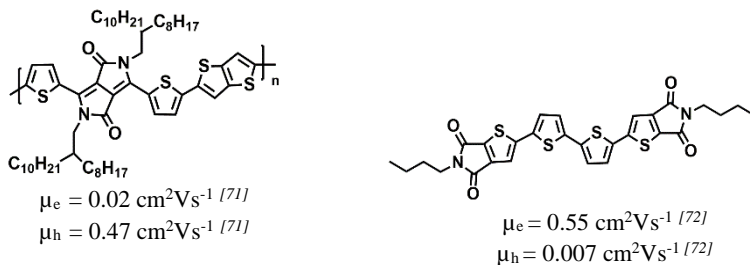


Figure 10 Hole and electron charge mobilities of selected ambipolar thiophene materials.

As already mentioned, the reported FET charge mobilities should not be viewed as only depending on the molecular structure of the organic semiconductor. The right balance between molecular design, packing properties in the solid state, thin film morphology, interfacial layers and device fabrication is needed in order to achieve competitive values for the output of the FET device. Note that the same holds for the photovoltaic devices recalled below.

3.2 Photovoltaic devices. Thiophene oligomers and polymers are among the most important active elements of organic devices for the photovoltaic conversion of solar energy, i.e. the green transformation of solar energy into electricity for the solution of modern energy and environmental problems. Existing commercial solar cells are mostly based on the costly crystalline or amorphous silicon technologies. Organic photovoltaics - based on π -conjugated small molecules, oligomers or polymers - represents an interesting alternative to low-cost solar energy conversion, owing to its compatibility with flexible substrates, inexpensive room-temperature large area film deposition and property tunability of the active materials *via* organic synthesis [73]. The extensive studies of the last few years have led to remarkable improvements not only in power conversion efficiency of organic solar cells (today >10% vs >28% for silicon solar cells) but also in terms of device stability and reliability [74]. There are two fundamental architectures for organic solar cells, namely bilayer structure and bulk heterojunction (BHJ), as illustrated in Figure 11. The former is obtained by separate vacuum deposition of donor and acceptor components; the latter is based on blends of soluble donor and acceptor components in a bulk volume to maximize the interfacial area between components. The advantage of BHJ devices is that the composite active layer can be processed in solution in a single step. Typical donor components are π -conjugated polymers, including thiophene-based ones. Because of its high electron affinity and charge transport properties (n-type) fullerene and its derivatives are the best acceptor component currently available for these devices. However, research is going on to attain equal or better results employing non-fullerene acceptors [75].

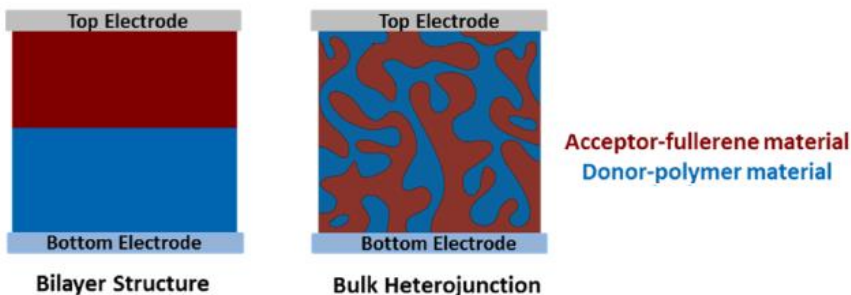


Figure 11. Architectures for organic solar cells: bilayer structure and bulk-heterojunction. Adapted with permission from reference [76].

The first step in the photovoltaic process is light absorption. Solar cells are tested using solar simulators with a spectral intensity distribution matching that of the sun on the earth's surface (AM 1.5 spectrum). In this process, the incident photon is absorbed by the active organic material leading to the generation of excitons (coulombically bound hole-electron pairs) in the excited state which subsequently diffuse to a region where exciton dissociation, i.e. charge separation, takes place followed by migration of the charges within the organic medium to the respective electrodes. Exciton dissociation occurs at the interfaces of the donor and acceptor materials because of their different chemical potentials (Figure 12).

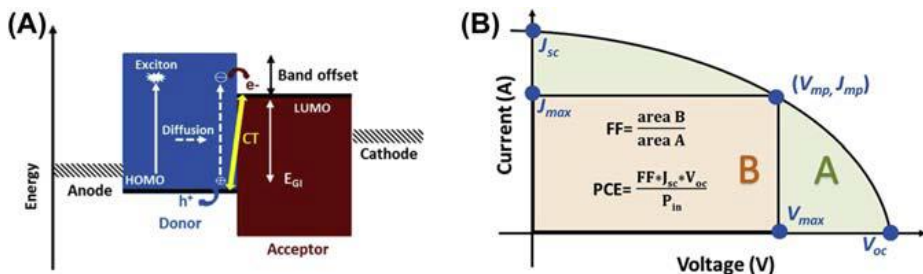


Figure 12. (A) Energy band diagram and interface optical transitions of the bulk-heterojunction cell and (B) typical current-voltage J/V plot of an organic solar cell. Adapted with permission from reference [76].

To achieve substantial power conversion efficiencies, excitons need to be dissociated into free charge carriers with a high yield. For efficient charge separation a large interface between the donor/acceptor phases is needed. The device efficiency is largely influenced by the morphology of donor/acceptor composites at the nanoscale, which, in turn, is dependent on the composition of the blend and on factors such as the solvent used and the processing temperature [77]. As the positive electrode, indium tin-oxide (ITO) coated glass is generally used. ITO, a transparent conducting substrate, acts as hole contact matching the HOMO levels of most conjugated

polymers. On ITO, a PEDOT:PSS layer is generally coated from an aqueous solution. PEDOT:PSS, namely poly(ethylene-dioxythiophene) doped with polystyrenesulfonic acid (also transparent), improves the surface quality of the electrode and facilitates hole injection/extraction. The active layer, consisting of the donor-acceptor blend, is coated on top of this electrode. As the negative electrode, a metal layer whose work function matches the LUMO of most acceptors is evaporated. The device performance of a photovoltaic cell is characterized by the short circuit current I_{SC} (related to the photoinduced charge carrier density and the charge carrier mobility within the organic semiconductors), the open-circuit voltage V_{OC} (related to the energy difference between the HOMO of the donor and the LUMO of the acceptor) and the fill factor FF (related to the charge carriers reaching the electrodes and to device quality). The higher the value of these parameters the larger the light to electricity power conversion efficiency defined by $\eta_e = (I_{SC} \cdot V_{OC} \cdot FF) / P_{in}$, where P_{in} is the incident light power. The control of the positions of the HOMO and LUMO energy levels of the donor and acceptor materials is a stringent condition to achieve good performance in PVDs. Figure 12 shows the energy bands diagram and the interface optical transitions of the BHJ cell. Owing to their optical properties and charge transport characteristics, oligo and polythiophenes are among the best-conjugated materials for solar cells. The control of the HOMO-LUMO energy levels and energy gap of thiophene-based materials has been the focus of the synthetic chemistry of functional π -conjugated systems for photovoltaic applications in the last few years. Most researches were aimed to prepare thiophene oligomers and polymers with HOMO-LUMO energy gaps much lower than that of poly(3-hexylthiophene), P3HT. P3HT is one of the best electron-donor materials and devices with P3HT as electron donor material and a fullerene derivative as electron acceptor counterpart have attained 7.40% conversion efficiency ^[78]. Thiophene based polymers with lower energy gap than P3HT (Low Band Gap polymers ^[79]) can achieve higher efficiency but the devices based on these polymers present stability and reproducibility problems. Moreover, the syntheses generally suffer from scalability problems and the electron acceptor counterparts are fullerene derivatives, which not only are expensive materials but also display limited spectral absorption and morphological instability. Very recently, high-efficiency and air-stable P3HT-based solar cells with a new non-fullerene acceptor have been reported ^[80]. The molecular structure of the non-fullerene acceptor, compound O-IDTBR, is shown in Figure 13. Solar cells with P3HT and O-IDTBR as active materials display very high air stability. Taking into account that P3HT is one of the very few polymers available in quantities over 10 kg ^[81], the P3HT/O-IDTBR donor-acceptor combination has great potential for future technological applications in the field of photovoltaic devices. Figure 13 shows the molecular structure of a thiophene-based polymer (PDBCT) and a thiophene-based oligomer (DRCN7T) that combined to the electron acceptor [6,6]-phenyl-C71-butyric acid methyl ester (PC₇₁BM) allow the fabrication of solar cells with high conversion efficiency.

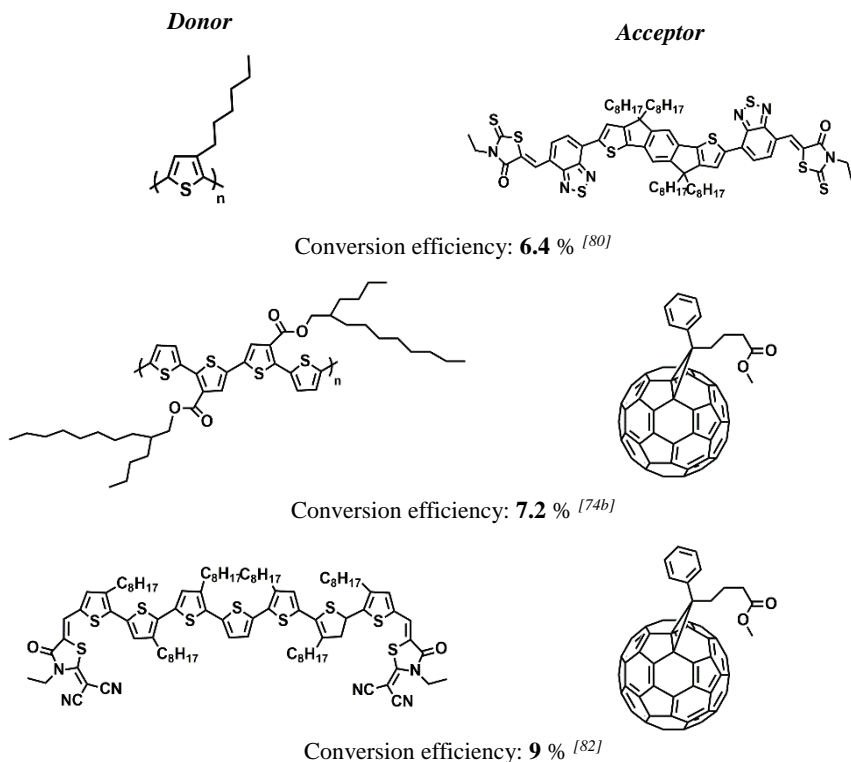


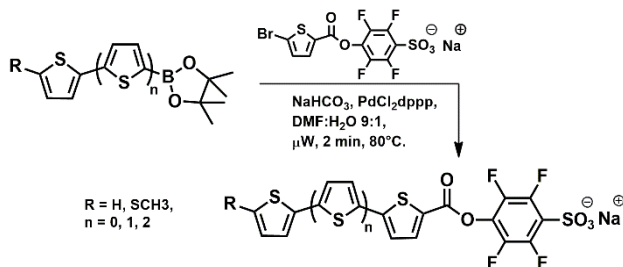
Figure 13. Donor/Acceptor molecular structures and conversion efficiencies of the corresponding photovoltaic devices

IV. THIOPHENE OLIGOMERS AS FLUORESCENT PROBES.

Similar to polythiophenes, the fluorescence emission of thiophene oligomers can be tuned from blue to near infrared by accurate choice of size and substituents ^[83]. Oligothiophenes are chemically and optically very stable compounds. Contrary to most organic fluorescent probes, they do not undergo photobleaching nor blinking but give an intense and persistent signal. They display large Stokes shifts (difference between absorption and emission signals) mainly due to planarization in the excited state. This characteristic, which is in principle an advantage due to no overlap between emission and absorption signals, is presently an inconvenience due to the fact that the currently employed instrumentation for fluorescence detection is set on fluorescein which has a very small Stokes shifts. The rigidity of the market has prevented so far the exploitation of the advantageous properties of oligothiophene fluorophores, including the fact that they are the only fluorophores possessing semiconducting characteristics. Moreover, the

wide light emission tunability of thiophene fluorophores via organic synthesis renders it possible to do multilabeling experiments using fluorophores belonging to the same chemical family and functionalized with the same reactive group for covalently binding molecules of biological interest. Finally, another characteristic that makes oligothiophene fluorophores unique is their capability to recognize specific proteins inside live cells and live animals, as shown in the sections below.

4.1 Labeling of proteins and DNA and staining of live cells. A series of thiophene fluorophores functionalized at the one terminal position with the amine-reactive 4-sulfo-2,3,5,6-tetrafluorophenyl (STP) ester group was prepared rapidly, in good yield and in very pure form by means of Suzuki coupling with microwave assistance [84]. In this class of fluorophores, the tuning of the emission frequency was achieved by changing the oligomer size and/or adding one terminal SCH₃ substituent. Scheme 19 shows the preparation of the fluorophores, while table 3 and figure 14 illustrate their optical activity.



Scheme 19

Table 3. Absorption (λ_{max} , nm) and photoluminescence (λ_{PL} , nm) wavelengths, molar absorption coefficients (ϵ , mol⁻¹cm⁻¹) and fluorescence quantum yields (ϕ)^a of fluorophores **1-6** 10⁻⁵ M in DMSO.

Item	λ_{max}	ϵ	λ_{PL}	Φ	Item	λ_{max}	ϵ	λ_{PL}	ϕ
1 ^b	353	23200	430	0.78	4	410	21200	580	0.35
2	376	19900	503	0.70	5	429	31900	555	0.26
3	400	24100	508	0.27	6	434	34300	515	0.26
								625 ^c	

^a Estimated error: ± 0.05 .

^b 1 \rightarrow n = 0, R = H; 2 \rightarrow n = 0, R = SCH₃; 3 \rightarrow n = 1, R = H; 4 \rightarrow n = 1, R = SCH₃;

5 \rightarrow n = 2, R = H; 6 \rightarrow n = 2, R = SCH₃.

^c DMSO:H₂O 90:10.

Adapted with permission from reference [84]. Copyright 2009 American Chemical Society.

It is seen that on increasing the oligomer size there is a progressive *increase* in both absorption (λ_{max}) and emission (λ_{PL}) wavelengths accompanied by a progressive *decrease* in quantum yield (ϕ , the ratio of photon absorbed to photons emitted).

The decrease in ϕ on increasing the oligomer's size is opposite to what is observed for unsubstituted oligomers [85]. Fluorophores 1-6 can be covalently bonded to proteins, including monoclonal antibodies (MoAb), since the STP ester functionality reacts with the ϵ -NH₂ groups of lysine residues in basic conditions to form an amidic bond according to:

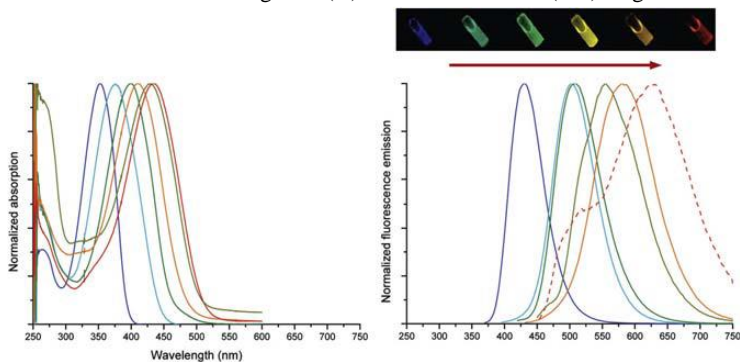


Figure 14. Normalized absorption and emission spectra of thiophene-based fluorophores (1-6). Adapted with permission from reference [84]. Copyright 2009 American Chemical Society.

Figure 15 shows the normalized absorption and emission spectra of anti-CD38 monoclonal antibody (MoAb) labeled with 1-6 (incubation time: 30 min). The arrows in figure 15 indicate the 286 nm absorption signal of the antibody. Fluorophore to protein ratios up to 12 were achieved. The labeled antibodies were chemically and optically very stable, with unaltered biological activity and fluorescence properties for years when stored at 4°C [84].

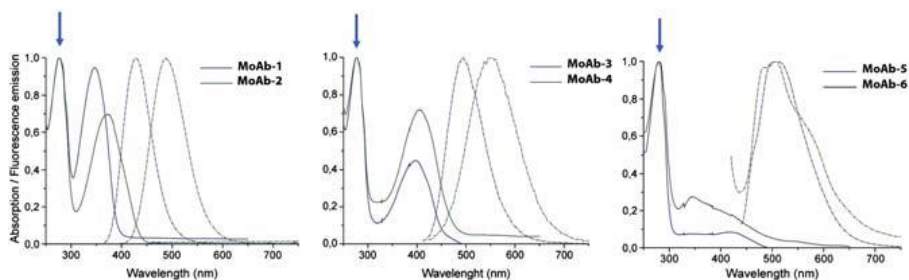


Figure 15. Normalized absorption and emission spectra of anti-CD38 monoclonal antibody (MoAb) labeled with thiophene-based 1-6 fluorophores. Adapted with permission from reference [84]. Copyright 2009 American Chemical Society.

The photostability of fluorophores 1-6 (figure 14) allowed the easy achievement of multilabeling experiments. Figure 16 shows the normalized absorption and emission spectra of a white fluorescent anti-CD38 MoAb obtained by simultaneous reaction with fluorophores 1 (blue

emitting) and 4 (orange emitting) in appropriate proportion [84]. The photograph reported in Figure 16 is that of the anti-CD38 MoAb within a Sephadex column under irradiation with a 15W UV lamp at $\lambda_{exc} = 364$ nm and displaying intense white fluorescence.

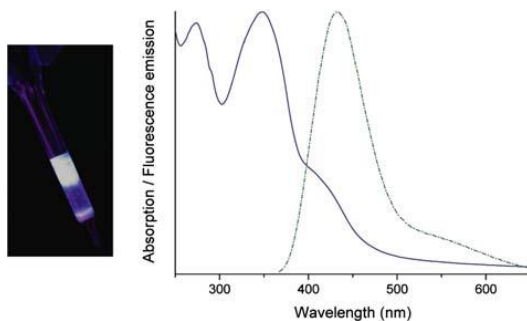


Figure 16. Anti-CD38 MoAb labeled with fluorophores 1 (blue emitting) and 4 (orange emitting) displaying white fluorescence in sephadex column under illumination. Reprinted with permission from reference [84]. Copyright 2009 American Chemical Society.

An alternative approach to obtain a wide emission range was achieved with compounds 7-10 whose molecular structure and emission region is shown in Figure 17 while the corresponding synthetic patterns are reported in Scheme 20.

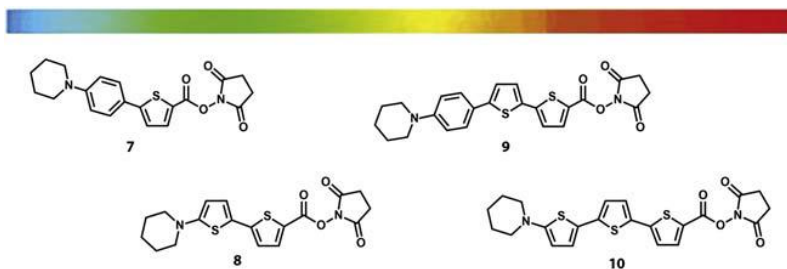
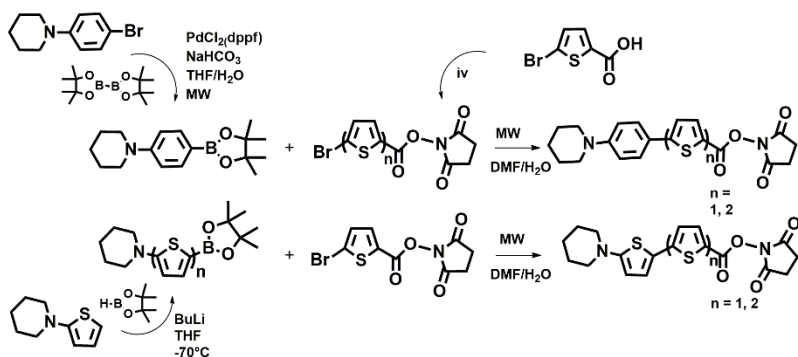


Figure 17. Molecular structures and emission region of thiophene-based fluorophores 7-10. Adapted with permission from reference [86]. Copyright 2014 Royal Society of Chemistry.

The synthesis is again based on the Suzuki reaction and microwave assistance, a methodology affording the desired compounds rapidly, in high yields and very pure. The optical properties of **7-10** in solution are reported in Table 4. In this case very high fluorescence quantum yields were achieved also in the case of tetramer 4. Fluorophores **7-10** (as well as those of Table 3) are able to cross the membrane of the cells and were not toxic to them. Their cytotoxicity towards NIH-3T3 mouse fibroblast cells was investigated by the MTT cytotoxicity test (Figure 18). This test is commonly used to assess the viability of live cells through mitochondrial dehydrogenase

activity measured by the presence of 3-[4,5-dimethylthiazol-2-yl]-2,5-diphenyl tetrazolium bromide [87].



Scheme 20

Table 4. Absorption (λ_{\max} , nm) and photoluminescence (λ_{PL} , nm) wavelengths, molar absorption coefficients (ϵ , $\text{mol}^{-1}\text{cm}^{-1}$) and fluorescence quantum yields (Φ)^a of fluorophores **7-10**.

Item	λ_{\max}	λ_{PL}	ϵ	Φ ^b
7	381	465	28400	1
8	430	509	22300	0.92
9	414	530	59800	0.92
10	443	581	19200	0.80

^a In toluene.

^b With respect to perylene in ethanol, $\Phi_{\text{ref}} = 0.92$.

Adapted with permission from reference [86]. Copyright 2014 Royal Society of Chemistry.

The tests indicated that cell viability upon treatment with fluorophores **7-10** was close to that of nontreated cells.

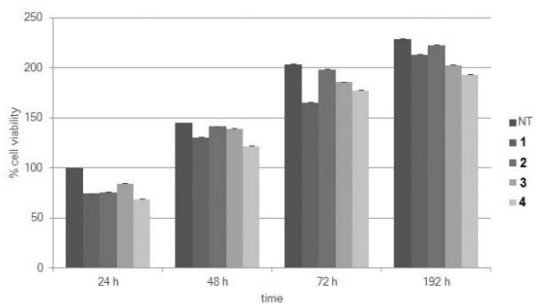


Figure 18. MTT cytotoxicity test of fluorophores 7-10 towards NIH-3T3 mouse fibroblast cells. Reprinted with permission from reference [86]. Copyright 2014 Royal Society of Chemistry.

Figure 19 shows the Laser Scanning Confocal Microscopy (LSCM) images of live NIH-3T3 cells treated with the green emitting fluorophore **7** and the red emitting fluorophore **10** monitored after 24 h from cell treatment with the fluorophores in physiological solution ^[86].

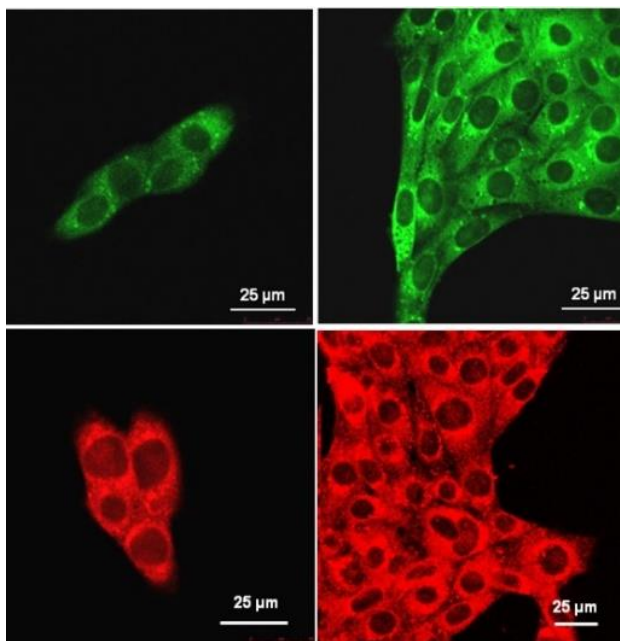


Figure 19. Laser Scanning Confocal Microscopy images of NIH-3T3 cells treated with the green emitting fluorophore **7** and the red emitting fluorophore **10**. Reproduced with permission from reference [86]. Copyright 2014 Royal Society of Chemistry.

It is seen that both fluorophores caused the staining of cells cytoplasm, green or red depending on the fluorophore, while the nucleus of the cells remained unstained. The staining of the cells was caused by the reaction of the N-hydroxysuccinimidyl (NHS) ester groups of the fluorophores with the primary amine groups of the proteins present in the cytoplasm. During cell proliferation, the fluorescence is transmitted from mother to daughter cells, and fluorescent cells were observed even after one week from treatment with the fluorophores ^[86]. Several studies have been carried out on the labeling of oligonucleotides with thiophene fluorophores, described in some detail in the review ^[88]. There are several methods for the fluorescent labeling of oligonucleotides, including the use of oligothiophenes functionalized with the NHS. This route has been used to synthesize a series of oligonucleotides to be employed as molecular beacons ^[89]. MB are dual-labeled oligonucleotides having self-complementary ends that spontaneously form a hairpin structure (see Figure 20) that puts their 5' and 3' ends in close proximity ^[90].

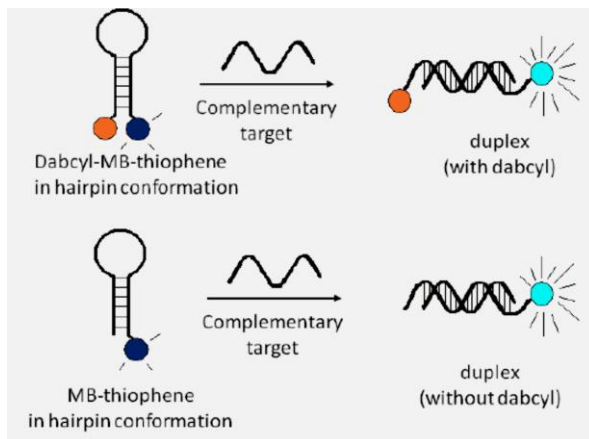


Figure 20. Dabcyl and thiophene fluorophore labeled oligonucleotide in hairpin structure (molecular beacon = MB) and the effect of hybridization in the presence in the complementary strand. Reprinted with permission from reference [88].

A MB, its complementary target and the MB functionalized with 4-([4-(Dimethylamino)phenyl]azo)benzoic acid succinimidyl ester (Dabcyl) at one terminal position were prepared. Figure 21A shows the structure of the MB (where the underlined bases form the hairpin system) together with the structure of the complementary oligonucleotide. The MB was functionalized at the 5' position with Dabcyl, which is a well-known fluorescence resonance energy acceptor (quencher), *characterized by an intense visible absorption but no fluorescence*. Afterwards the Dabcyl-MB was reacted at the 3' position with a series of thiophene fluorophores functionalized with the NHS ester group to form Dabcyl-MB-Thio systems, as shown in Figure 21B.

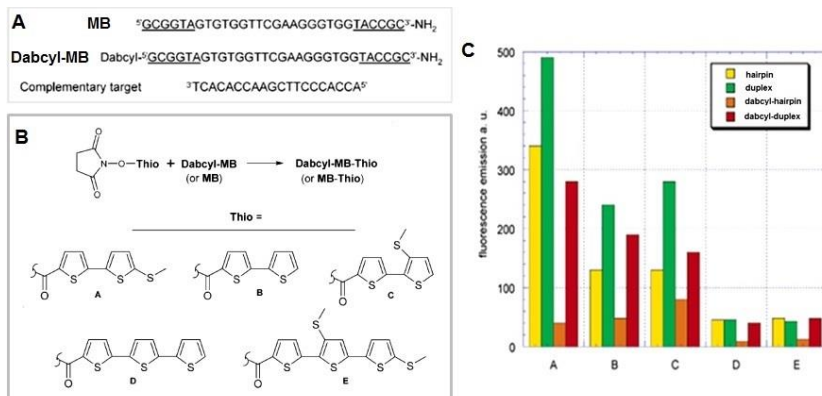


Figure 21. Adapted with permission from reference [89]. Copyright 2007 American Chemical Society.

The thiophene fluorophores were chosen for their intense fluorescence in water and the overlap of their emission with the absorption signal of Dabcyl. In the hairpin form the Dabcyl-MB-Thio system is not fluorescent owing to the proximity between the fluorophore and the quencher. However, when the complementary strand is added, hybridization occurs (figure 20) causing the removal of the hairpine conformation so that the dabcyl and fluorophore terminals become distant and the fluorescence is restored. Figure 21C shows the relative fluorescence variations for the process described in Figure 20.

4.2 Side-chain functionalized quinquethiophenes as optical ligands for the detection of protein aggregates present in neurodegenerative diseases. In recent years, it has been demonstrated that some thiophene oligomers display a striking capability to specifically bind protein aggregates such as amyloid fibrils. Amyloid fibrils are abnormal aggregations of misfolded proteins involved in several neurovegetative diseases like Alzheimer’s and prion diseases. Despite significant advances in the understanding of amyloid aggregates, detailed knowledge on the initial stages of their formation hence on the pathogenesis underlying the disease is still lacking. A few fluorescent quinquethiophenes have been demonstrated to be important diagnostic tools and potential pharmacophores in amyloid diseases, in particular in Alzheimer’s disease. They are able to selectively target the amyloid plaques inside cells, tissues and even *in vivo*, discriminating among the myriads of proteins and biomolecules present in the environment. In particular, great effort has been put into early, ideally pre-symptomatic detection of amyloid plaques in Alzheimer’s disease [91]. Figure 22 shows the molecular structure of two typical functionalized quinquethiophenes, p-HTAA and p-FTAA employed in those studies, both prepared via Suzuki coupling. The conjugated backbone of p-HTAA is flexible and torsional rotations modify the π -conjugation degree hence the absorption and emission signals.

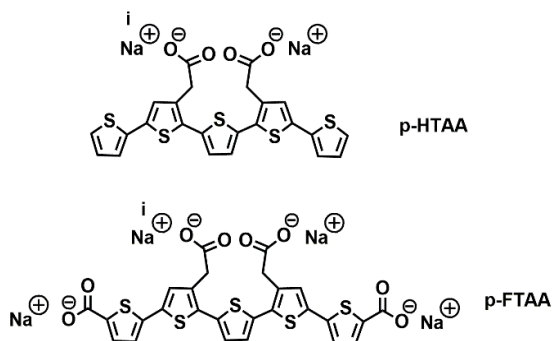
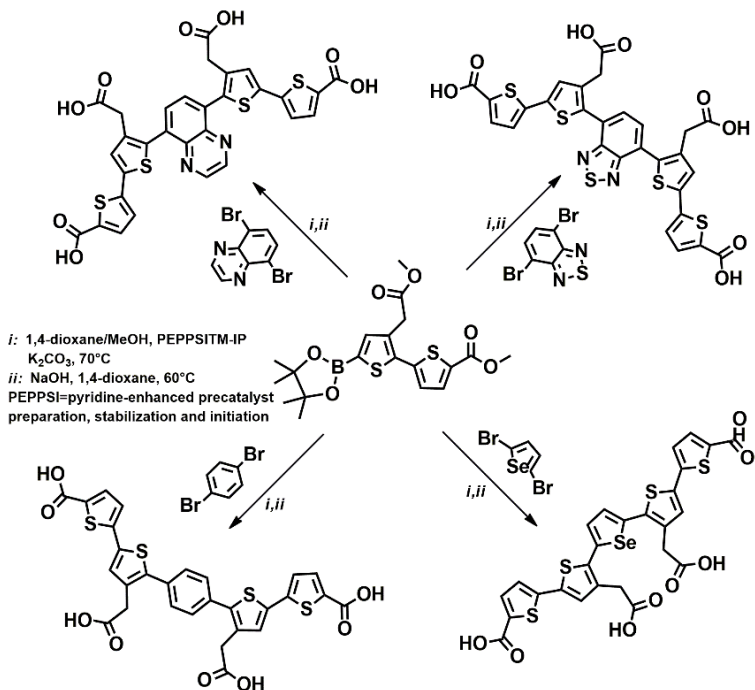


Figure 22

The geometry variations of the flexible thiophene backbone modulate absorption and fluorescence emission. It was found that, owing to changes in the conformation of the aromatic backbone, both absorption and emission wavelengths of the oligothiophenes undergo a red shift upon exposure to amyloid fibrils. Thus, such changes were used to monitor the kinetics of

amyloid formation *in vitro* as well as to discriminate amyloid from non-amyloid protein fibrils [92]. The fluorophore was able to bind to both the native form of the proteins as well as to the amyloid fibrillar form. The binding of the different forms caused different changes in the thiophene backbone conformation resulting in wavelength changes capable to distinguish the two forms of the proteins. A modification of p-HTAA, namely quinquethiophene p-FTAA (Figure 22) was developed for *in vivo* staining of amyloid deposits. It effectively was able to cross the blood-brain barrier and imaging could be performed [91a,2]. The probe p-FTAA shows the unique property to detect soluble prefibrillar assemblies, in contrast to conventional amyloid probes [91a]. It has been reported that p-FTTA is not only a diagnostic tool but it is also capable to reduce the pool of soluble toxic amyloid plaques in favor of larger insoluble nontoxic amyloid fibrils suggesting that it might have therapeutic potential [91f]. Several chemical modifications of p-FTAA have been studied in the attempt to obtain compounds capable of enhancing the spectral discrimination between different amyloid plaques and fibrils [35, 91d]. Scheme 21 reports the synthesis of several pentamers starting from a boron derivative whose preparation is reported in reference [91d]. As illustrated in Scheme 21, the inner thiophene unit was replaced by selenophene or phenylene moieties by employing the Suzuki reaction.



Scheme 21. Adapted with permission from reference [91d]. Copyright 2015 Wiley-VCH Verlag GmbH.

These replacements allowed to obtain a wide range of emission colors, generally accompanied by a decrease in fluorescence intensity. Moreover, they also led to the rigidification of the aromatic backbone while conformational freedom of the backbone was essential for discrimination of the hallmark of Alzheimer's disease. In other words, conformational freedom and extended π -conjugation were identified as crucial factors for detection and spectral assignment of disease-associated protein aggregates. Several side-chain functionalized quinquethiophenes were also tested for fluorescent staining of fixed and live cells with the aim of identifying by fluorescence microscopy and cytometry probes capable of distinguishing between normal and malignant cells (2014C628, 2015FC58); among them p-HTIm and p-HTMI (Figure 23) which are characterized by intense orange-red fluorescence.

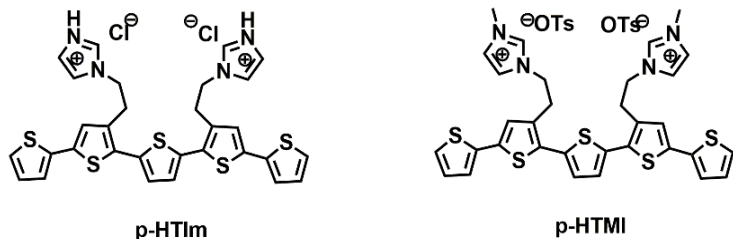
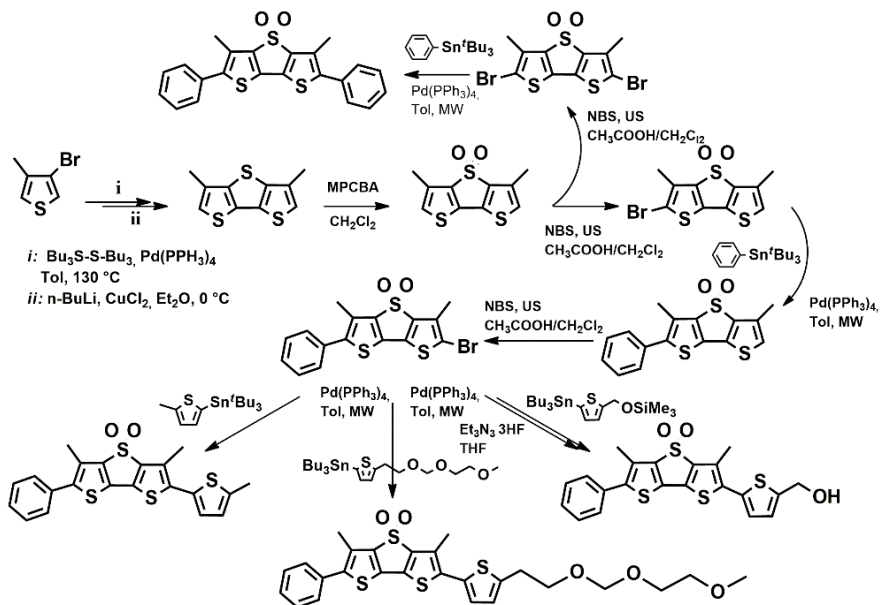


Figure 23

The absorption and emission spectra of p-HTIm and p-HTMI were recorded 1.5 mM in PBS (pH=7.4). Several normal and tumor cells were tested ^[12, 93]. The quinquethiophenes were able to stain both fixed and live cells. Confocal imaging showed that they accumulate in cell cytoplasm while the nucleus remains unstained. In the case of live cells the staining of the quinquethiophenes was not toxic to the cells and the staining persisted for up to four days. Quinquethiophene p-HTIm labeled the cells with the highest intensity as revealed by flow cytometry. Further studies on p-HTIm showed that it displays different staining patterns in normal and malignant cells ^[93]. Both the staining ability and the cells selectivity were reduced when the side chains underwent chemical modifications, demonstrating that staining and selectivity towards specific cellular targets can only be achieved with precise functionalization and regiochemistry of substitution of the aromatic backbone.

4.3 Physiologically driven co-assembly of oligothiophene fluorophores with specific proteins inside live cells Scheme 22 shows the the microwave and ultrasound assisted synthesis of a set of green fluorescent derivatives of 3,5-dimethyl-dithieno[3,2-*b*:2',3'-*d*]thiophene-4,4'-dioxide. These compounds were able to cross the cell membrane of live mouse embryonic fibroblasts (NIH-3T3) and cervix carcinoma (HeLa) cells and recognize and coassemble with specific intracellular proteins ^[94, 8b]. Membrane-permeable molecules enter the cells predominantly by diffusion across cellular lipid bilayers ^[87] hence the compounds possess the right balance of hydrophobicity and hydrophilicity needed to cross the membrane. The compounds are not toxic to the cells with the exception of the CH₂OH substituted derivative.



Scheme 22. Adapted from reference [94]. Copyright 2011 American Chemical Society.

Upon spontaneous uptake of the fluorophores, the cells secrete nanostructured green fluorescent microfibers displaying helical supramolecular organization and being mainly made of type-I-collagen. The fluorescent microfibers were not the result of the mere labeling by the fluorophore of already present fibrillar collagen inside live cells. Instead, the fluorophore, which was accumulating in the perinuclear region where the intracellular proteins are formed, was recognized and progressively incorporated during the phase of protocollagen formation, leading to nanostructured protein-fluorophore microfibers and protein-templated supramolecular organization of the fluorophore. The stereoelectronic characteristics of the fluorophore were such that the subsequent formation of collagen triple helices is not perturbed. The collagen-fluorophore microfibers were then extruded into the extracellular matrix from where they could be isolated and analyzed. Thanks to the semiconducting properties of the fluorophore, besides being fluorescent, the microfibers were also conductive. Thus the fluorophore did transfer additional properties to the protein without perturbing its morphology and function^[95]. The formation of the fluorescent microfibers was followed in real time by Laser Scanning Confocal Microscopy. Figure 24 shows the LSCM images of live human fibroblasts upon spontaneous uptake of the 2,6-diphenyl derivative (compound **11** in Figure 24). It can be seen that after 120 hours from incubation a thick network of green fluorescent microfibers is formed (Figure 24 A(b), scale bar: 25 μm). LSCM 3D spatial reconstruction displayed in Figure 24A(c-e) reveals the helical morphology of the microfibers [scale bars: (c) 50 μm ; (d,e) 25 μm].

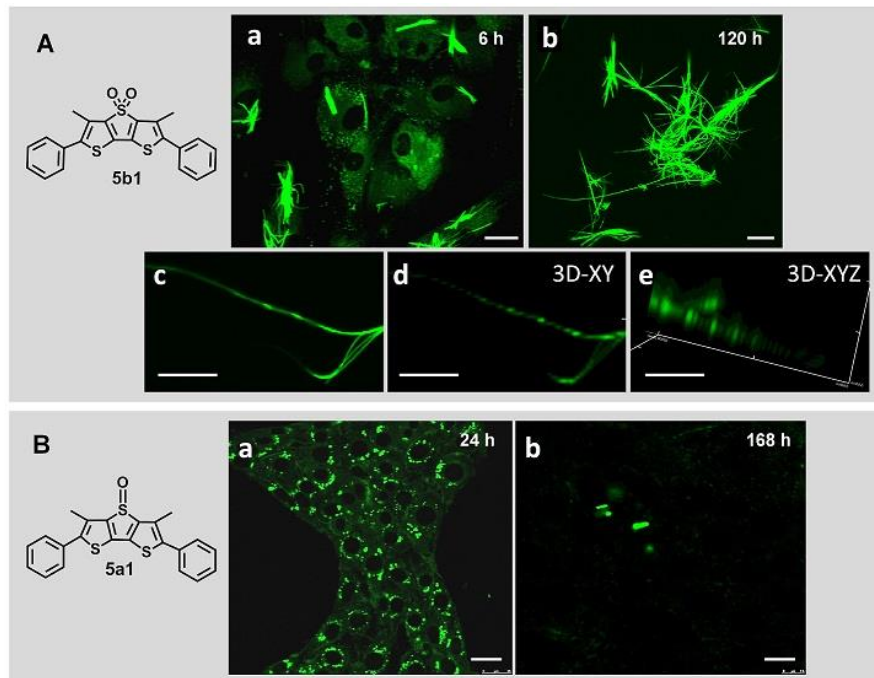


Figure 24. Different behavior of live NIH-3T3 mouse embryonic fibroblast cells upon uptake of S,S-dioxide **11** and the corresponding S-oxide **12** in buffer (pH 7.4) solution. In the first case the physiological formation of type-I collagen/**11** coassembled green fluorescent microfibers is observed, in the second case **12** is eliminated by the cells. Scale bars: 25 μm (A: a, b); 50 μm (A: c) 25 μm (A: d, e) 75 μm (B: a, b). Adapted with permission from reference [5b]. Copyright 2016 Wiley-VCH Verlag GmbH.

Due to the semiconducting nature of the fluorophore, the microfibers also display electrical conductivity [95]. The corresponding S-oxide (compound **12** in Figure 24) is also a green fluorescent cell-permeant compound not toxic to the cells. However, contrary to the S,S-dioxide, the uptake by live human fibroblasts does not lead to the formation of fluorescent microfibers. Figure 24B(b) (scale bar: 75 μm) shows that 168 hours from spontaneous uptake the compound has been almost entirely eliminated by the cells. The different behavior of the S,S-dioxide and the S-oxide has been accounted for in terms of hydrogen bond formation between the fluorophore and the hydroxyproline component of collagen [5b]. The capability of 2,6-diphenyl-3,5-dimethyl-dithiolo[3,2-b:2',3'-d]thiophene-4,4-dioxide (**11**, DTTO) to cause the physiological secretion of fluorescent microfibers upon spontaneous uptake from fibroblasts extends also to living cells derived by different tissue contexts. Indeed, the compound is also specifically recognized by the fibrillar protein vimentin inside live neuroblastoma B104 cells, leading to the physiological secretion of fluorescent vimentin-DTTO microfibers [96].

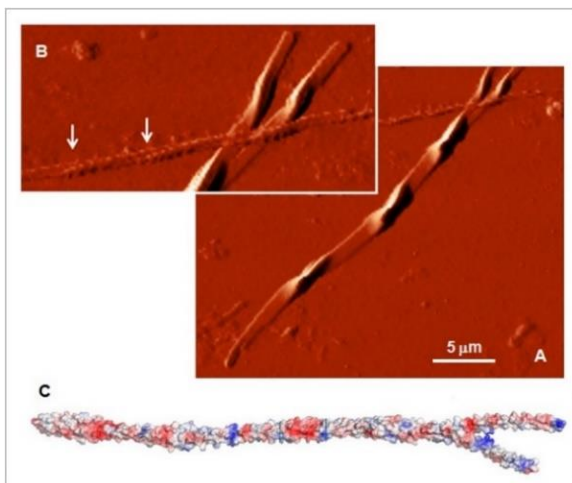


Figure 25. (A), (B) Atomic force microscopy image of a vimentin/**11** coassembled green fluorescent microfiber physiologically formed upon spontaneous uptake of **11** in buffer (pH 7.4) solution by live neuroblastoma B104 cells. Reprinted from reference [96] with permission. Copyright 2015 Royal Society of Chemistry.

Figure 25 shows the Atomic Force Microscopy (AFM) image of fluorescent microfibers isolated from the cellular milieu. The morphology of the largest microfiber is similar to the structure of the dimer of vimentin corresponding to the first level of vimentin self-assembly^[97]. The arrows in the inset indicate the coiled-coil arrangement of two smaller microfibers. It has **also** been demonstrated that various types of live cells seeded on the physiologically produced fluorescent microfibers are able to internalize and degrade them experiencing in turn a different fate in terms of cellular morphology, cytoskeleton rearrangement and viability. These results suggest that the microfibers could be used as biomaterials to direct cell behavior.

V. OLIGO/POLYTHIOPHENE-BASED NANOPARTICLES AND MICROFIBERS

It is well established that for thiophene-based materials the morphology in the solid state has a significant impact on the optical and electrical properties hence on the performance of thin film devices employed in organic electronics. Owing to different processing conditions, to the ‘plasticity’ of the thiophene ring and to multiple possible non-bonding interactions^[8b], there is a great diversity of possible morphologies for the same molecular structure when passing from solution to the solid state (see for example reference^[98] for P3HT). In the lack of well-defined criteria to predict and obtain the ideal thin film morphology for a specific application, a trial and error procedure is required to achieve the optimization of the deposition technique, of the solvent, of the post-fabrication treatment. Moreover, to meet environmental and health safety standards the devices should be fabricated avoiding the use of toxic organic solvents (chlorinated in

particular) to obtain thin film active layers. It is why there is current interest in the use of colloidal nanoparticles as an alternative to obtain semicrystalline active layers deposited from water for use in organic electronics. The expectation is that conjugated systems preorganized into nanostructures would furnish an easier access to the desired morphology without altering the initial optical and electronic properties. In addition, the active layers could be deposited over large areas through methods such as ink-jet printing or spray-coating of nanoparticle dispersions in water.

Water dispersed poly(3-hexylthiophene) nanoparticles deposited on appropriate substrates have been investigated as active layers in field-effect transistors and photovoltaic cells [17, 99]. Figure 25 shows a sketch illustrating the preparation of P3HT nanoparticles (NPs-P3HT) by the reprecipitation method [100]. In a typical preparation a 0.5 wt % P3HT solution in THF (or other organic solvent miscible with water) is loaded into a syringe and introduced dropwise into water (5 mL) under magnetic stirring. The preparation can also be carried out in the presence of surfactants directly dissolved in the aqueous medium, such as sodium dodecyl sulfate (SDS), to stabilize the resulting colloidal suspension. After nanoprecipitation, the residual organic solvent is removed by dialyzing the nanoparticle suspension with dialysis membrane against large amounts of pure water. Finally, centrifugation at different rates and separation of supernatant from the precipitate gives monodisperse nanoparticles samples with a wide range of dimensions from 100 nm to 1 μm .

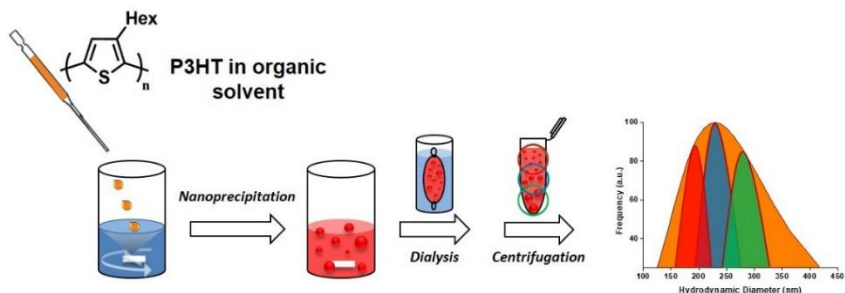


Figure 26

The dimension of the nanoparticles depends on the organic solvent (or mixture of solvents) used, on polymer concentration, on polydispersity and regioregularity of the polymer. Size and size-dispersity of the nanoparticles are determined by Dynamic Light Scattering (DLS). By appropriate use of solvent mixtures it is also possible to tune the P3HT organization both in the internal and the external region of the nanoparticles [101]. Figure 27 shows the Transmission Electron Microscopy (TEM) images of P3HT nanoparticles synthesized from different mixtures of organic solvents using 0.5 wt % P3HT solution and 1 mM SDS surfactant [101]. The plots in the figure indicate the size, measured by DLS, of NPs-P3HT obtained with different solvents.

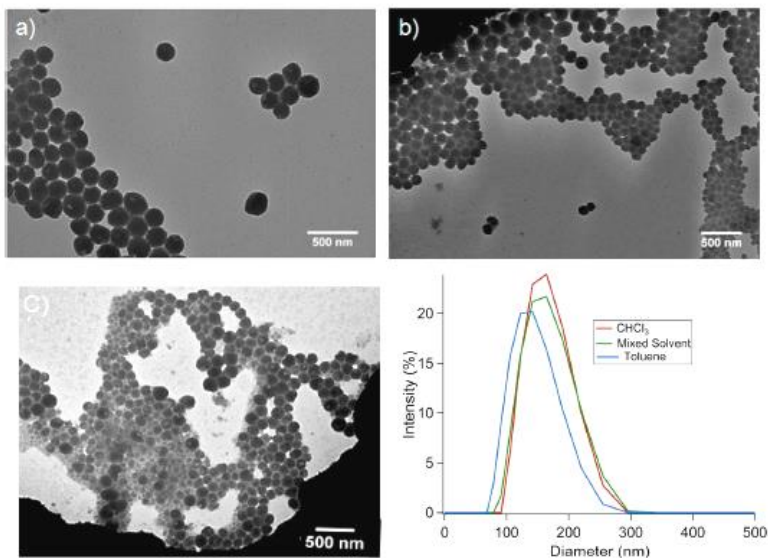


Figure 27. (A), (B), and (C): Transmission Electron Microscopy images of poly(3-hexyl)thiophene nanoparticles synthesized from different mixtures of organic solvents. The plots in the figure indicate the Dynamic Light Scattering size of the nanoparticles obtained with different solvents. From reference [101]. Copyright 2012 American Chemical Society.

Based on a detailed analysis of absorption and emission spectra it was found that NPs-P3HT prepared using chloroform as the solvent have the largest degree of internal structural disorder while there is a higher structural order in NPs-P3HT prepared using a mixture of organic solvents. It is to note that the impact of solvent on P3HT aggregation within nanoparticles is quite different from the impact observed in thin films^[101].

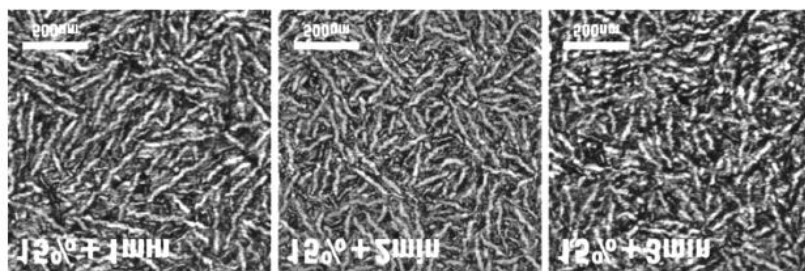


Figure 28. Atomic force microscopy images of poly(3-hexyl)thiophene thin films prepared as a function of ultrasound irradiation time. Reprinted with permission from reference [103b]. Copyright 2015 Wiley-VCH Verlag GmbH.

Field-effect transistors having spin-coated NPs-P3HT active layers showed *p*-type charge mobilities comparable to those obtained for cast films of P3HT from solution ^[102], indicating that the semiconducting properties of the polymer are not degraded by the formation of the nanoparticles. Recently, aqueous suspensions of P3HT-PCBM nanoparticles (P3HT electron donor, PCBM = [6,6]-phenyl C61 butyric acid methyl ester electron acceptor) have been employed to obtain the active layer of photovoltaic cells ^[99b]. Two types of nanoparticles were prepared, namely nanoparticles obtained from a blend of P3HT with PCBM or separate nanoparticles containing either P3HT or PCBM. Solar cells having up to 2.15% power conversion efficiencies were obtained. Great attention has been paid in the last few years to regioregular poly(3-hexylthiophene) self-assembly process into nano and microstructures to achieve efficient charge transport for high-performance organic electronic devices ^[103]. Various methodologies aimed at enhancing molecular ordering at the nano- through mesoscale have been introduced. In particular, the use of ultrasound assistance was investigated in the tuning of fibers length. Figure 28 shows AFM images of P3HT thin films prepared as a function of sonication time, from 1 to 3 minutes. On increasing the sonication time, a decrease in fibers length is observed. A detailed study on film formation as a function of deposition solvent (or mixture of solvents) and sonication time has allowed to elucidate the mechanism of nanostructured P3HT film formation and to highlight the importance of the interplay of molecular level interactions and long-range order for achieving effective macroscale charge carrier transport. The controlled assembly of nanostructured P3HT afforded films with superior charge transport characteristics ^[103a].

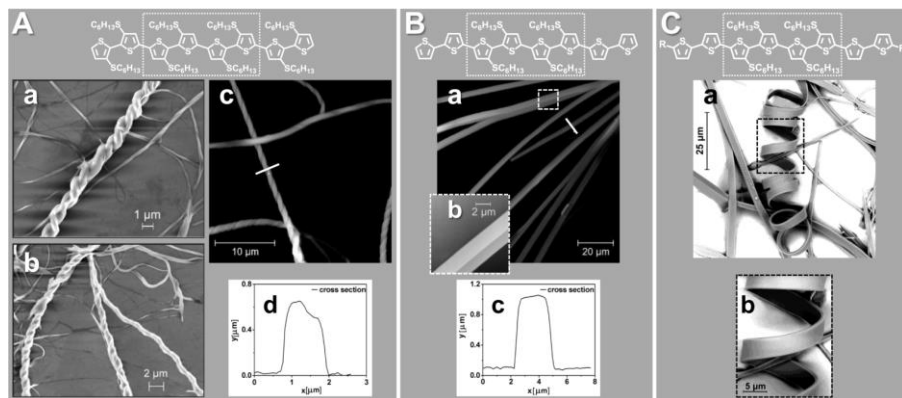


Figure 29. Room temperature self-assembly into helical or rod-like microfibers of octithiophenes having the same tetrameric inner core and different terminal bithiophene units. (A) SEM (a and b, on SiO₂), AFM (c, on glass) and AFM profile (d) of the helical fibers formed by the octithiophene with a S-hexyl group per ring; (B) AFM (a, on glass) and AFM profile (b) of rod-like fibers formed by the bithiophene terminated octamer; (C) SEM (a and b, on glass) images of helical fibers formed by the octamer terminated by alkyl-substituted bithiophene unit. Reproduced with permission from reference [37a]. Copyright 2011 American Chemical Society.

An alternative approach to promote the formation of targeted nanostructured supramolecular systems is through appropriate molecular design favoring specific nonbonding interactions. Figure 29 shows the molecular structure of a few octithiophenes having the same tetrameric inner core but different terminal bithiophene units ^[37a]. The octamers were designed to obtain compounds with an intrinsic tendency to self-assemble anisotropically into nano and microfibers by virtue of the combination of thioalkyl substituents and head-to-head regiochemistry of substitution, promoting the self-assembly mainly through directional nonbonding S-S interactions and weak H-S hydrogen bondings.

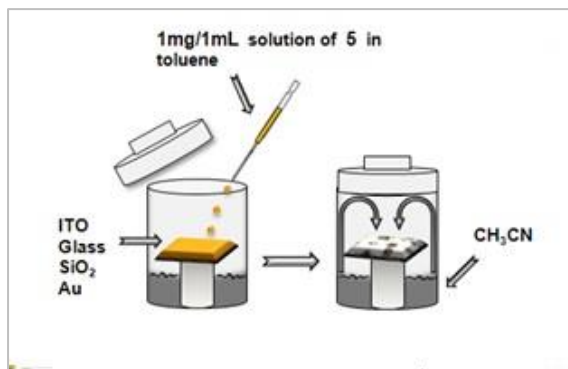


Figure 30. Deposition modalities of the octathiophenes on different substrates.

Figure 30 illustrate the deposition modalities of the octathiophenes on different substrates. The oligomers were first dissolved in toluene, a solvent in which they were very soluble, then deposited dropwise on the substrate and finally exposed to vapors of acetonitrile, in which they are insoluble. The different octamers crystallized with a morphology independent on the substrate and only related to the molecular structure, as illustrated in Figure 29. Minor changes in the molecular structure allow the tuning of morphology from helical to flat rod-like supramolecular architectures ^[37a]. The microfibers are fluorescent and electroactive.

Figure 31 shows the AFM images of microfibers directly grown on indium tin oxide (ITO, a conducting substrate) and the relative charge transport characteristics (panels A, B) measured by tunneling atomic force microscopy in torsion mode (Tr-TUNA), a scanning probe technique capable to simultaneously measure surface topography and local current at the nanoscale ^[104]. Panel C shows the charge conduction characteristics (more exactly, the transfer characteristics in saturation regime) of helical and rod-like microfibers directly grown on the SiO₂ substrate of a field effect transistor. The FET charge mobility of the rod-like octamer was significantly improved by orienting the microfibers into functional arrays by template-directed growth. In this way an impressive enhancement (three orders of magnitude) of charge mobility was achieved ^[105].

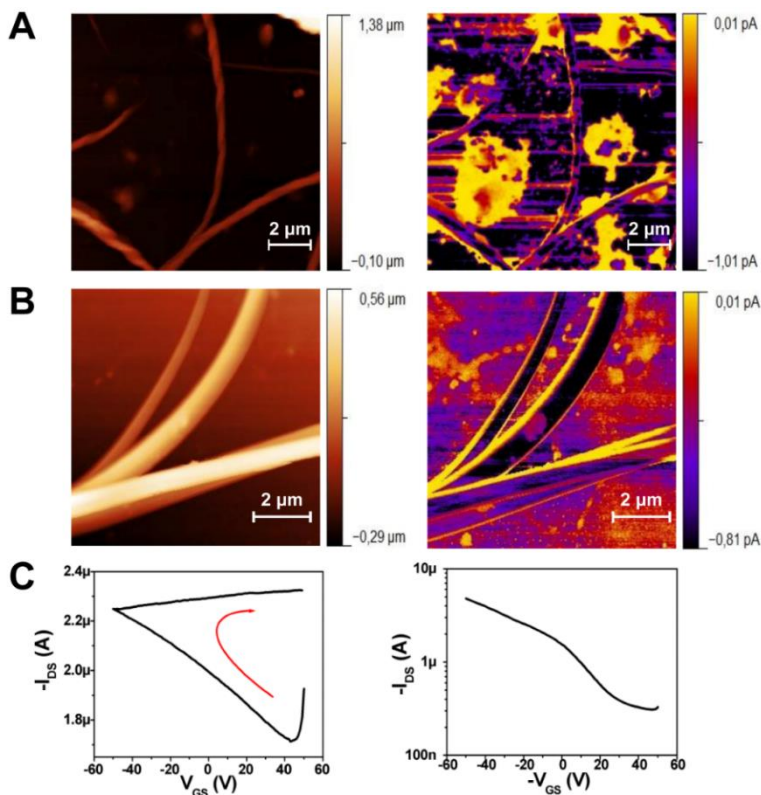


Figure 31. (A) Atomic force microscopy (AFM) images of helical and rod-like octithiophene microfibers grown on indium tin oxide. (B) Charge transport characteristic of the same microfibers measured by tunneling AFM in torsion mode (Tr-TUNA). (C) Charge conduction characteristics of the microfibers directly grown on the SiO₂ substrate of a field-effect transistor. Reprinted from reference [37a]. Copyright 2011 American Chemical Society.

VI. CONCLUDING REMARKS

Thousands of articles on thiophene-based materials and their applications have been published. The present introduction is just a short updated account from the point of view of the author and aimed to give the reader an idea of the countless research opportunities related to thiophene compounds as organic materials. There is growing interest in developing methods for the scalable cost-effective syntheses of oligo/polythiophenes affording the best performance in organic electronics and photovoltaics. There is a considerable potential for performance improvements in both fields promoted by the creation of innovative molecular structures with better properties. Currently, the design of thiophene-based materials is still largely empirical, many fundamental aspects of the physical and chemical properties of oligo/ polythiophenes being still unaddressed. Much deeper knowledge is needed before the full elucidation of the relationships between the

structures and properties of these compounds enables the rational design of molecular structures, which are unpredictable on the basis of current information. Results achieved in this direction will create new opportunities pushing up the performance of organic (opto)electronic devices. In our opinion, there is even greater potential for the study of thiophene-based fluorescent compounds for applications in medicine and biology, nano bioelectronics, and biosensing. The impressive advances achieved in imaging technology allow unprecedented real time studies of the interaction of these compounds with living cells and organisms for diagnostic purposes and even to confer additional properties such as electroactivity to specific intracellular proteins. It is likely that the unique mixture of fundamental studies and applications in electronics, optics, chemistry, medicine, and biology peculiar to thiophene materials will make possible the creation of materials with novel characteristics and functions and even to applications that are currently unforeseen but which could have a major impact in the future.

REFERENCES

- [1] K. Kawashima, Y. Tamai, H. Ohkita, I. Osaka, and K. Takimiya, *Nat. Commun.*, **2015**, 6, 10085.
- [2] P. Hammarström, R. Simon, S. Nystrom, P. Konradsson, A. Åslund, and K.P.R. Nilsson, *Biochemistry*, **2010**, 49, 6838-6845.
- [3] ^{a)} I. F. Perepichka, D. F. Perepichka, H. Meng, and F. Wudl, *Adv. Mater.*, **2005**, 17, 2281-2305. ^{b)} G. Barbarella, M. Melucci, and G. Sotgiu, *Adv. Mater.*, **2005**, 17, 1581-1593. ^{c)} D. Fichou, editor: Handbook of Oligo- and Polythiophenes, **2008**, Wiley-VCH. ^{d)} I. F. Perepichka and D. F. Perepichka, editors: Handbook of Thiophene-Based Materials: Applications in Organic Electronics and Photonics, **2009**, Wiley-VCH.
- [4] J. I. Musher, *Angew. Chem. Int. Ed.*, **1969**, 8, 54-68.
- [5] ^{a)} S. Potash and S. Rozen, *Chem. Eur. J.*, **2013**, 19, 5289-5296. ^{b)} E. Busby, J. Xia, Q. Wu, J. Z. Low, R. Song, J. R. Miller, X. Y. Zhu, L. M. Campos, and M. Y. Sfeir, *Nat. Mater.*, **2015**, 14, 426-433. ^{c)} E. J. Dell, B. Capozzi, J. Xia, L. Venkataraman, and L. M. Campos, *Nat. Chem.*, **2015**, 7, 209-214. ^{d)} F. Di Maria, M. Zangoli, I. E. Palamà, E. Fabiano, A. Zanelli, M. Monari, A. Perinot, M. Caironi, V. Maiorano, A. Maggiore, M. Pugliese, E. Salatelli, G. Gigli, I. Viola, and G. Barbarella, *Adv. Funct. Mater.*, 2016, 26, 6970-6984.
- [6] G.v.A. Diaz-Quijada, N. Weinberg, S. Holdcroft, and B. M. Pinto, *J. Phys. Chem. A*, **2002**, 106, 1266-1276.
- [7] M. S. Vezie, S. Few, I. Meager, G. Pieridou, B. Döring, R. S. Ashraf, A. R. Goñi, H. Bronstein, I. McCulloch, S. C. Hayes, M. Campoy-Quiles, and J. Nelson, *Nat. Mater.*, **2016**, 15, 746-753.
- [8] ^{a)} G. Barbarella, M. Zambianchi, A. Bongini, and L. Antolini, *Adv. Mater.*, **1993**, 5, 834-838. ^{b)} G. Barbarella and F. Di Maria, *Acc. Chem. Res.*, **2015**, 48, 2230-2241.
- [9] ^{a)} F. Cicoira and C. Santato, editors: Organic Electronics: Emerging Concepts and Technologies, **2013**, Blackwell Science Publ. ^{b)} A. D. Printz and D. J. Lipomi, *Appl. Phys. Rev.*, **2016**, 3, 021302.

- [10] P. Wilson, V. Kumar, C. Parashar, C. Vilch_eze, R. Veyron- Churlet, J. S. Freundlich, S. W. Barnes, J. R. Walker, M. J. Szymonifka, E. Marchiano, S. Shenai, R. Colangeli, W. R. Jacobs Jr., M. B. Neiditch, L. Kremer, and D. Alland, *Nat. Chem. Biol.*, **2013**, 9, 499-506.
- [11] M. Zambianchi, F. Di Maria, A. Cazzato, G. Gigli, M. Piacenza, F. Della Sala, and G. Barbarella, *J. Am. Chem. Soc.*, **2009**, 131, 10892-10900.
- [12] A. Cieslar-Pobuda, M. Back, K. Magnusson, M. V. Jain, M. Rafat, S. Ghavami, K. P. R. Nilsson, and M. J. Los, *Cytometry Part A*, **2014**, 85A, 628-635.
- [13] T. Klingstedt, C. Blechschmidt, A. Nogalska, S. Prokop, B. Haggqvist, O. Danielsson, W. K. Engel, V. Askanas, F. L. Heppner, and K. P. R. Nilsson, *ChemBioChem*, **2013**, 14, 607-616.
- [14] J. Ries, V. Udayar, A. Soragni, S. Hornemann, K. P. R. Nilsson, R. Riek, C. Hock, H. Ewers, A. A. Aguzzi, and L. Rajendra, *ACS Chem. Neurosci.*, **2013**, 4, 1057-1061.
- [15] ^{a)} J. Hassan, M. Sévignon, C. Gozzi, E. Schulz, and M. Lemaire, *Chem. Rev.*, **2002**, 102, 1359-1469. ^{b)} D. Alberico, M. E. Scott, and M. Lautens, *Chem. Rev.*, **2007**, 107, 174-238. ^{c)} L. Ackermann, R. Vicente, and A. R. Kapdi, *Angew. Chem. Int. Ed.*, **2009**, 48, 9792-9826. ^{d)} D. J. Schipper and K. Fagnou, *Chem. Mater.*, **2011**, 23, 1594e1600. ^{e)} L. G. Mercier and M. Leclerc, *Acc. Chem. Res.*, **2013**, 46, 1597-1605.
- [16] D. Demeter, J. Roncali, S. Jungsuttiwong, F. Melchiorre, P. Biagini, and R. Po, *J. Mater. Chem. C*, **2015**, 3, 7756-7761.
- [17] J. M. Koenen, A. Bilge, S. Allard, R. Alle, K. Meerholz, and U. Scherf, *Org. Lett.*, **2009**, 11, 2149-2152.
- [18] L. Favaretto, G. Barbarella, I. Räu, F. Kajzar, S. Caria, M. Murgia, and R. Zamboni, *Opt. Express*, **2009**, 17, 2557-2562.
- [19] I. Osaka and R. D. McCullough, *Acc. Chem. Res.*, **2008**, 41, 1202-1214.
- [20] F. Zhang, G. Götz, H. D. F. Winkler, C.A. Schalley, and P. Bäuerle, *Angew. Chem. Int. Ed.*, **2009**, 48, 6632-6635.
- [21] H. Chung, T. Narita, J. Yang, P. Kim, M. Takase, M. Iyoda, and D. Kim, *Chem. Eur. J.*, **2013**, 19, 9699-9709.
- [22] T. V. Richter, S. Link, R. Hanselmann, and S. Ludwigs, *Macromol. Rapid Commun.*, **2009**, 30, 1323-1327.
- [23] C. Xia, X. Fan, J. Locklin, and R. C. Advincula, *Org. Lett.*, **2002**, 4, 2067e-2070.
- [24] M. Liu, Y. Chen, C. Zhang, C. Li, W. Li, and Z. Bo, *Polym. Chem.*, **2013**, 4, 895-899.
- [25] K. Adachi, Y. Hirao, K. Matsumoto, T. Kubo, and H. Kurata, *Org. Lett.*, **2014**, 16, 5870-5873.
- [26] R. D. McCullough and R. D. Lowe, *J. Chem. Soc. Chem. Commun.*, **1992**, 70-72.
- [27] T. A. Chen and R. D. Rieke, *J. Am. Chem. Soc.*, **1992**, 114, 10087-10088.
- [28] J. K. Stille, *Angew. Chem. Int. Ed. Engl.*, **1986**, 25, 508-524.
- [29] B. Carsten, F. He, H. J. Son, T. Xu, and L. Yu, *Chem. Rev.*, **2011**, 111, 1493-1528.

- [30] C. Cordovilla, C. Bartolome, J. M. Martínez-Illarduya, and P. Espinet, *ACS Catal.*, **2015**, 5, 3040-3053.
- [31] P. Qin, H. Kast, M. K. Nazeeruddin, S. M. Zakeeruddin, A. Mishra, P. Bäuerle, and M. Grätzel, *Energy Environ. Sci.*, **2014**, 7, 2981-2985.
- [32] K. Mitsudo, S. Shimohara, J. Mizoguchi, H. Mandai, and S. Suga, *Org. Lett.*, **2012**, 14, 2702-2705.
- [33] X. Yin, F. Guo, R. A. Lalancette, and F. Jakle, *Macromolecules*, **2016** 49, 537-546.
- [34] ^{a)} N. Miyaura and A. Suzuki, *J. Chem. Soc. Chem. Commun.*, **1979**, 866-867. ^{b)} N. Miyaura and A. Suzuki, *Chem. Rev.*, **1995**, 95, 2457-2483. ^{c)} A. Suzuki, *Angew. Chem. Int. Ed.*, **2011**, 50, 6722-6737.
- [35] C. Amatore, G. Le Duc, and A. Jutand, *Chem. Eur. J.*, **2013**, 19, 10082-10093.
- [36] A. A. Thomas and S. E. Denmark, *Science*, **2016**, 352, 329-332.
- [37] ^{a)} F. Di Maria, P. Olivelli, M. Gazzano, A. Zanelli, M. Biasiucci, G. Gigli, D. Gentili, P. D'Angelo, M. Cavallini, and G. Barbarella, *J. Am. Chem. Soc.*, **2011**, 133, 8654-8661. ^{b)} F. Di Maria, M. Gazzano, A. Zanelli, G. Gigli, A. Loiudice, A. Rizzo, M. Biasiucci, E. Salatelli, P. D'Angelo, and G. Barbarella, *Macromolecules*, **2012**, 45, 8284-8291.
- [38] J. Hassan, M. Sévignon, C. Gozzi, E. Schulz, and M. Lemaire, *Chem. Rev.*, **2002**, 102, 1359-1469.
- [39] Y. Yao, J. Gao, F. Bao, S. Jiang, X. Zhanga, and R. Ma, *RSC Adv.*, **2015**, 5, 42754-42761.
- [40] D. J. Schipper and K. Fagnou, *Chem. Mater.*, **2011**, 23, 1594-1600.
- [41] L. G. Mercier and M. Leclerc, *Acc. Chem. Res.*, **2013**, 46, 1597-1605.
- [42] C. Colletto, S. Islam, F. Julia-Hernandez, and I. Larrosa, *J. Am. Chem. Soc.*, **2016**, 138, 1677-1683.
- [43] K. Wang, Wang, and M. Wang, *Polym. Chem.*, **2015**, 6, 1846-1855.
- [44] J. Kuwabara, T. Yasuda, S.J. Choi, W. Lu, K. Yamazaki, S. Kagaya, L. Han, and T. Kanbara, *Adv. Funct. Mater.*, **2014** 24, 3226-3233.
- [45] Q. Wang, R. Takita, Y. Kikuzaki, and F. Ozawa, *J. Am. Chem. Soc.*, **2010** 132, 11420-11421.
- [46] S. L. Suraru, J.A. Lee, and C. K. Luscombe, *ACS Macro Lett.*, **2016**, 5, 724-729.
- [47] ^{a)} J. I. Musher, *Angew. Chem. Int. Ed.*, **1969**, 8, 54-68. ^{b)} R.J. Gillespie and B. Silvi, *Coord. Chem. Rev.*, **2002**, 233-234, 53-62.
- [48] O. Hollóczki and L. Nyulászi, *Struct. Chem.*, **2011**, 22, 1385e1392.
- [49] S. Rozen, *Eur. J. Org. Chem.*, **2005**, 2433-2447.
- [50] ^{a)} S. Potash and S. Rozen, *Chem. Eur. J.*, **2013**, 19, 5289-5296. ^{b)} S. Wei, J. Xia, E. J. Dell, Y. Jiang, R. Song, H. Lee, P. Rodenbough, A. L. Briseno, and L. M. Campos, *Angew. Chem.*, **2014**, 126, 1863-1867.
- [51] G. Barbarella, L. Favaretto, G. Sotgiu, M. Zambianchi, C. Arbizzani, A. Bongini, and M. Mastragostino, *Chem. Mater.*, **1999**, 11, 2533-2541.

- [52] ^{a)} A. Kirschning, W. Solodenko, and K. Mennecke, *Chem. Eur. J.*, **2016**, 12, 5972-5990. ^{b)} D. E. Fitzpatrick, C. Battilocchio, and S. V. Ley, *ACS Cent. Sci.*, **2016**, 2, 131-138. ^{c)} J. Wegner, S. Ceylan, and A. Kirschning, *Adv. Synth. Catal.*, **2012**, 354, 17-57. ^{d)} S. Marre and K. F. Jensen, *Chem. Soc. Rev.*, **2010**, 39, 1183-12022 (2010).
- [53] R. Gedye, F. Smith, K. Westaway, H. Ali, L. Baldisera, L. Laberge, and J. Rousell, *Tetrahedron Lett.*, **1986**, 27, 279-282.
- [54] C. O. Kappe, *Angew. Chem. Int. Ed.*, **2004**, 43, 6250-6284.
- [55] S. Alesi, F. Di Maria, M. Melucci, D. J. Macquarrie, R. Luque, and G. Barbarella, *Green Chem.*, **2008**, 10, 517-523.
- [56] P. Arsenyan, E. Paegle, and S. Belyakov, *Tetrahedron Lett.*, **2010**, 51, 205-208.
- [57] C. Liao, M. Zhang, M. Yu Yao, T. Hua, L. Li, and F. Yan, *Adv. Mater.*, **2015**, 27, 7493-7527.
- [58] C. Zhang, P. Chen, and W. Hu, *Small*, **2016**, 12, 1252-1294.
- [59] D. Pisignano, L. Persano, E. Mele, P. Visconti, R. Cingolani, G. Gigli, G. Barbarella, and L. Favaretto, *Opt. Lett.*, **2005**, 30, 260-262.
- [60] Y. Coskun, A. Cirpan, and L. J. Toppare, *J. Mater. Sci.*, **2007**, 42, 368-372.
- [61] T. P. Huynha, P.S. Sharma, M. Sosnowska, F. D'Souza, and W. Kutner, *Prog. Polym. Sci.*, **2015**, 47, 1-25.
- [62] A. Facchetti, *Mater. Today*, **2007**, 10, 28-37.
- [63] C. K. Chiang, C. R. Fincher, Y. W. Park, A. J. Heeger, H. Shirakawa, E. J. Louis, S. C. Gau, and A. G. MacDiarmid, *Phys. Rev. Lett.*, **1977**, 39, 1098-1101.
- [64] H. Sirringhaus, *Adv. Mater.*, **2005**, 17, 2411-2425.
- [65] G. R. Hutchison, M. A. Ratner, and T. J. Marks, *J. Am. Chem. Soc.*, **2005**, 127, 16866-16881.
- [66] I. McCulloch, M. Heeney, M. L. Chabynyc, D. DeLongchamp, R. J. Kline, M. Cölle, W. Duffy, D. Fischer, D. Gundlach, B. Hamadani, R. Hamilton, L. Richter, A. Salleo, M. Shkunov, D. Sparrowe, S. Tierney, and W. Zhang, *Adv. Mater.*, **2009**, 21, 1091-1109.
- [67] M. Halik, H. Klauk, U. Zschieschang, G. Schmid, S. Ponomarenko, S. Kirchmeyer, and W. Weber, *Adv. Mater.*, **2003**, 13, 917-922.
- [68] H. Usta, A. Facchetti, and T. Marks, *Acc. Chem. Res.*, **2011**, 44, 501-510.
- [69] C. Wang, H. Dong, W. Hu, Y. Liu, and D. Zhu, *Chem. Rev.*, **2012**, 112, 2208-2267.
- [70] H. Sirringhaus, P. J. Brown, R.H. Friend, M. M. Nielsen, K. Bechgaard, B. M. W. Langeveld-Voss, A. J. H. Spiering, R.A.J. Janssen, E. W. Meijer, P. Herwig, and D. M. de Leeuw, *Nature*, **1999**, 401, 685-688.
- [71] Z. Chen, M. J. Lee, R.S. Ashraf, Y. Gu, S. Albert-Seifried, M. M. Nielsen, B. Schroeder, T. D. Anthopoulos, M. Heeney, I. McCulloch, and H. Sirringhaus, *Adv. Mater.*, **2012**, 24, 647-652.
- [72] M. Melucci, L. Favaretto, M. Zambianchi, M. Durso, M. Gazzano, A. Zanelli, M. Monari, M.G. Lobello, F. De Angelis, V. Biondo, G. Generali, S. Troisi, W.

- Koopman, S. Toffanin, R. Capelli, and M. Muccini, *Chem. Mater.*, **2013**, 25, 668-676.
- [73] Y. Lin and X. Zhan, *Acc. Chem. Res.*, **2016**, 49, 175e183.
- [74] ^{a)} Y. Chen, X. Wan, and G. Long *Acc. Chem. Res.*, **2013**, 46, 2645-2655. ^{b)} M. Zhang, X. Guo, W. Ma, H. Ade, and J. Hou, *Adv. Mater.*, **2014**, 26, 5880-5885. ^{c)} W. Cao and J. Xue, *Energy Environ. Sci.*, **2014**, 7, 2123-2144.
- [75] C.B. Nielsen, S. Holliday, H. Y. Chen, S.J. Cryer, and I. McCulloch, *Acc. Chem. Res.*, **2015**, 48, 2803-2812.
- [76] H. J. Wang, C. P. Ping Chen, and R. J. Jeng, *Materials*, **2014**, 7, 2411-2439.
- [77] B. C. Thompson and J. M. J. Freché, *Angew. Chem. Int. Ed.*, **2008**, 47, 58-77.
- [78] X. Guo, C. Cui, M. Zhang, L. Huo, Y. Huang, J. Hou, and Y. Li, *Energy Environ. Sci.*, **2012**, 5, 7943-7949.
- [79] A. Casey, S. D. Dimitrov, P. Shakya-Tuladhar, Z. Fei, M. Nguyen, Y. Han, T. D. Anthopoulos, J. R. Durrant, and M. Heeney, *Chem. Mater.*, **2016**, 28, 5110-5120.
- [80] S. Holliday, R. S. Ashraf, A. Wadsworth, D. Baran, S. A. Yousaf, C. B. Nielsen, C. H. Tan, S. D. Dimitrov, Z. Shang, N. Gasparini, M. Alamoudi, F. Laquai, C. J. Brabec, A. Salleo, J. R. Durrant, and I. McCulloch, *Nat Commun.*, **2016**, 7, 11585.
- [81] R. Po, A. Bernardi, A. Calabrese, C. Carbonera, G. Corso, and A. Pellegrino, *Energy Environ. Sci.*, **2014**, 7, 925-943.
- [82] Q. Zhang, B. Kan, F. Liu, G. Long, X. Wan, X. Chen, Y. Zuo, W. Ni, H. Zhang, M. Li, Z. Hu, F. Huang, Y. Cao, Z. Liang, M. Zhang, T. P. Russell, and Y. Chen, *Nat. Photon.*, **2014**, 9, 35-41.
- [83] S. C. Rasmussen, S. J. Evenson, and C. B. McCausland, *Chem. Commun.*, **2015**, 51, 4528-4543.
- [84] M. Zambianchi, F. Di Maria, A. Cazzato, G. Gigli, M. Piacenza, F. Della Sala, and G. Barbarella, *J. Am. Chem. Soc.*, **2009**, 131, 10892-10900.
- [85] R. S. Becker, J. Seixas de Melo, A. L. Macuanita, and F. Elisei, *J. Phys. Chem.*, **1996**, 100, 18683-18695.
- [86] F. Di Maria, E. Palamà, M. Baroncini, A. Barbieri, A. Bongini, R. Bizzarri, G. Gigli, and G. Barbarella, *Org. Biomol. Chem.*, **2014**, 12, 1603-1610.
- [87] F. Denizot and R. Lang, *J. Immunol. Methods*, **1986**, 89, 271-277.
- [88] M. L. Capobianco, G. Barbarella, and A. Manetto, *Molecules*, **2012**, 17, 910-933.
- [89] A. Cazzato, M. L. Capobianco, M. Zambianchi, L. Favaretto, C. Bettini, and G. Barbarella, *Bioconjugate Chem.*, **2007**, 18, 318-322.
- [90] S. Tyagi and F. R. Kramer, *Nat. Biotechnol.*, **1996**, 14, 303-308.
- [91] ^{a)} A. Åslund, C. J. Sigurdson, T. Klingstedt, S. Grathwohl, T. Bolmont, D. L. Dickstein, E. Glimsdal, S. Prokop, M. Lindgren, P. Konradsson, D. M. Holtzman, P. R. Hof, F.L. Heppner, S. Gandy, M. Jucker, A. Aguzzi, P. Hammarström, and K. P. R. Nilsson, *ACS Chem. Biol.*, **2009**, 4, 673-684. ^{b)} A. Herland, K. P. R. Nilsson, J. D. M. Olsson, P. Hammarström, P. Konradsson, and O. Inganäs, *J. Am. Chem. Soc.*,

- 2005**, 127, 2317- 2323. [○]T. Klingstedt, A. Åslund, R. A. Simon, L. B. G. Johansson, J. J. Mason, S. Nyström, P. Hammarström, and K. P. R. Nilsson, *Org. Biomol. Chem.*, **2001**, 9, 8356-8370. [ⓓ]H. Shirani, M. Linares, C. J. Sigurdson, M. Lindgren, P. Norman, and K. P. R. Nilsson, *Chem. Eur. J.*, **2015**, 21, 15133-15137. [ⓓ]D. Sjölander, C. Röcken, P. Westermark, K. P. R. Nilsson, and P. Hammarström, *Amyloid*, 23, 98-108 (2016). [ⓓ]L. Civitelli, L. Sandin, E. Nelson, S. I. Khattak, A. C. Brorsson, and K. Kägedal, *J. Biol. Chem.*, **2016**, 291, 9233.
- [92] K. P. R. Nilsson, A. Herland, P. Hammarström, and O. Inganäs, *Biochemistry*, **2005**, 44, 3718-3724.
- [93] K. Magnusson, A. Appelqvist, A. Cieslar-Pobuda, M. Bäck, B. Kägedal, J. A. Jonasson, M.J. Łos, and K. P. R. Nilsson, *Front. Chem.*, **2015**, 3, Article 58.
- [94] I. Palamà, F. Di Maria, I. Viola, E. Fabiano, G. Gigli, C. Bettini, and G. Barbarella, *J. Am. Chem. Soc.*, **2011**, 133, 17777-17785.
- [95] I. Viola, I. E. Palamà, A. M. L. Coluccia, M. Biasiucci, B. Dozza, E. Lucarelli, F. Di Maria, G. Barbarella, and G. Gigli, *Integr. Biol.*, **2013**, 5, 1057-1066.
- [96] I. E. Palamà, F. Di Maria, S. D'Amone, G. Barbarella, and G. Gigli, *J. Mater. Chem. B*, **2015**, 3, 151-158.
- [97] H. Herrmann and U. Aebi, *Annu. Rev. Biochem.*, **2004**, 73, 749-789.
- [98] K. Tremel and S. Ludwig, *Adv. Polym. Sci.*, **2014**, 265, 39-82.
- [99] [ⓐ]M. Bag, T. S. Gehan, D. D. Algaier, F. Liu, G. Nagarjuna, P. M. Lahti, T. P. Russell, and D. Venkataraman, *Adv. Mater.*, **2013**, 25, 6411-6415. [ⓑ]M. Bag, T. S. Gehan, L. A. Renna, D. D. Algaier, P. M. Lahti, and D. Venkataraman, *RSC Adv.*, **2014**, 4, 45325-45331.
- [100] H. Shimizu, M. Yamada, R. Wada, and M. Okabe, *Polymer J.*, 40, 33-36 (2008). C.E. Mora-Huertas and A. Elaissari, *Adv. Colloid Interfac.*, **2011**, 163, 90-122.
- [101] G. Nagarjuna, M. Baghgar, J. A. Labastide, D. D. Algaier, M. D. Barnes, and D. Venkataraman, *ACS Nano*, **2012**, 6, 10750-10758.
- [102] J. E. Millstone, D. F. J. Kavulak, C. H. Woo, T. W. Holcombe, E. J. Westling, A. L. Briseno, M. F. Toney, and J. M. J. Fréchet, *Langmuir*, **2010**, 26, 13056-13061.
- [103] [ⓐ]N. Kleinhenz, N. Persson, Z. Xue, P. H. Chu, G. Wang, Z. Yuan, M. A. McBride, D. Choi, M. A. Grover, and E. Reichmanis, *Chem. Mater.*, **2016**, 28, 3905-3913. [ⓑ]D. Choi, M. Chang, and E. Reichmanis, *Adv. Funct. Mater.*, **2015**, 25, 920-927.
- [104] R. Berger, H. J. Butt, M. B. Retschke, and S. A. L. Weber, *Macromol. Rapid Commun.*, **2009**, 30, 1167-1178.
- [105] D. Gentili, F. Di Maria, F. Liscio, L. Ferlauto, F. Leonardi, L. Maini, M. Gazzano, S. Milita, G. Barbarella, and M. Cavallini, *J. Mater. Chem.*, **2012**, 22, 20852-20856.

CHAPTER II PROPERTY-FUNCTION CONTROL IN THIOPHENE MATERIALS BY STEPWISE OXIDATION OF THIOPHENE SULPHUR

This chapter describes new classes of thiophene-based materials obtained by functionalization of thiophene sulfur with oxygen: Oligo/Polythiophene-S-Oxides and Mixed Oligo/Polythiophene-S-Oxides/Oligo/Polythiophene-S,S-Dioxides. New synthetic methodologies employing ultrasound and microwave irradiation are described for the selective sulfur derivatization with oxygen. The application of the new materials in devices as well as inside living cells are described.

Published as:

F. Di Maria, **M. Zangoli**, I. E. Palamà, E. Fabiano, A. Zanelli, M. Monari, A. Perinot, M. Caironi, V. Maiorano, A. Maggiore, M. Pugliese, E. Salatelli, G. Gilgli, I. Viola and G. Barbarella. *Adv. Funct. Mater.*, 2016; 26; 6970-6984.

I. INTRODUCTION

Oligo- and polythiophenes are of outstanding importance in organic materials science and technology ^[1]. Numerous studies on their chemical and physical properties, their applications as active device components in organic electronics and bioelectronics, as selective chemosensors and biosensors for a variety of target analytes and as fluorescent reporters in bioimaging have been published. There is great current interest for their applications in photovoltaic cells ^[2], field-effect transistors (FETs) ^[3], the identification of intracellular protein aggregated associated with Alzheimer's disease ^[4], and as membrane probes with high mechanosensitivity ^[5]. Nevertheless, despite the innumerable studies reports so far there are still many unexplored sides of these multifaceted materials. Indeed, the property tuning of oligo- and polythiophenes has as yet mainly been focused on changes in molecular size and shape or on the grafting of various substituents to the aromatic backbone ^[1]. Much less attention has been devoted to the functionalisation of thiophene sulfur. In thiophene, a 6 π -electrons aromatic system, sulfur has two unshared lone pair electrons, which can be employed in the formation of thiophene-S-oxides ^[6], thiophene-S,S-dioxides ^[7a], thiophene-sulfilimines ^[7b], thiophene sulfoximides ^[7c], and thiophene sulfonium salts ^[8]. Removal of thiophene sulfur lone pair leads to the loss of thiophene aromaticity and consequent changes in frontier orbital energies ^[9, 10]. Until now of all possible thiophene sulfur functionalisations, only sulfur dioxide has been taken into account in thiophene-based materials ^[9, 11]. Oligo- and polythiophene-S,S-dioxides display smaller energy gaps, grater electron affinities, and greater ionization energies than their nonoxygenated all-aromatic counterparts. Very recently it has been reported that oligomers and polymers containing thiophene-S,S-dioxide groups can undergo efficient intramolecular singlet fission ad are consequently candidates for the development of the next generation of photovoltaic devices based on multiple exciton generation processes ^[12]. A quinque-thiophene containing one central thiophene-S,S-dioxide group has been employed for the first experimental demonstration of replica symmetry breaking in random lasers ^[13]. Also several biological application of small thiophene oligomers containing thiophene-S,S-dioxide units have been reported ^[5, 15]. Drawbacks related to the presence of thiophene-S,S-dioxide units in the molecular structure are the marked increase in oxidation potential and the fact that the materials become rapidly insoluble and intractable as the number of these units increases, probably due to the planarity of the $-SO_2$ group and the increased aggregation capabilities via H-bonding promoted by the presence of the oxygen atoms ^[9d]. In this context a challenging frontier is represented by investigations on synthetic approaches to the as yet unexplored classes of oligo and polythiophene-S-oxides. These compounds should indeed be more soluble than the dioxygenated counterparts due to the nonplanarity of the SO group ^[6], have similar electron affinities but smaller oxidation potentials and energy gaps ^[6b], hence extending the range of structure–property tunability of thiophene materials. Owing to the aromatic character of thiophene, the oxidation of thiophene sulfur requires strong oxidants such as meta-chloroperoxybenzoic acid (MPCBA) ^[6] or the Rozen's reagent ^[11]. However, the oxidation with these reagents can hardly be stopped at the S-oxide stage. In consequence, owing to synthetic difficulties, only spare data on oligothiophene-S-oxides

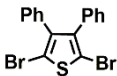
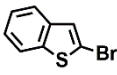
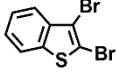
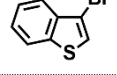
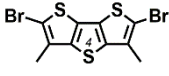
^[15] and no data on polythiophene-S-oxides have been reported so far. In this work, we describe a synthetic platform for the facile synthesis of oligo- and polythiophene-S-oxides and -S,S-dioxide in mild condition and room temperature taking advantage of ultrasound (US) assistance. We show that the cross-coupling reaction of these building blocks with metalated thiophenes affords innovative regioregular oligo- and polythiophenes containing thiophene-S-oxides or mixed thiophene-S-oxide and thiophene-S,S-dioxide moieties in the desired number and position of the molecular backbone. We demonstrate that the presence of monooxygenated thiophene units and their alternation with thiophene and thiophene-S,S-dioxide units allow for the fine modulation of properties such as frontier orbital energies, p- or n-type charge transport, photo, and electroluminescence and even the biological behaviour inside live cells.

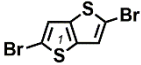
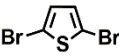
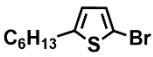
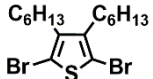
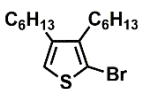
II. RESULTS AND DISCUSSION

2.1 Synthesis and Characterization. The number of reagents shown in Table 1 is necessarily limited and many other examples could have been reported. Our choice was made on the grounds that thiophene S-oxides undergo more facile Diels–Alder type dimerization or other side reactions such as epoxidation of the double bond than thiophene- S,S-dioxides ^[6]. Rapid dimerization of the transiently formed S-oxides renders difficult the separation of many of these compounds from the reaction medium. However, studies on variously substituted thiophene rings show that stabilization of thiophene-S-oxides can be achieved by introduction of sterically hindering groups, mesomeric effects or fusion of thiophene with phenyl as in dibenzothiophene ^[6]. Bromoderivatives **1–10** were prepared taking advantage of ultrasound assistance ^[16], see synthetic details in the Experimental Section. We have found that ultrasound assistance renders also possible the stepwise oxidation of thiophene derivatives (Table 1 and Table S2, Experimental Section) using H₂O₂ as the oxidizing agent in trifluoroacetic acid (TFA):dichloromethane (DCM) 1:2 ^[17] at room temperature and employing just 1 eq H₂O₂ for the S-oxide and 2 eq for the -S,S-dioxide. The desired products were obtained in short reaction times and high yields while only the unreacted starting compound was recovered rendering the purification step easier. Table 1 shows that with bromoderivatives **1–6** and just 1 eq H₂O₂, the thiophene-S-oxide is formed in 15–30 min in yields varying in the range 70%–99%, depending on the substrate. Times and yields are the same for the formation of the -S,S-dioxide upon addition of a second equivalent of H₂O₂. We found that also the oxidation with the classical oxidizing agent m-chloroperoxybenzoic acid (MCPBA) in DCM is facilitated by the assistance of ultrasounds. In this case only the -S,S-dioxide and the starting compound are present in the reaction mixture. In our experience, in the absence of ultrasounds, a much greater amount of MCPBA would be needed; for example, for the preparation of compound **9b**, nearly 6 eq were required for overnight reaction and 52% yield ^[18]. Synthetic details are reported in the Experimental Section. When no substituents were present in the beta positions of the thiophene ring or when alkyl chains were present (items **7–10** in Table 1) the S-oxide could not be isolated, probably due to rapid Diels–Alder dimerization ^[6, 19]. By contrast, the formation of the -S,S-dioxide was rapid and efficient. The assistance of ultrasounds and the system

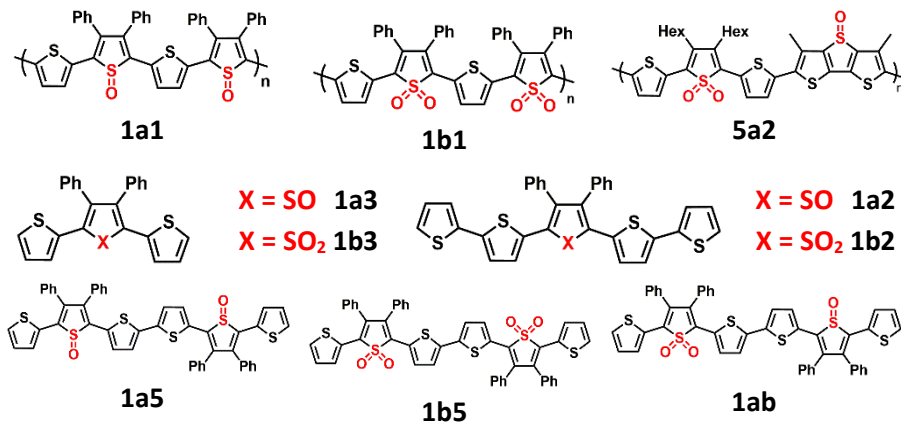
H₂O₂/CF₃COOH/CH₂Cl₂ made the yield of **7b** (room temperature, 30 min, 80% isolated yield) competitive with that obtained with Rozen's reagent (room temperature, 1 h, 95% yield)^[20]. The oxidation with MCPBA and US assistance is slower and furnishes the same yield in 90 min. From these results it is seen that the stepwise oxygenation of thiophene sulfur depends on the type of substituents on the thiophene ring. Finally, we found that for some nonbrominated thiophene derivatives (Table S1, Experimental Section) the S-oxide as well as the -S,S-dioxide can be isolated in good yields upon treatment with H₂O₂ in CF₃COOH/CH₂Cl₂ under ultrasound assistance. Afterward both oxygenated derivatives can be mono- or dibrominated in the alpha positions and employed in cross-coupling reactions with metalated thiophenes. The brominated S-oxides and -S,S-dioxides of Table 1 and Table S2 (Experimental Section) were stable compounds and could be purified by silicagel chromatography. Their characterization is reported in the Experimental Section. IR, UV, and NMR of the S-oxides are in agreement with those reported for the thiophene- S-oxides described in the literature^[7a]. Oligo- and polythiophenes having thiophene-S-oxide and/or thiophene-S,S-dioxide groups in precise position and number in the molecular backbone could easily be prepared by reacting compounds **1a–6a** and/or **1b–6b** and **7–10** with metalated thiophenes via palladium catalyzed cross-coupling Stille or Suzuki reactions^[21] to obtain the formation of the desired products in high yields.

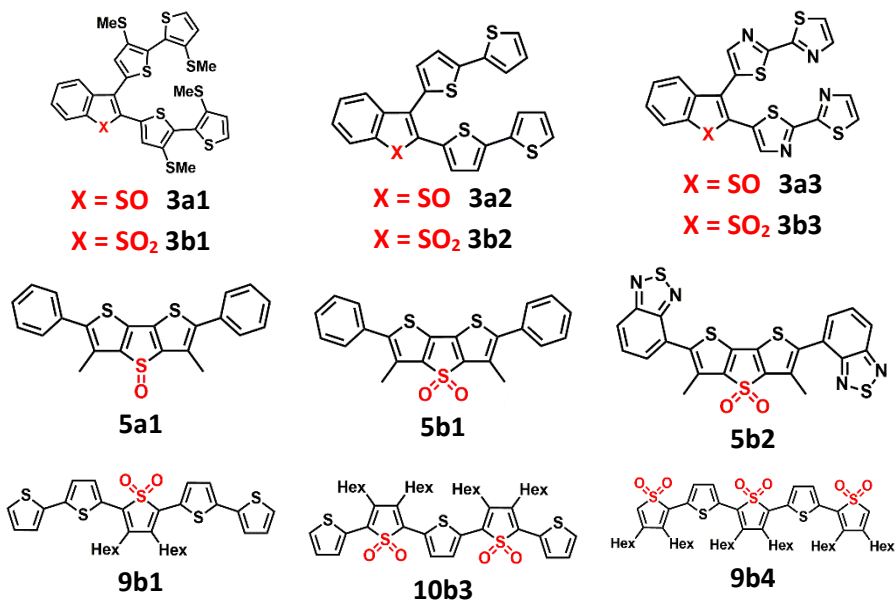
Table 1. Reagents and conditions for the ultrasound assisted synthesis of brominated thiophene-S-oxides and thiophene-S,S-dioxides

	Starting materials	Product	Experimental Conditions	Time (min)	Yield ^a (%)
1		a SO	DCM:TFA 2:1 H ₂ O ₂ 1 eq	30	70
		b SO ₂	DCM:TFA 2:1 H ₂ O ₂ 2 eq	30	80
			DCM/MPCBA 2 eq	60	80
2		a SO	DCM:TFA 2:1 H ₂ O ₂ 1 eq	15	99
		b SO ₂	DCM:TFA 2:1 H ₂ O ₂ 2 eq	15	99
			DCM/MPCBA 2 eq	45	>90
3		a SO	DCM:TFA 2:1 H ₂ O ₂ 1 eq	15	99
		b SO ₂	DCM:TFA 2:1 H ₂ O ₂ 2 eq	15	99
			DCM/MPCBA 2 eq	45	>90
4		a SO	DCM:TFA 2:1 H ₂ O ₂ 1 eq	15	>90
		b SO ₂	DCM:TFA 2:1 H ₂ O ₂ 2 eq	15	99
			DCM/MPCBA 2 eq	45	>90
5		a SO	DCM:TFA 2:1 H ₂ O ₂ 1 eq	20	75
		b SO ₂	DCM:TFA 2:1 H ₂ O ₂ 2 eq	15	90
			DCM/MPCBA 2 eq	15	80
		a SO	DCM:TFA 2:1 H ₂ O ₂ 1 eq	20	30

6		b SO ₂	DCM:TFA 2:1 H ₂ O ₂ 2 eq DCM/MPCBA 2 eq	20 45	90 80
7		b SO ₂	DCM:TFA 2:1 H ₂ O ₂ 2 eq DCM/MPCBA 2 eq	30 90	80 80
8		b SO ₂	DCM:TFA 2:1 H ₂ O ₂ 2 eq DCM/MPCBA 2 eq	20 20	80 80
9		b SO ₂	DCM:TFA 2:1 H ₂ O ₂ 2 eq DCM/MPCBA 2 eq	20 20	80 80
10		b SO ₂	DCM:TFA 2:1 H ₂ O ₂ 2 eq DCM/MPCBA 2 eq	25 60	60 70

A few examples of the innumerable structures that can be prepared on the basis of the simple chemical strategy described above are reported in Scheme 1. The corresponding detailed synthetic pattern is shown in Schemes S1–S4 (Experimental Section). Scheme S1 (Experimental Section) shows the synthetic pattern to prepare oligomers and polymers starting from dibromo derivatives **1a** and **1b**. The polymers (**1a1**, **1b1**) are made of alternating 3,4-diphenyl-thiophene-S-oxide or -S,S-dioxide units and unsubstituted thiophene. The oligomers are trimers (**1a3**, **1b3**) or pentamers (**1a2**, **1b2**) with one central thiophene-S-oxide or thiophene-S,S-dioxide and hexamers bearing two thiophene-S-oxide or thiophene-S,S-dioxide groups (**1a5** and **1b5**, respectively) or one thiophene-S-oxide and one thiophene-S,S-dioxide group (**1ab**).





Scheme 1. Molecular structure of polymers and oligomers obtained by cross-coupling reaction of selected thiophene-S-oxides and -S,S-dioxides with metalated thiophenes (detailed synthesis in the Experimental Section). The compounds reported in this scheme are all new molecules with the exception of **3b2** ^[22], **5b1** ^[14d], and **9b1** ^[9e].

Scheme S2 (Experimental Section) illustrates the preparation of V-shaped ^[22] oligomers obtained from **3a** and **3b**, while Scheme S3 (Experimental Section) describes the pattern to obtain the polymer, **5a2**, with alternating mono- and dioxygenated thiophene units. Scheme S4 (Experimental Section) describes the preparation of a quinquethiophene having one (**9b1**), two (**10b3**), and three (**9b4**) thiophene-S,S-dioxide groups in the backbone. As predicted, the oligomers containing only thiophene-S-oxide units were much more soluble in common organic solvents than those containing alternating thiophene-S-oxides and thiophene-S,S-dioxides and even more soluble than those containing only thiophene-S,S-dioxides units. Polymers **1a1** and **1b1** were weakly soluble in tetrahydrofuran (THF) and other organic solvents, while **5a2** displayed significant solubility attributable to the presence of long side chains. The characteristics of polymers **1a1**, **1b1**, and **5a2** are reported in Table S2 (Experimental Section).

2.1.1 Single Crystal X-Ray Structure of Hexamer 1a5. There are only sparse data on single crystal X-ray structure and conformation of thiophene-S-oxides ^[17, 23]. We have been able to obtain single crystals for hexamer **1a5** having a backbone containing two thiophene-S-oxide units. The X-ray diffraction molecular structure and packing of **1a5** are reported in Figure 1. The compound has a crystallographic inversion center in the middle of the C-C bond connecting the

inner thienyl rings. The orientation of the sulfur atoms in the adjacent rings is transoid. The central bithiophene unit is planar and is connected in the 2-positions to the thiophene-1-oxide rings bearing two phenyl groups in 3 and 4 and a thienyl ring in 5. The ring containing the oxidized sulfur atom loses its aromatic character and shows a diene structure with C5-C6, C6-C7, and C7-C8 bond distances of 1.354(7), 1.474(7), and 1.380(7) Å, respectively. In agreement with the already reported single crystal X-ray data^[17,23], the oxidized sulfur exhibits a pyramidal geometry and lies 0.186 Å out of the C5-C6-C7-C8 least-square plane. In addition, the S2-C bonds (S2-C5 1.816(5) and S2-C8 1.794(6) Å) are longer than the S-C distances in the other thiophene rings that fall in the range 1.683-1.749(5) Å. The C5-C6-C7-C8 mean plane makes dihedral angles of 20.1(3) and 8.7(3)° with the outer and inner thienyl rings, respectively. The deviation from planarity of the thiophene-S-oxide sulfur is small, indicating the possibility that some π -delocalization may still occur. In the crystal the molecules adopt a pseudoherringbone mode (Figure 1 B). The molecules pack in a parallel slipped arrangement but without π - π stacking (distance between the molecular plane 4.45 Å). The intermolecular interactions between the different stacks are mainly C-H- π interactions (H20-centroid(C19-C24)) 3.43 Å. It is worth noticing that the crystal conformation of **1a5** closely resembles the recently reported substituted hexamer having butyl groups in place of the phenyl rings, one methyl group in the outer thiophene ring and two thiophene -S,S-dioxides instead of two thiophene-S-oxide moieties^[24].

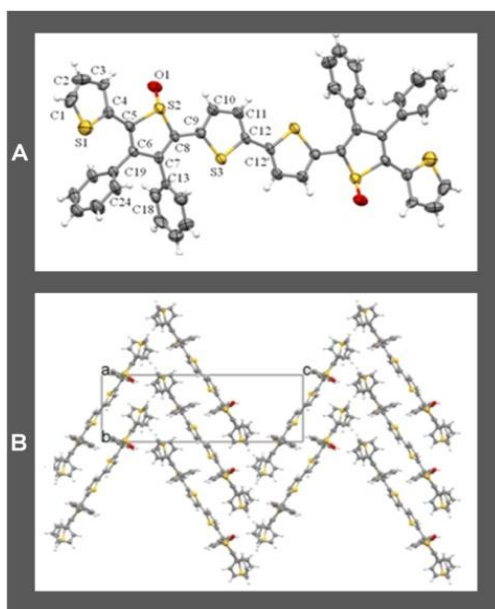


Figure 1. Crystal structure of hexamer **1a5** containing two thiophene-S-oxide moieties. A) Molecular conformation. The labelled atoms are related to the unlabelled ones by the symmetry operation $-x + 1, -y, z + 1$. B) View down the a axis of the crystal packing.

2.2 Electrochemical Characterization. Cyclic voltammetry (CV) was used to measure the redox potentials of the newly synthesized oligomers and polymers and to estimate the electrochemical energy gap between the highest occupied molecular orbital (HOMO) and the lowest unoccupied molecular orbital (LUMO). Table 2 reports the oxidation and reduction potentials and the corresponding energy gaps as well as HOMO and LUMO energies calculated according to known modalities^[25]. All CV plots are reported in Figures S54–S59 (Experimental Section). It is seen that, in agreement with expectations, for most compounds the presence of thiophene S-oxides results in lower oxidation potentials and lower (more negative) reduction potentials than the presence of thiophene-S,S-dioxides in the corresponding molecular structure.

Table 2. Redox potentials of oligo/polythiophene-S-oxides, -S,S-dioxides and mixed -S-oxides/-S,S-dioxides.

	$E_{\text{ox}}^{\text{onset}}$ versus SCE	$E_{\text{rid}}^{\text{onset}}$ versus SCE	E_{g} [eV]	HOMO [eV]	LUMO [eV]
1a1	0.69 ^{a)}	-0.56 ^{a)}	1.25	5.37	4.12
1b1	0.98 ^{b)}	-0.49 ^{a)}	1.37	5.66	4.19
5a2	0.95 ^{a)}	-0.97 ^{b)}	1.92	5.63	3.71
1a3	1.29 ^{b)}	-1.25 ^{c)}	2.54	5.97	3.43
1b3	1.47 ^{b)}	-1.11 ^{a)}	2.58	6.15	3.57
1a5	1.08 ^{c)}	-1.19 ^{c)}	2.27	5.76	3.49
1b5	1.42 ^{b)}	-0.92 ^{c)}	2.34	6.10	3.76
1ab	1.14 ^{b)}	-1.04 ^{b)}	2.18	5.82	3.64
1a2	1.04 ^{c)}	-1.18 ^{b)}	2.22	5.72	3.50
1b2	1.16 ^{b)}	-1.03 ^{b)}	2.19	5.84	3.65
3a1	1.04 ^{b)}	-1.31 ^{b)}	2.35	5.72	3.37
3b1	1.09 ^{c)}	-1.25 ^{b)}	2.35	5.72	3.37
3a2	1.20 ^{b)}	-1.28 ^{b)}	2.48	5.88	3.40
3b2	1.35 ^{a,d)}	-1.19 ^{a,d)}	2.54	6.03	3.49
3a3	>1.6	-1.08 ^{b)}	>2.68	>6.28	3.60
3b3	>1.6	-0.9 ^{b)}	>2.51	>6.28	3.77
5a1	1.23 ^{b)}	-1.53 ^{c)}	2.76	5.91	3.15
5b1	1.47 ^{b)}	-1.48 ^{b)}	2.95	6.15	3.20
5b2	1.46 ^{c)}	-1.25 ^{b)}	2.71	6.14	3.43
9b1	1.22 ^{a)}	-1.20 ^{a)}	2.42	5.90	3.48
10b3	1.38 ^{c)}	-1.00 ^{a)} , -1.00 ^{b)}	2.38	6.06	3.68
9b4	1.46 ^{c)}	-0.94 ^{b)}	2.40	6.14	3.74

^{a)} Reversible; ^{b)} Quasi-reversible; ^{c)} Irreversible; ^{d)} Ref. [22].

Compare, for example, polymers **1a** and **1b** or pentamer **1a5** and **1b5**. Generally, the shift of the oxidation potential is more significant than that of the reduction one hence the electrochemical energy gaps of oligo/polythiophene-S-oxides are smaller than those of the corresponding oligo/polythiophene-S,S-dioxides. However, for sulfoxide **1a2** the energy gap (2.22 eV) is

slightly higher than that of the corresponding sulfone **1b2** (1.19 eV). We cannot exclude that in this case conformational factors are at the origin of the discrepancy. Polymers **1a1**, **1b1**, and **5a2** whose CV plots are shown in Figure 2, having the HOMO–LUMO energy gap < 2 V, are all Low Band Gap polymers ^[26]. The optical energy gaps, estimated by the onset point of the absorption bands in solution (Figure 2) are in agreement with the electrochemical energy gaps. Polythiophene-S-oxide **1a1** has one of the lowest electrochemical gaps of polythiophenes described to date, 1.25 V.

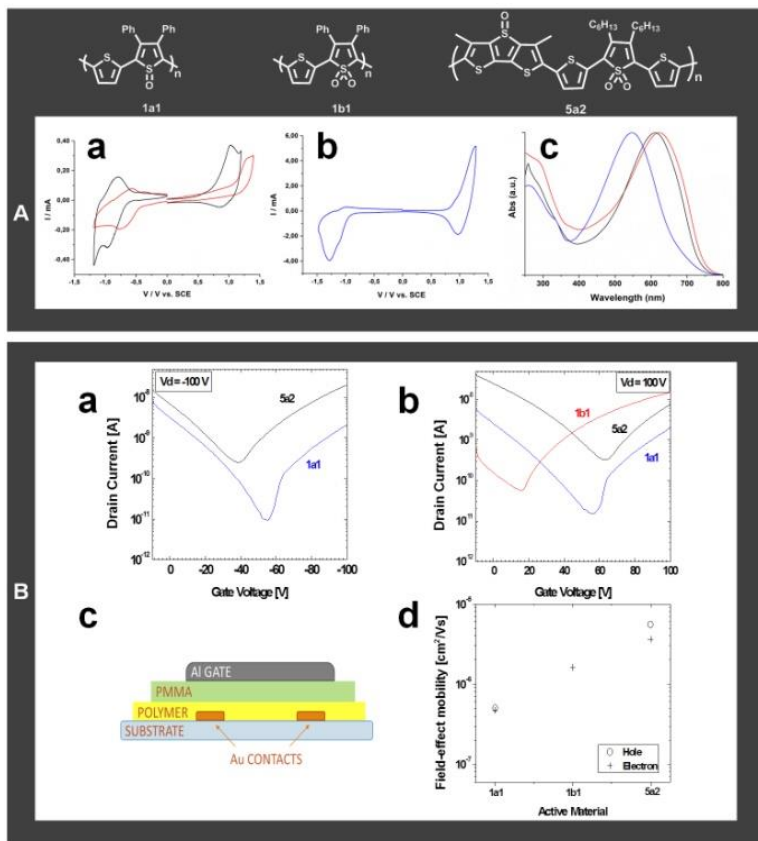


Figure 2. A) a,b) Cyclic voltammeteries of polymers **1a1**, **1b1**, **5a2** ; c) absorption spectra in DCM (red trace: **1a1** , blue trace: **5a2** , black trace: **1b1**). B) Transfer curves for the fabricated FETs in a) hole accumulation regime ($V_{\text{drain}} = -100$ V) and b) electron accumulation regime ($V_{\text{drain}} = 100$ V); c) the FETs stack; d) the extracted field-effect charge mobilities for the polymers. Geometrical dimensions for the FETs channel are $L = 20 \mu\text{m}$ for polymers **5a2** and **1b1**, $L = 10 \mu\text{m}$ for polymer **1a1**, and $W = 10 \mu\text{m}$ in all cases.

Remarkably, both polymers **1a1** and **1b1** display reduction potentials similar to those of phenyl-C61-butyric acid methyl ester (PCBM) ^[27], indicating significant electron affinities. The reduction potential of the mixed polymer **5a2**, with a different molecular structure, is sizeably

more negative than that of the other two polymers while the energy gap is much higher (1.92 V). Of the series of hexamers bearing two oxidized thiophenes, namely compounds **1a5** (two S-oxides), **1b5** (two -S,S-dioxides), and **1ab** (one S-oxide and one -S,S-dioxide) — see the CV plots in Figure S54 (Experimental Section) — the former displays the lowest oxidation potential (1.08 V), the second the highest (1.42 V) while the third is intermediate between the two (1.14 V). The comparison of the redox potentials of pentamers **9b1**, **10b3**, and **9b4** (see CV plots in Figure S55, Experimental Section) shows that passing from one thiophene-S,S-dioxide unit to two and three in the same molecular skeleton leads to a progressive increase in ionization potential paralleled by a progressive increase in reduction potential. Thus, the advantage of increasing the electron affinity of the system is paid by the increase in ionization energy. The three dithienothiophene derivatives, **5a1**, **5b1**, and **5b2** — see CV plots in Figure S56 (Experimental Section) — display quasi-reversible oxidation waves. On the contrary, only **5b1** with two terminal benzothiadiazole units, displays a reversible reduction wave, the other two being irreversible. Note that the oxidation potential of **5b2** is very close to that of **5b1** having two phenyl groups, suggesting that the HOMO of the former is mainly concentrated on the dithienothiophene-S,S-dioxide unit.

2.3 Optical Properties. Absorption and emission wavelengths and molar absorption coefficients of all oligomers and the absorption wavelength of all polymers are reported in Table S3 (Experimental Section). The corresponding spectra are shown in Figure 2 and Figures S60–S65 (Experimental Section). To time the photophysical properties of oxygenated thiophene derivatives have been poorly investigated. Very recently, Busby et al. have reported that the photodynamics of compounds containing thiophene-S,S-oxide moieties is profoundly different from that of the nonoxygenated counterparts ^[28], owing to the formation of fast singlet deactivation pathways which reduce the excited state lifetime by several orders of magnitude depending on the number and sequence of oxygenated thiophene units present in the molecular structure. Probably due to analogous reasons, none of polymers **1a1**, **1b1**, and **5a2** displays light emission in the visible or NIR range upon irradiation at the maximum absorption wavelength. The oligomers having only one single inner thiophene-S,S-dioxide or thiophene-S-oxide moiety — whether in linear trimers (**1a3**, **1b3**, Figure S65, Experimental Section) and pentamers (**1a2**, **1b2**, Figure S61, Experimental Section) or in V-shaped systems (**3a1-3**, **3b1-3**, Figure S62, Experimental Section) or in dithienothiophene derivatives (**5a1**, **5b1**, **5b2**, Figure S64, Experimental Section) — display photoluminescence in the visible region. However, on increasing the number of oxygenated units present in the molecular backbone, the intensity of the photoluminescence signal progressively decreases. This effect is nicely illustrated by the sequence of pentamers **9b1**, **10b3**, and **9b4** having one, two, and three thiophene-S,S-dioxide moieties, respectively, in the backbone. Figure S60 (Experimental Section) shows that the photoluminescence progressively vanishes as the number of S,S-dioxide moieties increases. A similar effect is observed for the hexamers having two thiophene-S-oxide groups (**1a5**), two thiophene-S,S-dioxide groups (**1b5**) and one thiophene-S-oxide and one thiophene-S,S-dioxide group (**1ab**), which display the same absorption spectra and extremely weak photoluminescence

spectra in solution. Of the three hexamers only the former one displays a sizeable photoluminescence signal in cast film (Figure S63, Experimental Section). Although we are aware of the fact that only deeper photophysical studies — far beyond the objective of the present study — would allow to unambiguously shed light on the photophysical properties of oxygenated thiophene derivatives, to give an insight into the properties of the newly synthesized compounds Figure S66 (Experimental Section) compares the spectra of **3a1** and **3b1** in 1.0×10^{-5} M solution in DCM, in thin film 0.1 wt% in poly(methylmethacrylate) (PMMA) and in neat film (100%). The UV–vis spectra show that passing from isolated monomers dispersed into the PMMA inert matrix to the neat film there is a considerable redshift indicating the formation of aggregate absorbing states (dimers) [29, 30a]. For both oligomers, the absorption profile of isolated monomer finely matches that obtained in solution. The photoluminescence spectra show that for both compounds the spectral profiles change considerably passing from 0.1% in PMMA to the pure dye for which a marked redshift is again observed. The redshift of about 60 nm in both oligomers can be ascribed to the interaction of adjacent molecules leading to the formation of dimer emitting states. According to the data reported in Table 3, the highest photoluminescence quantum yields (PLQY) are those of the samples 0.1% in PMMA ($\Phi_{PL} \approx 0.1, 0.2$) and the lowest those of the pure samples ($\Phi_{PL} = 0.04, 0.07$), possibly due to quenching activities of the excited states by molecular oxygen and/or self-quenching phenomena.

Table 3. Maximum emission wavelengths, decay times τ_1 , τ_2 , τ_3 and photoluminescence quantum yields of **3a1** and **3b1**.

	λ [nm]	τ_1 [ns]	τ_2 [ns]	τ_3 [ns]	PLQY [%]
3b1 1.0^{-5} M in DCM	650	0.8		5.3	A
3b1 0.1% in PMMA	600	1.1		5.6	19%
3b1 100 %	650	0.6	2.0	4.4	0.7%
3a1 1.0^{-5} M in DCM	650	0.8		5.6	A
3a1 0.1% in PMMA	650	1.0		5.6	11%
3a1 100 %	650	0.7	2.6	7.8	0.4%

For both **3a1** and **3b1** multiple photoluminescence decay times were also observed, as illustrated in Figure S67 (Experimental Section) and Table 3. The analysis of lifetime decays in PMMA and in diluted solution shows that both compounds follow a biexponential behaviour, most probably due to a double emitting state already described for some thiophene derivatives [30]. Table 3 shows that in the neat films a third decay time (τ_3) was found that can be ascribed to the deexcitation of the aggregates.

2.4 Thin Film Devices. Here we report experimental evidence that oligo- and polythiophenes containing thiophene-S-oxide moieties are charge transporting and electroluminescent materials, which, in contrast to the corresponding -S,S-dioxides (n-type semiconductors), are characterized by ambipolar charge transport properties. Note that the choice of the molecular structures to test

in devices is somewhat arbitrary, owing to the very limited number of studies on charge transport properties of such type of compounds (see references reported below).

2.4.1 Field-Effect Transistors with Polymers 1a1, 1b1, and 5a2. The polymers were tested as active materials in staggered topgate FETs operating both in p- and n-accumulation regimes. A staggered architecture was adopted since it typically suffers less from charge injection limitations at the contacts ^[31], and a top-gate configuration with a low-k polymer dielectric, in this case PMMA, offers a dielectric/polymer interface which is more ideal for charge transport ^[32]. We measured the transfer curves of the fabricated devices both in p- (Figure 2 Ba) and n-type (Figure 2 Bb) mode. When operated in p-type mode, only **1a1** and **5a2** — having thiophene-S-oxide units — display an appreciable holes current at bias voltages below -60 and -40 V, respectively; while at higher voltages a channel current due to electrons can be observed. Instead, all compounds can sustain electrons current when the FETs are operated in n-type mode, with **1b1** — having only thiophene-S,S-dioxides units — displaying the highest current and lowest threshold voltage. Therefore these measurements highlight a capability of all three materials for electron transport. The extracted electron field effect mobilities (Figure 2 Bd) are $4.7 \times 10^{-7} \text{ cm}^2 \text{ V}^{-1} \text{ s}^{-1}$ for **1a1**, $1.6 \times 10^{-6} \text{ cm}^2 \text{ V}^{-1} \text{ s}^{-1}$ for **1b1**, and $3.6 \times 10^{-6} \text{ cm}^2 \text{ V}^{-1} \text{ s}^{-1}$ for **5a2**: the higher mobility for **5a2**, despite the lower FET current with respect to **1b1**, can be explained with a much higher threshold voltage of 62 V for **5a2**, with respect to 19 V for **1b1**. On the contrary only **1a1** and **5a2** can appreciably conduct holes, achieving holes field-effect mobilities of 5×10^{-7} and $5.5 \times 10^{-6} \text{ cm}^2 \text{ V}^{-1} \text{ s}^{-1}$, respectively. Although many factors, including a complex structure–property relationship, can affect charge-transport properties, it is to stress how the ambipolarity feature of the latter two materials is fairly balanced with respect to the opposite charged species. To date FET charge mobilities of polymers bearing thiophene-S,S-dioxides moieties into the aromatic backbone have been assessed only in two cases. The first case concerns a polythiophene with varying ratios of alkylated thiophene to thiophene-S,S-dioxide units in the backbone ^[33a]. According to that study *I*-*V* measurements showed that the polymers never exhibited clear field-effect behaviour in either hole or electron accumulation regimes. Moreover, the authors report that the SO₂ functionality was labile on heating and increasing above 50% the number of oxygenated thiophene units present in the backbone resulted in significant degradation negatively impacting on charge-transport properties. In particular, they report that an incorporation of oxygenated thiophene higher than 20% led to complete failure of the FETs after a 110 °C thermal annealing. By contrast, the FET devices reported here, realized using active materials featuring 30%–50% incorporation, showed proper field-effect behaviour even after a thermal annealing at 150 °C. The second case concerns two polymers alternating acenaphtho[1,2-c]thiophene-S,S-dioxide units and thieno-thiophene or benzo [1,2-b:4,5-b']-dithiophene units ^[33b]. The polymers displayed p-type charge mobility on the order of 10^{-3} – $10^{-4} \text{ V cm}^{-1} \text{ s}^{-1}$. It is well known that FET charge mobilities can be enhanced by optimizing device fabrication and film morphology ^[31, 32, 34] or appropriate surface treatment ^[35]. The optimization of film morphology requires a good knowledge of the self-assembly properties of oligomers and polymers bearing thiophene oxidized moieties in the backbone. Although some data are available

on single crystal X-ray structure of oligothiophene-S,S-dioxides^[36] and powder X-ray studies of polythiophene-S,S-dioxides outlining the importance of H-bonding on molecular packing,^[37] no detailed investigations have been carried out so far on the self-assembly pathways in thin films of oligomers and polymers containing thiophene oxygenated units. It is reasonable to expect that these studies will result in the preparation of thin films with optimized morphology and consequently higher charge mobility values than those reported in Figure 1 B. However, independently of the FET charge mobility values, our data unambiguously indicate that charge carrier types in thiophene materials can be modulated via mono- or dioxygenation of thiophene sulfur. Concerning the compounds containing thiophene-S-oxide units in the backbone, we suggest that their ambipolar charge conduction properties are related to lower oxidation potentials compared to the corresponding compounds having thiophene-S,S-dioxide units.

2.4.2 Light Emitting Devices with Oligomers 3a1 and 3b1. Further evidence that oligothiophene-S-oxides have ambipolar charge transport properties while the corresponding -S,S-dioxides are n-type charge carriers comes from comparison of electroluminescent devices with V-shaped oligomers **3a1** and **3b1**. It is known that V-shaped thiophene-S,S-dioxides are active materials in electroluminescent devices^[22], that they form noncentrosymmetric thin films and one member of the series displays second order susceptibility $\chi(2)$ values as high as the reference LiNbO₃ single crystal, without poling processing^[38]. No data are available for the corresponding S-oxides. Light emitting diodes were fabricated using either the neat films of both **3a1** and **3b1** or films where the compounds were dispersed in 15% concentration (chosen following optimized photoluminescence quantum yield measurements) within two different host matrices: BCPO, namely ambipolar 9,9'-(4,4'-(Phenylphosphoryl) bis-(4,1-phenylene))bis(9H-carbazole) and TPBI, namely electron transporting 1,3,5-tris-(*N*-phenylbenzimidazole-2-yl)-benzene. Both compounds were electroluminescent systems as shown in Figure 3 and Figures S68 and S69 (Experimental Section). Figure 3 shows that the electroluminescent spectra are in accordance with the photophysical characterization displaying emission peaks around 620 nm (**3a1**) and 635 nm (**3b1**) for the host-guest system light emitting diodes (LEDs) and around 645 and 660 nm, respectively, for LEDs with neat films. Due to self-quenching phenomena in the neat films, high current density values are measured, demonstrating inefficient exciton radiative recombination within the emitting layers, which leads to low luminance and low current efficiencies. In the case of host-guest systems, better results were obtained in terms of luminance and current efficiencies. Figure 3 shows that the S-oxide **3a1** exhibits close values of electroluminescence efficiency in both matrices with the highest one being obtained for the film dispersed within the ambipolar BCPO matrix. By contrast, there is a much greater difference in the electroluminescence efficiency of **3b1** dispersed into the two different matrices, the highest value being attained when the compound is dispersed within the electron transporting TPBI matrix. Since the electrooptical characteristics of the devices depend on the intrinsic transport properties of the active materials^[39] it can be argued that the S-oxide **3a1** has ambipolar charge transport properties whereas **3b1** has predominant electron transporting behaviour.

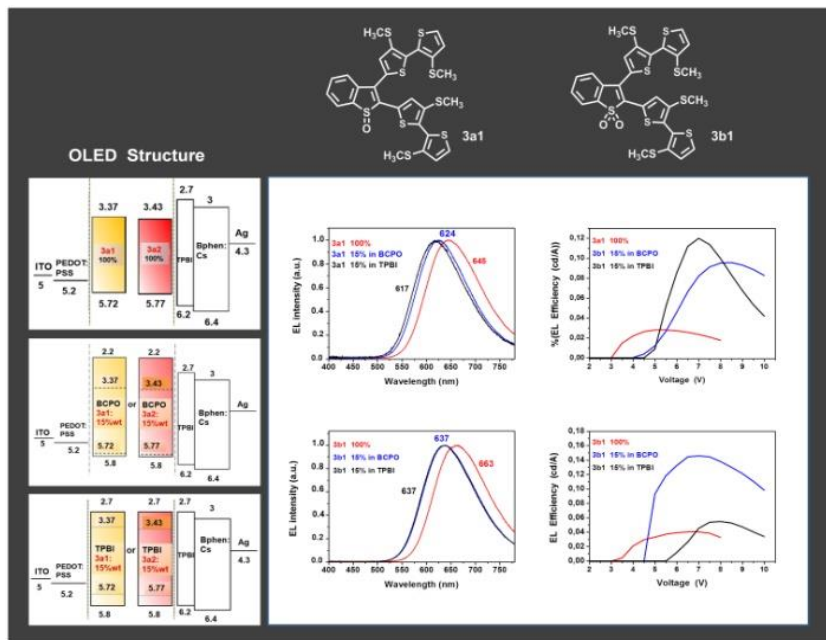


Figure 3. Structure of electroluminescent devices (left), electroluminescence intensity (right), and efficiency (lower right) of V-shaped oligomers **3a1** and **3b1** in thin films: 15% in BCPO, namely ambipolar 9,9'-(4,4'-(Phenylphosphoryl)bis-(4,1-phenylene))bis(9H-carbazole) and 15% in TPBI, namely electron transporting 1,3,5-tris-(*N*-phenylbenzimidazole-2-yl)-benzene.

2.5 Oligomers 5a1 and 5b1 Inside Live Cells. The presence of thiophene-S,S-dioxide moieties into the molecular backbone not only changes the frontier orbital energies but also affects the aggregation properties through the formation of H-bondings involving the oxygen atoms. We have already reported that the green fluorescent dithienothiophene-S,S-dioxide **5b1** is able to spontaneously cross the membrane of live mouse and bone-marrow human tumor fibroblasts [14]. In the perinuclear region, **5b1** is recognized by the hydroxyproline component of procollagen polypeptide chains through the formation of hydrogen bondings between the O-H group of hydroxyproline and the oxygen atom of the O=S=O group. As a consequence, the formation of coassembled fluorescent and conductive type-I collagen-**5b1** microfibers is observed inside the cells. Having now the possibility to prepare in fair amount and free of contaminants the corresponding S-oxide, **5a1**, we could repeatedly and reproducibly test its behaviour inside live cells in the same conditions. We found that both **5a1** and **5b1** were spontaneously internalized by live fibroblasts and that however, they displayed completely different behaviour inside the cells. The results are reported in Figure 5 A,B comparing the behaviour of **5a1** and **5b1**.

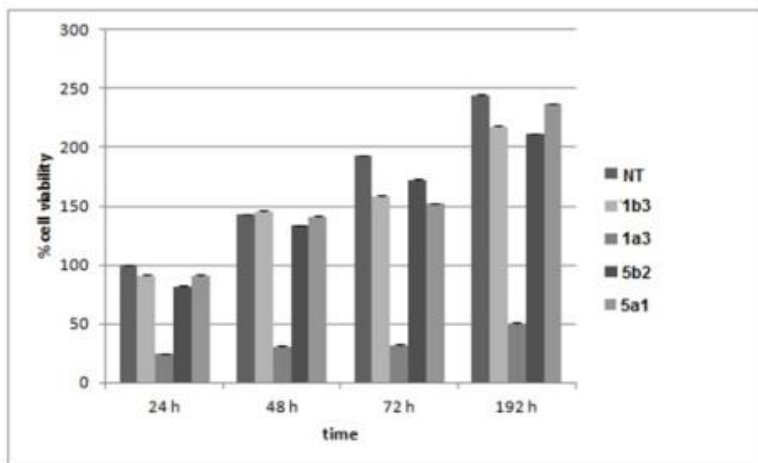


Figure 4. MTT cytotoxicity tests on NIH 3T3 cells treated with **1b3**, **1a3**, **5b1**, and **5a1** compared to untreated cells (NT). Representative measurements of three distinct sets of data and no significant difference between, values at different time points are observed at $P < 0.05$ with Student t -test. See ref. [14d] for **5b1**.

Figure 5 A shows the formation of fluorescent microfibers after 6 h (a) and 120 h (b) upon spontaneous uptake of **5b1** by live human fibroblasts. The diffusion of **5b1** inside the cells is rather uniform as the cytoplasm appears entirely stained, while the compound does not enter the nucleus of the cells which remains dark. Figure 5 A(c–e) shows the 3D laser scanning confocal microscopy (LSCM) reconstruction indicating that most microfibers display helical supramolecular organization. The fluorescent microfibers are mainly made of type-I collagen coassembled with **5b1**, as demonstrated by sodium dodecyl sulphate polyacrylamide gel electrophoresis (SDSPAGE) and immunoblotting analysis [14]. Similar to **5b1**, sulfoxide **5a1** — is not toxic to the cells and does not alter their viability and proliferation ability. Figure 4 reports the 3-(4,5-dimethylthiazol-2-yl)-2,5-diphenyltetrazolium bromide cytotoxicity tests (MTT) [40] on NIH 3T3 cells treated with **5a1** and a few other S-oxides and -S,S-dioxides. The corresponding cytotoxicity test for **5b1** is reported in ref. [14d]. Contrary to the -S,S-dioxide **5b1**, the S-oxide **5a1** once internalized by the cells is not recognized by any intracellular component and is physiologically and progressively eliminated. Figure 5 B shows that after 24 h from spontaneous uptake by the fibroblasts, **5a1** accumulates in the perinuclear region forming bright green fluorescent spots. However, there is no sign of formation of fluorescent fibers and after 168 h (7 d) only a few fluorescent aggregates of **5a1** are still present inside the cells. To account for the different behaviour of the monooxygenated **5a1** with respect to the dioxygenated **5b1** inside the cells, we performed a theoretical study using the density functional theory (DFT) at the BLOC-D3/def2-TZVPP level [41].

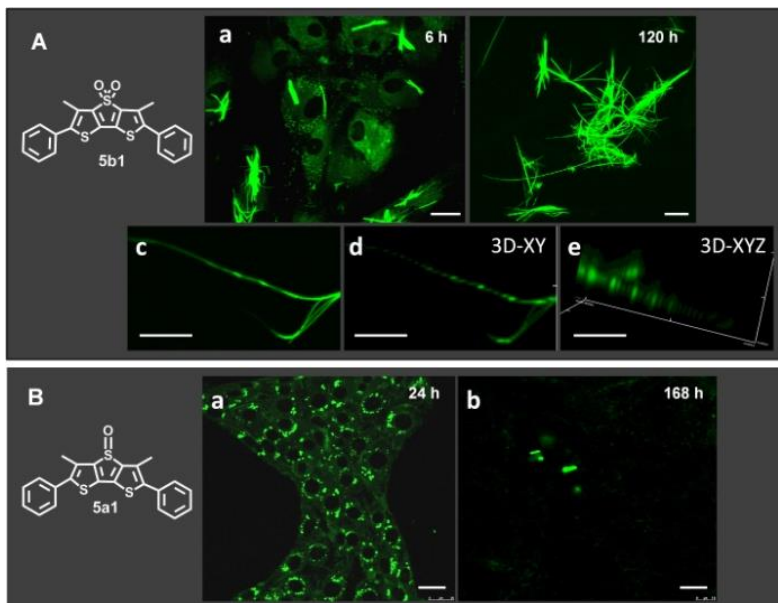


Figure 5. LSCM images of live fibroblasts upon spontaneous uptake of **5b1** and **5a1**. A) View (a,b) of the cell culture after 6 and 120 h from uptake of **5b1** by human fibroblasts showing the formation of green fluorescent microfibers on the surface of the cells (scale bars: 25 μm), c) a detail of the microfibers structure and d,e) the corresponding 3D spatial reconstruction displaying the helical morphology of the microfibers (scale bars: c) 50 μm ; d,e) 25 μm). B) LSCM images of live N3 HT3 fibroblasts a) 24 h and b) 168 h from spontaneous uptake of **5a1** showing that in this case there is no formation of fluorescent microfibers (scale bars: 75 μm).

To elucidate the nature of the noncovalent interaction between the S-oxide and collagen, and especially the role of the hydrogen bonding, an analysis of the reduced gradient as a function of the electron density (ρ) times the second eigenvalue of the electron-density Hessian (λ_2) was performed in the collagen-5a1 (5b1)-Collagen [C-5a1(5b1)-C] bonding region. This is the so called non-covalent interaction (NCI) indicator, which is able to characterize different kinds of noncovalent bonds ^[42]. Since the fluorescent microfibers generated by the cells upon uptake of **5b1** are mainly made of type-1 collagen, the theoretical investigation considered a model system consisting of one molecule (either **5b1** or **5a1**) sandwiched between two collagen strands simulated by a sequence of three tripeptide Gly-Pro-HyPro (Figure 6 A). A similar model for collagen but with only a single tripeptide chain was also used in ref. [14d]. The results of this analysis, reported in Figure 6, unambiguously show the importance of oxygen to promote a H-bonding between the oxidized compounds and the collagen strand. In fact, in the case of -S,S-dioxide **5b1** (case 1) a clear hydrogen bond nature is observed due to the interaction of the oxygen atoms with the hydrogen atoms of the HyPro rings in front of it.

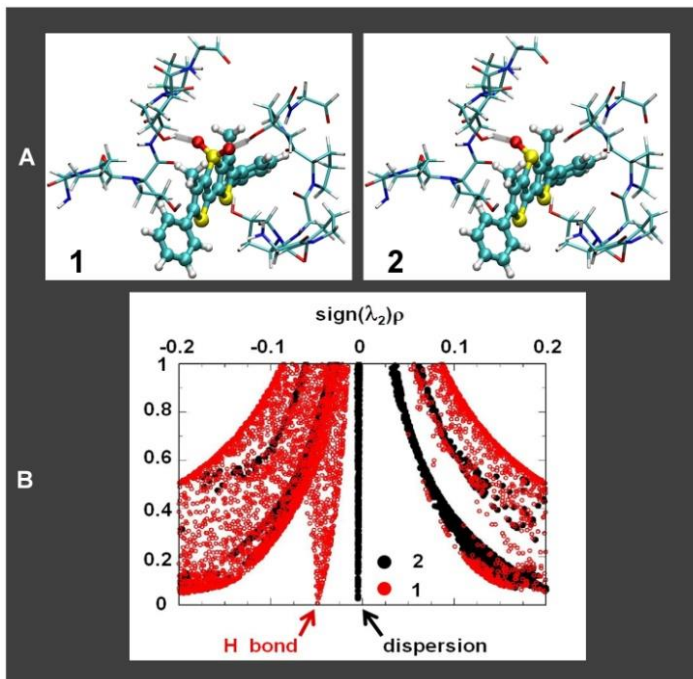


Figure 6. A) Model systems considered for DFT calculations with **5b1** (1) and **5a1** (2) interacting with two collagen strands built up of three Gly-Pro-HyPro tripeptide chains. B) NCI indicator analysis of the bonding region between the collagen-fluorophore and the additional collagen strand in cases **1** and **2**. In the x -axis label ρ denotes the electron density and λ_2 the second eigenvalue of the electron-density Hessian.

By contrast, when the corresponding S-oxide **5a1** is considered (case 2), where no oxygen atom is present to mediate the interaction between C-**5a1** and the second collagen strand, no signature of hydrogen bonding was found in the relevant bonding region and the interaction between **5a1** and the collagen strand is only due to dispersion contributions. These results not only provide a key to understand why **5a1** does not lead to the physiological formation of fluorescent microfibrils but also confirm our previous interpretation according to which the collagen-**5b1** coassembly inside live fibroblasts is mainly due to the hydrogen bonding capabilities of the sulfone groups^[14d]. We can anticipate that we have tested several other thiophene-S,S-dioxides and the corresponding S-oxides for their behaviour inside live cells. We have found that the former were not toxic to the cells (as shown in Figure 4 for **1b3** and **5b2**) and always formed fluorescent microfibrils inside the cells, the composition of which varied with the molecular structure of the dioxide and is currently under study. On the contrary, the corresponding S-oxides never led to the formation of fluorescent microfibrils inside live cells and some of them were even toxic to the cells (as shown in Figure 4 for **1a3**).

III CONCLUSION

The straightforward and low-cost chemical strategy outlined in this work opens a wide range of opportunities for the development of innovative thiophene materials with tailored properties and function. It relies on the easy synthesis of monooxygenated thiophene units, namely thiophene-S-oxides, very difficult to access with previously developed synthetic methodologies for thiophene oxygenation. Monooxygenated, dioxygenated and nonoxygenated thiophene units can be viewed as Lego bricks which can be mixed at will to create innumerable new molecular structures to add to the already vast land of thiophene materials with little synthetic effort. The introduction of thiophene-S-oxides into the conjugated backbone of polythiophenes has several consequences, in particular a marked increase in electron affinity which, in contrast with the introduction of thiophene-S,S-dioxides, is *not* paralleled by the increase in ionization potential and the induction of ambipolar charge transport properties, again in contrast with the introduction of thiophene-S,S-dioxides causing n-type charge transport. New limits of important properties can be attained such as reduction potentials on the order of -0.4 V, near the values of fullerene, and energy gaps in the order of 1.2 V. Moreover, new exciting fields of application can be foreseen. For example, taking into account that in thiophene-S-oxide the sulfur atom is pyramidal, it will be possible to design and synthesize configurationally stable building blocks for the preparation of semiconducting chiral systems for chiral voltammetry ^[43] or innovative electronic devices such as spin-OLEDs that do not require magnetic elements to define the spin orientation ^[44]. Owing to their peculiar electronic and optical properties, several conjugated oligomers and polymers have been investigated in the past few years for biological applications, from fluorescent imaging of live cells to protein and DNA labelling, drug delivery, analyte recognition and so forth. We believe that oligo and polythiophene-S-oxides, -S,S-dioxides, and mixed -S-oxides/-S,S-dioxides will gain wide interest in these fields due to the main possibilities of subtle changes in molecular structure which might have important consequences for specific applications. In the present paper we show—in the context of our previous biological applications of thiophene materials ^[14d] — the very different cytotoxicity of thiophene-S-oxides and thiophene-S,S-dioxides with regard to live cells, although both systems have the appropriate hydrophilicity/hydrophobicity balance to be spontaneously internalized by live cells. Even more important is the finding that the two systems display very different recognition capabilities for specific intracellular proteins through H bonding intermolecular interactions.

IV METHODS

4.1 Synthesis and Characterization. The synthesis of oxygenated thiophenes (Table 1) was performed in a FALC LBS1 50 KHZ Ultrasonic bath. Cross-coupling reactions involving boron derivatives were carried out under microwave assistance in a Milestone Microsynth Labstation operating at 2450 MHz monitored by a proprietary control unit. All operations were carried out

under a dry, oxygen-free nitrogen atmosphere. Organic solvents were dried by standard procedures. Thin layer chromatography (TLC) was carried out with 0.2 mm thick of silica gel 60 F254 (Merck). Visualization was accomplished by UV light or phosphomolybdic acid solution. Preparative column chromatographies was performed on glass columns of different sizes hand packed with silica gel 60 (particle sizes 0.040–0.063 mm, Merck). H-1 and C-13 NMR spectra were recorded with a Varian Mercury-400 spectrometer equipped with a 5 mm probe. Chemical shifts were calibrated using the internal CDC13 resonance which was referenced to tetramethylsilane (TMS). Mass spectra were collected on a Thermo Scientific TRACE 1300 gas chromatograph. UV–vis spectra were recorded using a Agilent Technologies CARY 100 UV–vis spectrophotometer. Photoluminescence spectra were collected on a Perkin Elmer LS50 spectrofluorometer. The detailed preparation of all compounds and their characterization are reported in the Experimental Section.

4.2 Cyclic Voltammetry. Solid state CVs were obtained employing an AMEL 5000 electrochemical cell under argon. Working electrodes were solid films of the oligomers or polymers deposited on indium-tin oxide (ITO). An electrolytic solution of anhydrous propylene carbonate (Sigma-Aldrich) containing 0.1 mol L⁻¹ tetraethylammonium tetrafluoroborate (Fluka for electrochemical analysis) was used. The oxidation potential of ferrocene/ferricinium (Fc/ Fc⁺ = -4.84 eV) versus aqueous saturated calomel electrode (SCE) was 0.50 V. The CVs of 1 mmol L⁻¹ oligomers were performed on Pt disc-electrode in DCM (Sigma-Aldrich, distilled on P 2 O 5 and stored under Ar) 0.1 mmol L⁻¹ tetrabutyl-ammonium perchlorate (Fluka, recrystallized form methanol) where Fc/Fc⁺ = 0.47 V versus SCE.

4.3 Single Crystal X-Ray Diffraction. Crystallographic data collection and structure determination were performed with a single crystals of hexamer 1a5 grown from toluene. The X-ray intensity data of the compound were measured on a Bruker Apex II charge coupled device (CCD) diffractometer. Cell dimensions and the orientation matrix were initially determined from a least-squares refinement on reflections measured in three sets of 20 exposures, collected in three different ω regions and eventually refined against all data. A full sphere of reciprocal space was scanned by 0.3° ω steps. The software SMART^[45] was used for collecting frames of data, indexing reflections and determination of lattice parameters. The collected frames were then processed for integration by the SAINT program^[45], and an empirical absorption correction was applied using SADABS^[46]. The structure was solved by direct methods (SIR 2004^[47]) and subsequent Fourier syntheses and refined by full-matrix least-squares on F^2 (SHELXTL^[48]) using anisotropic thermal parameters for all nonhydrogen atoms. All the hydrogen atoms were added in calculated positions, included in the final stage of refinement and refined with $U(H) = 1.2 U_{eq}(C)$ and allowed to ride on their carrier atoms. The oxygen atom of the sulfoxide group was found to be disordered over two sites with occupancy factor of 0.90 and 0.10, respectively. The SQUEEZE routine of the PLATON software^[49] revealed that the structure contains solvent accessible voids (352 Å³ unit⁻¹ cell), filled with disordered solvent molecules (99 electrons unit⁻¹ cell) that is most likely disordered toluene. Molecular graphics were generated by using

Mercury 3.3^[50]. Color codes for all molecular graphics: orange (Cu), blue (N), red (O), gray (C), white (H). Crystal data and details of data collections for compound A are reported in Table S4 (Experimental Section).

4.4 Field-Effect Transistors. Top-gate, staggered FETs operating both in p- and n-accumulation regimes were fabricated using polymers **1a1**, **1b1**, **5a2** as the active materials. Low alkali 1737F Corning glass was used as substrate, cleaned aequentially in an ultrasonic bath of deionized water, acetone, and 2-propanol for 10 min each, then exposed to oxygen plasma at 100 W for 10 min. Bottom source and drain electrodes were defined by photolithography and evaporation of 1.5 nm of Cr and 25 nm of Au. The defined patterns feature a channel width $W = 10$ nm and channel length $L = 20$ μm or $L = 10$ μm (2) Solutions of the three polymers with a concentration of 5 g L⁻¹ in chloroform were prepared and deposited via spin coating at 1000 rpm in nitrogen atmosphere, then the samples were annealed at 150 °C for 8 h. PMMA, was purchased from Sigma-Aldrich and dissolved in *n*-butyl acetate with a concentration of 80 g L⁻¹, then spin coated over the active material layer at 1500 rpm yielding a 500 nm thick dielectric layer. The devices were then annealed at 80 °C for 30 min. The gate electrodes were defined via evaporation of Al through a shadow mask. Electrical characterization was performed in a nitrogen atmosphere using an Agilent B1500A Semiconductor Parameter Analyzer.

4.5 Photoluminescence Measurements in Thin Films. Emission spectra were obtained with an Edinburgh FLS980 spectrometer equipped with a peltier-cooled Hamamatsu R928 photomultiplier tube (185–850 nm). An Edinburgh Xe900 450 W Xenon arc lamp was used as exciting light source. Emission lifetimes in the ns– μs range were determined with the single photon counting technique by means of the same Edinburgh FLS980 spectrometer using a laser diode as excitation source (1 MHz, $\lambda_{\text{exc}} = 407$ nm, 200 ps time resolution after deconvolution) and the above-mentioned photomultiplier tube (PMT) as detector. Analysis of the luminescence decay profiles versus time was accomplished with the Decay Analysis Software provided by the manufacturer. Photoluminescence yields were calculated by corrected emission spectra obtained from an apparatus consisting of a barium sulfate coated integrating sphere (4 inches), a 450W Xe lamp ($\lambda_{\text{exc}} =$ tunable by a monochromator supplied with the instrument) as light sources, and a R928 photomultiplier tube as signal detectors, following the procedure described by De Mello et al.^[51]. Experimental uncertainties are estimated to be $\pm 8\%$ for lifetime determinations, ± 2 – 0% for emission quantum yields, ± 2 and ± 5 nm for absorption and emission peaks, respectively. Absorption spectra were recorded with a Cary 5000 UV–vis–NIR Varian spectrophotometer.

4.6 OLEDs Fabrication and Characterization. The OLEDs were fully fabricated by high vacuum thermal evaporation in a Kurt J. Lesker multiple high vacuum chamber system. The electrical–optical characteristics of the devices were measured under vacuum with an Optronics OL770 spectrometer, coupled, through an optical fiber, to the OL610 telescope unit for the luminance measurements, with an experimental uncertainty of around $\pm 10\%$. The whole system

was National Institute of Standards and Technology calibrated using a standard lamp and was directly connected by RS232 cable to a Keithley 2420 current–voltage source meter.

4.7. Cell Viability. Mouse embryonic fibroblasts (NIH-3T3) were seeded at a density of 100000 cells in tissue culture plate in 1 mL of complete culture medium. Compounds **5a1**, **5b1**, and **5b2** were dissolved in the minimum amount of dimethylsulfoxide (DMSO) in order to obtain a stock solution and then were administered to the cells by adding the appropriate dilution in Dulbecco's Modified Eagle Medium (DMEM) serum free to obtain the final concentration of 0.05 mg mL⁻¹ and incubated at 37 °C in 5% CO₂, 95% relative humidity for 1 h. At the end of the incubation period, the cell cultures were repeatedly washed with DMEM medium serum free. The cells were examined after 1, 24, 48, 72 h, and 7 d upon treatment by LSCM. Confocal images were taken with Leica confocal scanning system mounted into a Leica TCS SP5 (Leica Microsystem GmbH, Mannheim, Germany), equipped with a 63X oil immersion objective and spatial resolution of approximately 200 nm in *x* - *y* and 100 nm in *z*. After an appropriate incubation period, the cultures were removed from the incubator and the MTT (3-(4,5-dimethylthiazol-2-yl)-2,5-diphenyl tetra-zolium bromide) solution added in an amount equal to 10% of the culture volume. Then the cultures were returned to incubator and incubated for 3 h. After the incubation period, the cultures were removed from the incubator and the resulting MTT formazan crystals were dissolved with acidified isopropanol solution to an equal culture volume. The plates were read within 1 h after adding acidified isopropanol solution. The absorbance was spectrophotometrically measured at wavelength 570 nm and the background absorbance measured at 690 nm subtracted. The percentage viability is expressed as the relative growth rate (RGR) by equation: $RGR = (D_{sample}/D_{control}) * 100\%$ where D_{sample} and $D_{control}$ are the absorbances of the sample and the negative control ^[24]. Representative measurements of three distinct sets of data are reported (*Student t-test*, $P < 0.05$).

V. EXPERIMENTAL SECTION

5.1 Synthesis. General: unless otherwise noted, all operations were carried out under a dry, oxygen-free nitrogen atmosphere. Organic solvents were dried by standard procedures. TLC was carried out with 0.2-mm thick of silica gel 60 F254 (Merck). Visualization was accomplished by UV light or phosphomolybdic acid solution. Preparative column chromatographies was performed on glass columns of different sizes hand packed with silica gel 60 (particle sizes 0.040-0.063 mm, Merck). Phenylboronic acid pinacol ester, 4-bromo-2,1,3-benzothiadiazole, 2-(tributylstannyl)thiophene, 2-(tributylstannyl)-2':2'.bithiophene, 2,3-dibromobenzo[b]thiophene, thianaphthene, thieno[3,2-b]thiophene, tributyltin chloride, 2,5-bis(tributylstannyl)thiophene, 2-hexylthiophene, 3,4-dihexylthiophene, hydrogen peroxide solution (30 wt. % in H₂O), 1,1'-bis(diphenylphosphino)ferrocene palladium(II)chloride dichloromethane complex (PdCl₂dppf), n-butyllithium 2.5 M solution in hexane, N-bromosuccinimide, sodium bicarbonate, tributylstannyl chloride, potassium tert-butoxide and trifluoroacetic acid were purchased from Sigma-Aldrich Co; 2-isopropoxy-4,4,5,5-tetramethyl-1,3,2-dioxaborolane,

Bis(pinacolato)diboron from Alfa Aesar GmbH & Co KG. All reagents and solvents were used as received. Microwave experiments were carried out in a Milestone Microsynth Labstation operating at 2450 MHz monitored by a proprietary control unit. The oven was equipped with magnetic stirring, pressure and temperature sensors. Reactions were performed in a glass vessel (capacity 10 mL) sealed with a septum. The microwave method was power controlled (100 W maximum power input) and the samples were irradiated with the required power output (setting at the maximum power) to achieve the desired temperature (80°C). Reactions with ultrasound were performed in a FALC LBS1 50KHz Ultrasonic bath. Melting points were determined on Kofler bank apparatus and are uncorrected. All ¹H NMR and ¹³C NMR spectra were recorded on a Varian Mercury-400 spectrometer equipped with a 5-mm probe. Chemical shifts were calibrated using the internal CDCl₃ resonance which was referenced to TMS. Mass spectra were collected on a Thermo Scientific TRACE 1300 gas chromatograph. UV-Vis spectra were recorded using a Agilent Technologies CARY 100 UV-Vis spectrophotometer. Photoluminescence spectra were collected on a Perkin Elmer LS50 spectrofluorometer. Fluorescence measurements were performed using an excitation wavelength corresponding to the maximum absorption lambda. Ultrasound assisted reactions were performed on a ELMASONIC S 40 (H).

General procedure for the synthesis of bromothieryl-derivatives: To a solution of the starting materials (1 mmol) in CH₂Cl₂ : CH₃COOH (6:4 v/v), 1 mmol or 2 mmol of NBS were added. The reaction mixture was sonicated for 30 min at room temperature. The solvent was removed and the products were purified by flash chromatography on silica gel.

2,5-dibromo-3,4-diphenylthiophene (1) → Cyclohexane: CH₂Cl₂ (80:20). Yield 100%. Pale yellow solid; EI-MS m/z 394 (M⁺); ¹H NMR (400 MHz, CDCl₃, TMS/ppm): δ 7.25-7.22 (m, 6H), 7.07-7.05 (m, 4H). ¹³C NMR (TMS/ppm): 141.9, 134.5, 130.2, 127.9, 127.7, 109.5.

2-bromobenzob[*b*]thiophene (2) → EI-MS m/z 213(M⁺); ¹H NMR (400 MHz, CDCl₃, TMS/ppm): δ 7.87-7.83 (m, 2H), 7.50-7.40 (m, 3H).

2-bromo-5-hexylthiophene (8) → EI-MS m/z 246(M⁺); ¹H NMR (400 MHz, CDCl₃, TMS/ppm): δ 6.84 (d, J=3.4 Hz, 1H), 6.52 (d, J=3.4 Hz, 1H), 2.73 (t, 2H), 1.63-1.54 (m, 2H), 1.40-1.15 (m, 6H), 0.88 (t, 3H); ¹³C NMR (TMS/ppm): 147.8, 129.4, 124.3, 108.5, 31.5, 31.4, 30.3, 28.7, 22.5, 14.0.

2,6-dibromo-3,5-dimethyldithieno[3,2-*b*:2',3'-*d*]thiophene (5) → White solid; EI-MS m/z 382(M⁺); ¹H NMR (400 MHz, CDCl₃, TMS/ppm): δ 2.37 (s, 6H).

2,5-dibromothieno[3,2-*b*]thiophene (6) → EI-MS m/z 298 (M⁺); ¹H NMR (400 MHz, CDCl₃, TMS/ppm): δ 7.17 (s, 2H); ¹³C NMR (TMS/ppm): 138.3, 121.7, 113.6.

5-bromo-3',4'-diphenyl-[2,2':5',2''-terthiophene] 1'-oxide (1a4) → Cyclohexane : CH₂Cl₂ : AcOEt (70:25:5). Yield 60%. Dark orange solid; EI-MS m/z 494(M⁺); ¹H NMR (400 MHz, CDCl₃, TMS/ppm): δ 7.63 (d, J=3.6, 1H), 7.63 (d, J=3.6, 1H), 7.35-7.27 (m, 6H), 7.13-7.12 (m, 4H), 7.06 (dd, 3J=3.6Hz, 3J=1.2 Hz, 1H), 7.02 (d, J=3.6, 1H).

5-bromo-3',4'-diphenyl-[2,2':5',2''-terthiophene] 1',1'-dioxide (1b4) → Cyclohexane : CH₂Cl₂ (70:30). Yield 74%. Dark orange solid; EI-MS m/z 511(M⁺); ¹H NMR (400 MHz, CDCl₃,

TMS/ppm): δ 7.74 (d, 3J=4 Hz, 4J=1.2 Hz, 1H), 7.51 (d, J=4, 1H), 7.34-7.25 (m, 6H), 7.11-7.06 (m, 6H), 7.02 (d, J=4, 1H).

5,5''-dibromo-3,3'',4,4''-tetrahexyl-[2,2':5',2''-terthiophene]-1,1,1'',1''-tetraoxide (10b2) \rightarrow Cyclohexane : CH₂Cl₂ : AcOEt (65:30:5). Yield 60%. Pale orange solid; EI-MS m/z 804 (M⁺); ¹H NMR (400 MHz, CDCl₃, TMS/ppm): δ 7.67 (s, 2H), 2.67-2.63 (m, 4H), 2.49-2.45 (m, 4H), 1.62-1.24 (m, 32H), 0.92-0.84 (m, 12H).

General procedure for the synthesis of thienyl-S-oxides and -S,S-dioxides.

METHOD A: To a solution of the starting material (1 mmol) in CH₂Cl₂/ CF₃COOH (2:1 v:v), were added 1 mmol of H₂O₂ (as a solution in H₂O 30 wt. %) for the synthesis of sulfoxide derivatives or 2 mmol of H₂O₂ (as a solution in H₂O 30 wt. %) for the synthesis of the sulfone derivatives. The reaction mixture was sonicated in a closed vessel by immersion in an ultrasonic bath (see table 1 for the reaction times of the different substrates). The crude product was extracted with NaHCO₃ sat. and the organic layers were collected. The solvent was removed under reduced pressure and the products were purified by flash chromatography.

METHOD B: To a solution of the starting material (1 mmol) in CH₂Cl₂, 2 mmol of meta-chloroperoxybenzoic acid (mCPBA) were added for the synthesis of the sulfone derivatives. The reaction mixture was sonicated in a closed vessel by immersion in an ultrasonic bath (see table 1 for the reaction times of different substrates). The solvent was removed and the products were purified by flash chromatography.

2,5-dibromo-3,4-diphenylthiophene-1-oxide (1a) \rightarrow METHOD A: Cyclohexane: CH₂Cl₂ : AcOEt (80:15:5). Yield 70%. Pale orange solid; EI-MS m/z 410 (M⁺); ¹H NMR (400 MHz, CDCl₃, TMS/ppm): δ 7.32-7.24 (m, 6H), 7.06-7.04 (m, 4H); ¹³C NMR (TMS/ppm): 145.6, 131.5, 129.4, 129.1, 128.3, 126.6.

2,5-dibromo-3,4-diphenylthiophene-1,1-dioxide (1b) \rightarrow Cyclohexane: CH₂Cl₂ : AcOEt (80:15:5). Yield 80% with METHOD A, 80% with METHOD B. Pale yellow solid; EI-MS m/z 426 (M⁺); ¹H NMR (400 MHz, CDCl₃, TMS/ppm): δ 7.35-7.28 (m, 6H), 7.04-7.02 (m, 4H); ¹³C NMR (TMS/ppm): 142.1, 129.9, 129.8, 129.1, 128.3, 116.5.

2-bromobenzo[b]thiophene-1-oxide (2a) \rightarrow METHOD A: Cyclohexane: CH₂Cl₂:AcOEt (80:15:5). Yield 99%. White solid; EI-MS m/z 229 (M⁺); ¹H NMR (400 MHz, CDCl₃, TMS/ppm): δ 7.92 (d, J=8 Hz, 1H), 7.66-7.54 (m, 3H), 7.27 (s, 1H); ¹³C NMR (TMS/ppm): 144.0, 136.3, 135.3, 132.4, 130.0, 128.6, 125.9, 124.6.

2-bromobenzo[b]thiophene-1,1-dioxide (2b) \rightarrow Cyclohexane : CH₂Cl₂ : AcOEt (80:15:5). Yield 80% with METHOD A, 80% with METHOD B. White solid; EI-MS m/z 245 (M⁺); ¹H NMR (400 MHz, CDCl₃, TMS/ppm): δ 7.73-7.55 (m, 4H), 6.96 (s, 1H); ¹³C NMR (TMS/ppm): 137.0, 133.8, 131.6, 131.1, 129.6, 129.57, 124.7, 120.8.

2,3-dibromobenzo[b]thiophene-1-oxide (3a) \rightarrow METHOD A: Cyclohexane: CH₂Cl₂ : AcOEt (80:15:5). Yield 99%. White solid; EI-MS m/z 308 (M⁺); ¹H NMR (400 MHz, CDCl₃, TMS/ppm): δ 7.87 (d, J=8 Hz, 1H), 7.63-7.51 (m, 3H); ¹³C NMR (TMS/ppm): 143.6, 136.7, 132.9, 131.2, 129.8, 128.8, 126.3, 124.3.

2,3-dibromobenzo[b]thiophene-1,1-dioxide (3b) → Cyclohexane: CH₂Cl₂ : AcOEt (80:15:5). Yield 80% with METHOD A, 80% with METHOD B. White solid; EI-MS m/z 324 (M⁺); ¹H NMR (400 MHz, CDCl₃, TMS/ppm): δ 7.76 (d, J=8 Hz, 1H), 7.69-7.65 (m, 1H), 7.61-7.57 (m, 2H); ¹³C NMR (TMS/ppm): 135.6, 134.2, 131.4, 131.0, 128.6, 124.4, 123.3, 121.7.

5-bromobenzo[b]thiophene-1-oxide (4a) → METHOD A: Cyclohexane : CH₂Cl₂ : AcOEt (80:15:5). Yield > 90%. White solid; EI-MS m/z 229 (M⁺); ¹H NMR (400 MHz, CDCl₃, TMS/ppm): δ 7.96 (d, J=8 Hz, 1H), 7.70-7.57 (m, 3H), 7.29 (s, 1H); ¹³C NMR (TMS/ppm): 144.0, 136.3, 135.4, 132.4, 130.0, 128.6, 125.9, 124.6.

5-bromobenzo[b]thiophene-1,1-dioxide (4b) → Cyclohexane : CH₂Cl₂ : AcOEt (80:15:5). Yield 80% with METHOD A, 80% with METHOD B. White solid; EI-MS m/z 245 (M⁺); ¹H NMR (400 MHz, CDCl₃, TMS/ppm): δ 7.74-7.56 (m, 4H), 6.97 (s, 1H); ¹³C NMR (TMS/ppm): 137.0, 133.8, 131.6, 131.1, 129.6, 129.57, 124.7, 120.8

2,6-dibromo-3,5-dimethyldithieno[3,2-b:2',3'-d]thiophene-4-oxide (5a) → METHOD A: Cyclohexane : AcOEt : CH₂Cl₂ 80:15:5. Yield 75%. Yellow solid; EI-MS m/z 398 (M⁺); ¹H NMR (400 MHz, CDCl₃, TMS/ppm) 2.39 (s, 6H); ¹³C NMR (TMS/ppm): 147.2, 136.2, 135.1, 112.2, 13.1.

2,6-dibromo-3,5-dimethyldithieno[3,2-b:2',3'-d]thiophene-4,4-dioxide (5b) → Cyclohexane : AcOEt : CH₂Cl₂ 80:15:5. Yield 80% with METHOD A, 80% with METHOD B. Yellow microcrystals; EI-MS m/z 414 (M⁺); ¹H NMR (400 MHz, CDCl₃, TMS/ppm) 2.34 (s, 6H); ¹³C NMR (TMS/ppm): 140.2, 133.5, 132.6, 113.8, 12.5.

2,5-dibromothieno[3,2-b]thiophene-1-oxide (6a) → METHOD A: Cyclohexane : CH₂Cl₂ : AcOEt (80:15:5). Yield 30%. Pale yellow oil; EI-MS m/z 314 (M⁺); ¹H NMR (400 MHz, CDCl₃, TMS/ppm): δ 7.37 (s, 1H), 7.12 (s, 1H); ¹³C NMR (TMS/ppm): 145.1, 142.9, 133.1, 126.6, 126.2, 117.1.

2,5-dibromothieno[3,2-b]thiophene 1,1-dioxide (6b) → Cyclohexane : CH₂Cl₂ : AcOEt (80:15:5). Yield 80% with METHOD A, 80% with METHOD B. Pale yellow solid; EI-MS m/z 330 (M⁺); ¹H NMR (400 MHz, CDCl₃, TMS/ppm): δ 7.28 (s, 1H), 7.08 (s, 1H); ¹³C NMR (TMS/ppm): 140.0, 135.9, 123.3, 123.2, 123.18, 118.8.

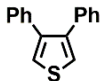
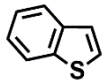
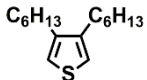
2,5-dibromothiophene-1,1-dioxide (7b) → Cyclohexane : CH₂Cl₂ : AcOEt (80:15:5). Yield 80% with METHOD A, 80% with METHOD B. Pale yellow solid; EI-MS m/z 274 (M⁺); ¹H NMR (400 MHz, CDCl₃, TMS/ppm): δ 6.91 (s, 2H); ¹³C NMR (TMS/ppm): 128.3, 119.4.

2-bromo-5-hexylthiophene-1,1-dioxide (8b) → Cyclohexane: CH₂Cl₂ : AcOEt (80:15:5). Yield 80% with METHOD A, 80% with METHOD B. Pale yellow solid; EI-MS m/z 246 (M⁺); ¹H NMR (400 MHz, CDCl₃, TMS/ppm): δ 6.76 (d, J=4.8 Hz, 1H), 6.36 (d, J=4.8 Hz, 1H), 2.50 (m, 2H), 1.65 (m, 2H), 1.30 (m, 6H), 0.90 (m, 3H); ¹³C NMR (TMS/ppm): 145.5, 127.5, 122.5, 119.2, 31.3, 28.6, 26.4, 25.3, 22.4, 13.9.

2,5-dibromo-3,4-dihexylthiophene 1,1-dioxide (9b) → Cyclohexane : CH₂Cl₂ : AcOEt (80:15:5). Yield 80% with METHOD A, 80% with METHOD B. Pale yellow solid; EI-MS m/z 442 (M⁺); ¹H NMR (400 MHz, CDCl₃, TMS/ppm): δ 2.41 (t, 4H), 1.53-1.28 (m, 16H), 0.89 (t, 6H); ¹³C NMR (TMS/ppm): 143.3, 115.3, 31.1, 28.9, 27.6, 27.4, 22.2, 13.8.

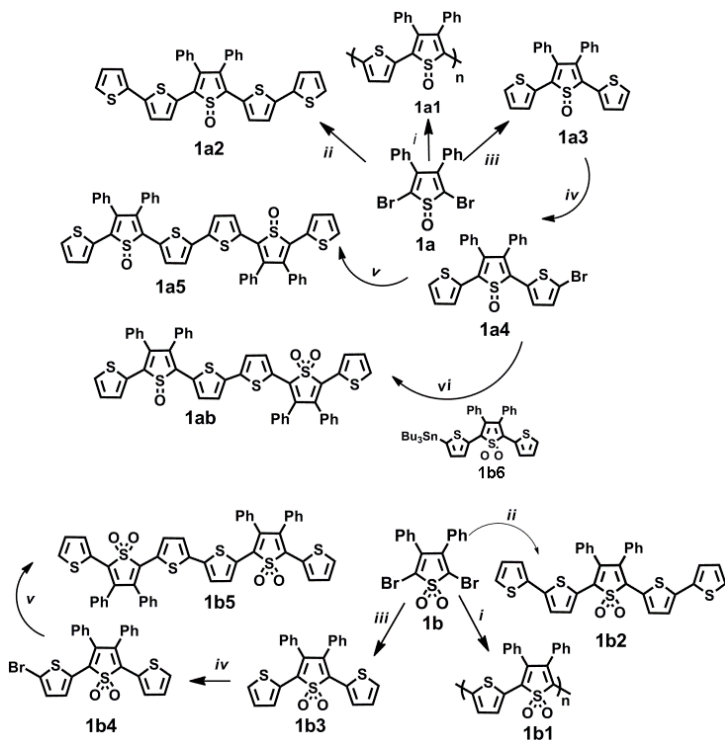
2-bromo-3,4-dihexylthiophene 1,1-dioxide (10b) → Cyclohexane:CH₂Cl₂:AcOEt (80:15:5). Yield 40% with METHOD A, 70% with METHOD B. Dark yellow oil. EI-MS m/z 364 (M⁺); ¹H NMR (400 MHz, CDCl₃, TMS/ppm): δ 6.4.9 (s, 1H), 2.39-2.34 (m, 4H), 1.57-1.29 (m, 20H), 0.92-0.88 (m, 6H). ¹³C NMR (TMS/ppm): 148.8, 141.8, 123.4, 118.3, 31.4, 31.3, 29.1, 28.7, 28.6, 27.6, 26.9, 26.8, 22.4, 13.9.

Table S1. Reagents and conditions for the ultrasound assisted synthesis of thiophene-S-oxides and -S,S-dioxides

	Starting Material		Experimental Conditions	Time (min)	Yield (%)
11		SO	CH ₂ Cl ₂ :CF ₃ COOH 2:1/ H ₂ O ₂ 1eq	20	60
		SO ₂	CH ₂ Cl ₂ :CF ₃ COOH 2:1 / H ₂ O ₂ 2eq	20	75
			CH ₂ Cl ₂ / MPCBA 2 eq	20	75
12		SO	CH ₂ Cl ₂ :CF ₃ COOH 2:1/ H ₂ O ₂ 1eq	15	>90
		SO ₂	CH ₂ Cl ₂ :CF ₃ COOH 2:1 / H ₂ O ₂ 2eq	15	>90
			CH ₂ Cl ₂ / MPCBA 2 eq	45	>90
13		SO ₂	CH ₂ Cl ₂ :CF ₃ COOH 2:1 / H ₂ O ₂ 2eq	15	80
			CH ₂ Cl ₂ / MPCBA 2 eq	60	45

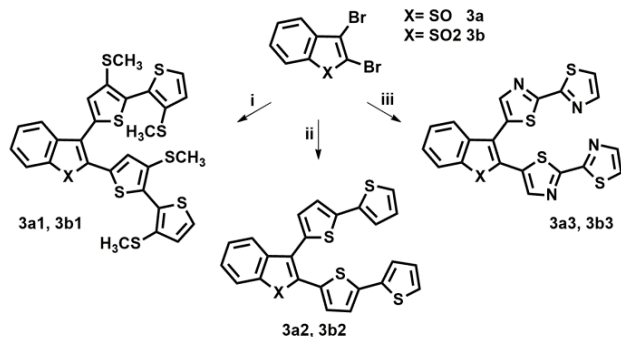
Synthetic pattern for the preparation of selected oligo/polythiophene-S-oxides and mixed S-oxides/-S,S-dioxides

Scheme 1. Preparation of oligomers and polymers from 2,5-dibromo-3,4-diphenyl-thiophene-1-oxide 1a and 1,1-dioxide 1b



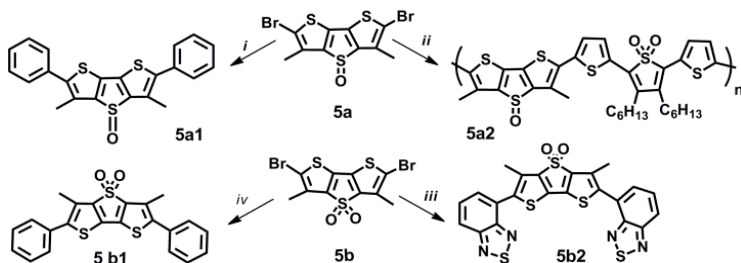
i) 2,5-bis(tributylstannyl)thiophene, $\text{Pd}(\text{PPh}_3)_4$, toluene, reflux overnight; ii) 2-tributylstannyl-2,2'-bithiophene, $\text{Pd}(\text{PPh}_3)_4$, toluene, reflux overnight; iii) 2-(tributylstannyl)thiophene, $\text{Pd}(\text{PPh}_3)_4$, toluene, reflux overnight; iv) *N*-bromosuccinimide (1 eq), CH_2Cl_2 : CH_3COOH , US; v) Bis(pinacolato)diboron, PdCl_2dppf , NaHCO_3 , $\text{THF}:\text{H}_2\text{O}$ 2:1, MW, 80°C ; vi) 3',4'-diphenyl-5-(tributylstannyl)-[2,2':5',2''-terthiophene]-1',1'-dioxide **1b6**, $\text{Pd}(\text{PPh}_3)_4$, toluene, reflux overnight. US=ultrasound assistance, MW=microwave assistance.

Scheme S2. Preparation of V-shaped oligomers from 2,3-dibromo-benzo[b]thiophene-S-oxide **3a** and -S,S-dioxide **3b**.



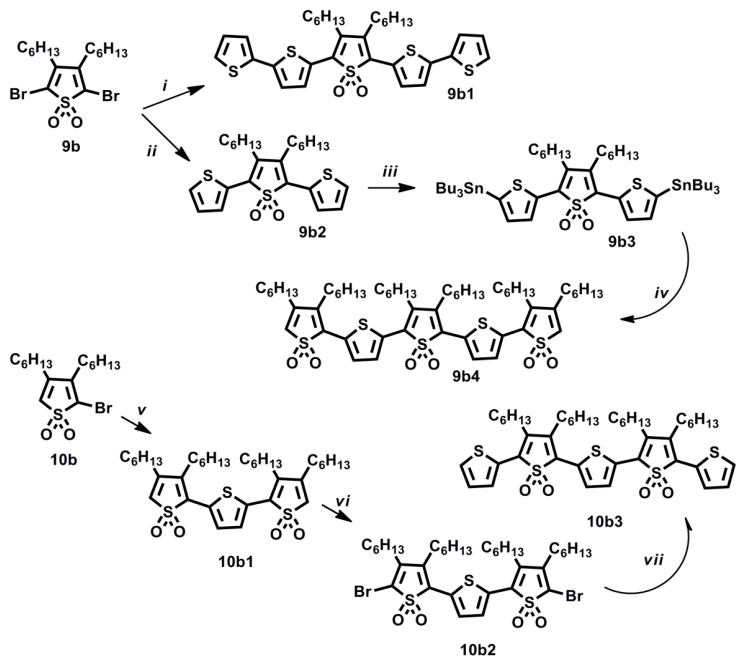
i) 5-tributylstannyl-3,3'-bis(methylthio)-2,2'-bithiophene, Pd(PPh₃)₄, toluene, reflux overnight; ii) 2-tributylstannyl-2,2'-bithiophene, Pd(PPh₃)₄, toluene, reflux overnight; iii) 5-tributylstannyl-2,2'-bithiazole, Pd(PPh₃)₄, toluene, reflux overnight.

Scheme S3. Preparation of oligomers from 2,6-dibromo-3,5-dimethyl-dithieno[3,2-b:2',3'-d]thiophene-4-oxide **5a** and -4,4-dioxide **5b**.



i) **5a** (1 mmol), phenylboronic acid pinacol ester (4 mmol), PdCl₂dppf (0.1 mmol) and NaHCO₃ (6 mmol) in THF/water 2:1 (3 mL), MW, 80°C, 15'; ii) 3',4'-dihexyl-5,5''-bis(tributylstannyl)-[2,2':5',2'':terthiophene]1',1'-dioxide, Pd(PPh₃)₄, toluene, reflux overnight; iii) 4-(4,4,5,5-tetramethyl-1,3,2-dioxaborolan-2-yl)-2,1,3-benzothiadiazole (4 mmol), PdCl₂dppf (0.1 mmol), NaHCO₃ (6 mmol), THF/H₂O 2:1 (3 mL), MW, 80°C, 15'; iv) phenylboronic acid pinacol ester (4 mmol), PdCl₂dppf (0.1 mmol), NaHCO₃ (6 mmol), THF/H₂O 2:1 (3 mL), MW, 80°C, 15'.

Scheme S4. Preparation of pentamers from 2,5-dibromo-3,4-dihexyl-thiophene-1,1-dioxide **9b** and 2-bromo-3,4-dihexyl-thiophene-1,1-dioxide **10b**.



i) 2-(tributylstannyl)-2,2'-bithiophene, $\text{Pd}(\text{PPh}_3)_4$, toluene, reflux overnight; ii) 2-(tributylstannyl)-thiophene, $\text{Pd}(\text{PPh}_3)_4$, toluene, reflux overnight; iii) THF, BuLi, Bu_3SnCl ; iv) 2-bromo-3,4-dihexylthiophene 1,1-dioxide **10b**, $\text{Pd}(\text{PPh}_3)_4$, toluene, reflux overnight; v) 2,5-bis(tributylstannyl)-thiophene, $\text{Pd}(\text{PPh}_3)_4$, toluene, reflux overnight; vi) *N*-bromosuccinimide, CH_2Cl_2 : CH_3COOH , US; vii) 2-(tributylstannyl)-thiophene, $\text{Pd}(\text{PPh}_3)_4$, toluene, reflux overnight.

General procedure for the synthesis of tributyl stannanes: To a solution of the starting material (1 mmol) in anhydrous THF (10 mL) at -78°C , LDA (1 mmol). The mixture was left rising to room temperature and after 1.5 h was lowered to -78°C and Bu_3SnCl (1.1 mmol) was added. The reaction mixture was stirred for 12 h at room temperature. The mixture was extracted with water and then the organic phase was evaporated under reduced pressure.

3',4'-dihexyl-5,5'-(tributylstannyl)-[2,2':5',2''-terthiophene]-1,1'-dioxide (9b3) → The compound was prepared starting from 9b2. Orange oil; EI-MS m/z 1026 (M^+); ^1H NMR (400 MHz, CDCl_3 , TMS/ppm) δ 7.85 (d, $3J=3.2$ Hz, 2H), 7.22 (d, $3J=3.2$ Hz, 2H), 1.64-1.49 (m, 20H), 1.41-1.27 (m, 20H), 1.18-1.09 (m, 10H), 0.93-0.88 (m, 24H).

3',4'-diphenyl-5-(tributylstannyl)-[2,2':5',2''-terthiophene]-1,1'-dioxide (1b6) → The compound was prepared starting from 1b4. Yield 60%. Orange solid; EI-MS m/z 722(M^+); ^1H NMR (400 MHz, CDCl_3 , TMS/ppm): δ 7.82 (d, $J=3.2$, 1H), 7.74 (d, $3J=3.2$ Hz, $4J=0.8$ Hz, 1H), 7.3-7.24 (m, 6H), 7.12-7.09 (m, 6H), 7.06 (dd, $3J=5.6$ Hz, $3J=4$ Hz, 1H), 1.47-1.41 (m, 6H), 1.31-1.21 (m, 6H), 1.02-0.98 (m, 6H), 0.85 (t, 9H).

3,3'-bis(methylthio)-[2,2'-bithiophen]-5-yl)tributylstannane → Brown-yellow oil; EI-MS m/z 547 (M⁺); Yield 90%. ¹H NMR (400 MHz, CDCl₃, TMS/ppm) δ 7.36 (d, 3J=5.6 Hz, 1H), 7.08 (s, 1H), 7.07 (d, 3J=5.6 Hz, 1H), 2.42-2.40 (m, 6H), 1.60-1.56 (m, 6H), 1.36-1.32 (m, 8H), 1.15-1.11 (m, 4H), 0.94-0.89 (m, 9H).

5-(tributylstannyl)-2,2'-bithiazole → Yellow oil; EI-MS m/z 457 (M⁺); Yield 60%. ¹H NMR (400 MHz, CDCl₃, TMS/ppm) δ 7.88 (d, 3J=3.6 Hz, 1H), 7.79 (s, 1H), 7.40 (d, 3J=3.6 Hz, 1H), 1.63-1.53 (m, 6H), 1.38-1.09 (m, 12H), 0.92-0.88 (m, 9H).

Synthesis of 4-(4,4,5,5-tetramethyl-1,3,2-dioxaboralan-2-yl)-2,1,3-benzothiadiazole: A mixture of 4-bromo-2,1,3-benzothiadiazole (1 mmol), bis(pinacolato)diboron (1.2 mmol) and potassium acetate (2.86 mmol) was dissolved in dry 1,4-dioxane (5 mL). The solution was purged with nitrogen for 20 min and then PdCl₂(dppf) (0.05 mmol) was added. The reaction mixture was heated, with stirring, at 105°C. After 24h the cooled mixture was extracted with diethyl ether and the solvent was evaporated under reduced pressure. Yield 90%. Dark white solid; EI-MS m/z 287; ¹H NMR (400 MHz, CDCl₃, ppm) δ 8.17 (d, J=6 Hz, 1H), 8.11 (d, J=9 Hz, 1H), 7.60 (t, J=6 Hz, 1H) 1.45 (s, 12H). ¹³C NMR: (400 MHz, CDCl₃, ppm) δ 157.0, 154.4, 138.5, 128.5, 124.3, 84.1, 24.7.

General procedure for the synthesis of 5a1, 5b1, 5b2. A mixture of the appropriate bromo compound (1 mmol), boronic ester derivatives (3 mmol), PdCl₂dppf (0.05 mmol) and NaHCO₃ (2 mmol) in THF/water 2:1 (3 mL) was irradiated with microwaves at 80°C for 15 min. The reaction mixture was brought to room temperature and the solvent was evaporated under reduced pressure.

2,6-Diphenyl-3,5-dimethyl-dithieno[3,2-b:2',3'-d]thiophene-4-oxide (5a1) The compound was prepared starting from 5a and phenylboronic ester. → Cyclohexane : CH₂Cl₂ : AcOEt (80:15:5). Yield 95% (0.390 g). Yellow solid; EI-MS m/z 392 (M⁺); ¹H NMR (400 MHz, CDCl₃, TMS/ppm) δ 7.47-7.46 (m, 8H), 7.42-7.37 (m, 2H), 2.53 (s, 6H); ¹³C NMR (CDCl₃, TMS/ppm) δ 149.8, 135.9, 133.3, 131.0, 128.9, 128.7, 128.2, 12.96; UV/Vis: λ_{max} 410 nm (ε 18220 cm⁻¹M⁻¹), λ_{em} 534 nm in CH₂Cl₂. IR: ν_{max} (NaCl) 3462, 2919, 1732, 1598, 1442, 1028 cm⁻¹.

2,6-Diphenyl-3,5-dimethyl-dithieno[3,2-b:2',3'-d]thiophene-4,4-dioxide (5b1). The compound was prepared starting from 5b and phenylboronic ester → Petroleum ether : AcOEt : CH₂Cl₂ (80:10:10). Yield 95% (0.390 g). Yellow solid, mp 199°C; EI-MS m/z 408 (M⁺); ¹H NMR (CDCl₃, TMS/ppm) δ 7.44 (m, 10H), 2.48 (s, 6H); ¹³C NMR (TMS/ppm): 144.3, 143.0, 133.1, 133.0, 129.1, 129.0, 128.9, 128.5, 12.2; UV/Vis: λ_{max} 408 nm (ε 18030 cm⁻¹M⁻¹), λ_{em} 514 nm in DMSO.

2,6-bis(benzo[c][1,2,5]thiadiazol-4-yl)-3,5-dimethyldithieno[3,2-b:2',3'-d]thiophene 4,4-dioxide (5b2) The compound was prepared starting from 5b and 4-(4,4,5,5-tetramethyl-1,3,2-dioxaboralan-2-yl)-2,1,3-benzothiadiazole. → Petroleum ether : CH₂Cl₂ : AcOEt (80:15:5). Yield 60%. Dark orange solid; EI-MS m/z 549 (M⁺); ¹H NMR (400 MHz, CDCl₃, TMS/ppm) δ 8.07 (d, 3J=8.4 Hz, 2H), 7.74-7.67 (m, 4H), 2.55 (s, 6H); ¹³C NMR (400 MHz, CDCl₃, TMS/ppm) δ 155.2, 153.1, 143.0, 137.6, 135.2, 131.2, 129.8, 129.2, 125.9, 122.0, 13.2; UV/Vis: λ_{max} 426 nm

(ϵ 21420 cm⁻¹M⁻¹), λ em. 549 nm in CH₂Cl₂. IR: ν max (NaCl) 3462, 2919, 2850, 1716, 1620, 1541, 1299, 1142 cm⁻¹.

General procedure for the synthesis of 1a5, 1b5: A mixture of the bromothieryl-derivative (1 mmol), bis(pinacolato)diboron (0.6 mmol), PdCl₂dppf (0.05 mmol), NaHCO₃ (2 mmol) in THF/water 2:1 (3 mL) was irradiated with microwaves at 80°C for 30 min. The reaction mixture was brought to room temperature and the solvent was evaporated under reduced pressure. All compounds were purified by flash chromatography with increasing amounts of CH₂Cl₂ in cyclohexane as eluent.

3',3''',4',4''''-tetraphenyl-[2,2':5',2''':5'',2''':5''',2''''':5''''',2''''':5'''''-sexithiophene]-1',1''''-dioxide (1a5) The compound was prepared starting from 1a4. → Cyclohexane : CH₂Cl₂ : AcOEt (60:35:5). Yield 70%. Deep purple solid; mp 240-242°C; EI-MS *m/z* 830(M⁺); ¹H NMR (400 MHz, CDCl₃, TMS/ppm): δ 7.57 (d, 3J = 3.6 Hz, 4J = 1.2 Hz, 2H), 7.40 (d, 3J = 4.4 Hz, 4J = 1.6 Hz, 2H), 7.28-7.23 (m, 12H), 7.21 (d, 3J = 5.2 Hz, 4J = 1.2 Hz, 2H), 7.09-7.05 (m, 8H), 6.99 (dd, 3J = 5.2 Hz, 3J = 3.6 Hz, 2H), 6.88 (d, 3J = 4.4 Hz, 4J = 1.2 Hz, 2H). ¹³C NMR: (400 MHz, CDCl₃) δ 140.3, 140.2, 140.15, 140.12, 139.3, 139.2, 138.94, 138.91, 138.7, 133.3, 133.1, 133.0, 132.8, 129.8, 129.4, 129.3, 129.0, 128.94, 128.9, 128.85, 128.8, 128.1, 127.3, 124.5. IR: ν max 3394, 2918, 2361, 1718, 1589, 1482, 1436, 1232, 1044, 789, 696. UV/Vis: λ max 528 nm (ϵ 38100 cm⁻¹M⁻¹) in CH₂Cl₂.

3',3''',4',4''''-tetraphenyl-[2,2':5',2''':5'',2''':5''',2''''':5''''',2''''':5'''''-sexithiophene] 1',1'',1''',1''''-tetraoxide (1b5) The compound was prepared starting from 1b4. → Cyclohexane : CH₂Cl₂ : AcOEt (60:30:10). Yield 70%. Deep red solid; mp > 300°C; EI-MS *m/z* 862(M⁺); ¹H NMR (400 MHz, CDCl₃, TMS/ppm): δ 7.74 (d, J = 4 Hz, 2H), 7.56 (d, J = 4 Hz, 2H), 7.33-7.21 (m, 10H), 7.10-7.05 (m, 14H), 6.93 (d, J = 4 Hz, 2H). IR: ν max 3442, 2921, 2358, 1728, 1599, 1463, 1300, 1135, 1073, 806, 701. UV/Vis: λ max 526 nm (ϵ 27000 cm⁻¹M⁻¹ poor solubility), in CH₂Cl₂.

General procedure for the Stille cross coupling reaction: A mixture of the appropriate bromo compound (1 mmol), stannane derivatives (1 mmol or 2 mmol), Pd(PPh₃)₄ (0.05 mmol) in Toluene (10 mL) was refluxed for 24 h. The reaction mixture was brought to room temperature and the solvent was evaporated under reduced pressure. The title compound was isolated by flash chromatography on silica gel.

3,3',4,4''-tetrahexyl-[2,2':5',2''-terthiophene] 1,1,1'',1''-tetraoxide (10b1) The compound was prepared starting from 2-bromo-3,4-dihexylthiophene 1,1-dioxide and 2,5-Bis(tributylstannyl)thiophene. → Cyclohexane : CH₂Cl₂ : AcOEt (65:30:5). Yield 50%. Pale yellow solid; EI-MS *m/z* 644 (M⁺); ¹H NMR (400 MHz, CDCl₃, TMS/ppm): δ 7.67 (s, 2H), 7.41 (s, 2H), 2.62-2.58 (m, 4H), 2.43-2.38 (m, 4H), 1.63-1.25 (m, 32H), 0.93-0.87 (m, 12H); ¹³C NMR (TMS/ppm): 149.6, 138.0, 132.2, 131.3, 129.9, 123.3, 31.9, 31.8, 30.0, 29.3, 28.9, 28.8, 28.7, 27.7, 27.4, 27.2, 22.98, 22.93, 17.8, 14.2, 13.7.

3',4'-Dihexyl-2,2':5',2''-terthiophene 1',1'-Dioxide, 9b2. The compound was prepared starting from 1b and 2-(tributylstannyl)thiophene. → Cyclohexane:CH₂Cl₂:AcOEt (70:25:5).Yield 75%.

Light yellow microcrystalline powder; mp 49 °C; EI-MS m/z 448(M⁺); ¹H NMR (200 MHz, CDCl₃, TMS/ppm): δ 7.73 (q, 2H), 7.50 (q, 2H), 7.18 (q, 2H), 2.65 (m, 4H), 1.40 (m, 16H), 0.90 (m, 6H); ¹³C NMR (TMS/ppm): δ 137.2, 130.2, 128.7, 128.4, 127.9, 31.2, 29.5, 28.4, 26.9, 22.4, 13.9.

3',4'-Dihexyl-2,2':5',2'':5'',2''':5''',2''''-quinquethiophene 1',1'-Dioxide, 9b1. The compound was prepared starting from 1b and 2-(tributylstannyl)bithiophene. → Cyclohexane:CH₂Cl₂:AcOEt (70:25:5). Yield 75%. Bright red microcrystalline powder, mp: 112 °C. EI-MS m/z 612(M⁺); ¹H NMR (400 MHz, CDCl₃, TMS/ppm): δ 7.65 (d, J=4.0 Hz, 2H), 7.29 (d, J=5.2 Hz 2H), 7.26 (d, J=3.6 Hz, 2H), 7.23 (d, J=4.0 Hz, 2H), 7.06 (dd, 3J=5.2 Hz, 4J=3.6, 2H), 2.71-2.67 (m, 4H), 1.66-1.52 (m, 8H), 1.43-1.28 (m, 8H), 0.95-0.88 (m, 6H); ¹³C NMR (TMS/ppm): 140.0, 136.8, 136.3, 130.1, 129.6, 128.1, 127.4, 125.6, 124.6, 124.5, 31.3, 29.7, 28.5, 27.1, , 22.5, 14.0.

3',3''',4',4''-tetrahexyl-[2,2':5',2'':5'',2''':5''',2''''-quinquethiophene] 1',1',1''',1''''-tetraoxide (10b3) The compound was prepared starting from 5,5"-dibromo-3,3",4,4"-tetrahexyl-[2,2':5',2"-terthiophene] 1,1,1",1"-tetraoxide and 2-(tributylstannyl)thiophene. → Cyclohexane: CH₂Cl₂: AcOEt (60:35:5). Yield 70%. Red solid; mp 95-97°C; EI-MS m/z 812(M⁺); ¹H NMR (400 MHz, CDCl₃, TMS/ppm): δ 7.77-7.57 (m, 4H), 7.53 (d, 3J=5.2 Hz, 4J=1.2 Hz, 2H), 7.20 (d, 3J =5.2 Hz, 4J=4 Hz, 2H), 2.72-2.66 (m, 8H), 1.65-1.62 (m, 16H), 1.36-1.32 (m, 16H), 0.94-0.90 (m, 12H); ¹³C NMR (400 MHz, CDCl₃) δ 138.8, 137.0, 130.9, 130.8, 129.7, 129.5, 129.0, 128.4, 128.2, 31.4, 31.3, 31.0, 29.8, 29.7, 29.6, 28.7, 28.5, 27.4, 27.0, 22.6, 22.56, 14.1, 14.0. IR: ν_{max} (NaCl) 3436, 2955, 2924, 2850, 2083, 1643, 1464, 1420, 1303, 1142, 1086, 800. UV/Vis: λ_{max} 480 nm (ε 27000 cm⁻¹M⁻¹) in CH₂Cl₂.

3,3''',3''''',4,4''-hexahexyl-[2,2':5',2'':5'',2''':5''',2''''-quinquethiophene]1',1',1''',1''''', 1''''-hexaoxide (9b4) The compound was prepared starting from 2-bromo-3,4-dihexylthiophene 1,1-dioxide and 3',4'-dihexyl-5,5"-bis(tributylstannyl)-[2,2':5',2"-terthiophene]1',1'-dioxide. → Cyclohexane : CH₂Cl₂ : AcOEt (65:25:10). Yield 70%. Deep red solid; mp 135-137°C; EI-MS m/z 1012(M⁺); ¹H NMR (400 MHz, CDCl₃, TMS/ppm): δ 7.75 (d, 3J =4.4 Hz, 2H), 7.72 (d, 3J=4.4 Hz, 2H), 6.43 (s, 2H), 2.62-2.60 (m, 8H), 2.44-2.39 (m, 4H), 1.63-1.33 (m, 22H), 0.93-0.89 (m, 18H); ¹³C NMR (400 MHz, CDCl₃) δ 149.1, 138.7, 137.0, 131.7, 130.9, 130.8, 130.3, 129.9, 129.7, 122.6, 31.5, 31.4, 31.36, 29.7, 29.69, 28.9, 28.6, 28.5, 28.4, 27.3, 27.1, 26.9, 22.6, 22.5, 14.0. IR: ν_{max} (NaCl) 3467, 2955, 2927, 2857, 2066, 1637, 1465, 1300, 1168, 1090, 800. UV/Vis: λ_{max} 475 nm (ε 32700 cm⁻¹M⁻¹), λ_{em}. 580 nm in CH₂Cl₂.

3',4'-diphenyl-[2,2':5',2"-terthiophene] 1'-oxide (1a3) The compound was prepared starting from 1a and 2-(tributylstannyl)thiophene. → Cyclohexane: CH₂Cl₂:AcOEt (65:30:5). Yield 77%. Orange solid, mp 188-190°C; EI-MS m/z 416(M⁺); ¹H NMR (400 MHz, CDCl₃, TMS/ppm): δ 7.75 (d, 3J=4 Hz, 4J=1.2 Hz, 2H), 7.31-7.25 (m, 8H), 7.11-7.09 (m, 4H), 7.06 (dd, 3J=4 Hz, 3J=5.2 Hz, 2H). ¹³C NMR: (400 MHz, CDCl₃) δ 140.1, 139.2, 133.2, 133.1, 129.4, 128.9, 128.8, 128.7, 127.9, 127.2. IR: ν_{max} (NaCl) 3460, 3102, 2929, 2362, 1605, 1420, 1051 cm⁻¹. UV/Vis: λ_{max} 443 nm, λ_{em}. 555 nm in CH₂Cl₂.

3',4'-diphenyl-[2,2':5',2"-terthiophene] 1',1'-dioxide (1b3) The compound was prepared starting from 1b and 2-(tributylstannyl)thiophene. → Cyclohexane: CH₂Cl₂:AcOEt (65:30:5).

Yield 77%. Orange solid, mp 228-230°C; EI-MS m/z 432(M⁺); ¹H NMR (400 MHz, CDCl₃, TMS/ppm): δ 7.75 (d, 3J=3.6Hz, 4J=1.2 Hz, 2H), 7.31-7.25 (m, 8H), 7.11-7.09 (m, 4H), 7.06 (dd, 3J=5.2 Hz, 3J=3.6 Hz, 2H). ¹³C NMR: (400 MHz, CDCl₃) δ 135.5, 131.5, 131.1, 129.5, 129.3, 129.2, 129.18, 129.0, 128.9, 127.4. IR: ν_{max} (NaCl) 3450, 1613, 1420, 1301, 1143 cm⁻¹. UV/Vis: λ_{max} 429 nm, λ_{em} 535 nm in CH₂Cl₂.

3',3''',4',4''''-tetraphenyl-[2,2':5',2'':5'',2''':5''',2''''-sexithiophene] 1',1',1''''-trioxide (1ab) The compound was prepared starting from 1a4 and 1b6. → Cyclohexane: CH₂Cl₂:AcOEt (60:30:10). Yield 65%. Deep purple solid; mp 270-272°C; EI-MS m/z 830(M⁺); ¹H NMR (400 MHz, CDCl₃, TMS/ppm): δ 7.73 (d, 3J =3.6 Hz, 1H), 7.57-7.56 (m, 2H), 7.41-7.38 (m, 2H), 7.32-7.24 (m, 8H), 7.21-7.20 (m, 2H), 7.10-7.05 (m, 12H), 7.00 (dd, 3J=4 Hz, 3J=5.2 Hz, 1H), 6.93 (d, J=4, 1H), 6.89-6.87 (m, 1H). IR: ν_{max} 3491, 2962, 2263, 1743, 1618, 1422, 1304, 1141,1094, 913, 797, 700. UV/Vis: λ_{max} 527nm (ε 35000 cm⁻¹M⁻¹) in CH₂Cl₂.

3'',4''-diphenyl-[2,2':5',2'':5'',2''':5''',2''''-quinquethiophene] 1''-oxide (1a2) The compound was prepared starting from 1a and 2-(tributylstannyl)bithiophene. → Cyclohexane : CH₂Cl₂ : AcOEt (60:30:10). Yield 60%. Red solid; mp 240-242°C EI-MS m/z 580 (M⁺); ¹H NMR (400 MHz, CDCl₃, TMS/ppm): δ 7.47 (d, 3J =4.4 Hz, 2H), 7.72-7.27 (m, 6H), 7.19 (d, 3J=4.4 Hz, 4J=0.8 Hz, 2H), 7.12-7.08 (m, 4H), 7.06 (d, 3J =3.6 Hz, 2H), 7.02 (d, 3J =3.6 Hz, 4J=0.8 Hz, 2H), 6.95 (dd, 3J=4.4 Hz, 3J=3.6 Hz, 2H). ¹³C NMR: (400 MHz, CDCl₃) δ 138.8, 132.9, 132.25, 132.12, 131.1, 129.8, 129.7, 129.3, 129.2, 129.0, 128.9, 128.8, 127.8, 125.2, 124.4, 123.8. IR: ν_{max} 3435, 2921, 2850, 2087, 1645, 1442, 1261, 1045, 790, 698. UV/Vis: λ_{max} 506 nm (ε 42200 cm⁻¹M⁻¹), λ_{em} 620 nm in CH₂Cl₂.

3'',4''-diphenyl-[2,2':5',2'':5'',2''':5''',2''''-quinquethiophene] 1'',1''-dioxide (1b2) The compound was prepared starting from 1b and 2-(tributylstannyl) bithiophene. → Cyclohexane : CH₂Cl₂ : AcOEt (60:30:10). Yield 60%. Red solid; mp 275-277°C; EI-MS m/z 596 (M⁺); ¹H NMR (400 MHz, CDCl₃, TMS/ppm): δ 7.64 (d, 3J =3.6 Hz, 2H), 7.73-7.27 (m, 6H), 7.21 (d, 3J=5.2 Hz, 4J=1.2 Hz, 2H), 7.14-7.11 (m, 6H), 7.02 (d, 3J =3.6 Hz, 4J=1.2 Hz, 2H), 6.95 (dd, 3J=5.2 Hz, 3J=3.6 Hz, 2H). ¹³C NMR: (400 MHz, CDCl₃) δ 140.8, 136.3, 135.0, 131.4, 130.9, 130.5, 129.3, 129.28, 129.2, 129.0, 128.97, 128.2, 127.9, 125.6, 124.8, 124.0. IR: ν_{max} 3447, 2954, 2854, 2095, 1654, 1440, 1289, 1130, 1068, 793. UV/Vis: λ_{max} 504 nm (ε 38450 cm⁻¹M⁻¹), λ_{em} 615 nm in CH₂Cl₂.

2,3-di([2,2'-bithiophen]-5-yl)benzo[b]thiophene 1-oxide (3a2) The compound was prepared starting from 4a and 2-(tributylstannyl)bithiophene. → Cyclohexane : CH₂Cl₂ : AcOEt (80:15:5). Yield 85%. Orange solid, mp 150-153°C; EI-MS m/z 478 (M⁺); ¹H NMR (400 MHz, CDCl₃, TMS/ppm) δ 7.96 (d, J=6.8 Hz, 1H), 7.59 (d, 3J=3.6 Hz, 1H), 7.55-7.45 (m, 2H), 7.42 (d, J=6.8 Hz, 1H), 7.30-7.28 (m, 2H), 7.26 (d, 3J=3.6 Hz, 1H), 7.22 (d, 3J=5.2 Hz, 4J=1.6 Hz, 1H), 7.16 (d, 3J=3.6 Hz, 1H), 7.14-7.12 (m, 2H), 7.06 (dd, 3J=5.2 Hz, 3J=3.6 Hz, 1H), 6.97 (dd, 3J=5.2 Hz, 3J=3.6 Hz, 1H); ¹³C NMR: (400 MHz, CDCl₃) δ 143.6, 142.0, 141.0, 140.8, 140.0, 136.4, 136.5, 132.6, 131.5, 131.0, 130.6, 130.3, 130.0, 128.6, 128.0, 127.9, 126.3, 125.5, 125.2, 124.7, 124.5, 124.3, 124.0, 123.9. IR: ν_{max} 3468, 3067, 2336, 1577, 1458, 1067, 1033, 838, 801, 695. UV/Vis: λ_{max} 430 nm (ε 11900 cm⁻¹M⁻¹), λ_{em} 578 nm in CH₂Cl₂. IR: ν_{max} (NaCl) 3442, 2923, 2361, 1621, 1446, 1034 cm⁻¹.

2,3-di([2,2'-bithiophen]-5-yl)benzo[b]thiophene-1,1-dioxide (3b2) The compound was prepared starting from **3b** and 2-(tributylstannyl)bithiophene. → Cyclohexane:CH₂Cl₂:AcOEt (80:18:2). Yield 88%. EI-MS m/z 494 (M⁺); Orange solid, mp 155-158°C. HRMS ESI+, [M+23(Na+)], Found 516.9495, C₂₄H₁₄O₂S₅Na₁. ¹H NMR (400 MHz, CDCl₃, TMS/ppm) δ 7.85 (d, J=7.6 Hz, 1H), 7.72 (d, 3J=4.0 Hz, 1H), 7.62-7.52 (m, 2H), 7.46 (d, J=7.6 Hz, 1H), 7.31-7.23 (m, 2H), 7.27 (d, J=3.6 Hz, 1H), 7.23 (d, J=5.2 Hz, 1H), 7.19 (d, J=4 Hz, 1H), 7.16 (d, J=4, 1H), 7.14 (d, J=3.6 Hz, 1H), 7.06 (dd, 3J=5.2 Hz, 3J=3.6 Hz, 1H), 6.97 (dd, 3J=5.2 Hz, 3J=3.6 Hz, 1H); ¹³C NMR (TMS/ppm): 133.8, 131.2, 130.9, 129.5, 127.9, 127.8, 125.7, 125.4, 125.0, 124.7, 124.3, 123.9, 123.7, 121.3. IR: ν_{max} 3070, 1583, 1440, 1304, 1154, 1058, 840, 802, 737, 698. UV/Vis: λ_{max} 429 nm (ε 10700 cm⁻¹M⁻¹), λ_{em} 520 nm in CH₂Cl₂.

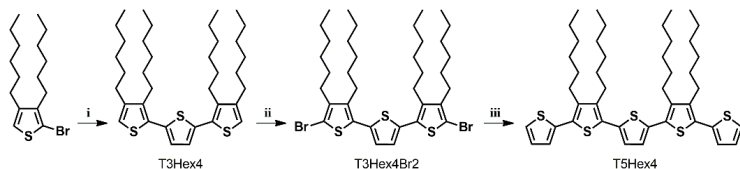
2,3-bis(3,3'-bis(methylthio)-[2,2'-bithiophen]-5-yl)benzo[b]thiophene 1-oxide (3a1) The compound was prepared starting from **3a** and 3,3'-bis(methylthio)-[2,2'-bithiophen]-5-yl)tributylstannane. → Cyclohexane : CH₂Cl₂ : AcOEt (80:18:2). Yield 65%. Red solid, mp 105-107°C; EI-MS m/z 662 (M⁺); ¹H NMR (400 MHz, CDCl₃, TMS/ppm) δ 7.97 (d, J=6.8 Hz, 1H), 7.67 (s, 1H), 7.57-7.43 (m, 3H), 7.42 (d, 3J=5.2 Hz, 1H), 7.37 (d, 3J=5.2 Hz, 1H), 7.22 (s, 1H), 7.09 (d, 3J=5.2 Hz, 1H), 7.04 (d, 3J=5.2 Hz, 1H), 2.46-2.36 (m, 12H); ¹³C NMR: (400 MHz, CDCl₃) δ 143.3, 142.2, 139.6, 134.4, 134.1, 134.0, 133.9, 133.6, 133.4, 132.6, 132.5, 131.5, 131.4, 131.3, 130.9, 129.8, 129.5, 129.4, 129.2, 128.9, 126.6, 126.5, 126.3, 124.1, 18.9, 18.8, 18.7, 18.6. IR: ν_{max} (NaCl) 3430, 3078, 2917, 2361, 1654, 1560, 1432, 1314, 1158, 1064, 1036, 970, 844, 717. UV/Vis: λ_{max} 430 nm (ε 12800 cm⁻¹M⁻¹), λ_{em} 602 nm in CH₂Cl₂.

2,3-bis(3,3'-bis(methylthio)-[2,2'-bithiophen]-5-yl)benzo[b]thiophene 1,1-dioxide (3b1) The compound was prepared starting from **4b** and 3,3'-bis(methylthio)-[2,2'-bithiophen]-5-yl)tributylstannane. → Cyclohexane: CH₂Cl₂:AcOEt (80:18:2). Yield 60%. Red solid, mp 178-180°C; EI-MS m/z 678 (M⁺); ¹H NMR (400 MHz, CDCl₃, TMS/ppm) δ 7.85 (d, J=6.8 Hz, 1H), 7.77 (s, 1H), 7.63-7.52 (m, 2H), 7.47 (d, J=6.8 Hz, 1H), 7.44 (d, 3J=5.6 Hz, 1H), 7.38 (d, 3J=5.2 Hz, 1H), 7.25 (s, 1H), 7.10 (d, 3J=5.6 Hz, 1H), 7.05 (d, 3J=5.2 Hz, 1H), 2.48-2.36 (m, 12H); ¹³C NMR: (400 MHz, CDCl₃) δ 135.3, 135.2, 134.7, 134.2, 134.18, 134.1, 134.0, 133.8, 133.5, 131.7, 131.6, 131.5, 129.9, 129.86, 129.8, 129.7, 129.5, 129.2, 128.0, 127.1, 126.8, 126.7, 124.0, 121.5, 19.0, 18.8, 18.77, 18.7. IR: ν_{max} (NaCl) 3435, 3078, 2918, 2361, 1654, 1580, 1420, 1303, 1154, 1121, 1054, 970, 845, 718. UV/Vis: λ_{max} 435 nm (ε 12500 cm⁻¹M⁻¹), λ_{em} 642 nm in CH₂Cl₂.

2,3-di([2,2'-bithiazol]-5-yl)benzo[b]thiophene 1-oxide (3a3) The compound was prepared starting from **3a** and 5-(tributylstannyl)-2,2'-bithiazole. → Cyclohexane: CH₂Cl₂:AcOEt (80:15:5). Yield 40%. Yellow solid, mp 210-212°C; EI-MS m/z 482 (M⁺); ¹H NMR (400 MHz, CDCl₃, TMS/ppm) δ 8.43 (s, 1H), 8.04-8.02 (m, 1H), 7.99 (s, 1H), 7.95 (d, J=3.2 Hz, 1H), 7.86 (d, J=3.2 Hz, 1H), 7.59-7.57 (m, 2H), 7.56 (d, J=3.2 Hz, 1H), 7.48 (d, J=3.6 Hz, 1H), 7.41-7.39 (m, 1H); ¹³C NMR: (400 MHz, CDCl₃) δ 164.6, 163.4, 160.8, 160.7, 145.8, 145.1, 144.3, 144.0, 142.7, 138.9, 132.9, 130.7, 129.7, 129.4, 127.9, 126.7, 124.0, 121.9. IR: ν_{max} 3418, 3073, 2918, 2360, 1715, 1540, 1471, 1374, 1251, 1062, 1036, 918, 870. UV/Vis: λ_{max} 404 nm (ε 19500 cm⁻¹M⁻¹), λ_{em} 530 nm in CH₂Cl₂.

2,3-di([2,2'-bithiazol]-5-yl)benzo[b]thiophene 1,1-dioxide (3b3) The compound was prepared starting from **4b** and 5-(tributylstannyl)-2,2'-bithiazole. → Cyclohexane : CH₂Cl₂ : AcOEt

(80:15:5). Yield 40%. Yellow solid, mp 150-153°C; EI-MS m/z 498 (M^+); ^1H NMR (400 MHz, CDCl_3 , TMS/ppm) δ 8.52 (s, 1H), 8.01 (s, 1H), 7.96 (d, $3J=3.2$ Hz, 1H), 7.92-7.89 (m, 1H), 7.86 (d, $3J=3.2$ Hz, 1H), 7.65-7.62 (m, 2H), 7.57 (d, $3J=3.2$ Hz, 1H), 7.49 (d, $3J=3.2$ Hz, 1H), 7.42-7.40 (m, 1H); ^{13}C NMR: (400 MHz, CDCl_3) δ 165.2, 163.8, 160.6, 160.4, 146.2, 145.5, 144.4, 144.3, 135.3, 134.4, 133.7, 132.6, 130.9, 127.3, 126.2, 124.9, 123.9, 122.4, 122.3, 121.9; IR: ν_{max} 3467, 2074, 1637, 1307, 1250, 1157, 1052, 920, 868. UV/Vis: λ_{max} 401 nm (ϵ 12800 $\text{cm}^{-1}\text{M}^{-1}$), λ_{em} 470 nm in CH_2Cl_2 .



i) 2,5-bis(tributylstannyl)-thiophene, $\text{Pd}(\text{PPh}_3)_4$, toluene, reflux overnight; ii) *N*-bromosuccinimide, CH_2Cl_2 , US; iii) 2(tributylstannyl)-thiophene, $\text{Pd}(\text{PPh}_3)_4$, toluene, reflux overnight.

3,3',4,4''-tetrahexyl-2,2':5',2''-terthiophene (T3Hex4) The compound was prepared starting from 2-bromo-3,4-dihexylthiophene and 2,5-Bis(tributylstannyl)thiophene. → Cyclohexane : CH_2Cl_2 (90:10). Yield 65%. Yellow oil; EI-MS m/z 584 (M^+); ^1H NMR (400 MHz, CDCl_3 , TMS/ppm) δ 7.04 (s, 2H), 6.86 (s, 2H), 2.71 (t, 4H), 2.53 (t, 4H), 1.68-1.62 (m, 4H), 1.57-1.51 (m, 4H), 1.43-1.29 (m, 24H), 0.93-0.87 (m, 12H); ^{13}C NMR (TMS/ppm): 143.6, 138.8, 136.5, 130.8, 125.8, 119.0, 31.7, 31.6, 30.5, 29.7, 29.6, 29.3, 29.2, 27.8, 22.6, 14.1, 14.08.

5,5''-dibromo-3,3',4,4''-tetrahexyl-2,2':5',2''-terthiophene (T3Hex4Br2) Cyclohexane: CH_2Cl_2 (95:5). Yield 95%. Yellow oil; EI-MS m/z 741 (M^+); ^1H NMR (400 MHz, CDCl_3 , TMS/ppm) δ 6.98 (s, 2H), 6.86 (s, 2H), 2.69 (t, 4H), 2.53 (t, 4H), 1.55-1.51 (m, 8H), 1.43- 1.23 (m, 24H), 0.93-0.87 (m, 12H); ^{13}C NMR (TMS/ppm): 142.6, 138.9, 135.6, 130.7, 126.2, 108.7, 31.6, 31.5, 30.7, 29.7, 29.6, 29.5, 29.4, 28.7, 28.5, 22.6, 14.09, 14.07.

3',3''',4,4''''-tetrahexyl-2,2':5',2''':5'',2''''-quinquethiophene (T5Hex4) The compound was prepared starting from 5,5''-dibromo-3,3',4,4''-tetrahexyl-2,2':5',2''-terthiophene and 2-(tributylstannyl)thiophene → Cyclohexane : CH_2Cl_2 (90:10). Yield 70%. Yellow solid; EI-MS m/z 748 (M^+); mp <50. ^1H NMR (400 MHz, CDCl_3 , TMS/ppm) δ 7.31 (d, $3J=5.2$ Hz, $4J=1.2$ Hz, 2H), 7.14 (d, $3J=3.6$ Hz, $4J=1.2$ Hz, 2H), 7.08 (s, 2H), 7.07 (dd, $3J=3.6$ Hz, $3J=5.2$ Hz, 2H), 2.76-2.68 (m, 8H), 1.62-1.54 (m, 8H), 1.46-1.30 (m, 24H), 0.92-0.89 (m, 12H); ^{13}C NMR (TMS/ppm): 140.2, 140.1, 136.2, 135.9, 129.9, 129.7, 127.3, 125.9, 125.8, 125.3, 31.55, 31.5, 30.7, 29.6, 29.58, 28.3, 28.1, 22.66, 22.62, 14.09, 14.07.

Synthesis of polymers 1a1, 1b1 and 5a2: To a solution of the appropriate dibromo compound (1 mmol), distannane derivatives (1 mmol) in 10 mL of Toluene, $\text{Pd}(\text{PPh}_3)_4$ (0.05 mmol) was added under a N_2 atmosphere and the solution was refluxed for 24 h. The reaction mixture was brought to room temperature and the solvent was evaporated under reduced pressure. All polymers were precipitated for three times by addition of methanol to a solution of the polymers in chloroform.

PSOS02 (5a2). The compound was prepared starting from 5a and 3',4'-dihexyl-5,5"-bis(tributylstannyl)-[2,2':5',2"-terthiophene]1',1'-dioxide → Yield 70%. Dark violet solid, mp > 300°C; ¹H NMR (400 MHz, CDCl₃, TMS/ppm) δ 7.80-7.70 (m), 7.60-7.50 (m), 7.40-7.24 (m), 2.75-2.70 (m), 1.70-1.14 (m), 0.98-0.92 (m). GPC: Mn= 30700, Mw = 40800, PDI = 2.06, DP = 55. UV/Vis: λ_{max} 550 nm in CH₂Cl₂. Td 160.1 °C (34.2% residual weight). Tg= -46.51. IR ν_{max} 3418, 2923, 1731, 1644, 1455, 1380, 1299, 1260, 1139, 1057, 799, 699. Mn = 30700, Mw/Mn = 2.1, DPn = 44 (Determined by GPC in THF and polystyrene standard); Td = 208°C (Determined by TGA under nitrogen); Tg = 34.2°C (Determined by DSC)

PSO (1a1) The compound was prepared starting from 1a and 2,5-bis(tributylstannyl)thiophene. → Yield 60%. Dark blue solid, mp > 300°C; ¹H NMR (400 MHz, CDCl₃, TMS/ppm) δ 7.73-7.68 (m), 7.31-7.21 (m), 7.15-7.09 (m), 7.06-6.92 (m), 6.84-6.81 (m), 6.77-6.70 (m). GPC: Mw 5881 Mn 3213, PDI = 1.83, DP = 17. UV/Vis: λ_{max} 625 nm in CH₂Cl₂. Td 171.9 °C (69.4% residual weight). IR: ν_{max} 3467, 2922, 2362, 1721, 1619, 1441, 1054. Mn(g/mol) = 5100, Mw/Mn = 1.7, DPn = 15 (Determined by GPC in THF and polystyrene standard); Td = 153°C (Determined by TGA under nitrogen).

PSO2 (1b1) The compound was prepared starting from 1b and 2,5-Bis(tributylstannyl)thiophene. → Yield 60%. Dark blue solid, mp > 300°C; ¹H NMR (400 MHz, CDCl₃, TMS/ppm) δ 7.73-7.68 (m), 7.31-7.21 (m), 7.15-7.09 (m), 7.06-6.92 (m), 6.84-6.81 (m), 6.77-6.70 (m). GPC: Mw 5320 Mn 2907, PDI = 1.83, DP = 15. UV/Vis: λ_{max} 610 nm in CH₂Cl₂. Td 158.0 °C (38.5% residual weight). IR: ν_{max} 3461, 2921, 1612, 1619, 1439, 1309, 1139.

Table S2. Characteristics of polymers **1a1**, **1b1** and **5a2**.

Sample	M _n ^a (g/mol)	M _w ^a /M _n	DP _n ^b	T _d ^c (°C)	T _g ^d (°C)
1a1	5100	1.7	15	182	n.d.
1b1	4200	1.8	12	153	n.d.
5a2	30700	2.1	44	208	34.2

^aDetermined by GPC in THF and polystyrene standard. ^bAverage degree of polymerization in terms of dimeric or tetrameric repeating units. ^cDetermined by TGA under nitrogen. ^dDetermined by DSC.

¹H and ¹³C NMR spectra

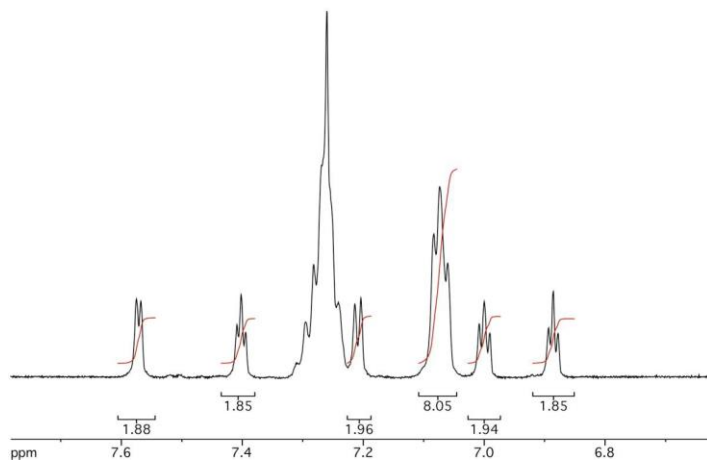
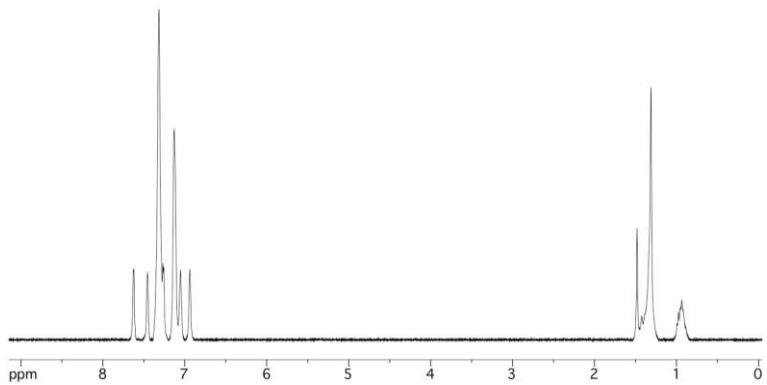


Figure S1. ¹H NMR spectrum of **1a5** (top) and expanded aromatic region (bottom).

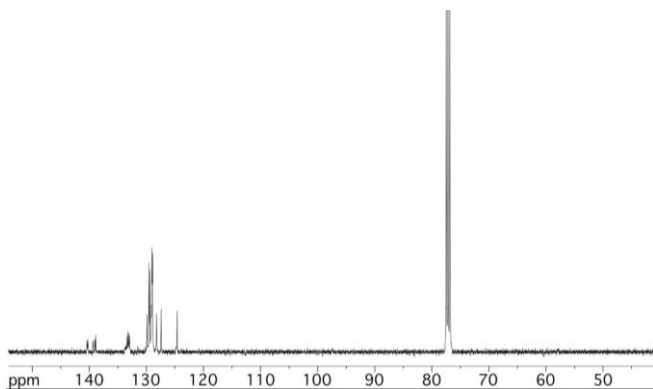


Figure S2. ^{13}C NMR spectrum of **1a5**.

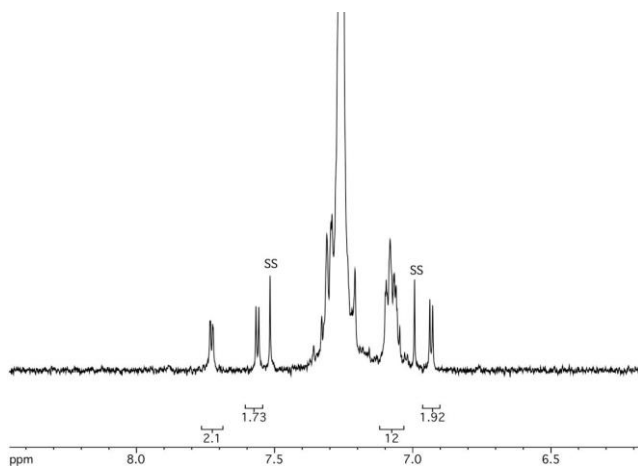
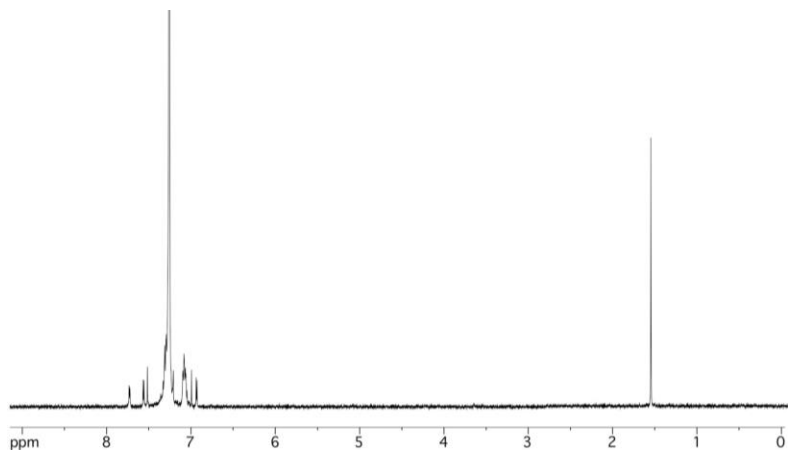


Figure S3. ^1H NMR spectrum of **1b5** (top) and expanded aromatic region (bottom). SS = spinning side bands.

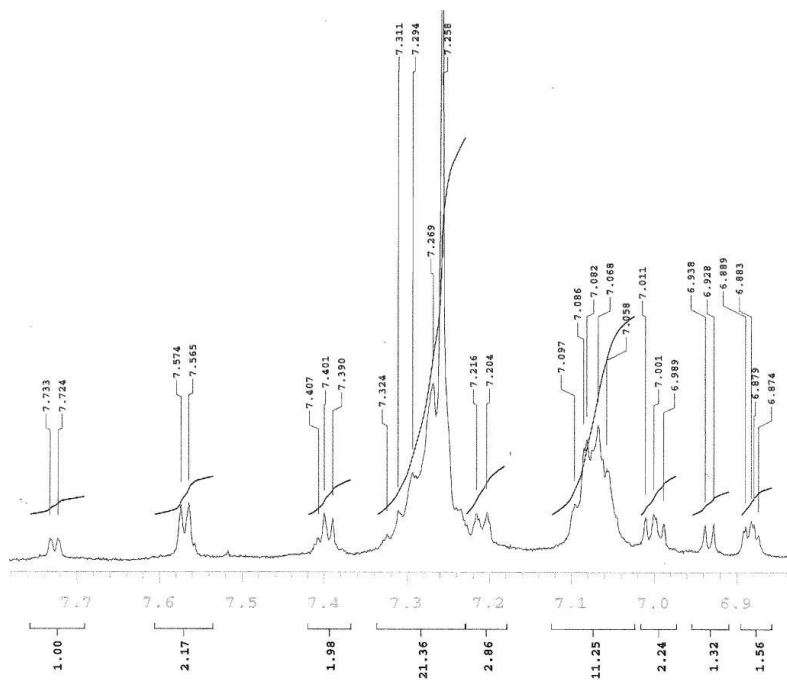
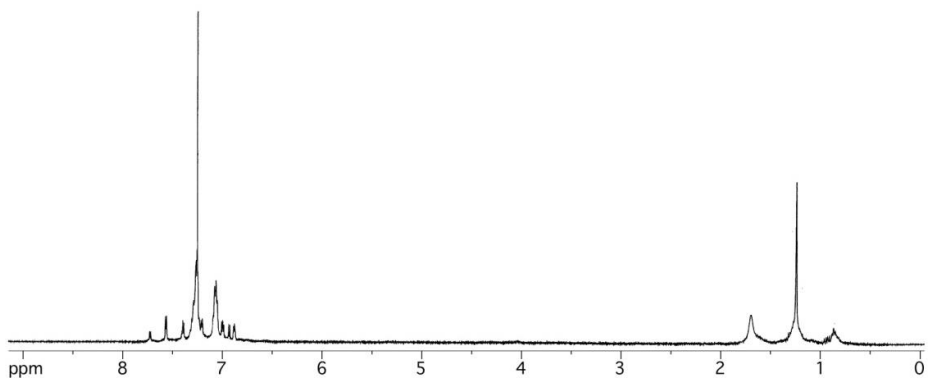


Figure S4. ^1H NMR spectrum of **1ab** (top) and expanded aromatic region (bottom). * = solvents, ° = grease.

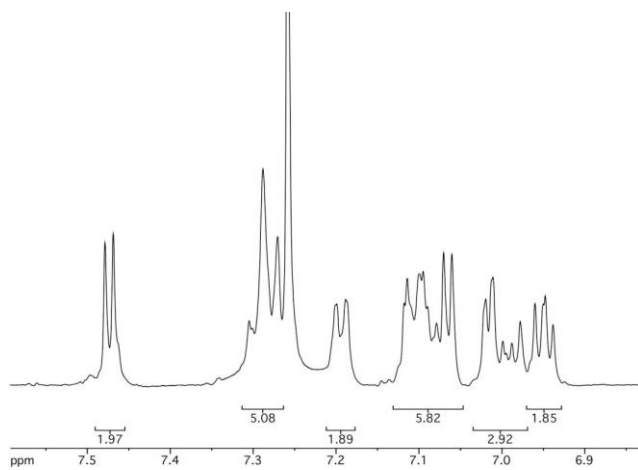
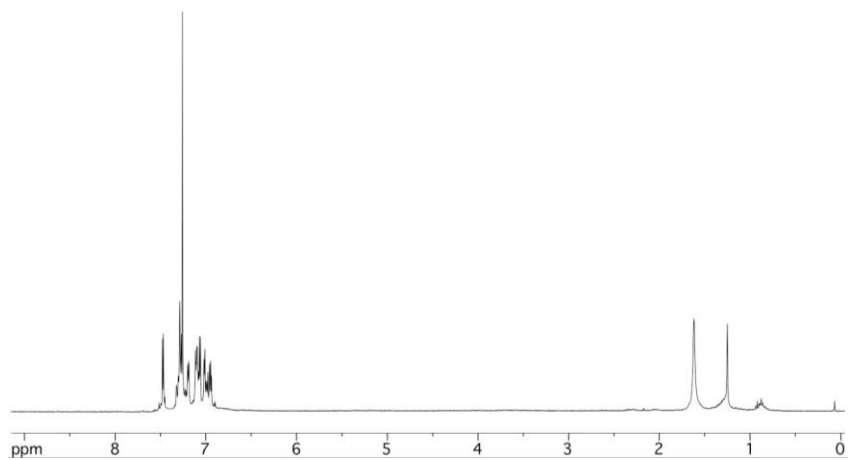


Figure S5. ^1H NMR spectrum of **1a2** (top) and expanded aromatic region (bottom). * = solvents, ° = grease.

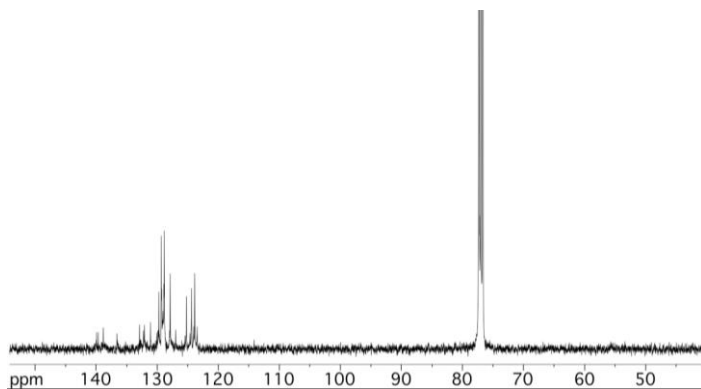


Figure S6. ^{13}C NMR spectra of *1a2*.

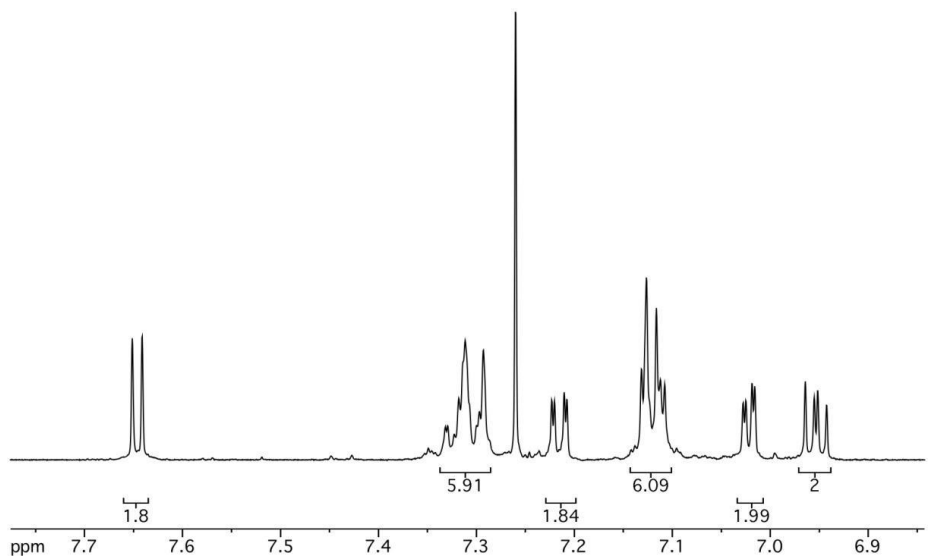
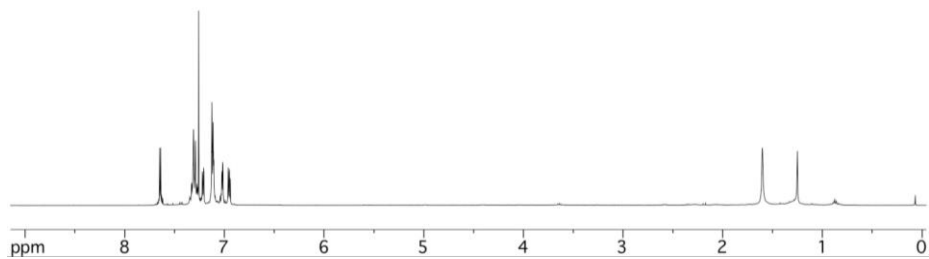


Figure S7. ^1H NMR spectrum of **1b2** (top) and expanded aromatic region (bottom). * = solvents, ° = H grease.

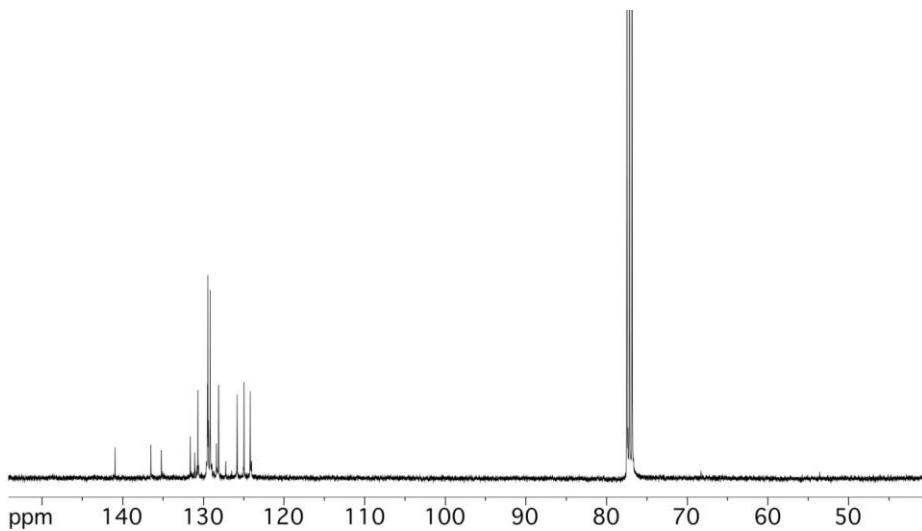


Figure S8. ^{13}C NMR spectra of **1b2**.

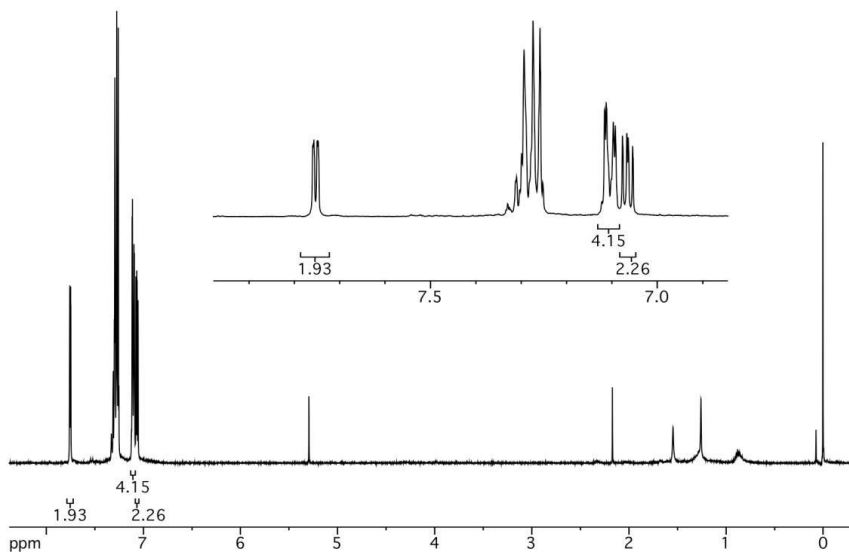


Figure S9. ^1H NMR spectra of **1a3**. Inset: aromatic region. * = solvents, ° = grease.

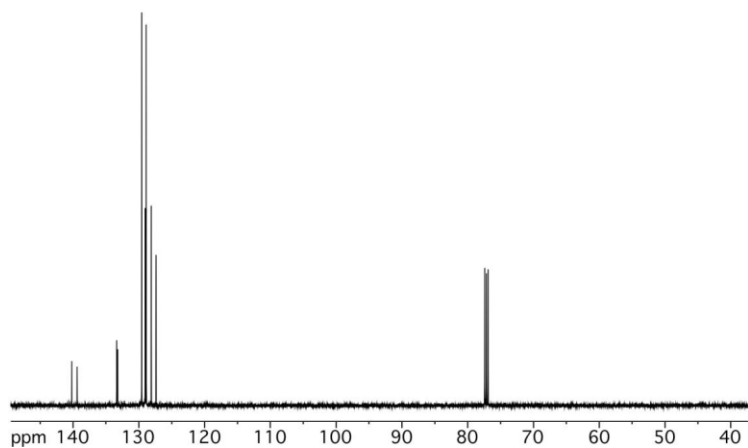


Figure S10. ^{13}C NMR spectrum of **1a3**.

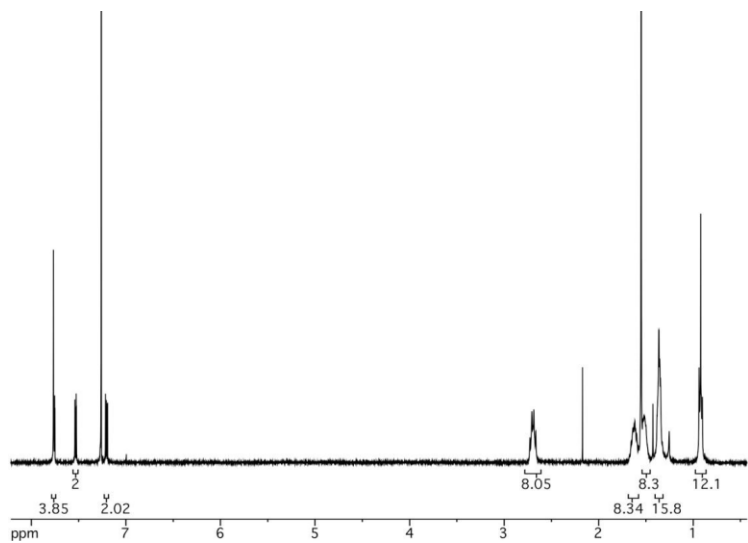


Figure S11. ^1H NMR spectrum of **10b3**.

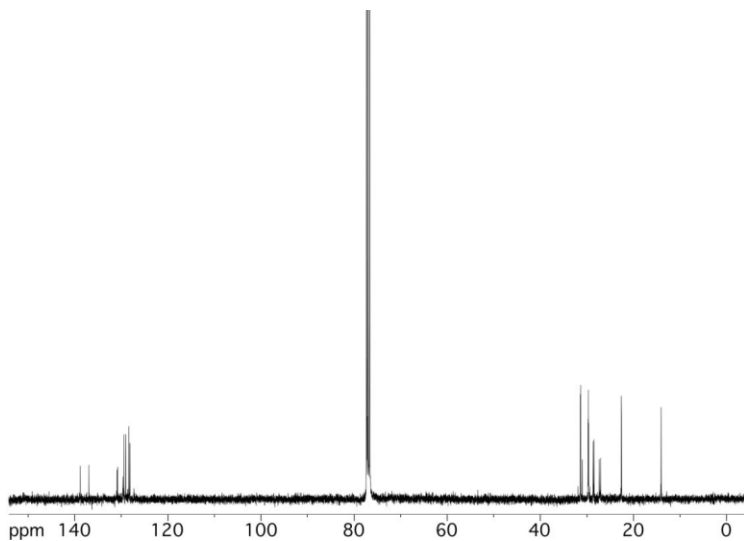


Figure S12. ^{13}C NMR spectrum of **10b3**.

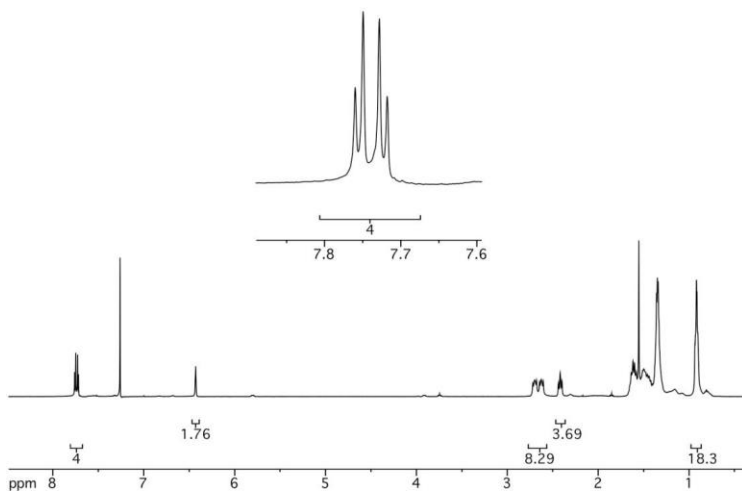


Figure S13. ^1H NMR spectrum of **9b4**. Inset: aromatic region.

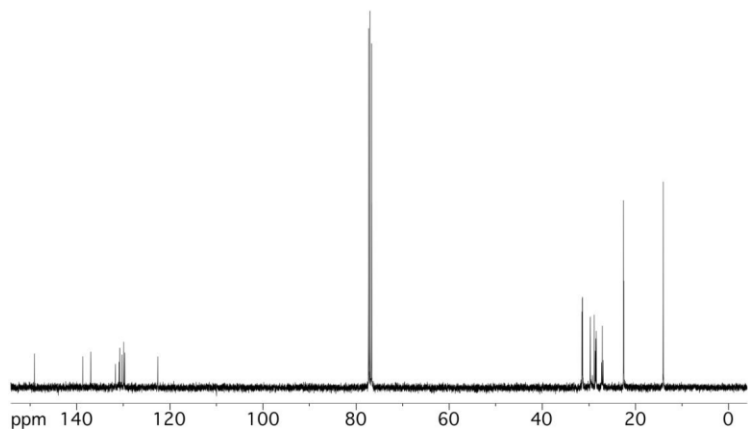


Figure S14. ^{13}C NMR spectrum of **9b4**.

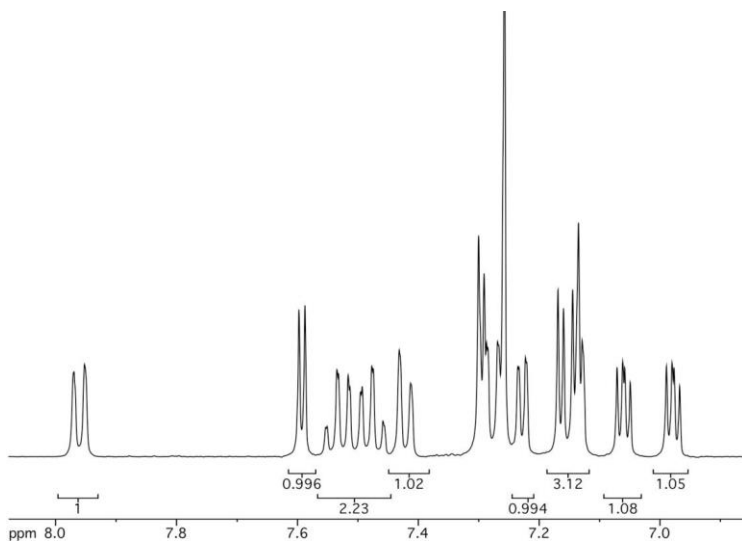
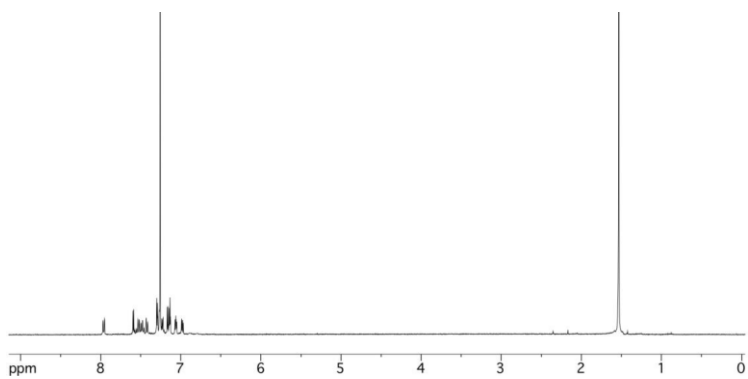


Figure S15. ^1H NMR spectrum of **3a2** (top) and expanded aromatic region (bottom).

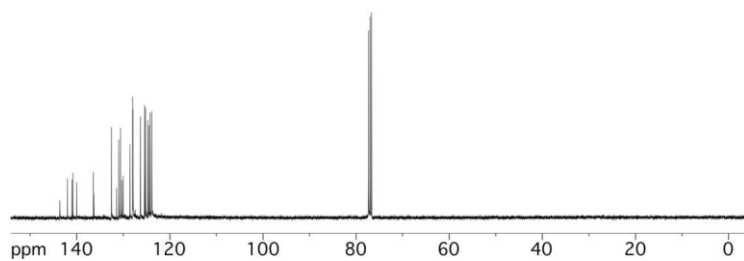


Figure S16. ^{13}C NMR spectrum of **3a2**.

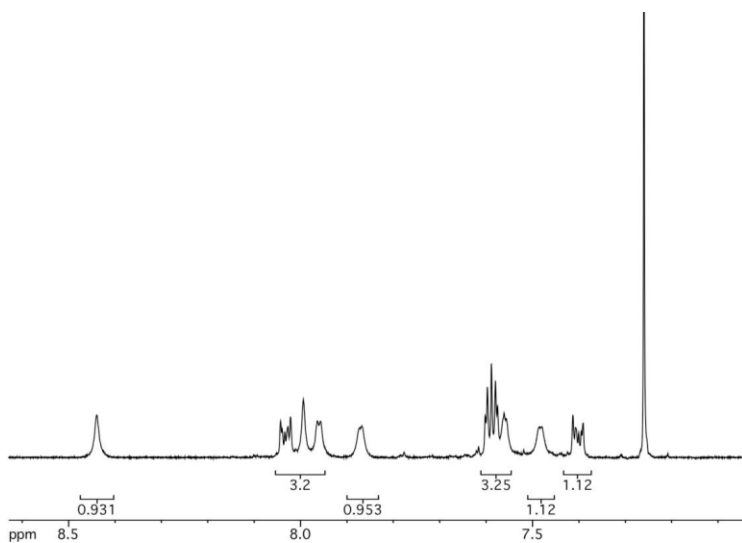
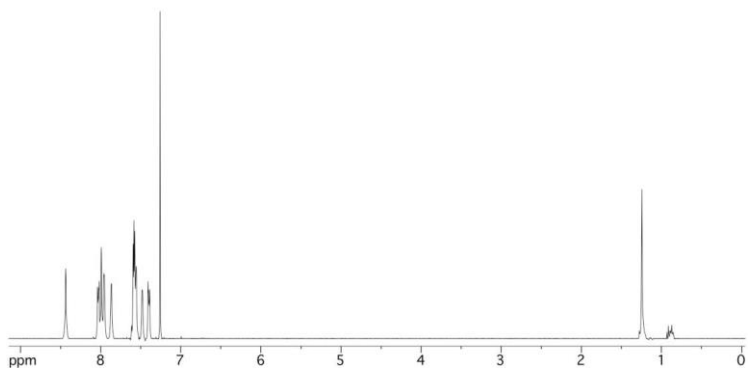


Figure S17. ¹H NMR spectrum of 3a3 (top) and expanded aromatic region (bottom).

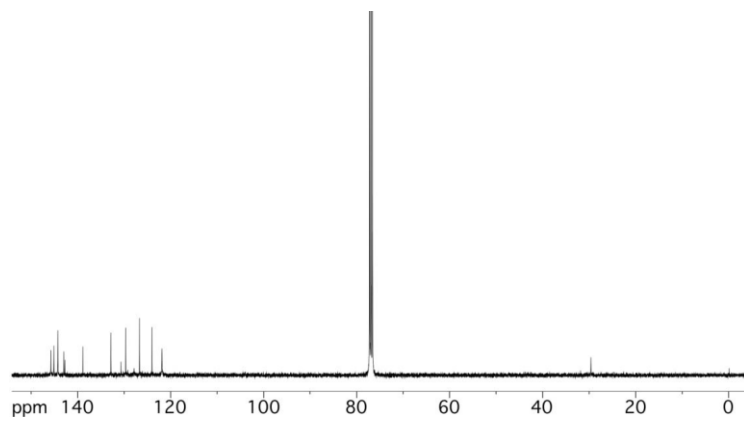


Figure S18. ^{13}C NMR spectrum of **3a3**.

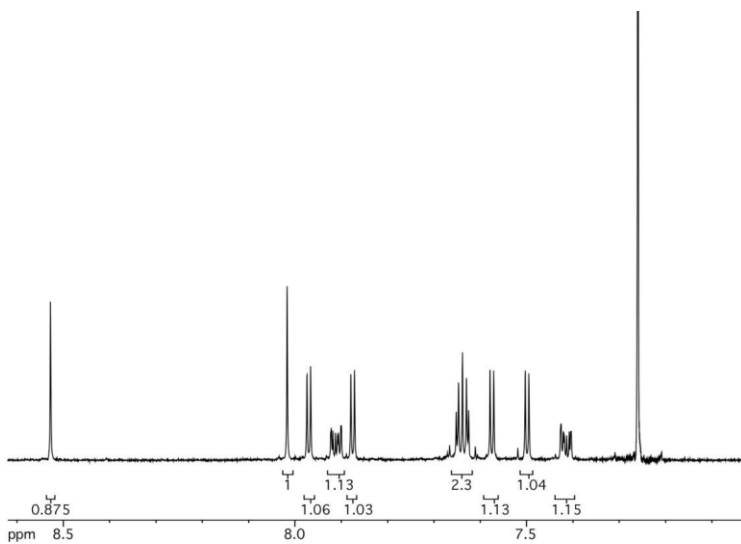
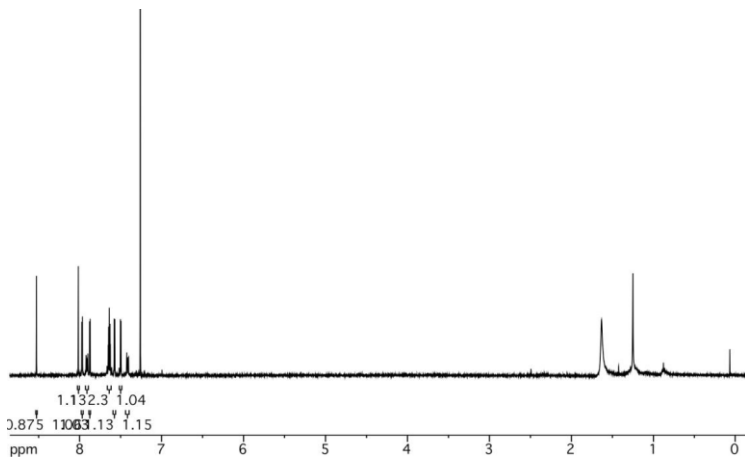


Figure S19. ^1H NMR spectrum of **3b3** (top) and expanded aromatic region (bottom). * = solvents, ° = grease.

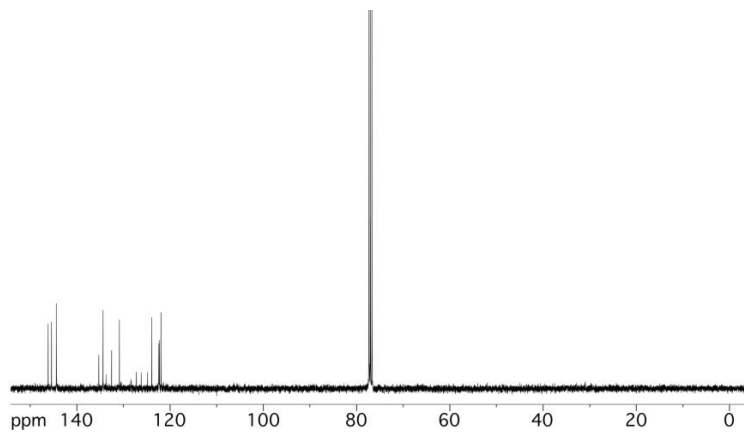


Figure S20. ^{13}C NMR spectrum of **3b3**.

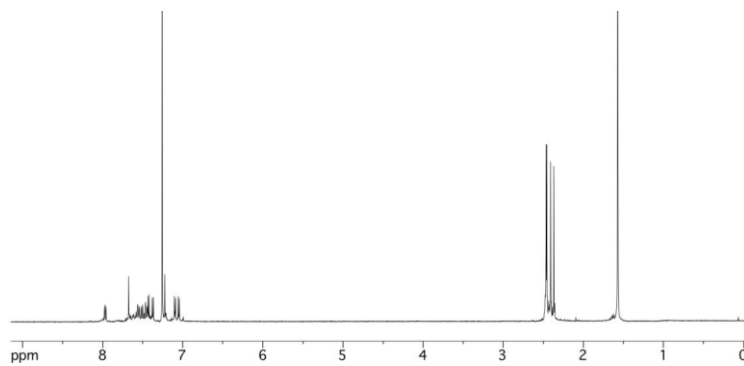


Figure S21. ^1H NMR spectrum of **3a1** in CDCl_3 .

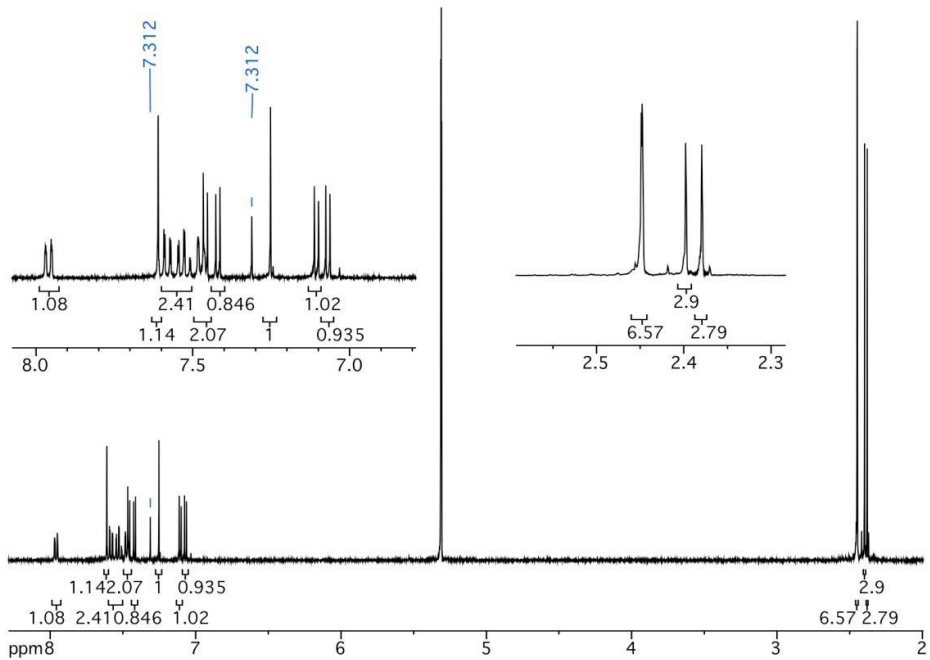


Figure S22. ^1H NMR spectrum of **3aI** in CD_2Cl_2 . Insets: aromatic and aliphatic region.

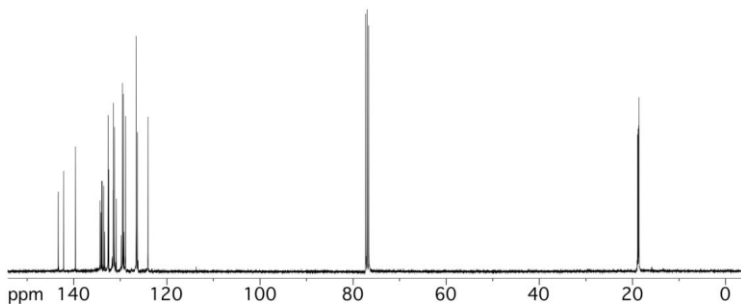


Figure S23. ^{13}C NMR spectrum of **3aI**.

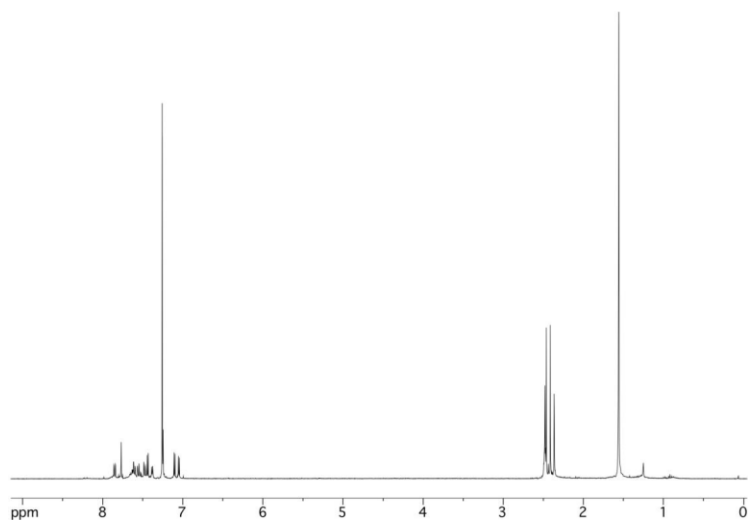


Figure S24. ^1H NMR spectrum of **3b1** in CDCl_3 .

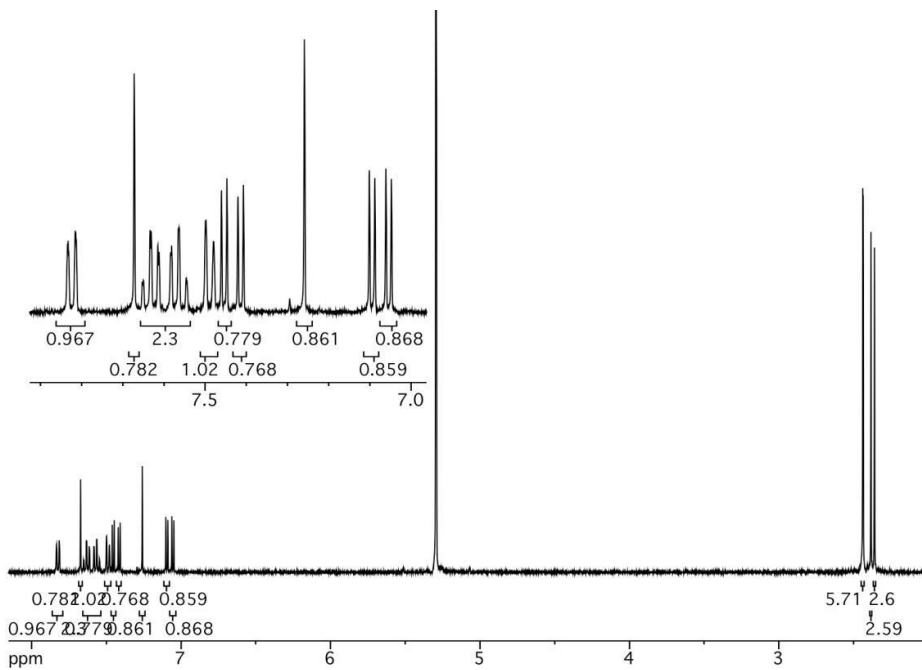


Figure S25. ^1H NMR spectrum of **3b1** in CD_2Cl_2 . Inset: aromatic region.

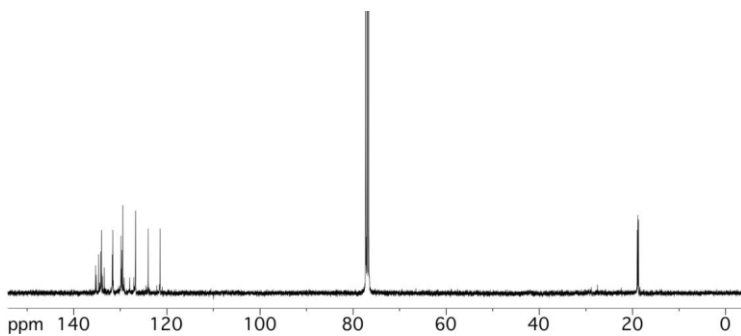


Figure S26. ^{13}C NMR spectrum of **3b1**.

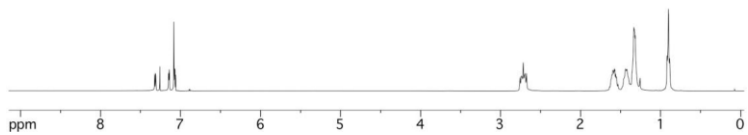


Figure S27. ^1H NMR spectrum of T5Hex4.

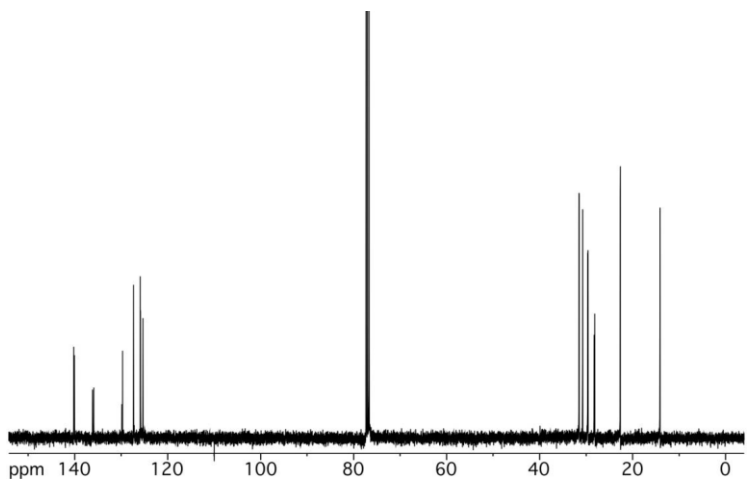


Figure S28. ^{13}C NMR spectrum of T5Hex4.

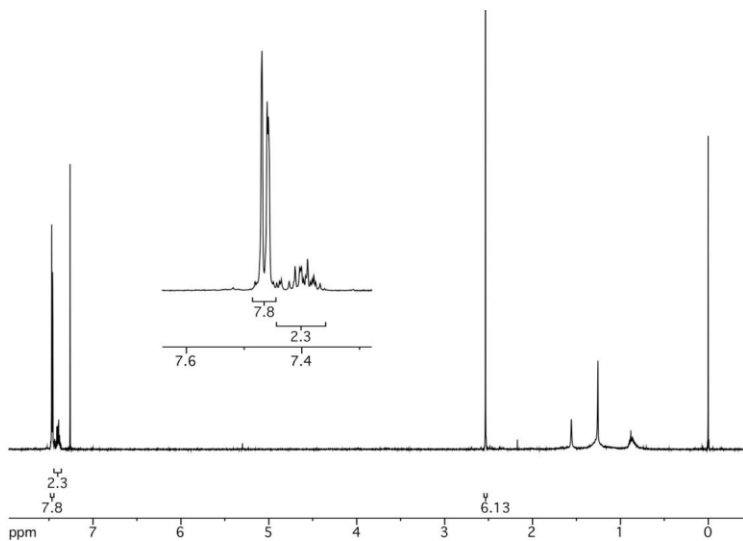


Figure S29. ^1H NMR spectrum of 5a1. Inset: aromatic region.

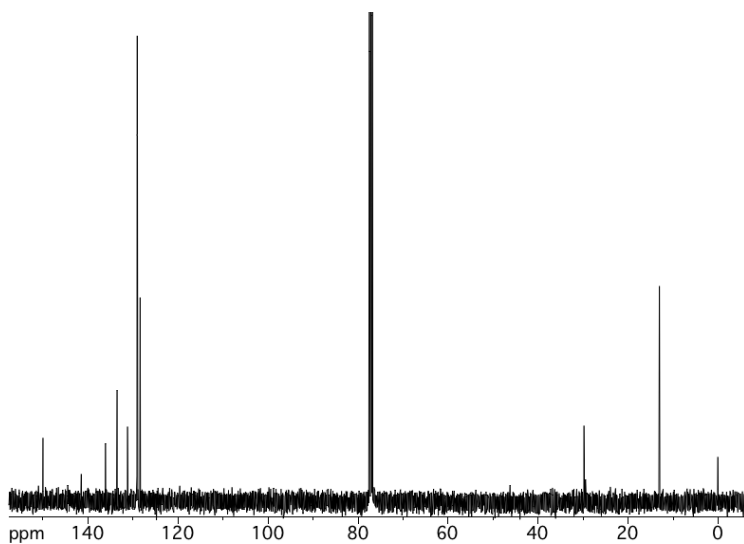


Figure S30. ^{13}C NMR spectrum of 5a1.

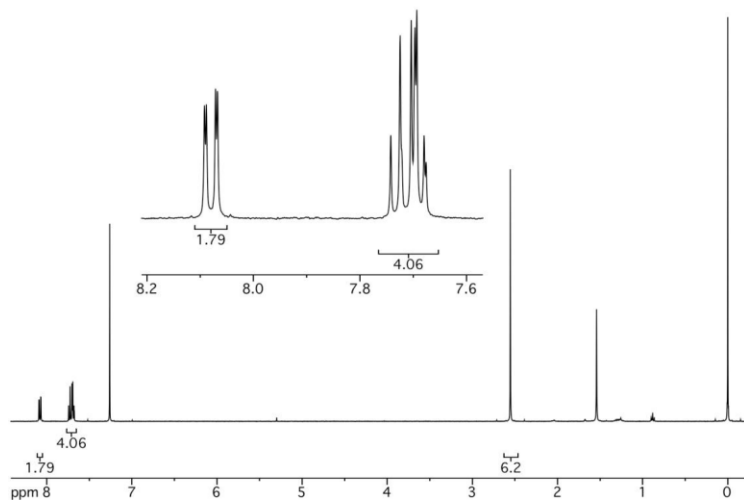


Figure S31. ^1H NMR spectrum of 5b2. Inset: aromatic region.

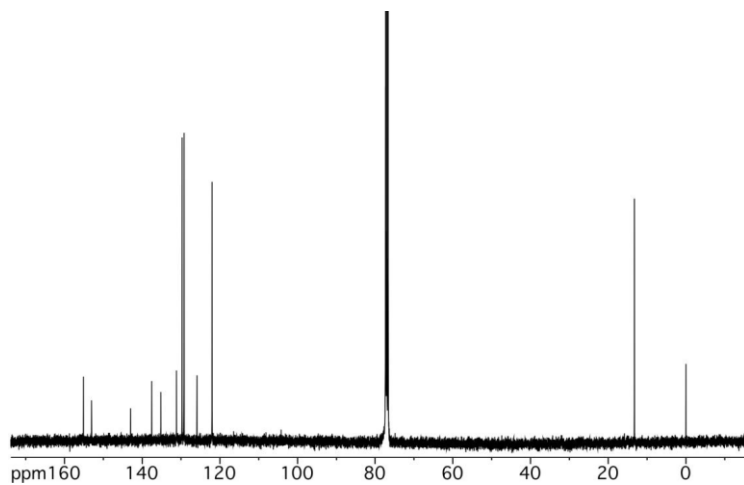


Figure S32. ^{13}C NMR spectrum of 5b2.

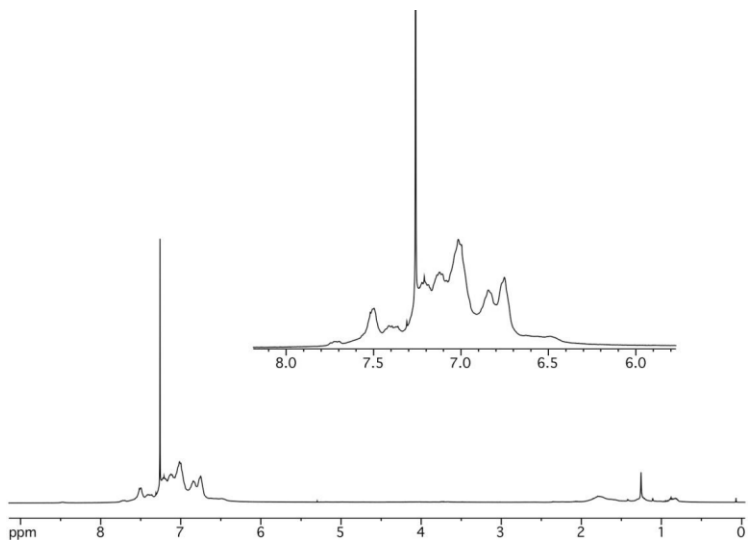


Figure S33. ^1H spectrum of polymer **1a1**. Inset: aromatic region.

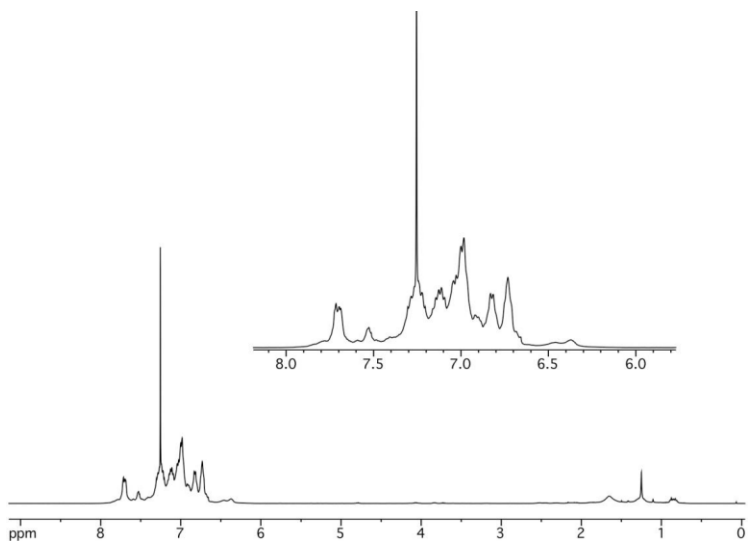


Figure S34. ^1H NMR spectrum of polymer **1b1**. Inset: aromatic region.

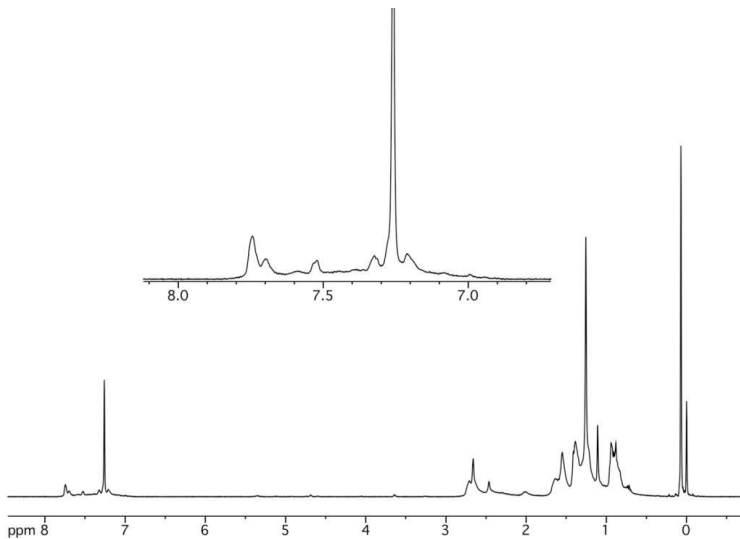


Figure S35. ^1H NMR spectrum of polymer **5a2**. Inset: aromatic region.

High Resolution Mass spectra

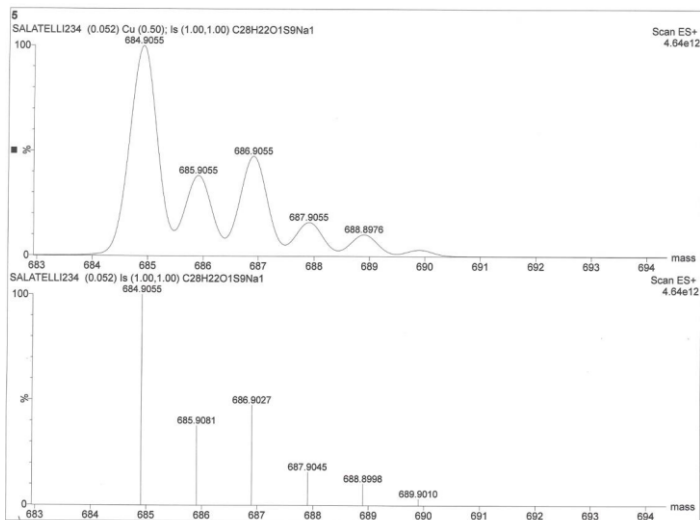


Figure S36. HR mass spectrum of **3a1**.

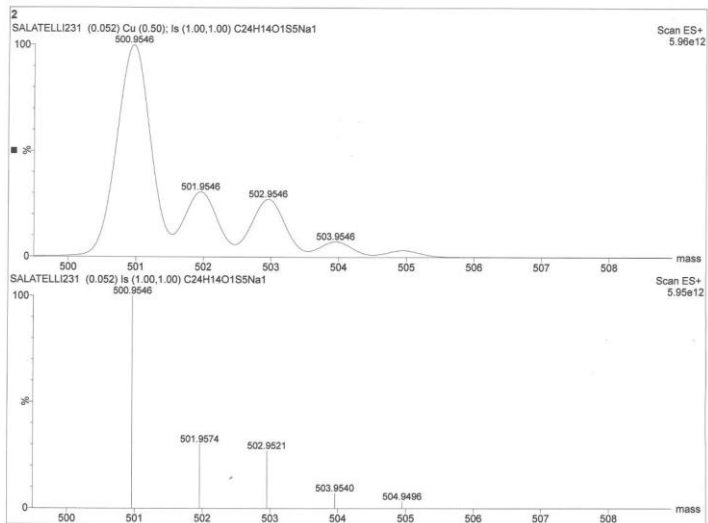


Figure S37. HR mass spectrum of **3a2**.

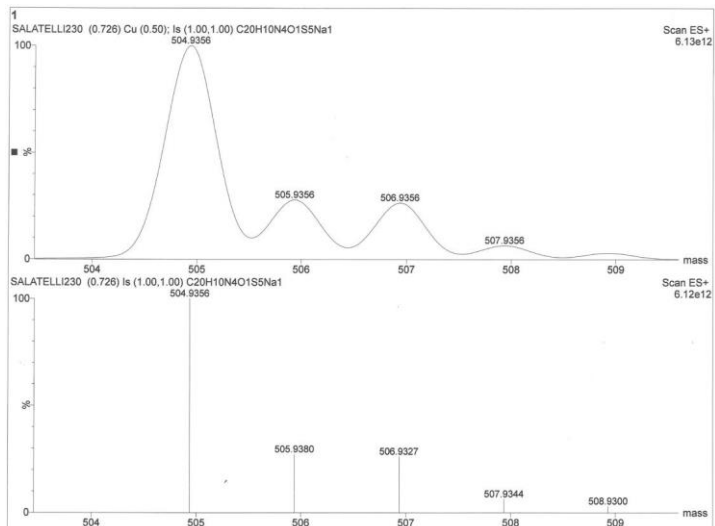


Figure S38. HR mass spectrum of **3a3**.

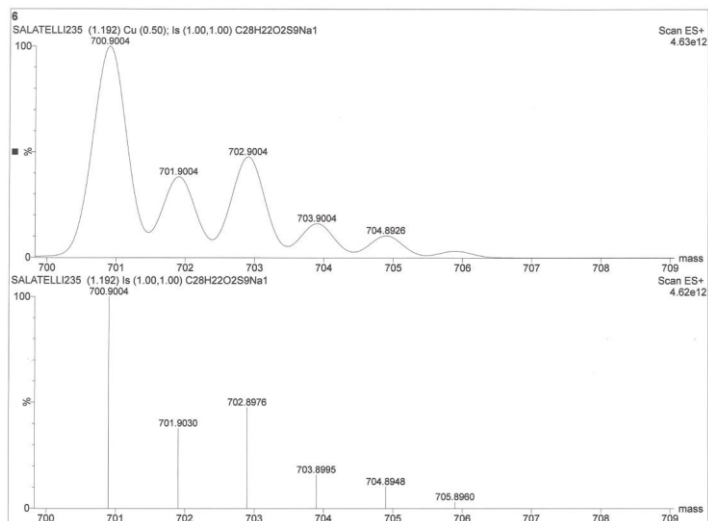


Figure S39. HR mass spectrum of 3b1.

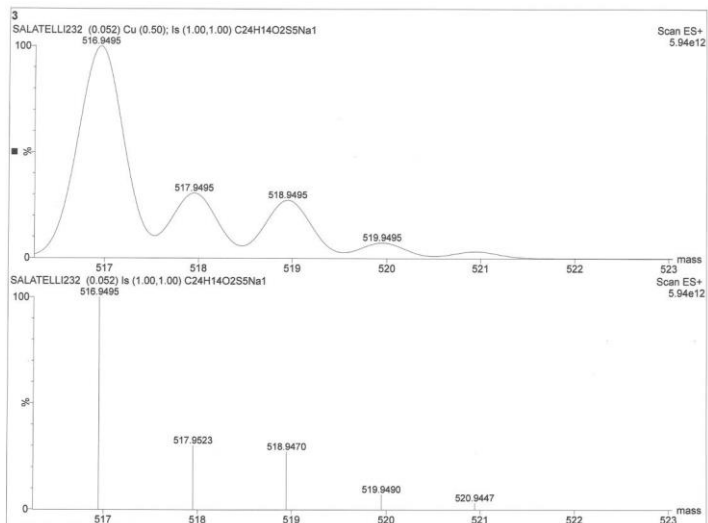


Figure S40. HR mass spectrum of 3b2.

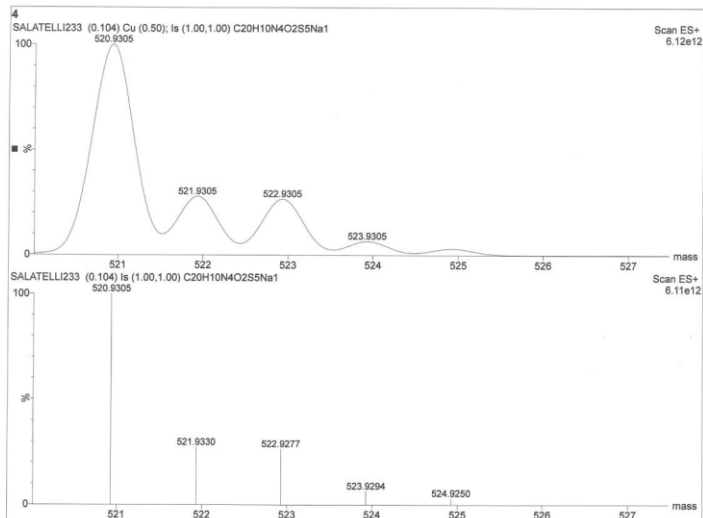


Figure S41. HR mass spectrum of **3b3**.

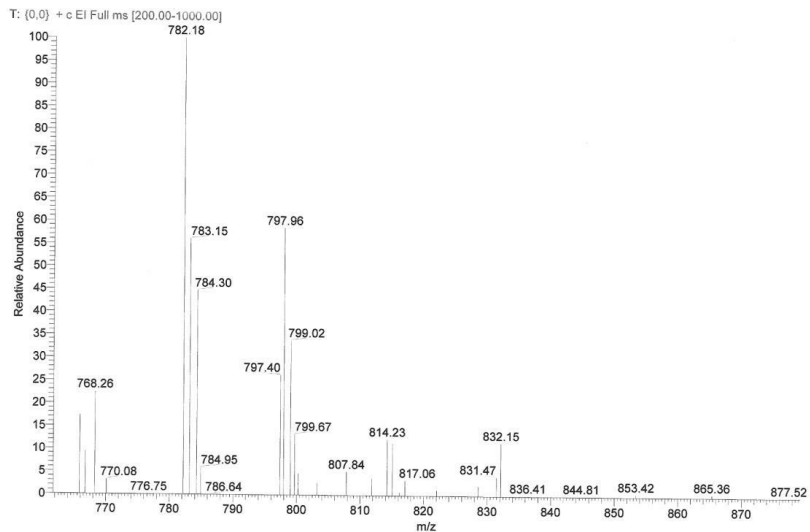
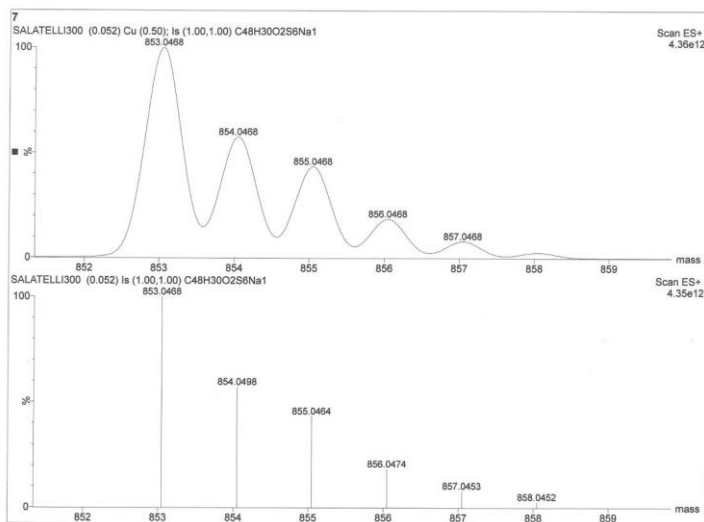


Figure S42. High Resolution (top) and Low Resolution (bottom) mass spectra of **1a5**.

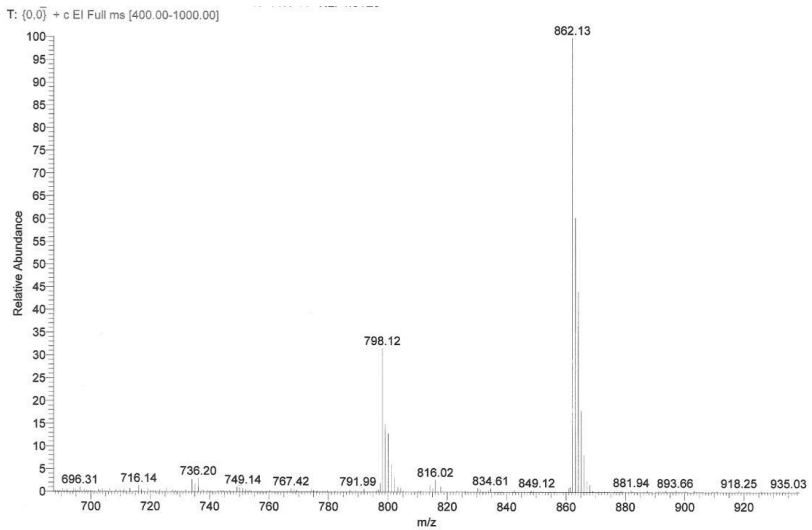
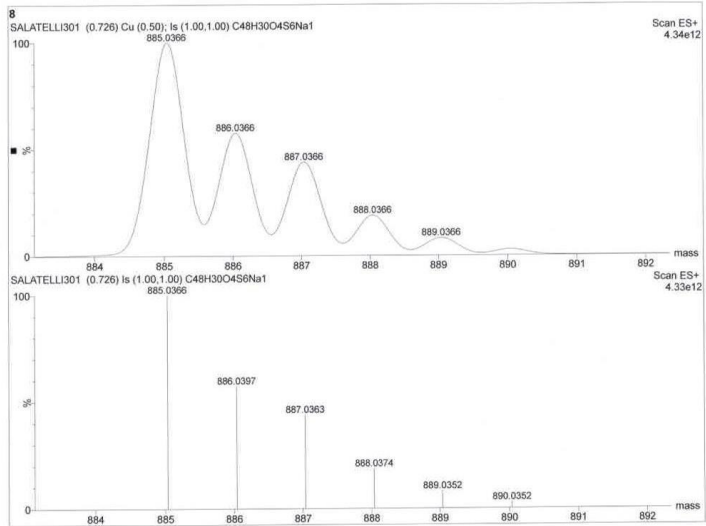
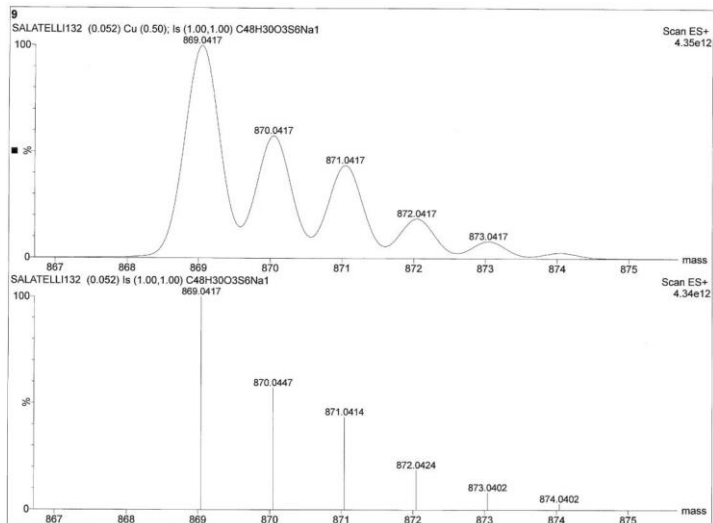


Figure S43. High Resolution (top) and Low Resolution (bottom) mass spectra of **1b5**.



T: (0,0) + c EI Full ms [400.00-1000.00]

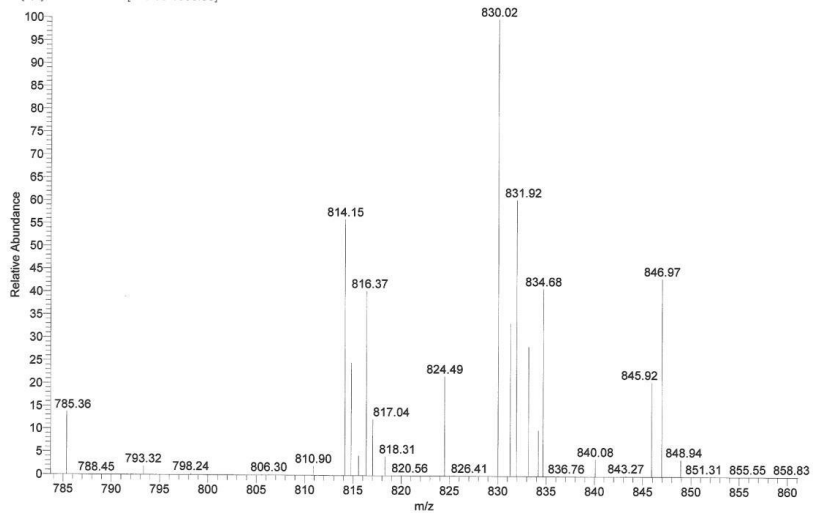


Figure S44. High Resolution (top) and Low Resolution (bottom) mass spectra of **1ab**.

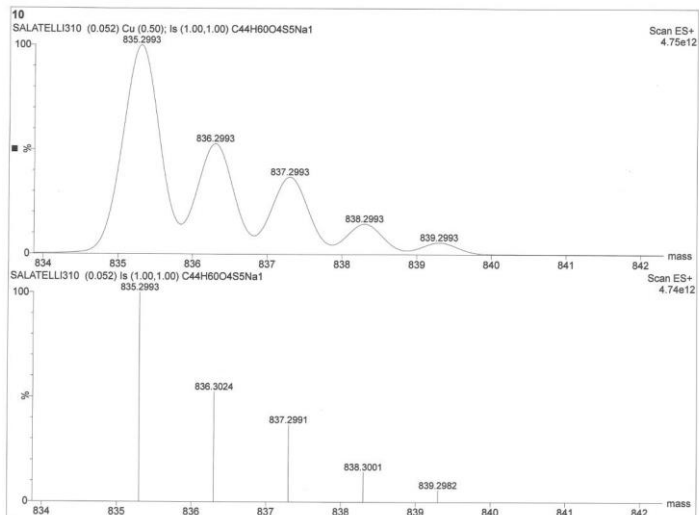


Figure S45. HR mass spectrum of **10b3**.

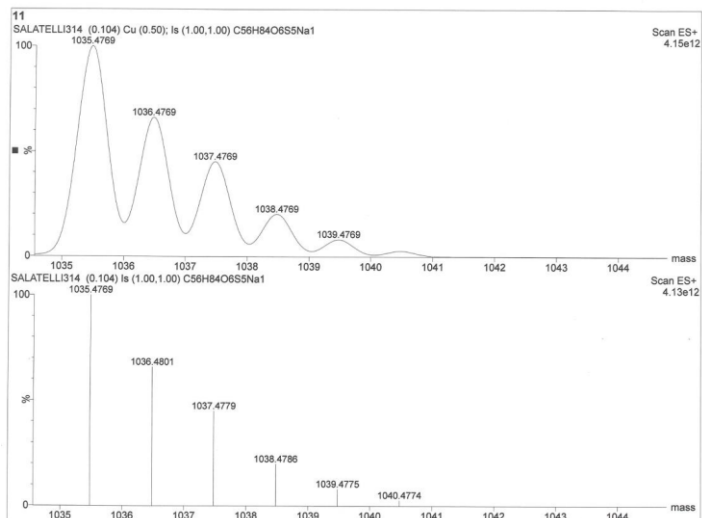


Figure S46. HR mass spectrum of **9b4**.

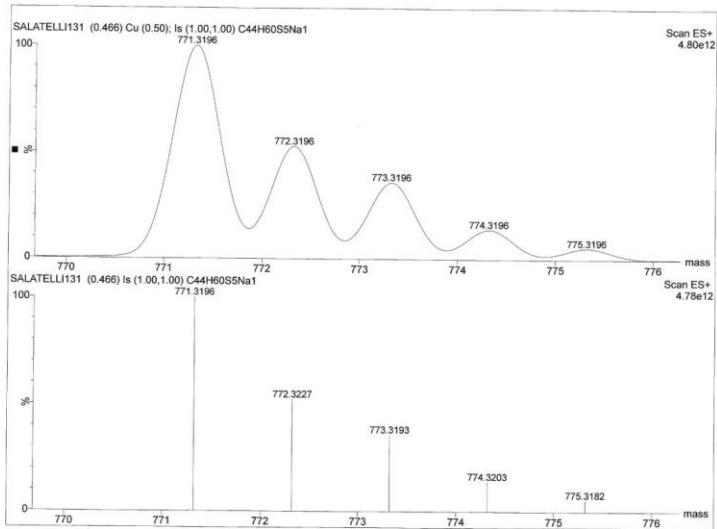


Figure S47. HR mass spectrum of *TSHex4*.

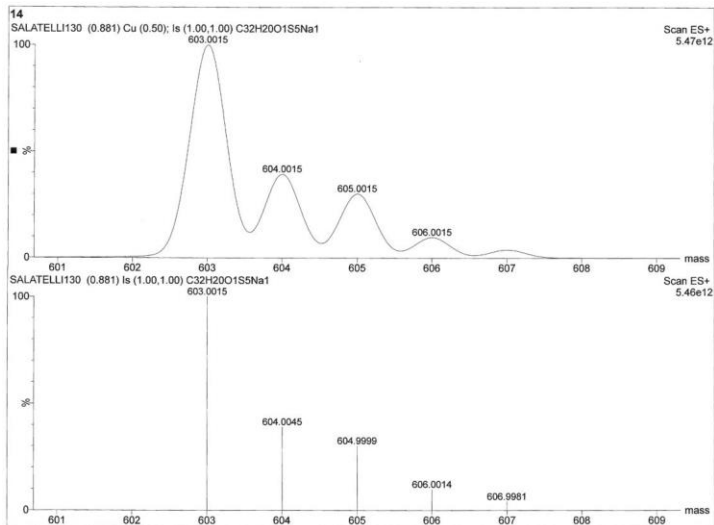


Figure S48. HR mass spectrum of *T5phSO*.

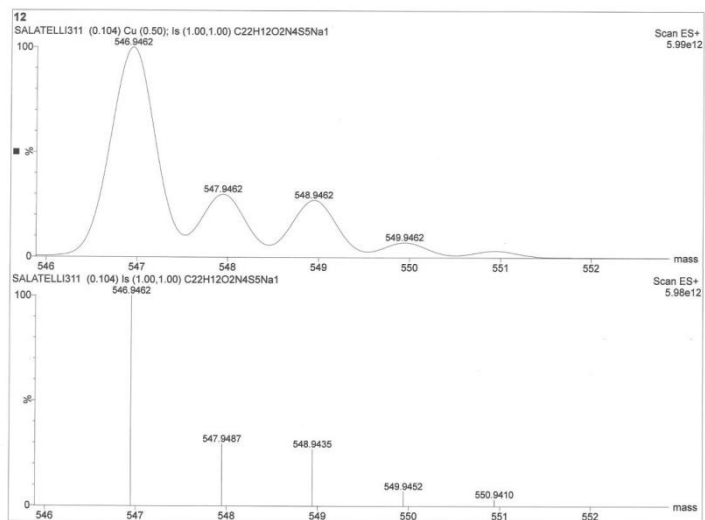


Figure S49. HR mass spectrum of 5b2.

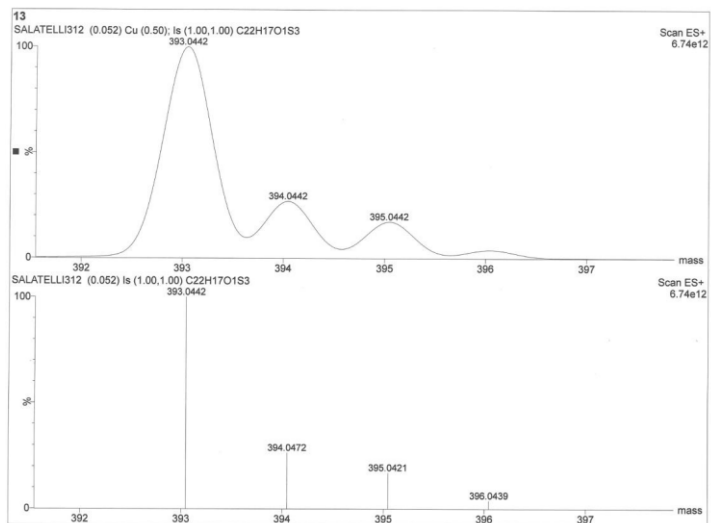


Figure S50. HR mass spectrum of 5a1.

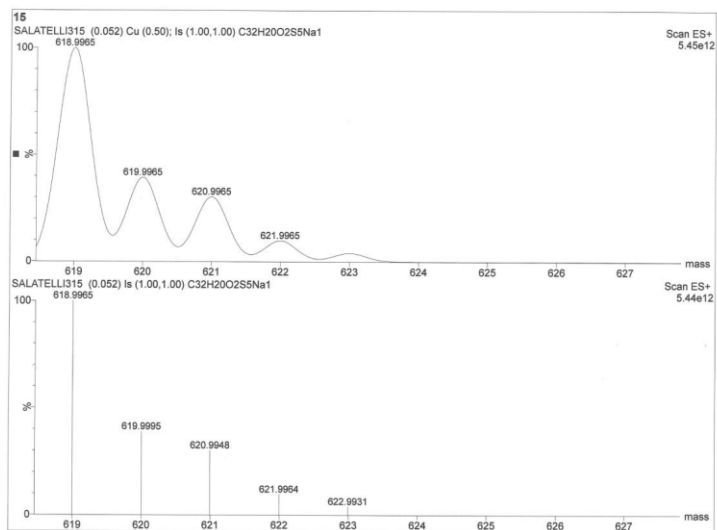


Figure S51. HR mass spectrum of **Ib2**.

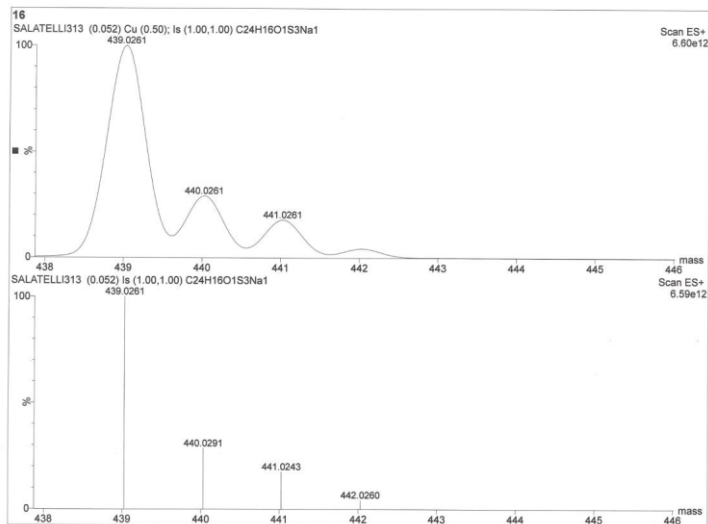


Figure S52. HR mass spectrum of **Ia3**.

TLC of compound 1b5, 1ab, 1b5

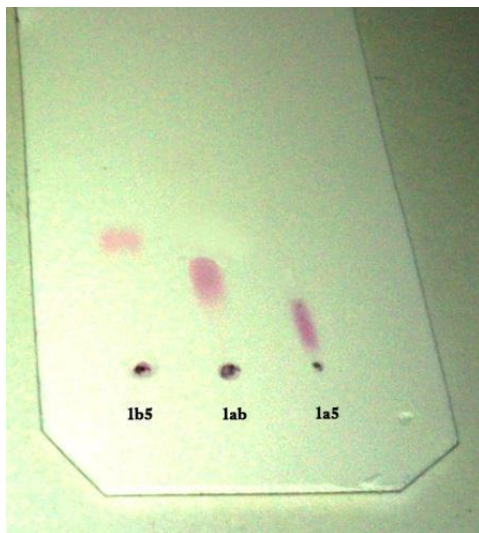


Figure S53. Thin Layer Chromatography of 1a5, 1b5 and 1ab.

5.2 Cyclic Voltammetry

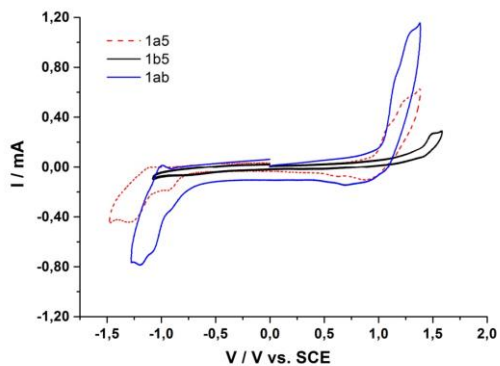


Figure S54. Cyclic voltammetry of hexamers 1a5, 1b5 and 1ab.

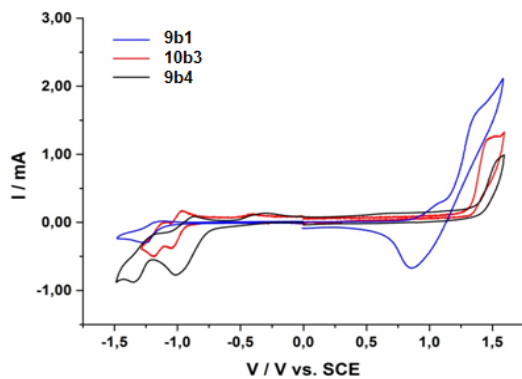


Figure S55. Cyclic Voltammetry of pentamers 9b1, 10b3 and 9b4.

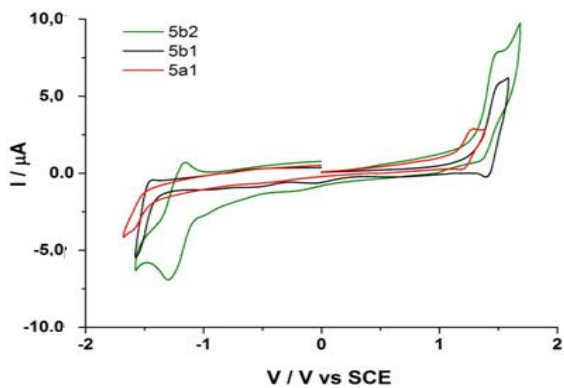


Figure S56. Cyclic voltammetry of dithienothiophene derivative 5a1, 5b1 and 5b2.

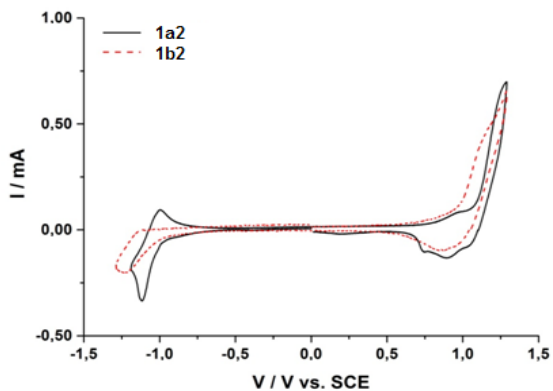


Figure S57. Cyclic voltammety of pentamers 1a2 and 1b2.

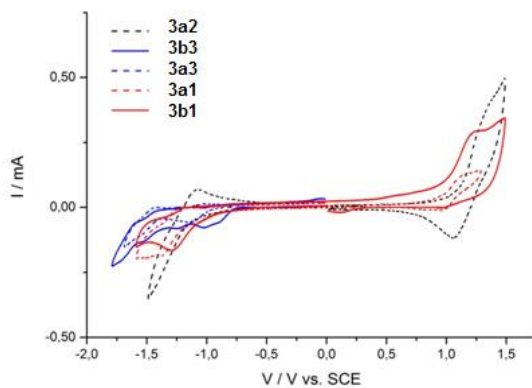


Figure S58. Cyclic voltammety of V-shaped oligomers 3a2, 3b3, 3a3, 3a1 and 3b1.

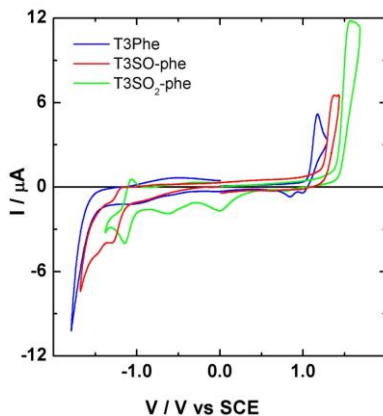


Figure S59. Cyclic voltammetry of **1a3** (T_3SO -Phe), **1b3** (T_3SO_2 -Phe) and the corresponding non oxygenated terthiophene (T_3Phe).

5.3 Optical properties.

Table S3. Absorption (λ_{max} , nm) and emission (λ_{PL} , nm) wavelengths and molar coefficients (ϵ , $\text{cm}^{-1}\text{mol}^{-1}$) in CHCl_3 of compounds.

<i>Item</i>	λ_{max}	λ_{PL}	ϵ	<i>Item</i>	λ_{max}	λ_{PL}	ϵ
1a1	622			5a1	409	534	18200
1b1	612			5b1	408	514	
5a2	548			5b2	426	549	21400
1a3	443	555	7553	8b1	470	590	
1b3	429	535	9164	9b2	480		27000
1b5	528	650,662 (solid)	38100	8b3	475	580	32700
1b5	526	~650	27000				
1ab	527	~650	35000				
1a2	506	620	42200				
1b2	504	615	38450				
3a1	428	602	12800				
3b1	435	642	12500				
3a2	430	578	11900				
3b2	429	520	10700				
3a3	404	530	19500				
3b3	401	470	12800				

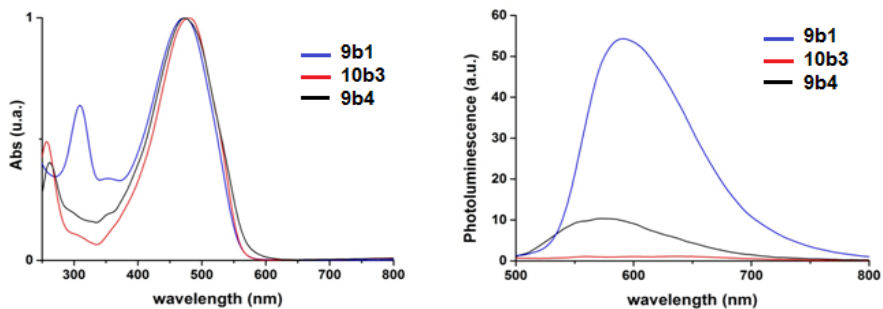


Figure S60. Absorption and emission spectra of pentamers **9b1**, **10b3** and **9b4** $\sim 10^{-5}$ M in CH_2Cl_2 .

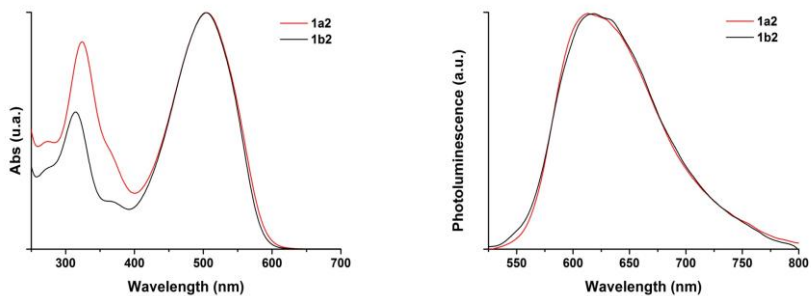


Figure S61. Absorption and emission spectra of pentamers **1a2** and **1b2** $\sim 10^{-5}$ M in CH_2Cl_2 .

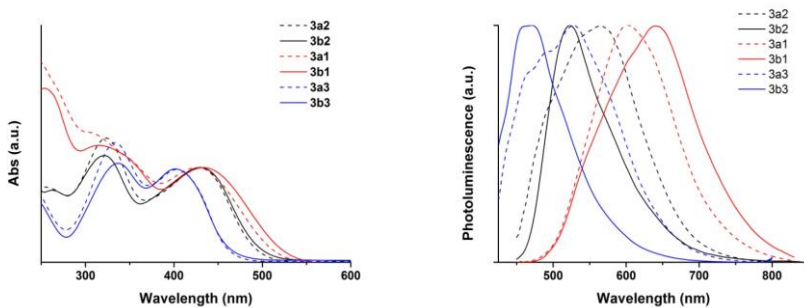


Figure S62. Absorption and emission spectra of V-shaped compounds $\sim 10^{-5}$ M in CH_2Cl_2 .

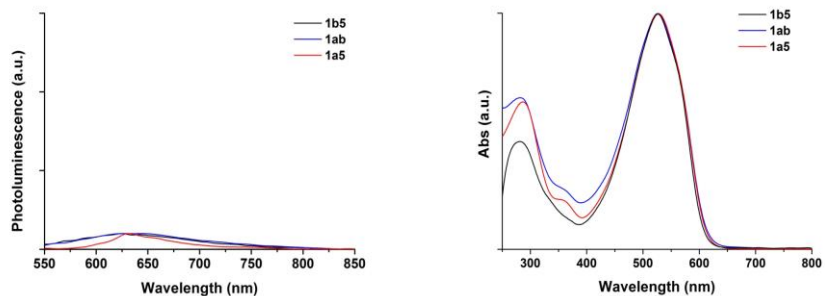


Figure S63. Absorption and emission spectra of hexamers **1a5**, **1b5** and **1ab** $\sim 10^{-5}$ M in CH_2Cl_2 .

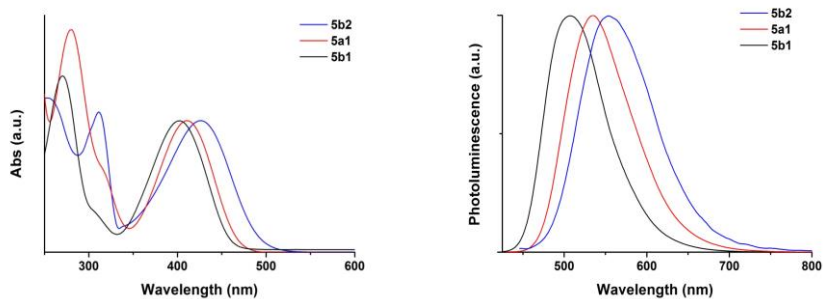


Figure S64. Absorption and emission spectra of dithienothiophene derivatives **5a1**, **5b1** and **5b2** $\sim 10^{-5}$ M in CH_2Cl_2 .

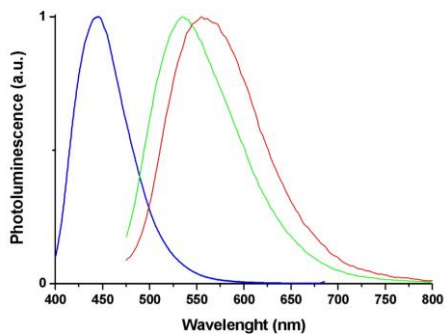


Figure S65. Photoluminescence spectra of **1a3** (red), **1b3** (green) and the corresponding non oxygenated terthiophene (blue) $\sim 10^{-5}$ M in CH_2Cl_2 .

5.4 Photophysical characterization and and electroluminescence properties of V-shaped oligomers 3a1 and 3b1.

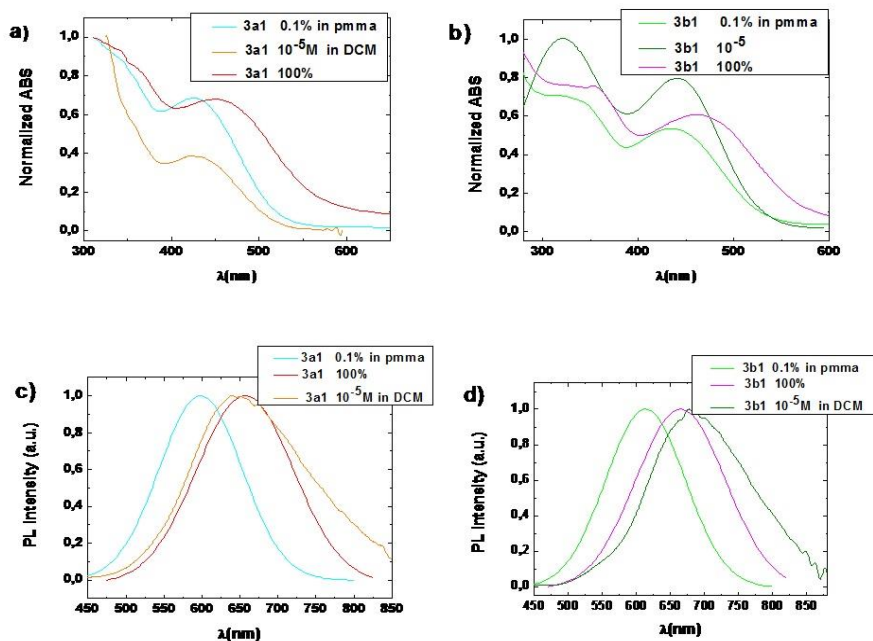


Figure S66. Photophysical characterization of 3a1 and 3b1 1.0×10^{-5} M in DCM, thin film 0.1wt% in PMMA and neat film: a), b) normalized absorption spectra, c), d) normalized photoluminescence spectra.

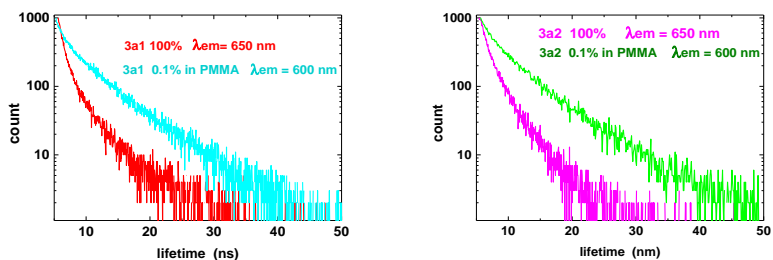


Figure S67. Decay times of 3a1 and 3b1 0.1% in PMMA and in neat films.

The complete OLED structures:

SO_OLED_1: ITO / PEDOT:PSS / **3a1 neat film** / TPBI / Bphen:Cs / Ag
SO_OLED_2: ITO / PEDOT:PSS / **BCPO:3a1 15wt%** / TPBI / Bphen:Cs / Ag
SO_OLED_3: ITO / PEDOT:PSS / **TPBI:3a1 15wt%** / TPBI / Bphen:Cs / Ag
SO₂_OLED_1: ITO / PEDOT:PSS / **3b1 neat film** / TPBI / Bphen:Cs / Ag
SO₂_OLED_2: ITO / PEDOT:PSS / **BCPO:3b1 15wt%** / TPBI / Bphen:Cs / Ag
SO₂_OLED_3: ITO / PEDOT:PSS / **TPBI:3b1 15wt%** / TPBI / Bphen:Cs / Ag

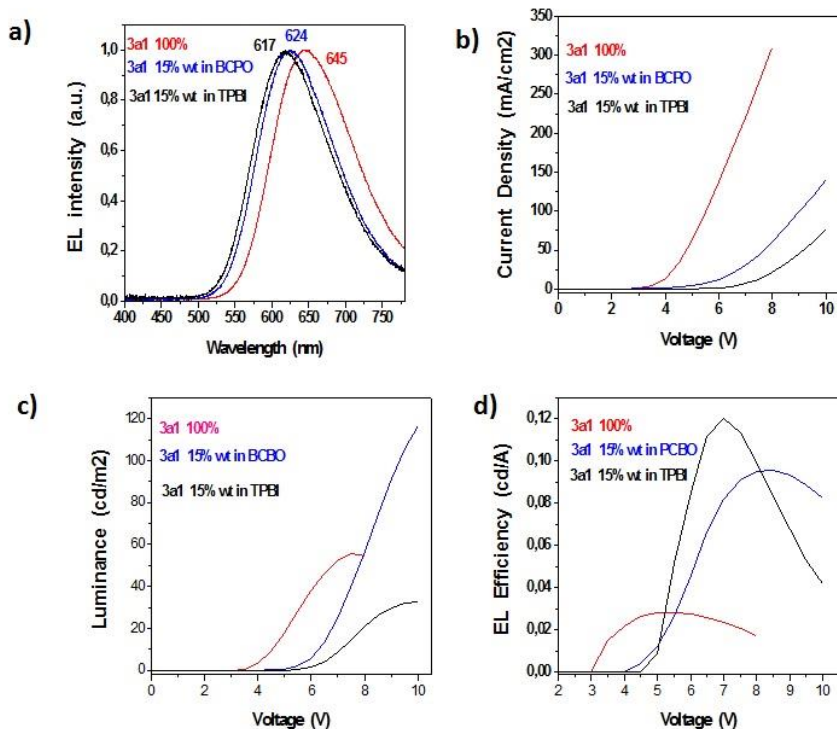


Figure S68. Electrical characterization of 3a1 based OLEDs.

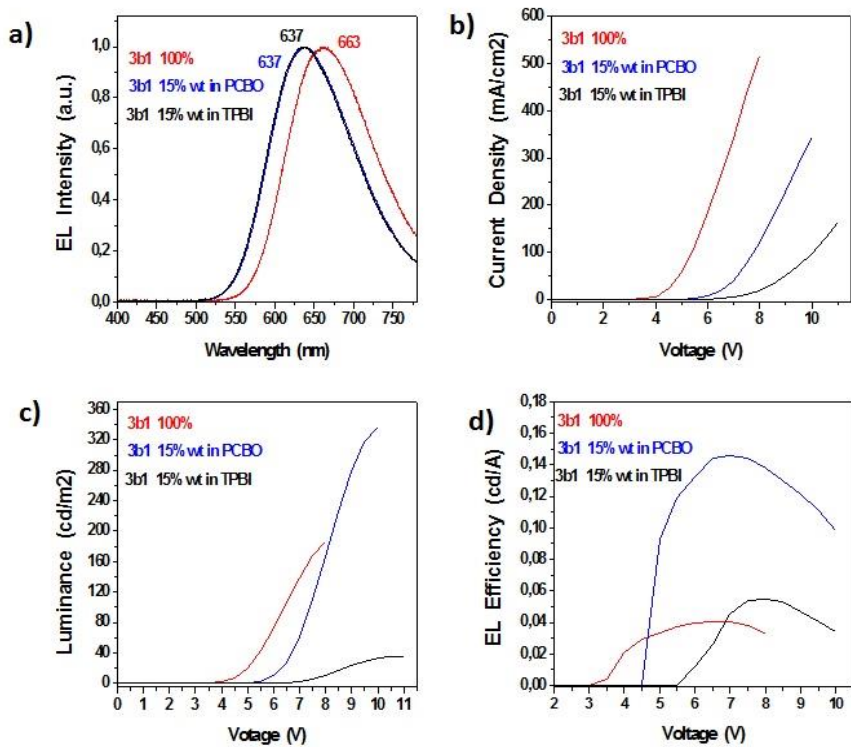


Figure S69. Electrical characterization of 3b1 based OLEDs.

5.5 Structural data of 1a5.

Table S4. Crystal Data and Structure Refinement for Compound A.

compound	A
formula	C ₄₈ H ₃₀ O ₂ S ₆
FW	831.08
Crystal symmetry	Monoclinic
Space group	<i>P2₁/c</i>
<i>a</i> , Å	10.748(5)
<i>b</i> , Å	8.699(4)
<i>c</i> , Å	25.388(11)
<i>α</i> , °	90
<i>β</i> , °	94.919(4)
<i>γ</i> , °	90
cell volume, Å ³	2365.0(17)
<i>Z</i>	2
D _c , Mg m ⁻³	1.167
μ(Mo Kα), mm ⁻¹	0.324
<i>F</i> (000)	860
crystal size, mm	0.20×0.10×0.05
<i>T</i> , K	296
<i>θ</i> limits, °	1.61-24.87
Refl. collected	12171
unique refl. (<i>R</i> _{int})	3922 [R(int) = 0.0844]
GooF on <i>F</i> ²	0.892
<i>R</i> ₁ (<i>F</i>) ^a , <i>wR</i> ₂ (<i>F</i> ²) ^b	0.0753, 0.1697
largest diff. peak and hole, e Å ⁻³	0.251 and -0.297

^a $R_1 = \sum ||F_o| - |F_c| / \sum |F_o|$. ^b $wR_2 = [\sum w(F_o^2 - F_c^2)^2 / \sum w(F_o^2)^2]^{1/2}$, where $w = 1/[\sigma^2(F_o^2) + (aP)^2 + bP]$ where $P = (F_o^2 + 2F_c^2)/3$. CCDC number 1445836 contains the supplementary crystallographic data for this paper. These data can be obtained free of charge from The Cambridge Crystallographic Data Center via www.ccdc.cam.ac.uk/data_request/cif.

REFERENCES

- [1] ^{a)} H. D. Magurudeniya, P. Huang, S. S. Gunathilake, E. A. Rainbolt, M. C. Biewer, M. C. Stefan, *Encyclopedia of Polymer Science and Technology*, John Wiley & Sons, Inc., Chichester, UK, **2014**, p. 1; ^{b)} T. P. Huynha, P. S. Sharma, M. Sosnowska, F. D'Souza, W. Kutnera, *Prog. Polym. Sci.*, **2015**, 47, 1; ^{c)} M. E. Cinar, T. Ozturk, *Chem. Rev.*, **2015**, 115, 3036; ^{d)} L. Dou, Y. Liu, Z. Hong, G. Li, Y. Yang, *Chem. Rev.*, **2015**, 115, 12633; ^{e)} M. Iyoda, H. Shimizu, *Chem. Soc. Rev.*, **2015**, 44, 6411; ^{f)} S. C. Rasmussen, S. J. Evenson, C. B. McCausland, *Chem. Commun.*, **2015**, 51, 4528; ^{g)} G. Barbarella, F. Di Maria, *Acc. Chem. Res.*, **2015**, 48, 2230; h) *Thiophenes (Topics in Heterocyclic Chemistry)* (Ed: J. A. Joule), Springer International Publishing, Switzerland **2015**; ⁱ⁾ *Handbook of Thiophene-Based Materials: Applications in Organic Electronics and Photonics* (Eds: I. Perepichka, D. F. Perepichka), John Wiley & Sons, Ltd, Chichester, UK, **2009**.
- [2] ^{a)} V. Malytskyi, J. J. Simon, L. Patrone, J. M. Raimundo, *RSC Adv.*, **2015**, 5, 354; ^{b)} P. Qin, H. Kast, M. K. Nazeeruddin, S. M. Zakeeruddin, A. Mishra, P. Bäuerle, M. Grätzel, *Energy Environ. Sci.*, **2014**, 7, 2981.
- [3] ^{a)} K. Takimiya, I. Osaka, I. T. Mori, M. Nakano, *Acc. Chem. Res.*, **2014**, 47, 1493; ^{b)} R. S. Ashraf, A. J. Kronemeijer, *Chem. Commun.*, **2012**, 48, 3939; ^{c)} A. Facchetti, *Chem. Mater.*, **2011**, 23, 733.
- [4] ^{a)} L. B. G. Johansson, R. Simon, G. Bergström, M. Eriksson, S. Prokop, C. F. Mandenius, F. L. Heppner, A. K. O. Åslund, K. P. R. Nilsson, *Biosens. Bioelectron.*, **2015**, 63, 204; ^{b)} J. Ries, V. Udayar, A. Soragni, S. Hornemann, K. P. R. Nilsson, R. Riek, C. Hock, H. Ewers, A. A. Aguzzi, L. Rajendran, *ACS Chem. Neurosci.*, **2013**, 4, 1057.
- [5] M. Dal Molin, Q. Verolet, A. Colom, R. Letrun, E. Derivery, M. Gonzalez-Gaitan, E. Vauthey, A. Roux, N. Sakai, S. Matile, *J. Am. Chem. Soc.*, **2015**, 137, 568.
- [6] ^{a)} J. Nakayama, Y. Sugihara, *Sulfur Rep.*, **1997**, 19, 349; ^{b)} A. Bongini, G. Barbarella, M. Zambianchi, C. Arbizzani, M. Mastragostino, *Chem. Commun.*, **2000**, 439; ^{c)} T. Thiemann, K. G. Dongol, *J. Chem. Res.*, **2002**, 7, 0701.
- [7] ^{a)} J. Nakayama, H. Nagasawa, Y. Sugihara, A. Ishii, *J. Am. Chem. Soc.*, **1997**, 119, 9077; ^{b)} J. Nakayama, *Sulfur Rep.*, **2000**, 22, 123; ^{c)} J. Nakayama, Y. Sano, Y. Sugihara, A. Ishii, *Tetrahedron Lett.*, **1999**, 40, 3785.
- [8] A. Stoffregen, M. Heying, W. S. Jenks, *J. Am. Chem. Soc.*, **2007**, 129, 15746.
- [9] ^{a)} M. M. Oliva, J. Casado, J. T. L. Navarrete, S. Patchkovskii, T. Goodson III, M. R. Harpham, J. S. S. deMelo, E. Amir, S. Rozen, *J. Am. Chem. Soc.*, **2010**, 132, 6231; ^{b)} G. Barbarella, L. Favaretto, M. Zambianchi, O. Pudova, C. Arbizzani, A. Bongini, M. Mastragostino, *Adv. Mater.*, **1998**, 10, 551; ^{c)} G. Barbarella, L. Favaretto, G. Sotgiu, M. Zambianchi, L. Antolini, O. Pudova, A. Bongini, *J. Org. Chem.*, **1998**, 63, 5497; ^{d)} L. Antolini, E. Tedesco, G. Barbarella, L. Favaretto, D. Casarini, G. Gigli, R. Cingolani, *J. Am. Chem. Soc.*, **2000**, 122, 9006; ^{e)} G. Barbarella, L. Favaretto, G.

- Sotgiu, M. Zambianchi, A. Bongini, C. Arbizzani, M. Mastragostino, M. Anni, G. Gigli, R. Cingolani, *J. Am. Chem. Soc.*, **2000**, 122, 11971.
- [10] ^{a)} J. Biwang, T. D. Tilley, *J. Am. Chem. Soc.*, **1999**, 121, 9744; ^{b)} M. C. Su, J. Biwang, T. D. Tilley, *Angew. Chem. Int. Ed.*, **2000**, 39, 2870.
- [11] ^{a)} S. Rozen, Y. Bareket, *J. Org. Chem.*, **1997**, 62, 1457; ^{b)} E. Amir, S. Rozen, *Angew. Chem. Int. Ed.*, **2005**, 44, 7374; ^{c)} N. Shefer, T. Harel, S. Rozen, *J. Org. Chem.*, **2009**, 74, 6993; ^{d)} S. Rozen, *Acc. Chem. Res.*, **2014**, 47, 2378.
- [12] ^{a)} E. J. Dell, B. Capozzi, J. Xia, L. Venkataraman, L. M. Campos, *Nat. Chem.*, **2015**, 7, 209; ^{b)} E. Busby, J. Xia, Q. Wu, J. Z. Low, R. Song, J. R. Miller, X. Y. Zhu, L. M. Campos, M. Y. Sfeir, *Nat. Mater.*, **2015**, 14, 426; ^{c)} B. Capozzi, J. Xia, O. Adak, E. J. Dell, Z. F. Liu, J. C. Taylor, J. B. Neaton, L. M. Campos, L. Venkataraman, *Nat. Nanotechnol.*, **2015**, 10, 522; ^{d)} E. J. Dell, L. M. Campos, *J. Mater. Chem.*, **2012**, 22, 12945.
- [13] N. Ghofraniha, I. Viola, F. Di Maria, G. Barbarella, G. Gigli, L. Leuzzi, C. Conti, *Nat. Commun.*, **2015**, 6, 6058.
- [14] ^{a)} G. Barbarella, F. Di Maria, *Acc. Chem. Res.*, **2015**, 48, 2230; ^{b)} I. E. Palamà, F. Di Maria, S. D'Amone, G. Barbarella, G. Gigli, *J. Mater. Chem. B*, **2015**, 3, 151; ^{c)} P. Ji, X. Xu, S. Ma, J. Fan, Q. Zhou, X. Mao, C. Qiao, **2015**, 6, 1010; ^{d)} I. E. Palamà, F. Di Maria, I. Viola, E. Fabiano, G. Gigli, C. Bettini, G. Barbarella, *J. Am. Chem. Soc.*, **2011**, 133, 17777.
- [15] C. Santato, L. Favaretto, M. Melucci, A. Zanelli, M. Gazzano, M. Monari, D. Isik, D. Banville, S. Bertolazzi, S. Loranger, F. Cicoira, *J. Mater. Chem.*, **2010**, 20, 669.
- [16] ^{a)} J. Lindley, T. Mason, *J. Chem. Soc. Rev.*, **1987**, 16, 275; ^{b)} P. Arsenyan, E. Paegle, S. Belyakov, *Tetrahedron Lett.*, **2010**, 51, 205.
- [17] P. Pouzet, P. I. Erdelmeier, D. Ginderow, J. P. Mornon, P. Dansette, D. Mansuy, *J. Chem. Soc., Chem. Commun.*, **1995**, 473.
- [18] G. Barbarella, L. Favaretto, G. Sotgiu, M. Zambianchi, C. Arbizzani, A. Bongini, A. M. Mastragostino, *Chem. Mater.*, **1999**, 11, 2533.
- [19] S. Raasch, in *Chemistry of Heterocyclic Compounds, Thiophene and its Derivatives*, Vol. 44 (Ed: S. Gronowitz), Wiley, New York **1985**, p. 871.
- [20] S. Rozen, Y. Bareket, *J. Org. Chem.* **1997**, 62, 1457.
- [21] C. C. C. Johansson Seechurn, M. O. Kitching, T. J. Colacot, V. Snieckus, *Angew. Chem. Int. Ed.*, **2012**, 51, 5062.
- [22] G. Barbarella, L. Favaretto, A. Zanelli, G. Gigli, M. Mazzeo, M. Anni, A. Bongini, *Adv. Funct. Mater.*, **2005**, 15, 664.
- [23] E. Lukevics, P. Arsenyan, S. Belyakov, O. Pudova, *Chem. Heterocycl. Compd.*, **2002**, 38, 632.
- [24] T. M. Pappenfus, J. H. Melby, B. B. Hansen, D. M. Sumption, S. A. Hubers, D. E. Janzen, P. C. Eubank, K. A. McGee, M. W. Burand, K. R. Mann, *Org. Lett.*, **2007**, 9, 3721.

- [25] ^{a)} C. M. Cardona, W. Li, A. E. Kaifer, D. Stockdale, G. C. Bazan, *Adv. Mater.*, **2011**, 23, 2367; ^{b)} S. Trasatti, *Pure Appl. Chem.*, **1986**, 58, 955; ^{c)} G. Gratzner, J. Kuta, *Pure Appl. Chem.*, **1984**, 56, 461.
- [26] E. Bundgaard, F. C. Krebs, *Sol. Energy Mater. Sol. Cells*, **2007**, 91, 954985.
- [27] ^{a)} L. Echegoyen, L. E. Echegoyen, *Acc. Chem. Res.*, **1998**, 31, 593; ^{b)} P. Damlin, M. Hätönen, S. E. Domínguez, T. Ääritalo, T. H. Kivelä, C. Kvarnström, *RSC Adv.*, **2014**, 4, 8391
- [28] E. Busby, J. Xia, J. Z. Low, Q. Wu, J. Hoy, L. M. Campos, M. Y. Sfeir, *J. Phys. Chem. B*, **2015**, 119, 7644.
- [29] M. A. Baldo, S. Lamansky, P. E. Burrows, M. E. Thompson, S. R. Forrest, *Appl. Phys. Lett.*, **1999**, 75, 4.
- [30] ^{a)} J. Kalinowski, W. Stampor, M. Cocchi, D. Virgili, V. Fattori, P. Di Marco, *Chem. Phys.*, **2004**, 297, 39; ^{b)} F. B. Dias, S. Pollock, G. Lars, L. O. Pålsson, A. Monkman, I. I. Perepichka, I. F. Perepichka, M. Tavasli, M. R. Bryce, *J. Phys. Chem. B*, **2006**, 110, 19329.
- [31] D. Natali, M. Caironi, *Adv. Mater.*, **2012**, 24, 1357.
- [32] H. Sirringhaus, *Adv. Mater.*, **2005**, 17, 2411.
- [33] ^{a)} J. E. Cochran, E. Amir, K. Sivanandan, S. Y. Ku, J. H. Seo, B. A. Collins, J. R. Tumbleston, M. F. Toney, H. Ade, C. J. Hawker, M. L Chabiny, *J. Polym. Sci., Part B: Polym. Phys.*, **2013**, 51, 48; ^{b)} Y. R. Shin, W. H. Lee, J. B. Park, H. Kim, S. K. Lee, W. S. Shin, D. H. Hwang, I. N. Kang, *J. Polym. Sci., Part A: Polym. Chem.*, **2016**, 54, 498.
- [34] ^{a)} A. R. Murphy, J. M. J. Fréchet, *Chem. Rev.*, **2007**, 107, 1066; ^{b)} A. Facchetti, *Chem. Mater.*, **2011**, 23, 733.
- [35] L. L. Chua, J. Zaumseil, J. F. Chang, E. C. W. Ou, P. K. H. Ho, H. Sirringhaus, R. H. Friend, *Nature*, **2005**, 434, 194.
- [36] L. Antolini, E. Tedesco, G. Barbarella, L. Favaretto, G. Sotgiu, M. Zambianchi, D. Casarini, G. Gigli, R. Cingolani, *J. Am. Chem. Soc.*, **2000**, 122, 9006.
- [37] ^{a)} E. Amir, K. Sivanandan, A. Cochran, *Polym. Chem.*, **2011**, 49, 1933; ^{b)} M. Pasini, S. Destri, W. Porzio, C. Botta, U. Giovanella, *J. Mater. Chem.*, **2003**, 13, 807.
- [38] L. Favaretto, G. Barbarella, I. Räu , F. Kajzar, S. Caria, M. Murgia, R. Zamboni, *Opt. Express*, **2009**, 17, 2557.
- [39] F. B. Dias, K. N. Bourdakos, V. Jankus, K. C. Moss, K. T. Kamtekar, V. Bhalla, J. Santos, M. R. Bryce, A. P. Monkman, *Adv. Mater.*, **2013**, 25, 3707.
- [40] F. Denizot, R. Lang, *J. Immunol. Methods*, **1986**, 89, 271.
- [41] ^{a)} L. A. Constantin, E. Fabiano, F. Della Sala, *Phys. Rev. B*, **2012**, 86, 035130; ^{b)} L. A. Constantin, E. Fabiano, F. Della Sala, *J. Chem. Theory Comput.*, **2013**, 9, 2256; ^{c)} L. A. Constantin, E. Fabiano, F. Della Sala, *Phys. Rev. B*, **2013**, 88, 125112.

- [42] ^{a)} J. Contreras-Garcia, E. R. Johnson, S. Keinan, R. Chaudret, J. P. Piquemal, D. N. Beratan, W. Yang, *J. Chem. Theory Comput.*, **2011**, 7, 625; ^{b)} J. Contreras-Garcia, W. Yang, E. R. Johnson, *J. Phys. Chem. A*, **2011**, 115, 12983.
- [43] P. C. Mondal, N. Kantor-Uriel, S. P. Mathew, F. Tassinari, C. Fontanesi, R. Naaman, *Adv. Mater.*, **2015**, 27, 1924.
- [44] ^{a)} S. Arnaboldi, T. Benincori, R. Cirilli, W. Kutner, M. Magni, P. R. Mussini, K. Noworyta, F. Sannicolò, *Chem. Sci.*, **2015**, 6, 1706; ^{b)} F. Sannicolò, S. Arnaboldi, T. Benincori, V. Bonometti, R. Cirilli, L. Dunsch, W. Kutner, G. Longhi, P. R. Mussini, M. Panigati, M. Pierini, S. Rizzo, *Angew. Chem. Int. Ed.*, **2014**, 53, 2623.
- [45] SMART & SAINT Software Reference Manuals, version 5.051 (Windows NT Version), Bruker Analytical X-ray Instruments Inc., Madison, WI **1998**.
- [46] G. M. Sheldrick, *SADABS, Program for Empirical Absorption Correction*, University of Göttingen, Germany, **1996**.
- [47] M. C. Burla, R. Caliendo, M. Camalli, B. Carrozzini, G. L. Cascarano, L. De Caro, C. Giacovazzo, G. Polidori, R. Spagna, *J. Appl. Crystallogr.*, **2005**, 38, 381.
- [48] G. M. Sheldrick, *SHELXTLplus (Windows NT Version) Structure Determination Package, Version 5.1.*, Bruker Analytical X-ray Instruments Inc., Madison, WI, USA, **1998**.
- [49] A. L. Spek, *Acta Crystallogr.*, **2009**, D65, 148.
- [50] C. F. Macrae, I. J. Bruno, J. A. Chisholm, P. R. Edgington, P. McCabe, E. Pidcock, L. Rodriguez-Monge, R. Taylor, J. van de Streek, P. A. Wood, *J. Appl. Crystallogr.*, **2008**, 41, 466.
- [51] J. C. De Mello, F. Wittmann, R. H. Friend, *Adv. Mater.*, **1997**, 9, 230.

CHAPTER III POLYTHIOPHENE BASED NANOPARTICLES FOR BIOPHOTONICS

In this chapter the preparation and characterization of poly(3-hexylthiophene) and properly functionalized polythiophenes nanospheres in the absence of surfactants is reported.

Three different studies were carried out:

- I. *Sterile poly(3-hexylthiophene) nanoparticles for biophotonics in living cells.* *A new synthetic strategy to prepare poly(3-hexylthiophene) nanospheres (P3HT-NPs) in sterile conditions was developed. It is demonstrated that P3HT-NPs have well-ordered morphology, high colloidal stability in water, excellent biocompatibility and are easily internalised by living cells. Electrophysiology and calcium imaging experiments demonstrate that cellular physiological functions are fully preserved.*

Published as:

E. Zucchetti, **M. Zangoli**, I. Bargigia, C. Bossio, F. DiMaria, G. Barbarella, C. D'Andrea, G. Lanzani and M. R. Antognazza.

J. Mater. Chem. B, 2017, 5, 565-574.

- II. *Semiconducting polymer are light nanotransducers in eyeless animals.* *It is shown that P3HT-NPs are uptaken within eyeless freshwater polyps Hydra vulgaris and are fully biocompatible. The nanospheres are able to modify the light sensitivity of the animals enhancing the contraction events of the polyp body and changing the transcriptional activation of the opsin3-like gene.*

Published as:

C. Tortiglione, M. R. Antognazza, A. Tino, C. Bossio, V. Marchesano, A. Bauduin, **M. Zangoli**, S. V. Morata and G. Lanzani.

Sci. Adv., 2017, 3:e1601699.

- III. *Engineering thiophene-based nanoparticles to induce phototransduction in live cells under illumination.* *Amine-reactive fluorescent nanospheres with pendant N-succinimidyl-ester groups (NPs-NHS) are prepared from 'ad hoc' functionalized polythiophenes. It is shown that the NPs-NHS remain docked on the cell membrane - as result of the amidic bond formation - and are capable to polarize the cell membrane under illumination.*

Published as:

M. Zangoli, F. Di Maria, E. Zucchetti, M. R. Antognazza, G. Lanzani, R. Mazzaro, F. Corticelli, M. Baroncini and G. Barbarella.

Nanoscale, 2017, 9, 9202-9209.

I. INTRODUCTION

Conjugated polymer nanoparticles (CP-NPs) are multifunctional nanoscale materials with huge potential in biotechnology applications ^[1]. CP-NPs are obtained by fairly simple synthetic methods and their surface can be easily functionalized to obtain specific properties like bio-recognition for labeling, drug delivery or selective docking. They typically have good photostability and low toxicity due to the intrinsic affinity of their carbon based chemical structure with that of bio molecules ^[2]. Furthermore CP-NP have large optical absorption cross section, providing easy access to optical excitation. The molecular-like nature of their electronic excited states implies a totally different correlation between size and properties as compared to inorganic nanocrystals. In particular, quantum confinement is not an issue, while morphology and surface properties play a crucial role. For this reason the strategies to achieve control and engineering of CP-NP are rather specific and partially to be explored. In the latest decade, several fluorescent conjugated polymers have been employed for live cell imaging, including, among the others, polyfluorene ^[3], polyphenylene ethynylene and several polyphenylenevinylene derivatives like MEH-PPV, BEHP-PPV and MDMO-PPV ^[4]. Recently, for instance, four conjugated polymers excitable at the same wavelength but with blue, green, yellow and red emission were synthesized and labeled with different antibodies, demonstrating high specificity in tumor cells detection ^[5]. Another interesting application of CP-NPs is in the field of drug delivery. Drugs can be chemically encapsulated by covalent linking to polymers, and released in a controlled way into targeted cells or tissues. Polymer-drug conjugates can improve drug solubility and targeting, facilitate higher drug payloads and prolong the drug circulation time. Drug delivery can be also achieved with high spatial selectivity, through interaction with the plasma membrane, due to excellent CP-NPs endocytosis efficiency ^[6]. In some cases, CP-NPs combine both drug delivery and imaging ^[3]. Carbon-based materials can also behave as exogenous components that bestow light sensitivity to the living tissue and enable light control of physiological functions ^[7]. Similarly, polypyrrole NPs were employed as light sensitive, photo-thermal transducers, able to release glutamate upon NIR excitation ^[8]. In this work, we report the preparation and characterization of NPs obtained from poly(3-hexyl)thiophene (P3HT) and explore their suitability for application in living cells. P3HT is a prototype conjugated polymer, among the most studied in its class, with proposed applications in photo-detection, photonics and photovoltaics. Recently it has been shown that P3HT is highly bio compatible ^[9] and can transduce a light signal into a cell stimulus in several circumstances ^[10] and cell types or tissues ^[11]. Its application as the active layer in a retina prosthesis to be implanted in blind animals is under investigation. These findings provided us with the foundation to the attempt of a downscaling of polymeric films to NPs for a new generation of bio-actuators that can be delivered to the biological sample, both *in vitro* and *in vivo*, avoiding complex surgery and allowing specific targeting. P3HT-NPs of size in the range 100-600 nm, with excellent colloidal stability in aqueous solution in the absence of surfactants, were prepared entirely under sterile conditions.

We show that once added to the culturing medium P3HT-NPs are efficiently internalized by Human Embryonic Kidney (HEK-293) cells, and that their presence does not impact neither on the morphology, nor on the viability, nor on the physiological activity of the living systems. Based on time resolved photoluminescence data we show that the spectral properties and dynamics of the particle emission are mainly preserved, with slight modifications ascribed to the specific contribution from the P3HT-NPs surface.

II. RESULTS AND DISCUSSION

2.1 Preparation and characterization of sterile P3HT-NPs. P3HT-NPs were prepared from preformed poly(3-hexylthiophene) synthesized and characterized as described in Experimental Section. Since attempts to prepare P3HT-NPs starting from commercial polymer were unsuccessful, P3HT was synthesized by oxidative polymerization of 3-hexyl-thiophene with ferric chloride according to a known procedure^[12] (Figure S1). Repeated preparations showed reproducibility in the characteristics of the polymer, namely regioregularity (as estimated from ¹H NMR, see Figure S1, panel c), polydispersity and spectroscopic features. The polymer displayed good solubility in common organic solvents. The NPs were obtained from freshly prepared P3HT using the reprecipitation technique (solvent displacement method, Figure 1a)^[13]. No surfactants were employed. Importantly, the whole process was carried out in sterile conditions using a laminar flow hood, sterilized laboratory glassware and water. Differential centrifugation, carried out employing sterilized centrifuge tubes, allowed to separate the NPs into fractions of different size. Two fractions were selected for this work, characterized by two different hydrodynamic diameters (HD, 148 ± 18 nm and 344 ± 60 nm) and low polydispersity indexes (PDI, 0.015 and 0.03 for 148 nm and 344 nm -sized NPs, respectively), which indicates a quite narrow particle size distribution, as determined by dynamic light scattering (DLS) measurements (Figure 1b). Standard deviation (SD) of the NPs HD values has been calculated according to the relationship $PDI = (SD / HD)^2$. Stability of P3HT-NPs, which may be seriously affected by counter-ions in the solution, screening the NPs surface charge^[14], was assessed by Z-potential measurements. Solubility and stability in water are actually key-parameters for any targeted biological application. A major limitation of the most widely studied inorganic nanomaterials for bio-imaging, such as inorganic quantum dots and magnetic NPs is that they tend to be insoluble in water and require some kind of phase-transfer treatment or encapsulation. Similar issues have been partially solved in CP-NPs by covalent linking with ionic side groups, grafting on hydroxyl side groups, use of surfactants, encapsulation within micelles and loading with polyethylene glycol (PEG)^[4a]. In P3HT-NPs, values lower than -30 mV (-30.44 mV and -36.84 mV for 148 nm and 344 nm -sized NPs, respectively) were obtained by Z-potential measurements for both NPs populations, thus indicating intrinsically good stability in the aqueous environment. The control of NPs morphology is another, essential part of the preparation of particles suspension. In particular, synthesis of geometrically isotropic polymer micro- or submicro- spheres, with a well-defined surface topography, has been rarely reported so far, since conjugated polymers naturally tend to anisotropically crystallize, due to their rigid and planar

backbone ^[15]. Figure 1c shows representative Scanning Electron Microscopy (SEM) images of the two selected P3HT-NPs fractions. NPs were cast on top of a silicon substrate and quickly dried by nitrogen. The isolated spots are due to individual NPs or small clusters generated by self-assembly process during the process of solvent evaporation. As expected, average spheres size is slightly lower than averaged values obtained by DLS, due to the absence of the hydration layer ^[16]. In addition, one should appreciate the very well-defined topology and the surface smoothness, which are relevant also for other applications, like the recently reported realization of polymer, fluorescent micro-resonators ^[17].

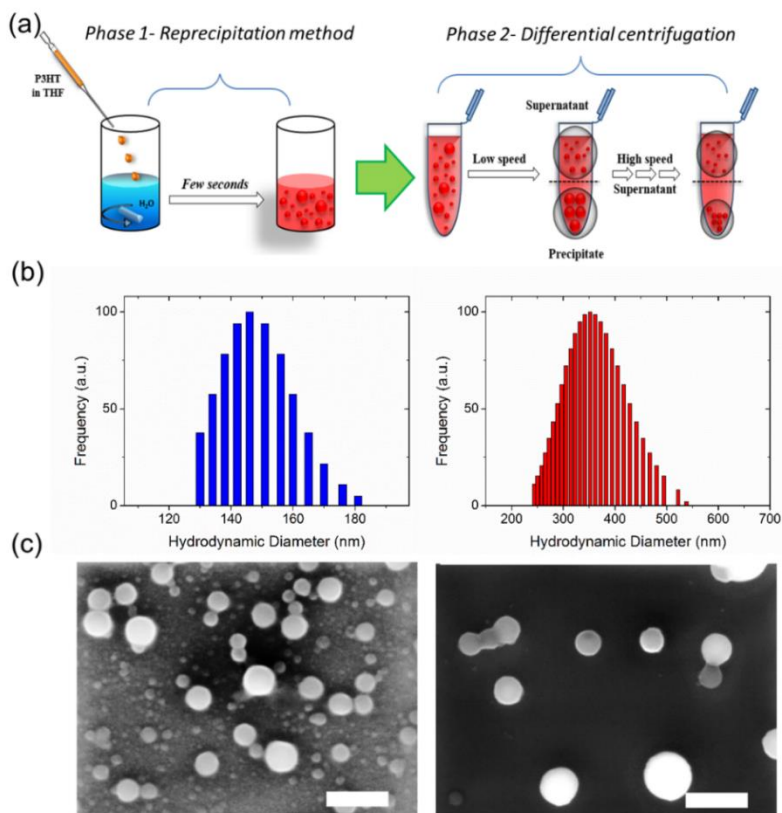


Figure 1. (a) General scheme for the preparation of sterile P3HT NPs, by use of reprecipitation and differential centrifugation methods. (b) Dynamic Light Scattering (DLS) and zeta-potential data of two different subpopulations of P3HT-NPs, of average diameter 148 ± 18 nm (left panel) and 344 ± 60 nm (right panel), calculated over 3 independent measurements. (c) SEM images of 148 nm- and 344 nm- sized (left and right panels, respectively). Scale bar, 500 nm.

Figure 2 shows the UV-VIS absorption and continuous-wave photoluminescence (CW-PL) spectra of P3HT-NPs suspensions in water. With respect to the absorption spectrum of the P3HT solution (Figure S1b), the NPs suspensions show broader spectra, probably caused by a distribution of chain packing configurations and chain conformations, and a red shift of the main peak, increasing with particle size (approximately 0.30 eV and 0.52 eV for 148 nm and 344 nm-sized NPs, respectively). This is ascribed to the different dielectric screening in the aggregate with respect to the solution and possibly to the flattening of the chain conformation. Formation of aggregates, enhancing inter- and intra-chain interactions, has been often considered to explain similar size-dependent red-shifts previously observed in other types of CP-NPs^[18]. In the planar conformation the enhanced π -conjugation leads to a smaller electronic gap. Scattering of the colloidal suspension is evident in the below gap region and contributes a background increasing at shorter wavelengths. CW-PL band further moves to lower energies respect to the P3HT solution, but differently from the absorption spectra the observed red shift does not increase upon increasing the particle size (about 0.22 eV for both NPs sizes). An apparent Stokes shift of about 0.54 eV and 0.34 eV is observed for the smallest and the largest NPs, respectively. All these features are consistent with spectral migration and emission occurring from lower energy, planar chains. This may occur either by planarization of the chain conformation in the excited state, driven by the quinoid electronic pattern that stiffens the inter ring torsion, or by energy transfer to planar chain^[19]. Last but not least, some re-absorption of the blue side PL cannot be ruled out. This is especially true for the larger aggregate that shows some overlap between emission and absorption spectra.

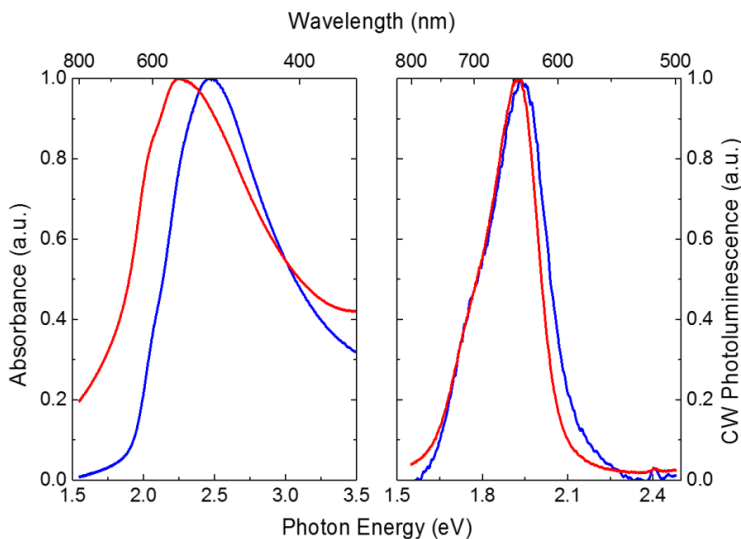


Figure 2. Normalized UV-Visible absorption and CW-PL spectra of P3HT NPs in water suspension (148 nm-sized in blue, 344 nm-sized in red). Fluorescence emission excitation wavelength, 470 nm.

2.2 Effect of P3HT-NPs on cell viability and physiology. The possibility to use P3HT-NPs for biotechnology applications is first assessed by *in vitro* cytotoxicity studies. Human Embryonic Kidney (HEK-293) cells are used here as a simple and reliable biological model, in line with several studies employing this cell line for testing different nanosystems, e.g. polymer particles [20], aluminum oxide nanorods [21] and magnetic nanoparticles [22].

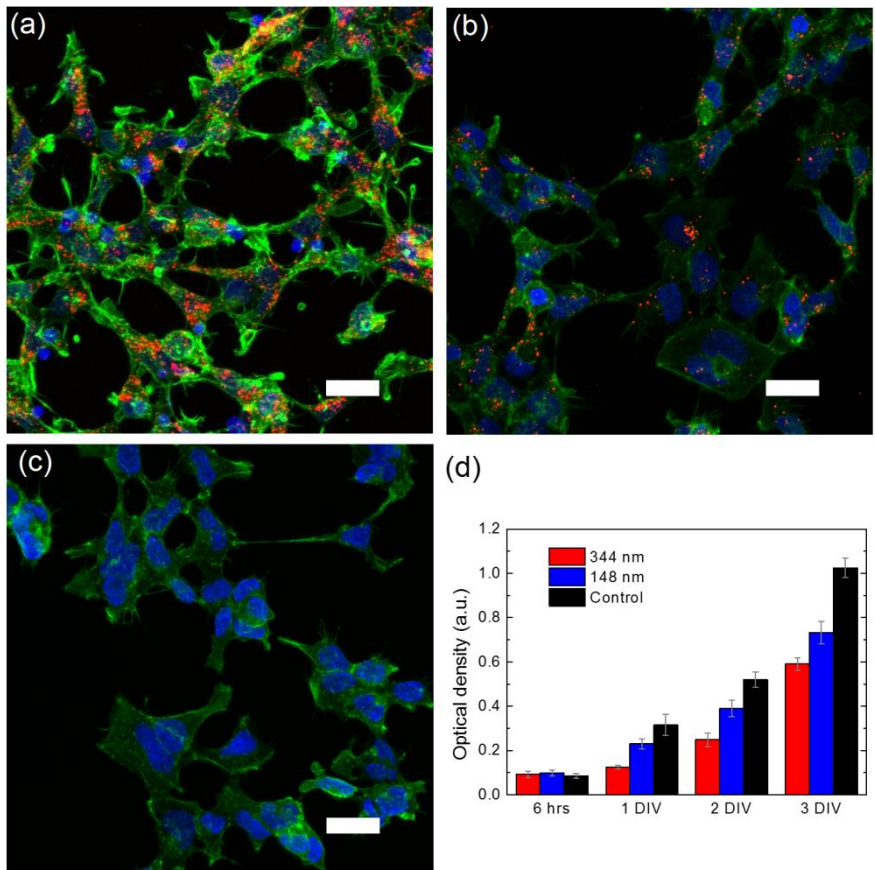


Figure 3. Fluorescence imaging of HEK-293 cells loaded with P3HT-NPs (panels a and b) and stained with DAPI (nuclei, blue) and Phalloidin (cytoskeleton, green), as compared to control cell cultures (panel c). In red the emission from P3HT NPs. Scale bar, 30 μ m. Panel (d) reports the MTT assay for cell growth up to 3 days in-vitro for treated and non-treated cell cultures (N=10).

Sterile NPs dispersions were mixed with growth media, added to HEK-293 cell cultures during plating and incubated with cells for 24 hours at 37°C. Finally, samples were washed 3 times with

a Phosphate Buffer Solution (PBS) to remove excess of NPs. Suitable NPs concentration was preliminarily assessed, within the range 10 - 100 $\mu\text{l/ml}$, by finding a good compromise between maximization of NPs cellular uptake and evident detrimental effects on cell morphology, as evidenced by Fluorescence Imaging experiments (Figure S2 in the SI section). We adjusted the dilution of the NPs water dispersion in order to work at fixed optical density, of 0.22 and 0.1 for 344 nm-sized and 148 nm-sized NPs, respectively. Figure 3 shows representative confocal images of HEK-cells after 24-hours incubation with P3HT-NPs and subsequent fixation with paraformaldehyde (see details in the Methods section). Actin filaments were stained with fluorescently conjugated phalloidin (green), cell nuclei with DAPI (blue), while NPs emission can be seen in the red channel. Importantly, neither cellular nor nuclear morphology of cultures treated either with smaller NPs (Figure 3a) or with bigger ones (Figure 3b) show relevant changes with respect to untreated, control samples (Figure 3c), suggesting little or no toxicological effect. In order to determine whether the NPs were internalized into the cells or they were simply anchored to the external side of the cellular membrane, optical sections were measured in incremental steps of few hundreds of nm from the lower, substrate surface up to the upper, cell surface (SI, Figure S3). The appearance of red emission spots not only around the cell peripheral regions but also around the center suggests that P3HT-NPs have been efficiently internalized within the cytosol. However, they do not cross the nuclear membrane, and appear to be distributed around the perinuclear region. P3HT-NPs cytotoxicity was evaluated by measuring cellular proliferation through the MTT method. The assay relies on the capability of living cells to metabolize/reduce a water-soluble tetrazolium salt (3-(4',5'-dimethylthiazol-2'-yl)-2,5-diphenyl-2H-tetrazolium hydrobromide, MTT) into a water insoluble formazan product, which has a characteristic purple color. The optical absorption of formazan is thus considered a clear indicator of cell viability and capability to proliferate, being proportional to the number of living cells. Figure 3d shows the formazan optical absorption recorded in treated and untreated samples at four different time points, 6 hours, 1, 2 and 3 days after incubation, by administration of 148 nm-size and 344 nm-size NPs at 50 $\mu\text{l/ml}$ and 60 $\mu\text{l/ml}$ concentration. The test indicates that cell proliferation increases with increasing incubation time. The presence of NPs leads in general to a reduced cell proliferation with respect to untreated samples, more evident in the case of larger particles. Notwithstanding this, cell growth is not at all compromised, indicating good biocompatibility of synthesized P3HT-NPs. Absence of relevant toxicity effects is confirmed by the analysis of physiological properties of cells incubated with P3HT-NPs. Calcium imaging and patch-clamp electrophysiology have been used to evaluate the cell functionality and the membrane electrical properties (Figure 4). It is well known that calcium ions Ca^{2+} play a major role in cellular signaling and have regulatory effects on many biochemical processes, such as enzyme activity, permeability of ions channels, activity of ion pumps, and components of the cytoskeleton^[23]. Studying alterations of calcium fluxes provides thus a direct way to distinguish between cell normal physiology and pathological conditions. Fluorescence calcium imaging, in particular, provides the most versatile and widely used method for analyzing cellular Ca^{2+} responses as a result of an extracellular stimulus. We loaded HEK-293 cell cultures with the

fluorophore Fluo-4 for 40 minutes in extracellular solution, and after two subsequent wash-outs we administrated ATP as calcium activator.

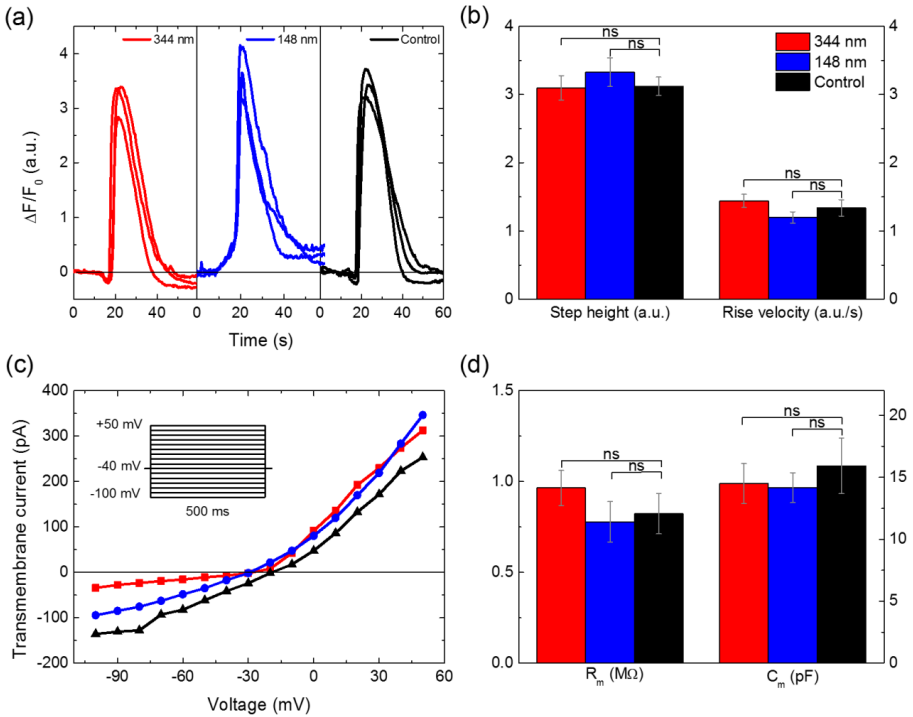


Figure 4. (a) Examples of Ca^{2+} transients evoked by ATP stimulus in HEK-293 cells treated with P3HT-NPs and untreated. (b) Amplitudes of calcium signals and rise times of calcium increase immediately after addition of ATP calculated ($N=14$, Student's t-test). (c) I-V characteristics of treated (blue and red lines, 148 nm- and 344 nm-sized NPs, respectively) and non-treated (black line) cells, extracted by voltage clamp measurements. The stimulation protocol is represented in the inset. Holding potential was fixed at -40mV . The experimental data are shown as symbols, solid lines are a guide to the eye. (d) Average values of membrane resistance and capacitance. No statistically significant difference is evidenced (Student's t-test).

Figure 4a shows three representative fluorescence dynamics $\Delta F/F_0$ obtained in control and treated samples, where F_0 is the baseline fluorescence, calculated as the pixel-averaged value of the selected region of interest (ROI) before the arrival of the stimulus, and $\Delta F = F - F_0$ is the relative change due to the administration of the stimulus. Treated and untreated cells display comparable levels of Ca^{2+} influx in response to ATP stimulation, and no specific, relevant changes due to the NPs uptake are evidenced in the fluorescence dynamics. In more detail (Figure 4b), neither the fluorescence amplitude variation nor the rise time of Ca^{2+} signal, calculated as the slope of the

linear fit of the rising component of curves between 10% and 90% of the step height, show a statistically significant difference with respect to control samples ($N = 14$, Student's *t*-test). P3HT NPs uptake may also have an impact on cell membrane electrical properties, e.g. resting membrane potential, capacitance and resistance. Strong variation in the equilibrium potential values, for instance, are related to changes in the ionic membrane permeability. The membrane capacitance (C_m), being proportional to the cell surface area, is considered a good indicator of exocytosis and/or endocytosis processes in a variety of cells [24]. Finally, changes in the electrical membrane resistance (R_m) often denote the occurrence of sub-structural changes in the cytosol organelles [25]. To analyze voltage- and time-dependence of conductance expressed by treated cells and control samples, cells are stimulated in whole cell, voltage clamp configuration by 500-ms voltage steps (holding potential, -40 mV), from -100 to 50 mV, in 10 mV increments. Representative current traces obtained in treated and control samples in response to the applied voltage are displayed in the SI section, Figure S4. Figure 4c displays the I-V characteristics extracted in the three samples sets (treated with 148 nm NPs, treated with 344 nm NPs, not treated, $N = 9$ for each set). The resting membrane potential is extracted from the intercept of the curves with the x-axis in the three cases, giving comparable values (-17.2 ± 2.1 mV for 148 nm-sized NPs; -19.1 ± 3.1 mV for 344 nm-sized NPs; -21.9 ± 1.8 mV for control samples). The membrane resistance is calculated as the inverse of the curves slopes, obtaining $R_m = 0.96 \pm 0.1$ M Ω , 0.78 ± 0.11 M Ω and 0.82 ± 0.11 M Ω for 344 nm NPs, 148 nm NPs and non treated samples, respectively (Figure 4d, left). The membrane capacitance is obtained from compensation of the transient portion of current response while a test pulse is running. Measured values are $C_m = 14.5 \pm 1.62$ pF, 14.17 ± 1.2 pF and 15.92 ± 2.24 pF for 344 nm NPs, 148 nm NPs and non-treated samples, respectively (Figure 4d, right). The data show that the most significant electrical properties of cell membrane are not significantly affected by the uptake of NPs occurred during 24-hours cell incubation. Altogether, reported experimental evidences demonstrate that the presence of P3HT-NPs does not significantly affect neither the cell morphology nor its physiological functions.

2.3 Effect of living cells on P3HT-NPs optical properties. Aiming at using P3HT-NPs as actuators or optical transducers, the study of the effect of the living cell environment on their photophysical properties is of utmost importance. To this goal, we employ time-resolved micro-fluorimetry spectroscopy, which enables to monitor fluorescence emission from P3HT-NPs (344 nm-sized) within the living cell. Both temporal and spectral features are compared with those observed in NPs dispersions in water and buffering media. In particular the study of time-resolved fluorescence provides significant information on the decay rates and relaxation dynamics which are particularly sensitive to NP environment. For comparison we first measured the fluorescence emission from P3HT-NPs suspended in ultrapure water and in a buffering medium (Krebs-Ringer-Hepes buffer, KRH). Figure 5a shows the time-integrated emission spectra of the P3HT-NPs acquired with our home-built time-resolved fluorescence set-up over an integration window of about 128 ps. In both spectra recorded from NPs suspensions in water (blue curve) and in KRH (gray curve) we can distinguish one main peak located around ~ 1.9 eV, a shoulder at higher

energies (~ 2.2 eV) and a shoulder at lower energies (~ 1.76 eV). The two spectra are virtually identical.

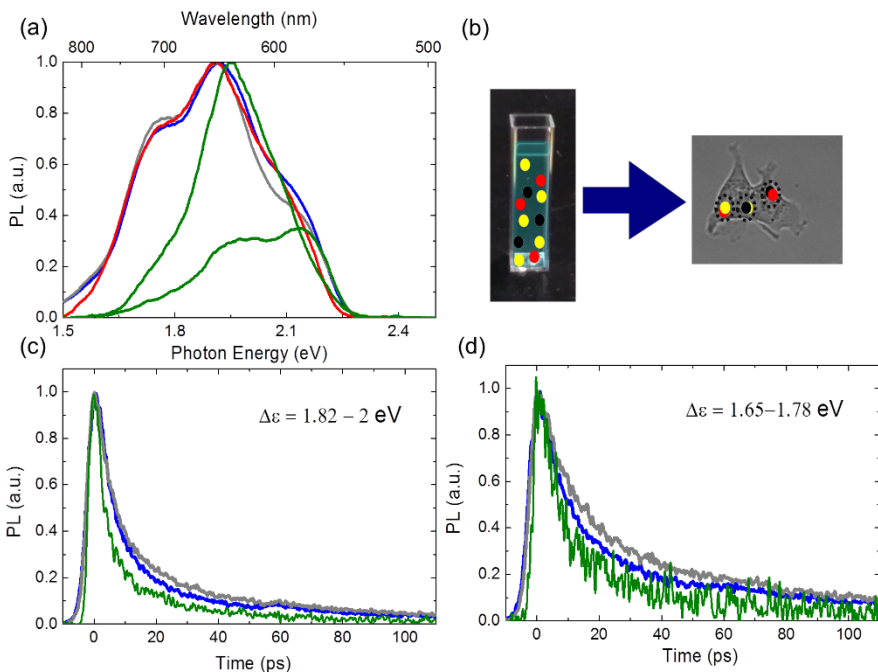


Figure 5. Time-Resolved Fluorescence spectroscopy data on P3HT-NPs. a) Time integrated spectra of NPs in suspension (water in blue, KRH in gray) and two examples of spectra obtained from inside living cells (green lines). The red line is the weighted sum of the two reported spectra obtained from NPs inside the cells and a Gaussian third component obtained fitting a Gaussian to the low energy shoulder of the spectrum of NPs in water suspension. b) Pictorial illustration of what happens when NPs are uptaken by cells and we probe different aggregates. c) Kinetic curves of suspensions (blue refers to water, gray to KRH) and of NPs (green line) inside cells for the energy interval 1.82 - 2 eV. d) Kinetic curves of suspensions (blue refers to water, gray to KRH) and of NPs (green line) inside cells for the energy interval 1.65 - 1.78 eV.

Figure 5c and 5d show the time-decay curves of NPs suspended in ultrapure water (blue curve) and in KRH (gray curve), integrated over two different energy regions: 1.82 - 2 eV and 1.65 - 1.78 eV, respectively. The decay dynamics in KRH is slightly slower, while in both media the shoulder at lower energy is longer lived with respect to the one at higher energy. This fact is consistent with the lower energy emission coming from more planar chains ^[26]. In order to investigate the effect of the intracellular environment we acquired time-resolved fluorescence spectra from NPs within the living cell using a custom micro-fluorimetry system. Figure 5a shows two representative examples of gated spectra obtained from NPs up-taken by cells (green

lines). In Supplementary Information (Figure S5) we report different spectra obtained from within the cells which differ one from the other in the relative weight of the two spectral features at higher energy (peaks at ~ 1.9 eV and ~ 2.2 eV, respectively). Beside these variations, we regularly observe the lack of the lowest energy emission in all the spectra acquired within cells. Figure 5c and 5d report (green lines) the kinetics of NP's emission inside the cells. We observe a faster decay of the P3HT-NPs emission inside the cells with respect to NPs in suspension indicating that other non-radiative paths are available. The changes of the P3HT-NPs PL spectra and dynamics when inside cells suggest an interaction of the NPs with the plasma environment or alternatively that NPs up-taken by the cell are in a different state from those in suspension. It is worth noting that P3HT-NPs spectra in KRH do not show this effect, thus, we believe that a different dielectric environment from water suspension is not enough to explain the difference. According to our interpretation the lower energy shoulder (~ 1.76 eV) is due to the emission of planarized polymer chains. We further conjecture that such chains are located at the NP's outskirts. Indeed, in the case of large aggregates of another conjugated polymer in an inert PMMA matrix, confocal time resolved spectroscopy clearly showed that the outbound region of the polymer aggregate consists of fairly free chains with respect to the core, which instead behaves like in a solid state ^[27]. Similarly, here we presume that planar or "free to planarize" chains dwell on the P3HT-NPs surface. Interaction with the cytoplasm proteins (protein corona) ^[28] or NPs aggregation upon endocytosis could provide less conformational freedom to the external chains causing the suppression of the low energy emission. Accordingly, we would expect a faster decay time, as indeed observed experimentally. Beside the low energy shoulder, the other two features at higher energy in the emission spectrum remain evident also inside the cell, yet with different relative weights with respect to the suspension. We can interpret these differences assuming that NPs are distributed in two sub-populations characterized by different spectra. Probably inside the cell there are isolated NPs or small aggregates of NPs, situations that we cannot distinguish with our spatial resolution. In this view, the emission spectrum from the suspension is the superposition of all the families in the sample, while the spectra from the living cells, originating from small aggregates or isolated NPs, single out a sub-population or a different composition of sub-populations, as pictorially described in Figure 5b. Accordingly, if we perform a weighted sum of the two spectra from inside the cell and we add the third component in the low energy region, otherwise missing, we can well reconstruct the spectrum measured in suspension (Figure 5a, red solid line). The low energy emission component is here reproduced by fitting a Gaussian to the low energy shoulder of the spectrum in water suspension.

III. CONCLUSION

In this work we report the successful synthesis of sterile P3HT-NPs with radius between 130 nm and 350 nm that are stable in water. This enables their application in biology and we test their up-take and interaction with HEK-293 cells. Our P3HT-NPs enter easily within the cytoplasm, but not in the cell nucleus, and are totally harmless for the cell life, with no effects on neither the viability nor the physiological equilibrium. Photoluminescence spectroscopy however highlights

the difference between spectra inside cells and in suspension. In particular, the low energy emission is quenched by the cytoplasm. Possible causes are the protein corona formed inside the cell, or the aggregation facilitated by the up-take process. This work demonstrates that P3HT-NPs are valid tools for both *in vitro* and *in vivo* bio photonics.

IV. METHODS

4.1 Preparation of P3HT-NPs dispersions. Colloidal P3HT-NPs were prepared by the reprecipitation method **Errore. L'origine riferimento non è stata trovata.** working in a laminar flow hood. Glassware previously sterilized at 200°C and ultrapure water sterilized in autoclave at 80°C were employed. P3HT (7 mg) was dissolved into 350 μ L of tetrahydrofuran (THF) and the resulting polymer solution was added dropwise into sterilized, ultrapure water (7 mL) under magnetic stirring. The resulting colloidal dispersion was first filtered through a filter paper to remove polymer macroscopic agglomerates, and then put in a dialysis sack (molecular weight cut off: 12000 g/mol) and subjected to dialysis against 2 L sterilized water overnight to remove organic residual solvent. Afterwards, the water colloidal suspension was centrifuged, using sterilized centrifuge tubes, at different rates for 10 min, from 2000 to 10000 rpm, separating every time the supernatant from the precipitate, to obtain a wide range of samples with different particle dimensions (from 100 nm to 600 nm). Importantly, the whole process was carried out in sterile conditions.

4.2 P3HT-NPs characterization. Dynamic Light Scattering (DLS) measurements were performed with a Nanobrook Omni Particle Size Analyzer, with a wavelength of 659 nm in back-scattering mode. Particles were dispersed in distilled water during analysis and measurements were taken at 25°C. Zeta potential measurements were performed using Smoluchowski equation. The absorption and photoemission spectra were recorded by using Perkin Elmer LAMBDA 1050 UV/Vis/NIR Spectrophotometer and HORIBA Jobin Yvon NanoLogTM, respectively. Scanning Electron Microscopy images were acquired by using Tescan MIRA 3.

4.3 Cell cultures and sample preparations. HEK-293 cells were grown in Dulbecco's Modified Eagles Medium (D-MEM, Sigma Aldrich) with 10% Fetal Bovine Serum (FBS, Euroclone) supplemented with 2 mM-glutamine (Sigma Aldrich), 100 μ g/ml streptomycin (Sigma Aldrich) and 100 U/ml penicillin (Sigma Aldrich). Cells were kept in T-75 culture flasks and maintained in incubators at 37 °C in a humidified atmosphere with 5% CO₂. After reaching 80-90% of confluence, cells were detached by incubation with 0.5% trypsin/0.2% EDTA (Sigma Aldrich) for 5 minutes and plated for further expansion and experiments. Prior to cell seeding, square 18x18 mm² glass substrates were cleaned in ultrasonic bath with successive cycles of 10 minutes in ultrapure water, acetone and isopropanol, and finally dried with N₂ gun. Samples were then thermally sterilized for 2 hours at 120°C. To promote cell adhesion, a layer of 2 μ g/ml fibronectin (from bovine plasma, Sigma Aldrich) in phosphate buffer saline (PBS, Sigma Aldrich) was deposited on the surface of the glasses and incubated for 30 minutes at 37 °C. After rinsing the

fibronectin with PBS, cells were plated in presence of their culture medium and in some cases with the addition of small amounts of NPs suspensions.

4.4 MTT assay. In order to evaluate the NPs cytotoxicity, the MTT [3-(4,5-dimethylthiazol-2-yl)-2,5-diphenyltetrazolium bromide] (Sigma Aldrich) assay was performed on HEK-293 cells. Cells were seeded in 96 well plates at a density of 2×10^4 cells/well with the NPs. Cell proliferation was evaluated after 6 h, 24 h, 48 h and 72 h of incubation. For each time point, the growing medium was replaced with RPMI without phenol red containing 0.5 mg/mL of MTT. The samples were incubated again for 3 h at 37° C in dark. Formazan salt produced by cells through reduction of MTT was then solubilized with 200 μ L of ethanol and the absorbance was read at 560 nm and 690 nm. The proliferation cell rate was calculated as the difference in absorbed intensity at 560 nm and 690 nm.

4.5 Immunofluorescence analysis. Cells grown on fibronectin-coated glass coverslips were washed twice with PBS and fixed for 20 min at RT in 4% paraformaldehyde and 4% sucrose in 0.12 M sodium phosphate buffer, pH 7.4. Fixed cells were pre-incubated for 20 min in gelatin dilution buffer (GDB: 0.02 M sodium phosphate buffer, pH 7.4, 0.45 M NaCl, 0.2% (w/v) gelatin) containing 0.3% (v/v) Triton X-100, and subsequently incubated with Phalloidin Alexa Fluor 488 conjugated in GDB for 1h at RT and finally washed with PBS, and incubated for 5 min with 1 μ M DAPI in PBS. The confocal images were acquired with Fluoview FV10i Olympus with 60x objective. The fluorescence images were analyzed with ImageJ software.

4.6 Intracellular Calcium Measurements. HEK-293 cultures were loaded for 40 min at 37 °C with 1 μ M Fluo-4 in extracellular solution (5mM HEPES; 135mM NaCl, 5.4 mM KCl, 1 mM MgCl₂, 1.8 mM CaCl₂, 10 mM glucose; pH7.4), and were washed twice with pre-warmed extracellular solution before recordings. Fluo-4 fluorescence videos were collected with Nikon Eclipse Ti provided with Analog-WDM Camera, and analyzed with Origin 8.0.

4.7 Electrophysiology. Intracellular recordings were performed with a patch-clamp setup (Axopatch 200B, Axon Instruments). HEK-293 cells were measured at 1-2 DIV in whole-cell configuration with freshly pulled glass pipettes (3-6 M Ω), filled with the following intracellular solution [mM]: 12 KCl, 125 K-Gluconate, 1 MgCl₂, 0.1 CaCl₂, 10 EGTA, 10 HEPES, 10 ATP-Na₂. The extracellular solution contained [mM]: 135 NaCl, 5.4 KCl, 5 HEPES, 10 Glucose, 1.8 CaCl₂, 1 MgCl₂. Only single HEK-293 cells were selected for recordings. All measurements were performed at room temperature. Acquisition was performed with pClamp 10 software suite (Axon Instruments) and all data were elaborated with Origin 8.0.

4.8 Time-Resolved Photoluminescence Set-Up. Time-Resolved Fluorescence Spectroscopy on NPs suspensions was performed using a tunable laser source (Ti:Sapphire laser) emitting a train of pulses each ~150 fs long at a repetition rate of 80 MHz. Samples were excited at 460 nm, frequency doubling the wavelength 920 nm of the laser. The fluorescence emitted from the samples was dispersed by a spectrometer (Princeton Instruments, USA) and then coupled to a

Streak Camera (Hamamatsu, Japan) for the acquisition of time-resolved curves. The maximum time resolution available is ~ 3 ps. For what concerns NPs inside cells, measurements were performed with a home-built micro-fluorimetry set up based on the same laser source, spectrometer and detector described above. Epiluminescence geometry was used, together with a 20x objective (Zeiss, Germany). Spot-size ~ 2.7 μm at full-width half-maximum. A dichroic mirror (550 nm long pass, Comar Optics, UK) separated the excitation wavelength (460 nm) from the emission of the sample. NPs inside cells were first imaged thanks to a CMOS camera, then a selected spot of the objective field-of-view was targeted with a focused beam and its fluorescence signal was coupled to the Streak Camera detection.

V. EXPERIMENTAL SECTION

5.1 Synthesis of poly(3-hexylthiophene). Commercial 3-hexylthiophene (1 g, 0.006 mol) was dissolved in 50 mL of distilled CHCl_3 , using dry FeCl_3 (3.87 g, 0.024 mol) suspended in 100 mL of distilled CHCl_3 as described in reference 22. The reaction mixture was stirred overnight at reflux under N_2 atmosphere. The resulting crude product was extracted with a 2% aqueous HCl solution until complete disappearance of FeCl_3 in excess, monitoring the dissociated iron in aqueous phases with ammonium thiocyanate. The resulting polymer was filtered and further purified by removing the shorter fractions soluble in methanol and acetone. Molecular weight (MW, 73600), Molar mass (M_n , 41530) and polydispersity index (PDI, 1.77) were determined by gel permeation chromatography in THF solvent with a polystyrene standard. Absorption and photoluminescence spectra both in chloroform solution and in solid film are reported in Figure S1, together with the $^1\text{H-NMR}$ spectrum.

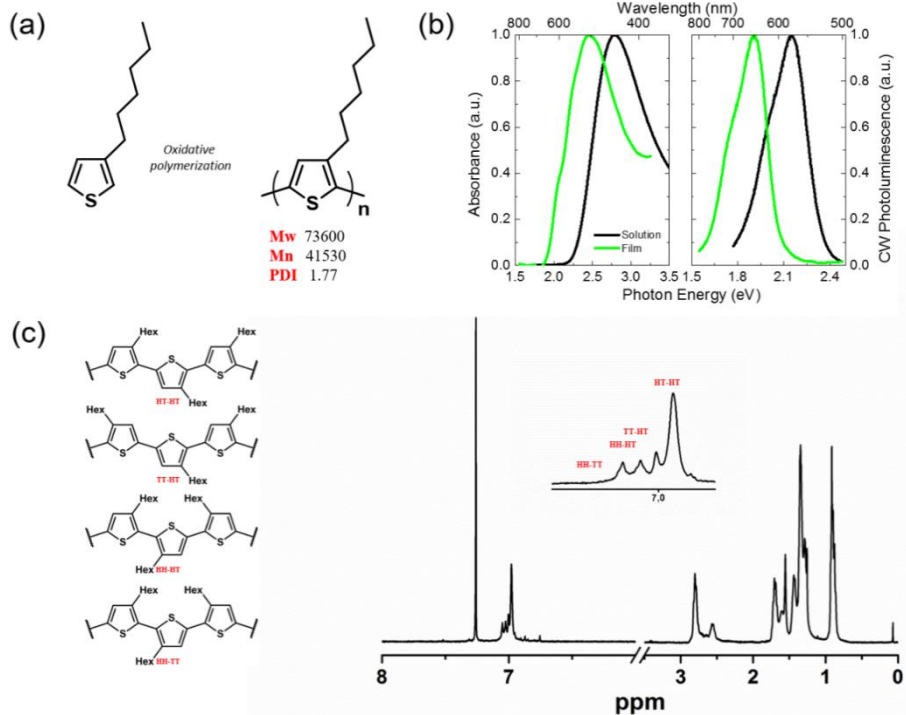


Figure S1. (a) Poly (3-hexylthiophene), P3HT, prepared by oxidative polymerization with FeCl_3 .-(b) Normalized photoluminescence and absorption spectra of P3HT in CHCl_3 (black trace) and cast film from CHCl_3 (green trace). (c) ^1H -NMR spectrum of P3HT in CHCl_3 .

5.2 Optical microscope images of stained cell loaded with P3HT-NPs.

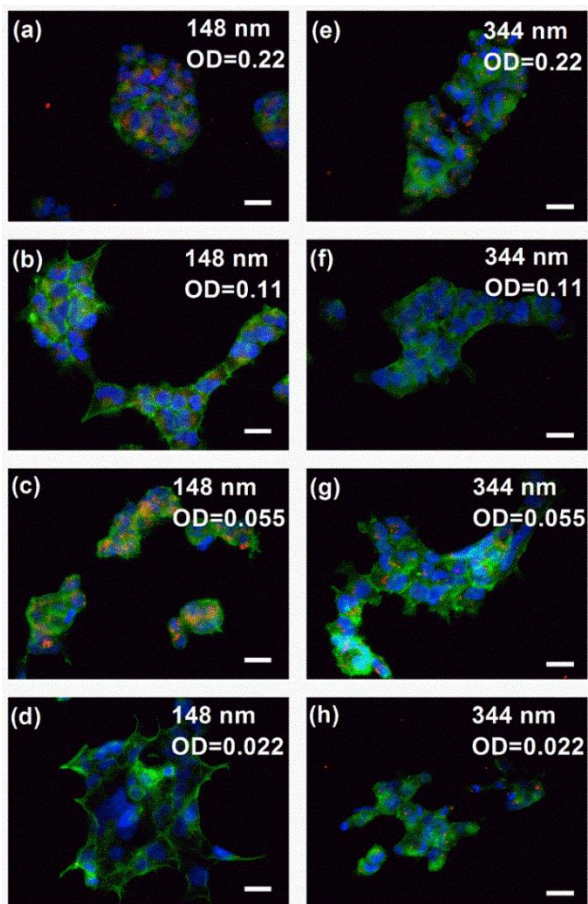
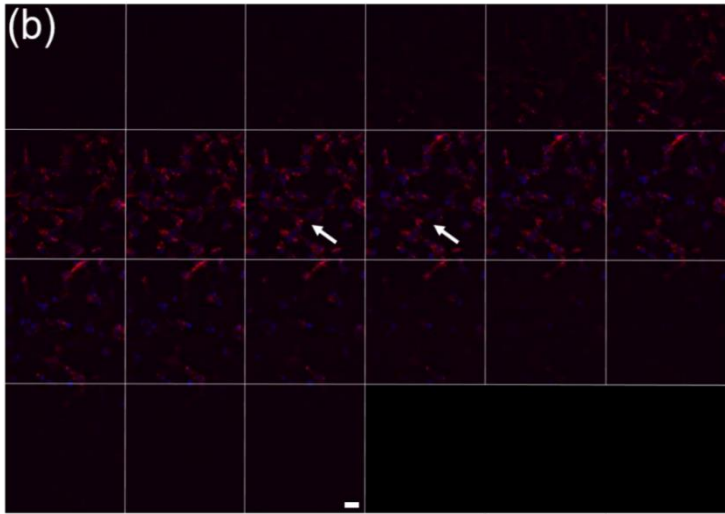
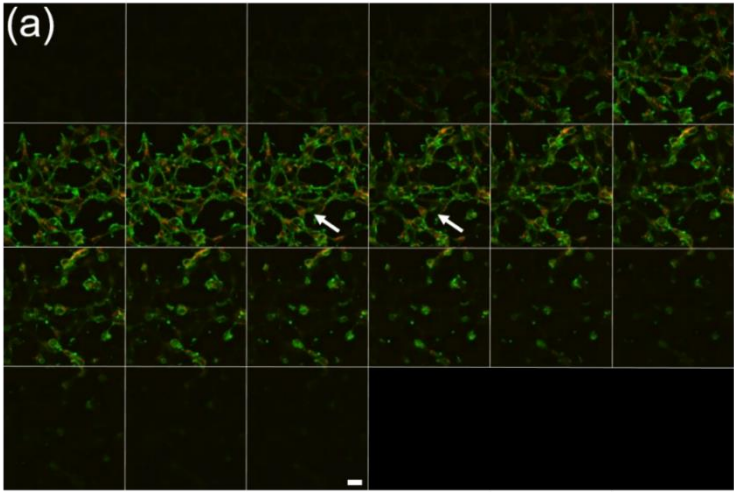


Figure S2. Optical microscope images of stained cell cultures showing nuclei (in blue), actin filaments (in green) and the emission of NPs (in red) for 148 nm and 344 nm NPs' suspensions. Scale bar, 10 μm . Each NPs dispersion was diluted at different concentrations in ultrapure water, in order to obtain four different optical densities values, measured at 460 nm and ranging from 0.022 to 0.22. We aimed at finding a suitable compromise between maximization of NPs cellular uptake and appearance of detrimental effects on cell morphology. In the case of smaller NPs, the highest considered concentration (panel a) clearly lead to altered cellular shape and reduced cellular membrane polarization, thus possibly indicating the occurrence of apoptotic processes. We thus fixed the working optical density of the dilution at 0.11 (panel b). Conversely, bigger NPs could be used at the highest tested concentration (panel e), which however could not be further increased in order not to add to the extracellular solution a water excess larger than 10% in volume.

5.3 Confocal optical sections of cells laded with P3HT-NPs



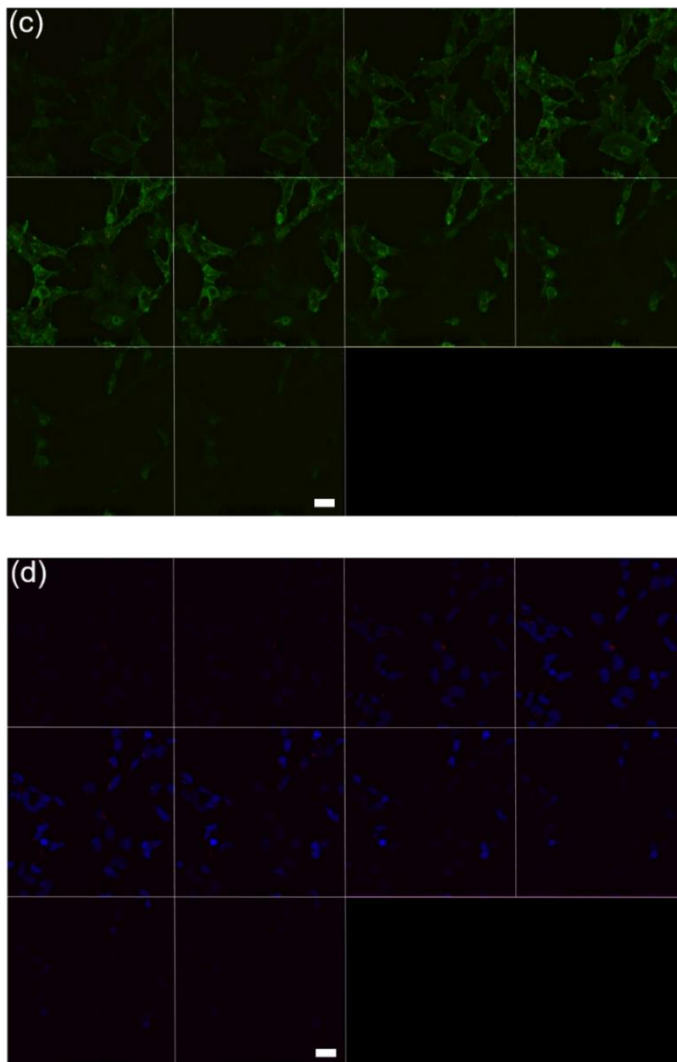


Figure S3. Confocal optical sections of cells loaded with 148 nm (panels (a) and (b)) and 344 nm (panels (c) and (d)), stained with DAPI (blue, nuclei) and phalloidin (green, actin). Emission from NPs is visible in the red channel. By inspection of subsequent stacks, acquired from the bottom to the upper cell surface, it is possible to appreciate that NPs have been internalized within the cytosol, but do not cross the nuclear membrane. Scale bar, 30 μm .

5.4 Membrane response to a voltage-clamp step protocol

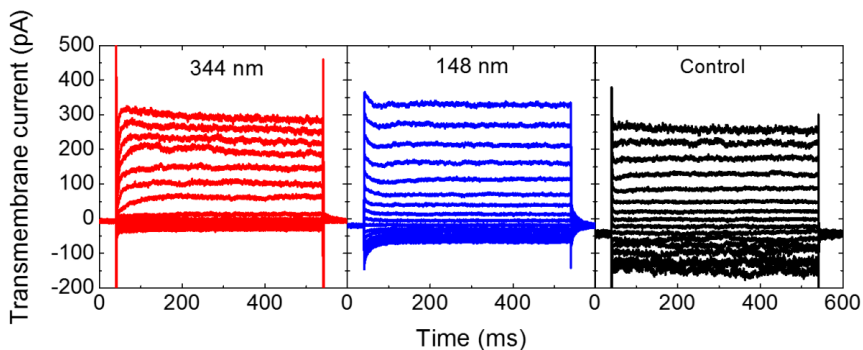


Figure S4. Representative trans-membrane current measured in whole-cell, voltage clamp configuration in samples treated with NPs (red and blue curves) and controls (black curves). 500-ms voltage steps have been subsequently applied (holding potential, -40 mV), ranging from -100 mV to 50 mV, in 10 mV increments.

5.4 Time-resolved fluorescence spectra from NPs within the living cell

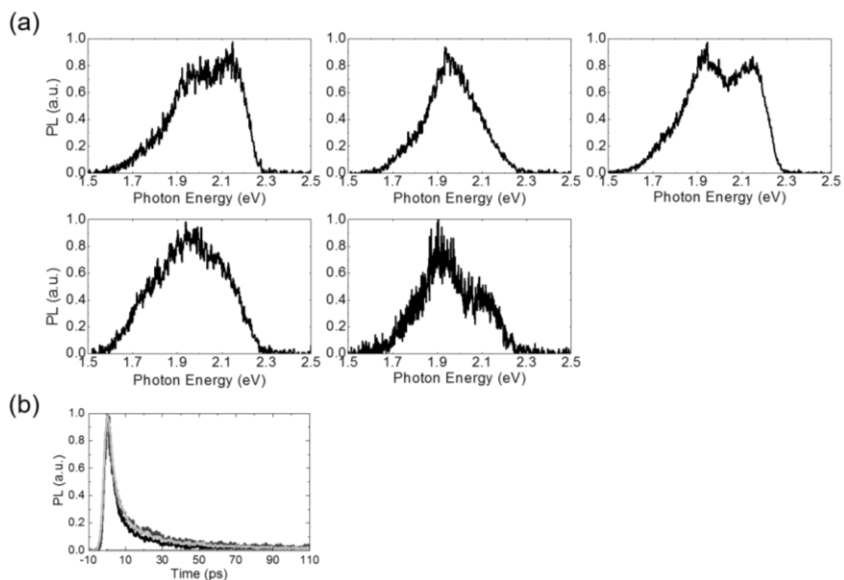


Figure S5. Examples of fluorescence spectra (a) integrated over the first 128 ps and representative kinetic traces (b) integrated between 1.82 and 2 eV obtained from measures of P3HT-NPs within living cells.

REFERENCES

- [1] ^{a)} O. V. Salata, *J. Bionanotech.* **2004**, DOI: 10.1186/1477-3155-2-3. ^{b)} B. Wang, H. Yuan, C. Zhu, Q. Yang, F. Lv, Liu, L.; S. Wang, *Sci. Rep.* **2012**, 2, 766. ^{c)} E. Colombo, P. Feyen, M. R. Antognazza, G. Lanzani, F. Benfenati, *Front. Neurosci.* **2016**, 10, 105
- [2] ^{a)} D. Tuncel, H. V. Demir, *Nanoscale*, **2010**, 2, 484-494. ^{b)} Lanzani G. *Nature Materials*, **2014**, 13, 775-776.
- [3] X. Feng, F. Lv, L. Liu, H. Tang, C. Xing, Q. Yang, S. Wang, *Appl. Mater. Interf.*, **2010**, 2, 2429-2435
- [4] ^{a)} P. Howes, M. Green, J. Levitt, K. Suhling, M. Hughes, *J. Am. Chem. Soc.* **2010**, 132, 3989-3996. ^{b)} M. Green, P. Howes, C. Berry, O. Argyros, M. S. Thanou, *Proc. R. Soc. A* **2009**, DOI: 10.1098/rspa.2009.0181.
- [5] L. Feng, L. Liu, F. Lv, G. C. Bazan, S. Wang, *Adv Mater.* **2014**, 26, 3926-3930.
- [6] ^{a)} J. Pennakalathil, A. Ozgun, I. Durmaz, R. Cetin-Atalay, D. Tuncel, *J. Polym. Sci. A: Polymer Chemistry* **2015**, 53, 114-122. ^{b)} K. P. Pu, B. Liu, *Adv. Funct. Mater.* **2008**, 2, 1487-1491.
- [7] ^{a)} F. Ye, C. Wu, J. Yuhui, Y. H. Chan, X. Zhang, D. T. Chiu, *J. Am. Chem. Soc.* **2011**, 133, 8146-8149. ^{b)} E. Miyako, J. Russier, M. Mauro, C. Cebrian, H. Yawo, C. Menard-Moyon, J. A. Hutchison, M. Yudasaka, S. Iijima, L. De Cola, A. Bianco, *Angew. Chem. Int. Ed.* **2014**, 53, 13121-13125.
- [8] W. Li, R. Luo, X. Lin, A. D. Jadhav, Z. Zhang, L. Yan, C. Y. Chan, X. Chen, J. He, C. H. Chen and P. Shi, *Biomaterials*, **2015**, 65, 76.
- [9] M. R. Antognazza, M. Di Paolo, D. Ghezzi, M. Mete, S. Di Marco, J. F. Maya-Vetencourt, R. Maccarone, A. Desii, F. Di Fonzo, M. Bramini, A. Russo, I. Donelli, M. Cilli, G. Freddi, G. Pertile, G. Lanzani, S. Bisti and F. Benfenati, *Adv. Healthcare Mater.*, **2016**, 5, 2271-2282.
- [10] M. R. Antognazza, D. Ghezzi, D. Musitelli, M. Garbugli and G. Lanzani, *Appl. Phys. Lett.*, **2009**, 94, 243501.
- [11] ^{a)} D. Ghezzi, M. R. Antognazza, M. Dal Maschio, E. Lanzarini, F. Benfenati and G. Lanzani, *Nat. Commun.*, **2011**, 2, 166. ^{b)} N. Martino, P. Feyen, M. Porro, C. Bossio, E. Zucchetti, D. Ghezzi, F. Benfenati, G. Lanzani and M. R. Antognazza, *Sci. Rep.*, **2015**, 5, 8911. ^{c)} P. Feyen, E. Colombo, D. Endeman, M. Nova, L. Laudato, N. Martino, M. R. Antognazza, G. Lanzani, F. Benfenati and D. Ghezzi, *Sci. Rep.*, **2016**, 6, 22718. ^{d)} D. Ghezzi, M. R. Antognazza, R. Maccarone, S. Bellani, E. Lanzarini, N. Martino, M. Mete, G. Pertile, S. Bisti, G. Lanzani and F. Benfenati, *Nat. Photonics*, **2013**, 7, 400.
- [12] G. Barbarella, A. Bongini and M. Zambianchi, *Macromolecules*, **1994**, 27, 3039.
- [13] ^{a)} C. E. Mora-Huertas, H. Fessi and A. Elaissari, *Adv. Colloid Interface Sci.*, **2011**, 163, 90. ^{b)} H. Shimizu, M. Yamada, R. Wada and M. Okabe, *Polym. J.*, **2008**, 40, 33.
- [14] A. M. Puertas and F. J. de las Nieves, *J. Colloid Interface Sci.*, **1999**, 216, 221.

- [15] ^{a)}J. Pecher and S. Mecking, *Chem. Rev.*, **2010**, 110, 6260. ^{b)}N. Anwar, T. Willms, B. Grimme and A. J. C. Kuehne, *ACS Macro Lett.*, **2013**, 2, 766.
- [16] C. Messerschmidt, D. Hofmann, A. Kroeger, K. Landfester, V. Mailänder and I. Lieberwirth, *Beilstein J. Nanotechnol.*, **2016**, 7, 1296.
- [17] K. Tabata, D. Braam, S. Kushida, L. Tong, J. Kuwabara, T. Kanbara, A. Beckel, A. Lorke and Y. Yamamoto, *Sci. Rep.*, **2014**, 4, 5902.
- [18] N. Kurokawa, H. Yoshikawa, N. Hirota, K. Hyodo and H. Masuhara, *Chem. Phys. Chem.*, **2004**, 5, 1609.
- [19] ^{a)}M. Heeney, C. Bailey, K. Genevicius, M. Shkunov, D. Sparrowe, S. Tierney and I. McCulloch, *J. Am. Chem. Soc.*, **2005**, 127, 1078. ^{b)}C. Scharsich, R. H. Lohwasser, M. Sommer, U. Asawapirom, U. Scherf, M. Thelakkat, D. Neher and A. Kohler, *J. Polym. Sci., Part B: Polym. Phys.*, **2012**, 50, 442. ^{c)}K. S. Wong, H. Wang and G. Lanzani, *Chem. Phys. Lett.*, **1998**, 288, 59. ^{d)}P. Parkinson, C. Muller, N. Stingelin, M. B. Johnson and L. M. Herz, *J. Phys. Chem. Lett.*, **2010**, 1, 2788.
- [20] C. He, Y. Hu, L. Yin, C. Tang and C. Yin, *Biomaterials*, **2010**, 31, 3657
- [21] A. K. Salem, P. C. Searson and K. W. Leong, *Nat. Mater.*, **2003**, 2, 668.
- [22] A. Kumar, B. Sahoo, A. Montpetit, S. Behera, R. F. Lockey and S. S. Mohapatra, *Nanomedicine*, **2007**, 3, 132.
- [23] A. Takahashi, P. Camacho, J. D. Lechleiter and B. Herman, *Physiol. Rev.*, **1999**, 79, 1089.
- [24] J. K. Angleson and W. J. Betz, *Trends Neurosci.*, **1997**, 20, 281.
- [25] P. W. Brandt and A. R. Freeman, *Science*, **1967**, 155, 582.
- [26] ^{a)}J. Clark, J.-F. Chang, F. C. Spano, R. H. Friend and C. Silva, *Appl. Phys. Lett.*, **2009**, 94, 1633061. ^{b)}T. G. Bjorklund, S.-H. Lim and C. J. Bardeen, *Synth. Met.*, **2004**, 142, 195. ^{c)}S. Tretiak, A. Saxena, R. L. Martin and A. R. Bishop, *Phys. Rev. Lett.*, **2002**, 89, 0974021. ^{d)}P. J. Brown, D. S. Thomas, A. Kohler, J. S. Wilson, J.-S. Kim, C. M. Ramsdale, H. Sirringhaus and R. H. Friend, *Phys. Rev. B: Condens. Matter Mater. Phys.*, **2003**, 67, 0642031.
- [27] D. Polli, G. Grancini, J. Clark, M. Celebrano, T. Virgili, G. Cerullo and G. Lanzani, *Adv. Mater.*, **2010**, 22, 3048.
- [28] M. P. Monopoli, D. Walczyk, A. Campbell, G. Elia, I. Lynch, F. Baldelli Bombelli and K. A. Dawson, *J. Am. Chem. Soc.*, **2011**, 133, 2525.

Part II: Semiconducting polymers are light nanotransducers in eyeless animals

I. INTRODUCTION

Inducing light sensitivity in living organisms provides groundbreaking opportunities in neuroscience. Optogenetics is a spectacular demonstration of this, yet it is limited by the viral transfection of exogenous genetic material ^[1]. The use of photosensitizers ^[2] represents an alternative tool for photostimulation of living tissues ^[3]. This led to the visionary proposal that the injection of dyes into the muscles of paraplegics could restore their functioning ^[4]. However, molecular dyes are difficult to localize in the hosting body and can be toxic or phototoxic. Conversely, nanoparticles (NPs) with size comparable to cell organelles can be easily delivered also in vivo, through water suspensions, and functionalized on the surface to somewhat control their localization and function. Metal NPs for photothermal stimulation, inorganic semiconducting rods for electrical stimulation, and inorganic NPs for magnetothermal stimulation ^[5] have been recently reported. Here, we report on the use of NPs based on semiconducting polymers. These materials have shown excellent biocompatibility, and their possible use in combination with living systems (both in vitro and in vivo conditions) has been intensively investigated, mainly for drug delivery and imaging applications ^[6]. However, the exploitation of their light absorption in the visible range and charge photogeneration capability was reported for opto-neuromodulation in very few cases ^[7], mainly focusing on photothermal effects ^[6c, 8]. Moreover, to the best of our knowledge, conjugated polymer NPs were never reported to play a direct role in vivo in the control of the animal physiology. Here, we show that NP based on poly(3-hexylthiophene) (P3HT) can be internalized in eyeless freshwater polyps ^[9] and are fully biocompatible. Under light, the NPs modify the light response of the animals and enhance opsin expression. This suggests a seamless and biomimetic interface between the polymer NP and the living organism. P3HT is a prototype conjugated polymer used in photodetection, photonics, and photovoltaics ^[10]. Recently, it has been shown that P3HT is highly biocompatible and can transduce a light signal into a cell stimulus ^[11]. Its application in a retinal prosthesis implanted in blind animals is under investigation ^[12]. Geometrically, isotropic nanospheres of P3HT (P3HT-NPs) with a hydrodynamic diameter between 150 and 300 nm, and a relatively low polydispersity index (0.07), have been realized in the absence of surfactants (Figure 1, A and C). The optical absorption and emission spectra of the aqueous dispersion, peaking at 520 and 640 nm, respectively, are red-shifted and slightly broader compared to the spectra from polymer chains in solution (Figure S1). The zeta potential has been calculated by the phase analysis light scattering technique on the basis of the Smoluchowski equation and amounts to -41.8 ± 0.4 mV, indicating excellent colloidal stability in an aqueous environment. Here, P3HT-NPs are tested as photoactuators in the freshwater polyp *Hydra vulgaris*, a primitive animal whose simple anatomy can be compared to a tissue. The direct exposure of the outer cell layer, the ectoderm, to the bathing medium enables testing of direct interaction with medium-suspended NPs using a variety of methods ^[13], including tools for testing the toxicity ^[14] and the bioactivity of nanomaterials ^[15]. This allows low-cost, high-throughput investigations, decreases

vertebrate experimentation, and avoids ethical issues. Despite the nonvisual photic behavior of this organism, the sequenced genome revealed the presence of all complex repertoire genes involved in vertebrate vision ^[16]. We find that soaking *Hydra* polyps with P3HT-NPs leads to efficient internalization. Using different approaches, we assess the nontoxicity of the P3HT-NPs and investigate their photo-bioactivity. Our results show that P3HT-NP photostimulation elicits two phenomena: the modulation of the photo-induced *Hydra* contraction behavior and the enhancement of an *opsin-like* gene transcription.

II. RESULTS

Hydra can react to chemical stressors displaying a broad range of morphological changes, grouped according to numerical values ranging from 10 (normal) to 0 (disintegrated) ^[17]. We assessed P3HT-NP toxicity in the dark against tissue integrity/polyp morphology by treating groups of 10 living polyps with increasing concentrations of P3HT-NPs (0.25 to 12.5 μM). Median morphological scores recorded at 24-hour intervals did not show the induction of morphological aberrations (such as contracted body or tentacles, or tissue damages), indicating the absence of macroscopic toxicity signs (Figure 1D). We next evaluated the impact of P3HT-NPs on *Hydra* reproduction by budding. Because the proliferation rate of ectodermal and endodermal cells depends on feeding regime and environmental condition ^[18], any compound affecting this process will in turn affect the growth rate of the population founded by the exposed polyp. Figure 1E shows no significant differences between population growth rates of untreated (black line) and treated polyps (red line), indicating that P3HT-NP exposure does not undermine *Hydra* growth. Estimation of population growth rate performed at higher concentration did not show any marked effect at up to 50 μM concentration, confirming the good biocompatibility of polymer beads, at least in physiological processes linked to cell proliferation (Figure S2). Biodistribution of P3HT-NPs in living polyps was inspected by fluorescence microscopy. Images from Figure 1F show an efficient uptake of P3HT-NPs in *Hydra* tissue throughout the body column, especially into tentacles. According to previous experiments carried out using fluorescent inorganic nanocrystals ^[19], gold NPs of different shapes ^[15b, 20], silica oxide NPs ^[14c], and iron oxide NPs ^[21], we speculate that the same internalization route might be active, that is, macropinocytosis of medium-suspended NPs and accumulation into cytoplasmic vacuoles. The natural *Hydra* behavior at ambient light is characterized by a continuous periodic alternation of body contractions and elongations ^[22] at an observed average of two contractions in 10 min ^[23].

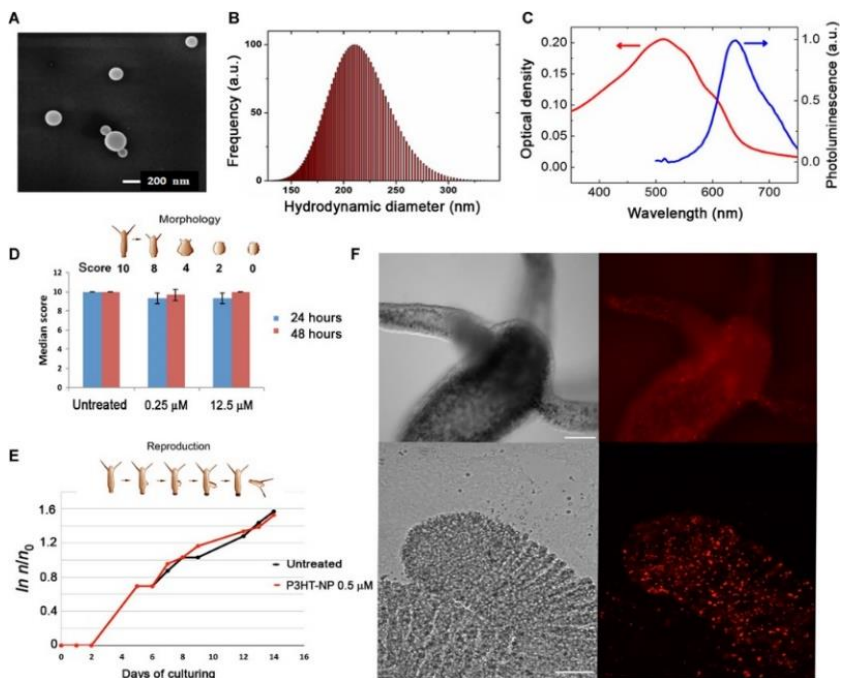


Figure 1. Characterization of P3HT-NPs and in vivo toxicological analysis. **(A and B)** Characterization of P3HT-NPs by scanning electron microscopy and dynamic light scattering (DLS) analysis. **(C)** Optical absorption (left axis) and photoluminescence spectra (right axis) of P3HT-NPs in an aqueous dispersion. Fluorescence emission excitation wavelength, 470 nm. **(D and E)** Determination of P3HT-NP toxicity endpoints in *H. vulgaris*. Numerical scores ranging from 10 (healthy polyp) to 0 (dead polyp) were assigned to progressive morphological changes possibly induced by P3HT-NP treatments, at the indicated doses, and recorded every 24 hours. No significant difference is evidenced between treated and untreated polyps **(D)**. P3HT-NP treatment does not affect the reproduction rate of *Hydra*. The logarithmic growth curve of a treated *Hydra* population (red) is fully comparable to the one obtained from a control population **(E)** (n_0 is the number of polyps at time 0, and n is the number of animals recorded at time t). **(F)** In vivo bright-field (left) and fluorescence (right) imaging of a living polyp treated with P3HT-NPs. Soaking the polyps with 0.25 μM P3HT-NPs causes a fluorescent staining of all tissues. NPs after a few hours appear as fluorescent spots located inside the ectodermal cells. The top images show a head with a crown of tentacles around the mouth. Bottom images show details of the tentacle tip. Scale bars, 200 and 50 μm (top and bottom images, respectively). a.u., arbitrary units.

Here, we compare observations in ambient light with observations under white light-emitting diode (LED). Groups of 20 polyps were incubated with P3HT-NPs (0.25 μM) for 2 and 24 hours, and animal behavior was monitored and recorded every 30 s, starting with exposure for 1 min to ambient light, 3 min to white light (at maximum power density of 530 nm, 0.43 mW/mm²), and 4 min back to ambient light condition (Figure 2A). To quantify the contraction behavior, we

introduced a scoring system, assigning progressive numerical scores to behavioral traits, ranging from 6 (maximal body contraction) to 11 (maximal body elongation). Figure 2B shows the average contraction score ($n = 60$) obtained for the two sets of animals (red and blue curves) and the comparison with untreated polyps (black curve). During the first minute of recording, all polyps are in the relaxed, physiological state. Under white light illumination, untreated *Hydra* tends to elongate, whereas P3HT-NP-treated animals tend to contract or at least suppress the elongation. A slightly stronger response is induced in animals treated for 2 hours with P3HT-NPs, compared to those treated for 24 hours, perhaps because at 2 hours, most P3HT-NPs are still located in the external cell layer, whereas afterward, they migrate into the internal layer, as reported for other fluorescent nanocrystals [19].

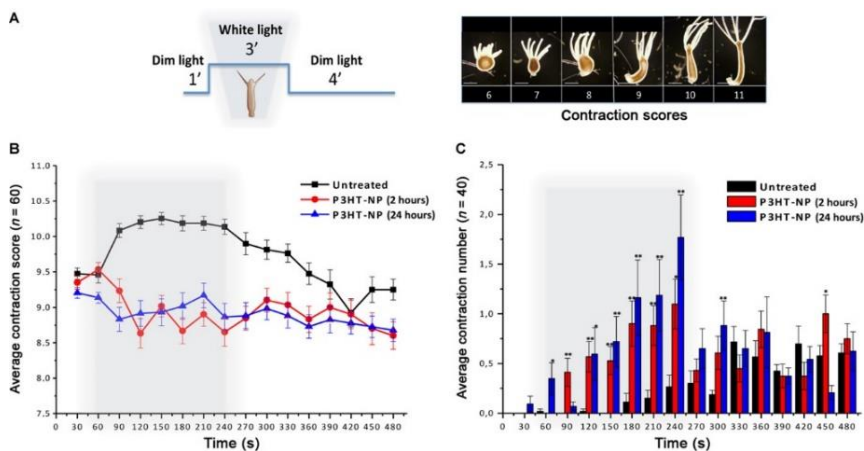


Figure 2. P3HT-NPs induce a behavioral response in *H. vulgaris*. (A) The behavioral response of *Hydra* to P3HT-NPs was evaluated using a contraction scoring system ranging from 6 (highly contracted) to 11 (elongated polyp). Animal behavior was monitored by continuous video recording for 8 min, according to the illumination protocol shown in the scheme, that is, 1-min dim light, 3-min white light illumination, 4-min dim light. Scale bars, 500 μm . (B) Average contraction scores and SD resulting from behavioral analysis ($n = 60$ polyps). Gray boxes indicate the 3-min light illumination period; black curves show contraction behavior of untreated polyps; red and blue curves show the contraction behavior of polyps treated with P3HT-NPs for 2 or 24 hours, respectively. SD values are reported as bars for each data set. (C) Average number of contraction events and relative SD estimated on treated (2 and 24 hours, red and blue lines, respectively) and untreated (black) polyps ($n = 40$, each condition). In most cases, statistically significant differences are observed (Student's *t* test, * $P < 0.05$, ** $P < 0.01$).

When the light is switched off, the untreated polyps clearly recover the original periodic elongation/contraction behaviour [22a], whereas the treated ones continue the light-induced contraction. Figure 2C shows that upon illumination, the average number of contractions significantly increases in treated polyps. Analog experiments carried out on light-insensitive, electrically inert NPs made of polystyrene (with comparable dimensions and zeta potential

values) did not show any sizable effect (fig. S3). We next carried out expression profiling of genes possibly involved in the P3HT-NP-mediated phototransduction. We used quantitative reverse transcription polymerase chain reaction (qRT-PCR) to reveal expression changes of genes involved (in mammals), in response to light, heat, and oxidative stress.

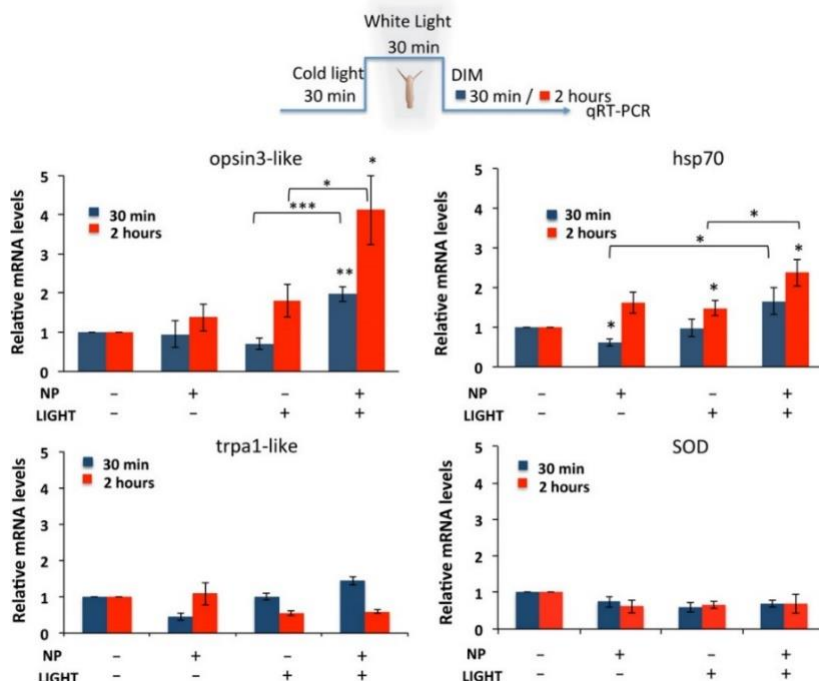


Figure 3 P3HT-NP photoactivation enhances *opsin3-like* gene transcript levels. *Hydra* exposure to P3HT-NPs and/or white light illumination elicits a number of molecular reactions, which may provide useful clues on the transduction pathways activated by each stimulus. Genes selected in this study belong to light transductions pathway (*opsin3-like*), heat response (*hsp70*, *trpa1-like*), and oxidative stress (*Cu-Zn SOD*). Gene accession numbers for the *Hydra* homologous genes are reported in table S1. The expression profile of selected genes was investigated by qRT-PCR analysis using *elongation factor 1 α* (*HyEf-1 α*) as reference gene. Polyps treated with 0.25 μ M P3HT-NPs for 24 hours underwent the illumination protocol shown on the upper part of the panel, then they were allowed to recover for either 30 min or 2 hours and were processed for RNA extraction and qRT-PCR analysis using specific primers (see table S1). *opsin3-like* gene expression shows great activation in response to both NPs and white light illumination, as compared to other conditions (untreated, not illuminated; treated, not illuminated). Data are presented as means \pm SE of three technical repeats from two biological replicates. Statistical comparisons are performed using unpaired *t* test, **P* < 0.05, ***P* < 0.01.

Gene selection was performed, whenever possible, among genes previously characterized in *Hydra*: *hsp70* (*heat shock protein 70*) is well characterized in *Hydra* for heat responsiveness [24],

and its expression has been profiled in response to temperatures ranging from 26° to 37°C [21]; *Cu-Zn SOD* (*copper-zinc superoxide dismutase*), encoding an antioxidant enzyme and converting superoxide radical into hydrogen peroxide, showed increased expression in *Hydra* in response to both heat (34°C) [25] and reactive oxygen species (ROS) [26]. Eventually, for *opsin3-like* and *trpa1-like* (*transient receptor potential A-subfamily*) selected genes, we characterized the transcriptional modulation mediated by both light and heat stresses. Animals were treated for 24 hours with P3HT-NPs, equilibrated for 30 min at room temperature under the cold light of a stereomicroscope, and then exposed for 30 min to white light illumination of the same power density as that used in behavioral assays. After recovering for 30 and 120 min, animals were processed for qRT-PCR. Figure 3 shows a significant increase of *opsin3-like* expression in polyps treated with P3HT-NPs and exposed to light, at both time points, compared to animals not illuminated. *Opsin3-like* gene expression levels increased, albeit in a lesser amount, also in untreated polyps, under LED illumination at a 2-hour time point, and this light responsiveness was further confirmed in polyps under normal dark/light cycling conditions (Figure S4). We found that *hsp70* expression levels were only slightly up-regulated and did not show a significant correlation with P3HT-NP treatment or light exposure. Because *hsp70* is involved in regulating protein stability and maturation, the slight overexpression observed in all experimental conditions may indicate the possible involvement of this chaperonin in P3HT-NP general “sensing” and involvement in maintaining cell homeostasis, rather than its participation in a specific light-activated process. *trpa1-like* and *SOD* gene transcription levels were not significantly changed in response to P3HT-NP treatment or LED irradiation. Experiments carried out with control polystyrene NPs, in the same experimental conditions and under the same experimental protocol, did not show marked effects on opsin expression, thus confirming the active role played by the chemical/physical properties of P3HT-NPs in the intracellular light transduction pathways (Figure S3). Molecular analysis performed under the illumination condition used for behavioral analysis (3 min) revealed significant expression changes for *opsin3-like* gene at a 2-hour time point (Figure S5), confirming modulation of *opsin* transcription by light and indicating the capability of a short illumination period to trigger the molecular response. To disentangle direct effects of light excitation from light-mediated thermal processes, we investigated gene responsiveness to heat. Results of gene profiling in fig. S6 confirmed heat responsiveness in transcription of *hsp70*, *trpa1-like*, and *SOD* genes, whereas *opsin3-like* transcript levels were not affected by heat stress. This strongly argues against a thermal effect consequent to photostimulation, although it does not necessarily rule out the involvement of ROS or other molecular transducers.

III. DISCUSSION

Here, we investigate whether nanostructured conjugated polymers could enhance light photosensitivity *in vivo*, providing a handle for controlling living organisms with light. We use *H. vulgaris* as a model system. This is a simple water invertebrate, which evolved before vision was established, yet it is able to react to light illumination, for instance, by heliotropism. First,

we demonstrate the successful uptake of polymer NPs in the living animal. Then, we explore the functional interaction of the light-activated NPs with the cells in living *Hydra* by a behavioral analysis and a quantitative estimation of expression fold changes of genes involved in light, heat, or ROS responses. Overall, both the behavioral and molecular outcomes indicate that P3HT-NPs enhance light-mediated processes boosting the animal's photosensitivity. In more detail, we find two effects. First, we observe that NPs photoexcitation modulates the elongation/contraction behavior of P3HT-NP-treated animals. The contraction of the body column in *Hydra* is regulated at two levels: (i) epitheliomuscular cells are connected by gap junctions and can propagate an electrical signal mediating contraction in response to a stimulus and (ii) nerve cells located in the lower body control the spontaneous initiation of epitheliomuscular cell contraction^[27]. We suggest that the photoexcitation both activates the surface of P3HT-NPs inducing electrochemical reactions and creates a localized electrical dipole, which causes the synchronous firing of nerve cells and the subsequent coordinated activation of effector epitheliomuscular cells. The second effect of photostimulation we report is the enhancement of *opsin* expression levels in treated *Hydra*, a downstream effect of single or multiple molecular cascades. The reason for such transcriptional activation, although not straightforward, unequivocally links the P3HT-NP photoexcitation to the opsin, the best investigated player underlying phototransduction. The *opsin3-like* gene belongs to a seven-transmembrane G protein-coupled receptor superfamily, which plays a key role in vision^[28]. All known visual pigments in Neurlia (Cnidaria, Ctenophora, and Bilateria) are composed of an opsin and a light-sensitive chromophore, generally a retinal, linked through a Schiff base involving a lysine found at position 296 (K296) of the reference bovine rhodopsin sequence. Considering the conserved position of this amino acid residue in the *Hydra* opsin3-like predicted protein sequence (figs. S7 and S8), this protein is likely to be involved in light reception in *Hydra* as well. Furthermore, the increased *opsin3-like* gene expression under white light illumination in untreated polyps suggests the "natural" responsiveness of the *opsin3* gene transcription to white light stimulation. This is also confirmed in polyps under normal light cycle (12-hour light/12-hour dark) (Figure S3). Other evidence supporting light dependence of *Hydra* opsin3-like protein comes from functional studies on the opsin subgroup 3 (opn3), including both vertebrate and invertebrate members. Originally named encephalopsin or panopsin, as expressed in the brain, liver, and other nonphotoreceptive tissues, they can form functional photosensitive pigments and activate G proteins in a light-dependent manner^[29]. Similarly, the *Hydra* *opsin3* homolog investigated here may act as a light sensor, mediating the intracellular transduction of the light signal. Together, these observations support the conjecture that P3HT-NPs behave as light nanotransducers, somewhat mimicking the role of natural photoreceptors and boosting *Hydra*'s photosensitivity. Although a definitive assignment of the coupling mechanism between the photoexcited NPs and the *Hydra* is beyond the scope of this work, we would like to briefly discuss three plausible effects: (i) thermal release, (ii) photochemical reactions, and (iii) electrical polarization (Figure 4).

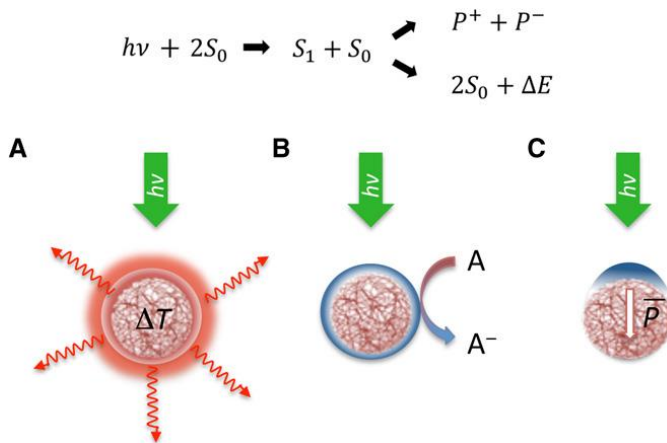


Figure 4. Mechanisms underlying photoexcitation of P3HT-NPs. **Top:** Upon visible light illumination, primary photoexcitation states S_1 are created within the polymer NPs, which can give rise to the creation of polaronic charged states P^\pm or to nonradiative release of the excess energy ΔE . **Bottom:** different decay paths of the NP photoexcited states are shown: (A) photothermal excitation and heat release, (B) photoelectrochemical oxidation processes, and (C) electrical polarization.

(i) Assuming a maximum light intensity of $I = 1 \text{ mW/mm}^2$, the expected rise in temperature ΔT of a NP at thermodynamic equilibrium in a medium is given by $\Delta T = \frac{RI}{4k}$, where R ($\sim 100 \text{ nm}$) is the NP radius and κ ($\sim 0.6 \text{ W/mK}$) is the water thermal conductivity. We obtain $\Delta T = 0.04 \text{ mK}$, which is at least four orders of magnitude below the threshold of interest. NP aggregation might increase the amount of energy deposited in a limited volume, thus enhancing the local temperature. However, given the linear dependence of ΔT with R , even an aggregate of 100 NPs would not be sufficient to increase the temperature by 1 K. These considerations rule out photothermal effects as a possible cause of interaction. Note that considering the estimated number of NPs up taken by a *Hydra* on average and the animal volume, even the total heating of the animal turns out to be negligible.

(ii) A P3HT chain is composed of conjugated segments of variable length. By and large, each segment behaves like an organic molecule supporting singlet states as primary photoexcitation. In the NPs, the polymer chains are closely packed, allowing interchain interactions. In addition, in the presence of oxygen, the particles are p-doped, due to electron trapping at oxygen complexes. Light, oxygen, and moisture boost the doping process, and the radiative decay path of the singlet state can be totally quenched in favor of charge separation. Charged states, known as polarons, become the dominant photoexcitation. They can live up to the millisecond time domain, contributing a steady-state population under continuous wave light, that can feed electrochemical reactions occurring at the NP surface. If we consider an average time constant $\tau = 1 \text{ }\mu\text{s}$ for the polaron states and an intensity of $I = 0.5 \text{ mW/mm}^2$ at an average photon energy of 2 eV, the steady-state population density N on a single NP is $N \approx 1.5 \times 10^{11} \text{ m}^{-2}$, corresponding

to about 50 charged pairs per particle, which can easily undergo surface photoelectrochemical phenomena.

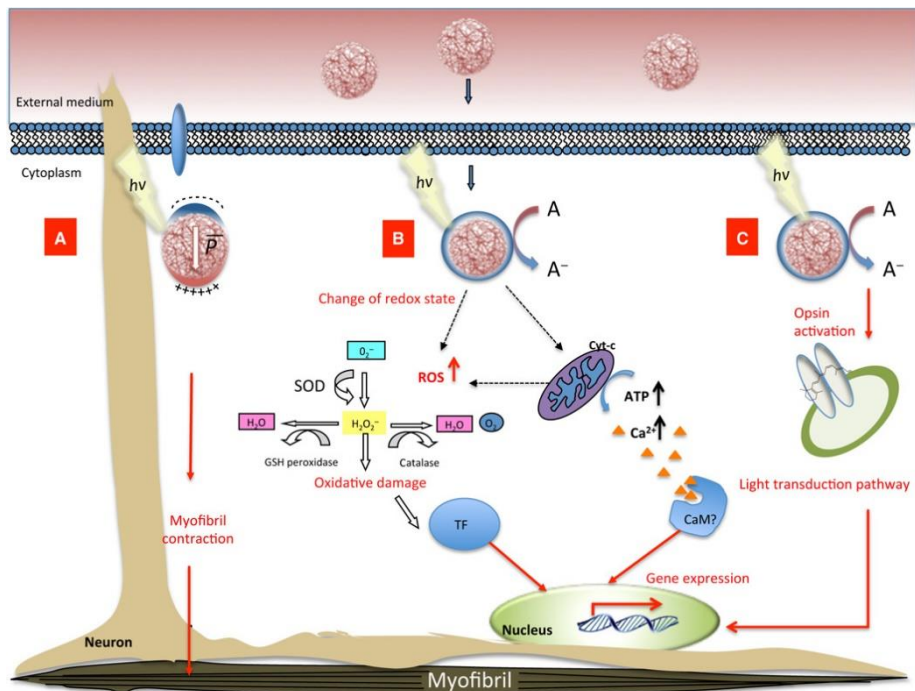


Figure 5. Biological pathways activated by P3HT-NP photostimulation. The sketch depicts a general epitheliomuscular ectodermal cell, presenting nucleus, mitochondria, and organelles. When light irradiates P3HT-NPs, both free and/or aggregated forms, electrons are generated in the photosensitive polymer, causing multiple biological responses. (A) NPs can localize within epitheliomuscular cells, and upon photoexcitation, a localized electrical dipole is established. In addition, photoelectrochemical reactions are promoted at the NP surface. These effects may locally act on neurons, leading to myofibril contraction and modulating the animal contracting behavior, as observed in behavioral studies. (B) Charged states sustain photoelectrochemical reactions, which increase the cytoplasmic concentration of ROS. This induces enzymatic reactions and acts on transcription factors (TF), or alternatively activates redox reactions of the respiratory chain and calcium binding transcription factors (CaM). In any case, targeted gene transcription is enhanced. (C) The retinal moiety of opsin3-like molecules or the P3HT-NPs themselves may initiate a light-dependent molecular cascade. GSH, glutathione.

(iii) The steady-state population of charges can also contribute to build up an electrical polarization of the NP. After photoexcitation, we expect that negative charges appear at the surface of the particle, due to water polarization. Because of the spherical shape of the particle, the surface charge is distributed according to the cosine law with respect to light direction. A trivial integration on the light-exposed hemisphere thus provides a formula for the effective

dipole $P = \frac{2\pi}{3} \sigma d R^2$, where d is the charge separation, building up the dipole layer. For $\sigma = 2.5 \times 10^{-5} \text{ cm}^{-2}$, according to $I = 0.5 \text{ mW/mm}^2$, the maximum electric field at a 10-nm distance from the NP surface is in the order of $5 \times 10^4 \text{ V/m}$. From the rough evaluation of the order of magnitude involved in the different phenomena, the thermal effect can be ruled out, in agreement with the lack of response of the heat markers (*trpa1-like and SOD*). Regarding electrical polarization, this is expected to lead to very localized effects, strongly depending on the specific position of P3HT-NPs with respect to target membranes or organelles. Epitheliomuscular cells have contracting fibers extending parallel to the main body axis. Ultrastructural evidence ^[27a] suggests that the contractile activity is controlled by neuronal cells, establishing chemical and electrical synaptic connection with epitheliomuscular cells. These cells are also connected to each other by gap junctions and can respond synchronously to electrical signaling, mediating contraction ^[27b]. When polymeric P3HT-NPs are added to the medium, they are possibly internalized into epitheliomuscular cells and elicit contraction events (Figure 5A). Both the creation of a localized electric dipole at the NPs surface and the activation of photoelectrochemical reactions may possibly account for this phenomenon. On the other side, the enhancement of the transcription of genes involved in the light transduction pathway would not necessarily require a spatially localized activation mechanism and a close contact between the NPs and the targeted organelle. Thus, although we cannot completely exclude a possible contribution of local polarization in this case as well, we believe that the most probable photoexcitation mechanism is sustained here by photoelectrochemical reactions occurring at the P3HT-NP surface. These can trigger specific bioelectrical signaling processes (Figure 5, B and/or C). Photogenerated charged states feed electrochemical reactions occurring at the NP surface, increasing the concentration of cytoplasmic ROS, as recently reported also for polythiophene-tamoxifen drug conjugates ^[30]. Changes in cellular redox may induce detoxifying enzymatic reactions to eliminate dangerous species or act on transcription factors, driving gene transcription. In the proximity of mitochondria, electrochemical reactions may excite flavins and cytochrome, activating redox reactions of the respiratory chain. The increased adenosine triphosphate (ATP) levels boost all the ATP-driven ion carriers such as Na^+/K^+ -ATPase (sodium-potassium adenosine triphosphatase) and Ca^{2+} pumps. The increase in the cytoplasmic Ca^{2+} levels activates calcium binding transcription factors, such as a hypothetical calmodulin (CaM)-like protein and, in turn, enhances expression of target genes (Figure 5B). Alternatively and/or in a complementary way, through either a capacitive or an inductive coupling, the retinal moiety of opsin-like molecules or the P3HT-NPs themselves may initiate a light-dependent molecular cascade (Figure 5C). We observe that the lack of *SOD* transcriptional activation (Figure 3) could stem from the limited number of ROS involved or be a consequence of the specific transducing path triggered by the P3HT-NPs, which fits the natural one. The complexity of the scenario reflects the variety of possible biological responses, whose elucidation will be an object of future investigations. Overall, we believe that P3HT-NPs behave as light nanotransducers, coping with or amplifying the function of primitive photoreceptors and leading to the enhancement of the light sensitivity in the whole animal. Our results put forward the potential of this approach to control physiological functions in living organisms with light. In perspective, the demonstration that

light-sensitive polymer NPs are well tolerated within animal models, and do play a functional role in enhancing the perception of light, may open interesting opportunities in biomedical applications. In particular, we recently demonstrated that P3HT thin films are able to partially restore light sensitivity in explanted blind retinas ^[12a] and are very well tolerated once implanted in the rat retina, in place of the photoreceptors ^[12b]. Despite the excellent mechanical flexibility and reduced thickness of the implant, a very complex and rather invasive procedure is required for subretinal implantation. The availability of fully biocompatible nanomaterials with comparable optoelectronic properties would allow circumvention of this major issue. To this goal, specific targeting capability of NPs should be properly implemented, and detailed long-term localization analysis of the NPs should be carried out. The results here presented demonstrate the possibility of exploiting P3HT-NP visible light absorption for transduction of the light stimuli into the complexity level of a living animal. This first proof of concept is key to proceed on the route of “injectable electronics,” as it was recently defined ^[31].

IV. MATERIALS AND METHODS

P3HT-NPs were prepared from freshly synthesized P3HT by the reprecipitation method in the absence of surfactants ^[32]. The polymer was dissolved in tetrahydrofuran, and the solution was added to distilled water (solvent/nonsolvent volume in a 1:20 ratio). By means of differential centrifugation, the NPs were separated into fractions of different sizes and characterized by DLS with a NanoBrook Omni particle size analyzer, with a wavelength of 659 nm in back scattering mode (see also the Supplementary Materials). Ultraviolet (UV)–visible (vis) spectroscopy measurements were carried out using a PerkinElmer Lambda 1050 UV/Vis/NIR spectrophotometer and a Horiba Jobin Yvon NanoLog fluorometer. Scanning electron microscopy images were acquired with a Tescan MIRA3.

4.1 Animal culture. *H. vulgaris* (strain Zurich) were asexually cultured in *Hydra* medium [1 mM CaCl₂ and 0.1 mM NaHCO₃ (pH 7)] according to the method of Loomis and Lenhoff ^[33] with minor modifications. The animals were kept at 18° ± 1°C and fed three times per week with freshly hatched *Artemia salina* nauplii. For morphological evaluation tests, groups of 20 animals were collected in plastic multiwells and allowed to equilibrate at room temperature in 300 µl of *Hydra* medium. The test was initiated by adding P3HT-NPs (0.5 µM) to each well and incubating as necessary. NP uptake was monitored by a stereomicroscope (Olympus SZX-RFL2). After extensive washes, *in vivo* imaging was accomplished using a standard inverted fluorescence microscope (Nikon Eclipse Ti-S, equipped with 4×/20× objective) and filtering the light with a bandpass filter (cut-on wavelength, 550 nm). Possible morphological changes induced by P3HT-NPs were monitored by using the scoring system introduced by Wilby ^[17] and assigning a numerical score to progressive morphological alterations [from 10 (healthy polyp) to 0 (disintegrated polyp)]. A healthy and well-fed *Hydra* population expands exponentially following the formula $\ln(n/n_0) = kt$, where n is the number of animals at time t , n_0 is the number of animals at t_0 , and k is the growth constant ^[18] To assess the effect of P3HT-NPs on *Hydra*

growth rate, five *Hydra* (population founders) were treated with P3HT-NPs for 24 hours, washed, and, in the following day, placed in 3.5-cm petri dishes (one *Hydra* per dish). Control polyps at the same developmental stage were not treated. Both treated and untreated *Hydra* were fed once daily for 14 days. The number of individuals was recorded daily and reported as the normalized logarithmic growth curves of treated *Hydra* population compared to a control population.

4.2 Behavioural activity. Groups of two *Hydra* were placed in a plastic petri dish containing *Hydra* medium to carry out the experiments. *Hydra* behavior upon white light illumination (Thorlabs LED MCWHL2-C4; power density, 0.43 mW/mm²) was investigated in the presence and absence of P3HT-NPs of 200-nm approximate diameter. P3HT-NPs were added to every single polyp at a concentration of 0.25 μM and incubated for 2 and 24 hours. After incubation, the illumination protocol illustrated in Figure 2 was adopted. Experiments were performed before addition of P3HT-NPs, after 2 and 24 hours of P3HT-NP incubation on 24-hour-starved animals at room temperature. Both the contraction per elongation average degree of the *Hydra* body and the total number of contractions were evaluated before (1 min), during (3 min), and after (4 min) visible light excitation.

4.3 RNA extraction and qRT-PCR. Total RNA from treated and untreated animals was purified using TRI Reagent (Molecular Research Center), and its concentration was determined on the NanoDrop ND-1000 spectrophotometer (Thermo Scientific). The first-strand complementary DNA (cDNA synthesis) was carried out with the SuperScript II retrotranscriptase (Invitrogen) and oligo(dT)s, using 0.5 μg of DNA-free RNA in a final volume of 25 μl, according to the manufacturer's instructions. qRT-PCR was performed in 25 μl of reaction mixture consisting of 1x Express SYBR GreenER qPCR SuperMix with premixed ROX (Invitrogen), serial cDNA dilutions, and 0.3 μM of each primer. The reactions were processed using the StepOne Real-Time PCR System (Applied Biosystem) under the following fast cycling steps: initial denaturation for 2 min at 94°C, followed by 40 cycles at 94°C for 2 s, 59°C for 30 s. In addition, melting curves (20 min, from 59° to 90°C) were generated to check any spurious amplification products. To normalize RNA levels, *Hydra elongation factor 1a* gene (*HyEf-1a*) was used as an internal calibrator. Nucleotide sequences and alignments were obtained from the *Hydra* genome database (<http://www.compagen.org/>). Specific primers of *Hydra* homolog genes of opsin (*opsin3-like*), *SOD*, *hsp70*, transient receptor potential-A family (*trpa1-like*) were designed using the Primer3 software (<http://frodo.wi.mit.edu/primer3/>) and are listed in table S1, together with the corresponding GenBank accession numbers. Further information is provided in the Supplementary Materials section (Table S2). At least three technical repeats from three biological replicates were carried out. Here, the $2^{-\Delta\Delta CT}$ method, for comparing relative expression results between treatments, was applied [34].

V. EXPERIMENTAL SECTION

5.1 P3HT-NPs synthesis and characterization. Spherical P3HT nanoparticles (P3HT-NPs) were prepared from freshly synthesized poly(3-hexylthiophene), P3HT, by the reprecipitation

method in the absence of surfactants. The polymer (7 mg) was dissolved in 350 μl of tetrahydrofuran (THF, solvent) at room temperature. The solution was subsequently added under magnetic stirring to 7 ml of ultrapure distilled water (non-solvent) ensuring a solvent:non-solvent 1:20 volume ratio. The colloidal suspension obtained in this way was washed repeatedly with ultrapure distilled water to remove THF. The preparation was carried out in sterile conditions employing sterilized laboratory glassware and water under laminar flow hood. Afterwards the nanoparticles were separated into fractions of different size by differential centrifugation employing sterilized centrifuge tubes. The nanoparticles employed in this study have a hydrodynamic diameter in the range 150-300 nm, as measured by Dynamic Light Scattering. Figure S1 shows the molecular structure of the polymer and a sketch illustrating the preparation of the P3HT-NPs. We also evaluated the total number of NPs present in the initial dispersion administrated to the animal, and the number of nanoparticles effectively uptaken within the Hydra animals. NPs have an initial concentration of 4.8 $\mu\text{g}/\text{ml}$. Considering the mass of isolated NP of about $38 * 10^{-15}$ g, we obtain that a dispersion containing approximately $25 * 10^6$ NP is administrated to the Hydra animals. The variation of the optical density of the dispersion before and after Hydra treatment is about 10%, meaning that an average of about 10^6 NPs are effectively internalized within the animal.

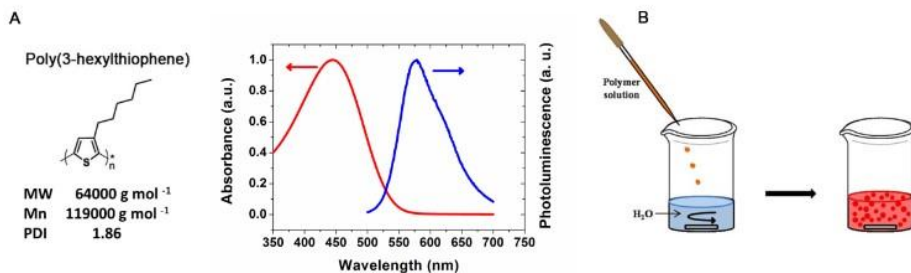


Figure S1. Characterization of P3HT-NPs. (A) Molecular structure, molecular mass and polydispersity index of the semiconducting polymer Poly(3-hexylthiophene). Absorption and photoluminescence spectra of the polymer in THF solution are also reported for direct comparison with the optical properties exhibited by the NPs in aqueous dispersion (see main text, Fig. 1). (B) Sketch of the preparation of P3HT-NPs by the reprecipitation method.

5.2 Influence of P3HT-NPs treatment on Hydra population growth rate.

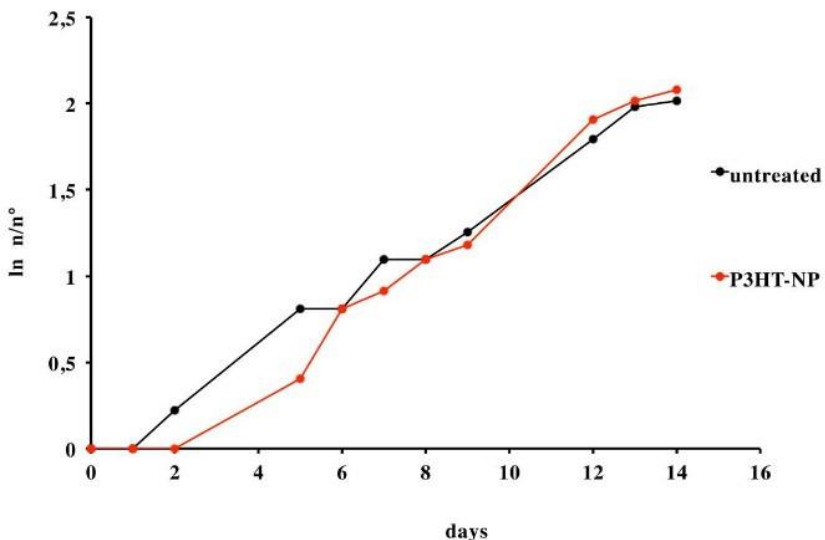


Figure S2. Impact of P3HT-NPs on Hydra population growth. The test started with a population of four polyps, treated 24 h with 50 μ M P3HT, washed and cultured under normal feeding regime. Every day new bud formation and detachment was monitored, along 14 days. The slope of the regression line for untreated animals which equation is $y=0,1588x -0,1196$ ($R^2 = 0,97205$) was similar to that of P3HT-NP treated animals $y = 0,1625x -0,2006$ ($R^2 = 0,96131$), showing similar growth rate for the two populations.

5.3 Polystyrene NPs do not alter Hydra behaviour nor modulate opsin expression.

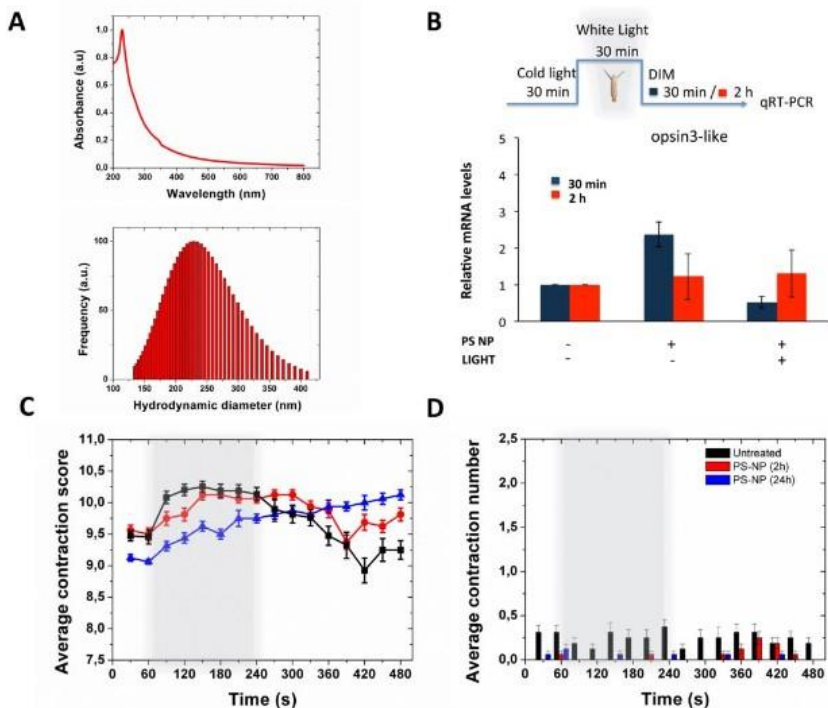


Figure S3. Evaluation of polystyrene NP impact on Hydra behaviour and gene expression. (A) Electrically inert NPs are entirely composed of polystyrene (PSNPs) and do have negligible absorption in the visible range. The zeta-potential is negative, with values amounting at -41.8 ± 1.1 mV. They present a spherical shape and dimensions comparable to the ones of P3HT-NPs. NPs were administrated to the animals at a $0.3 \mu\text{M}$ concentration, by following exactly the same protocols employed in the case of conjugated P3HT-NPs. No adverse toxicity effects were observed in treated animals. (B) The expression profile of opsin3-like gene was investigated by qRT-PCR analysis using Elongation factor 1-alpha (HyEf-1 α) as reference gene. Polyps treated with $0.3 \mu\text{M}$ PS-NPs for 24 hours underwent to the illumination protocol shown on the upper part of the panel, then they were allowed to recover for either 30 min or 2 hours and processed for RNA extraction and qRT-PCR analysis using specific primers. No direct correlation between PS-NP treatment and light illumination was found, the expression levels did not show significant differences among the considered experimental conditions. Data are presented as mean \pm SE of three technical repeats. (C, D) The animal behavior was not affected as well by the presence of PS-NPs, administrated at a $0.3 \mu\text{M}$ concentration for 2 hours and 24 hours. The adopted illumination protocol was the same as in experiments with P3HT-NPs. Neither the average contraction score nor the average number of contractions are significantly different from the values recorded in control, untreated samples. SD values are reported as bars for each data set ($n = 60$ and $n=16$, for untreated and treated animals, respectively).

5.4 Transcriptional profiling of opsin3-like gene under physiological light cycle.

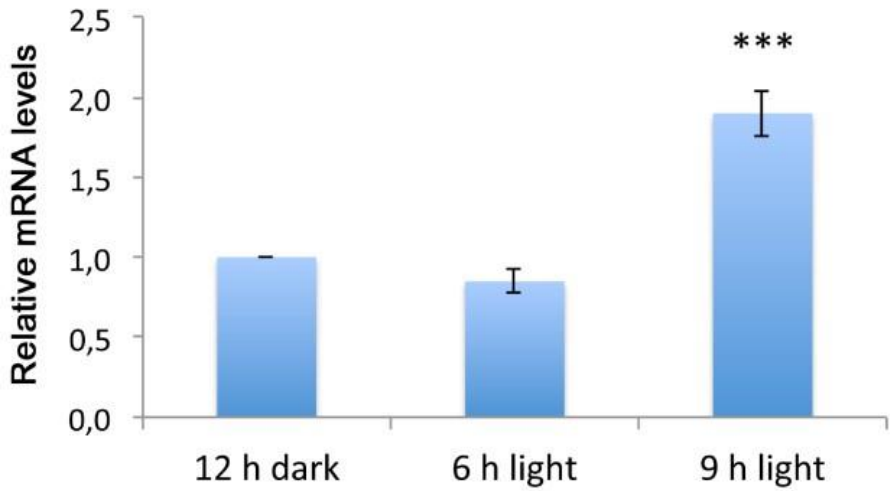


Figure S4. Light responsiveness of Hydra opsin3-like gene. Groups of 15 polyps from homogenous population, cultured under a 12:12 h light:dark regime, were collected in plastic multiwells, cultured in dark condition for 12 hours at 18°C and then exposed to further normal lighting condition for 6 hours and 9 hours. At each time point polyps were processed for RNA extraction and qRT-PCR analysis using specific oligonucleotides (table S1). The graph shows opsin3-like mRNA levels enhanced (~2-fold increase) at 9 hours, indicating the light response of this gene to normal light illumination. Data are presented as mean ± SE of three technical repeats from two biological replicates. Statistical comparisons are performed using unpaired t-test; ***P<0.0001.

5.5 Transcriptional analysis of opsin3-like and hsp70 genes under illumination condition employed for behavioural analysis.

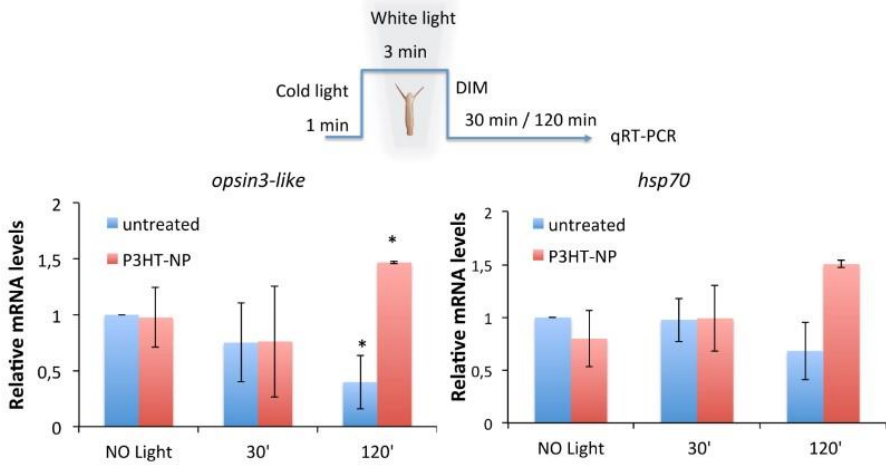


Figure S5. Gene profiling under short illumination condition. Animals were treated with P3HT-NPs (0.25 μ M) for 24 hours, then exposed 1 min to cold light, 3 min to white led (0.43 mW/mm²), and allowed to recover either 30 min or 120 min before processing for RNA extraction and qRT-PCR. The graphs show significant differences in the expression levels of *opsin3-like* gene in illuminated animals, at 2 hours time point, compared to control, not illuminated animals, while not differences were observed for *hsp70* expression levels. Data are the average \pm SD of three technical repeats from two biological replicates. Statistical comparisons are performed using unpaired t-test; *P<0.05.

5.6 Transcriptional profiling of *hsp70*, opsin3-like, *trpa1*-like and SOD genes under thermal stress.

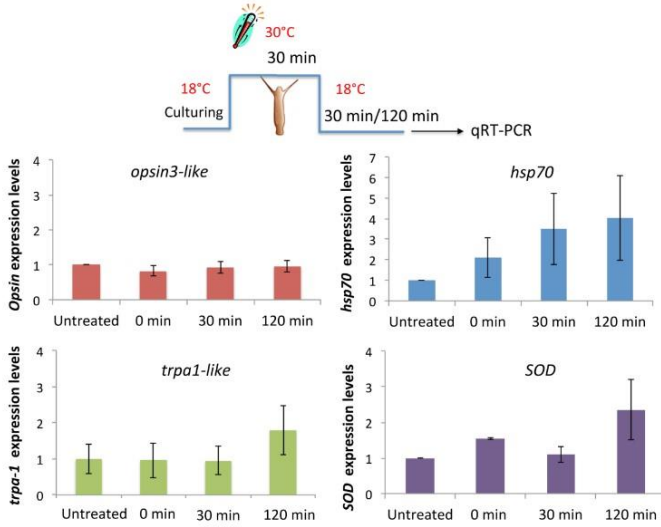


Figure S6. Hydra opsin3-like gene transcription does not respond to heat stress. Groups of 15 polyps were collected in plastic multiwells, heat shocked for 30 min at 30°C (using pre-warmed media) and allowed recovering for further 30 min and 120 min at 18°C. Polyps were then processed for RNA extraction and qRT-PCR analysis using specific oligonucleotides (table S1). The graph shows *hsp70* expression levels (blue bars) greatly enhanced (~ 4-fold increase) at both time points, confirming previous data (41); SOD gene expression (violet bars) was also activated 120 min post heat shock, indicating SOD heat responsiveness to 30°C (previous results obtained reported 34°C) (47); opsin3-like gene expression (red bars) was not affected by heat, while *trpa1* (green bars) shows a slight activation 120 min post thermal shock. These data ruled out the opsin responsiveness to heat shock, at least under these experimental conditions. Data represent mean \pm SE of three technical repeats from three biological replicates.

gene	accession number	Forward primer	reverse primer
<i>Opsin 3</i>	XP_012560869.1	ccattgtgtattcaagcggc	gccttaaccacatctcttgc
<i>Ef-1a</i>	XP_012553476.1	ccaggagacaatgctcggtt	gcttcaatggcaggatcatt
<i>hsp70.1</i>	XP_002159813	cgacgtattcagacaatcaacc	caattgaggaacacctctgg
<i>trpa</i>	XP_012561422.1	tgtaatctccattgcggc	cgattgcaagccatcagc
<i>SOD</i>	XP_12558939.1	agactccaattcccttgg	ccaatgacaccacaggacaa

Table S1. List of forward and reverse primers used in the qRT-PCR analysis.

5.7 Structural feature of Hydra predicted opsin3-like protein. Opsins are membrane proteins with molecular masses of 30-50 kDa related to the protein moiety of the photoreceptive molecule rhodopsin; the non-protein moiety is the retinal chromophore.

tax_id	Org_name	GeneID	CurrentID	Status	Symbol	Aliases	description	other_desig
6087	Hydra vulgaris	105848929	0	live	LOC105848929		opsin-3-like	
6087	Hydra vulgaris	105848626	0	live	LOC105848626		opsin-3-like	
6087	Hydra vulgaris	105847721	0	live	LOC105847721		opsin-3-like	
6087	Hydra vulgaris	105847534	0	live	LOC105847534		opsin-3-like	
6087	Hydra vulgaris	105847478	0	live	LOC105847478		opsin-3-like	
6087	Hydra vulgaris	105847123	0	live	LOC105847123		opsin-3-like	
6087	Hydra vulgaris	105846880	0	live	LOC105846880		opsin-3-like	
6087	Hydra vulgaris	105846852	0	live	LOC105846852		opsin-3-like	
6087	Hydra vulgaris	105846757	0	live	LOC105846757		opsin-3-like	
6087	Hydra vulgaris	105845815	0	live	LOC105845815		green-sensitive opsin-like	
6087	Hydra vulgaris	105845140	0	live	LOC105845140		opsin-3-like	
6087	Hydra vulgaris	105844887	0	live	LOC105844887		opsin-3-like	
6087	Hydra vulgaris	105844504	0	live	LOC105844504		opsin-3-like	
6087	Hydra vulgaris	105844139	0	live	LOC105844139		opsin-3-like	
6087	Hydra vulgaris	105843192	0	live	RLOC105843192	hydropsin4, opsin	rhodopsin, G0-coupled-like	
6087	Hydra vulgaris	101241514	0	live	LOC101241514		opsin-1, short-wave-sensitive 2-like	
6087	Hydra vulgaris	101241511	0	live	LOC101241511	hydropsin1, opsin	visual pigment-like receptor peropsin-like	
6087	Hydra vulgaris	101237418	0	live	LOC101237418	hydropsin2, opsin	melanopsin-A-like	
6087	Hydra vulgaris	101237290	0	live	LOC101237290	hydropsin3, opsin	melanopsin-B-like	
6087	Hydra vulgaris	101236896	0	live	LOC101236896	hydropsin6, opsin	opsin-3-like	
6087	Hydra vulgaris	101236169	0	live	LOC101236169	hydropsin7, opsin	opsin-3-like	
6087	Hydra vulgaris	101235476	0	live	LOC101235476		opsin-3-like	
6087	Hydra vulgaris	101235298	0	live	LOC101235298		opsin-3-like	
6087	Hydra vulgaris	101235253	0	live	LOC101235253		blue-sensitive opsin-like	
6087	Hydra vulgaris	101235116	0	live	LOC101235116		opsin-3-like	
6087	Hydra vulgaris	101234858	0	live	LOC101234858	hydropsin8, opsin	opsin-3-like	
6087	Hydra vulgaris	101234360	0	live	LOC101234360	hydropsin5, opsin	opsin RH1-like	
6087	Hydra vulgaris	100203903	0	live	LOC100203903		long-wave-sensitive opsin 1-like	
6087	Hydra vulgaris	100201535	0	live	LOC100201535		medium-wave-sensitive opsin 1-like	

Table S2. List of the opsin-like gene sequences present in the *H. vulgaris* genome database. Outputs from screening of Hydra genome database (table S2) revealed the presence of a wide repertoire of opsin which might be involved in light dependent phenomena different from vision, as suggested ^[37, 38].

Phylogenetic analyses showed the opsin family divided into seven subfamilies: the vertebrate visual (transducin-coupled) and non-visual opsin subfamily, the encephalopsin/tmt-opsin subfamily, the Gq-coupled opsin/melanopsin subfamily, the Go-coupled opsin subfamily, the neuropsin subfamily, the peropsin subfamily and the retinal photoisomerase subfamily (34, 51). Opsins have a seven-transmembrane structure similar to that of other GPCRs, but are distinguished by a lysine residue that is a retinal-binding site in the seventh helix. This residue is important for light absorption and its presence or absence can be used to judge whether or not a newly found rhodopsin-type GPCR is really an opsin. In both visual and non-visual systems opsins act as pigments by activating G proteins in a light-dependent manner. Several functional roles have been suggested, i.e. as retinal photoisomerases, generating the chromophore used by other opsins, in mechanosensation ^[35], temperature sensation ^[36], and some opsins have unknown functions ^[37]. Screening for opsin-like genes in the *Hydra vulgaris* genome database revealed multiple unique sequences annotated as opsins (Table S2). Although in literature Plachetzki characterized an opsin-like gene in Hydra ^[39], annotated as blue-sensitive opsin-like (XP_004208212.1), for our transcriptional analysis we selected an opsin3-like gene (XP_012560869), as representing one of the most abundant class of homologues. From predicted protein alignment it showed the conservation of the Lysine residue K296, the key position involved in retinal binding (Figure S7).

Hydra vulgaris	XP_012560869	AIFAKLSTITNVIINCFIVKSFKNQLLE
Homo sapiens	NP_055137	YLFAKSNTVYNPVIIYVFMIRKFRRSLLQ
Mus musculus	NP_034228	YLFAKSSTVYNPVIIYIFMNRKFRRSLLQ
Danio rerio	NP_001104634	SLFAKSSTAYNPVIIYAFMSRKFRRMCLQ

Figure S7. Alignment of opsin chromophore-binding transmembrane domain proteins from different animal species. The retinal binding amino acid conserved residues on opsin-3 primary sequence of chromophore-binding transmembrane domain is shown. Predicted Hydra opsin-3 like protein sequence is aligned with and human mouse and zebrafish opsin-3 protein sequences. Conserved residues are in light blue. In yellow the Lys 296 that forms a Schiff base with retinal.

We also aligned the Hydra vulgaris predicted protein sequences representative of different classes of opsin, i.e. opsin-3-like (XP_012560869.1), blue-sensitive opsin-like (XP_004208212.1) and long-wave-sensitive opsin1-like (XP_002163209.2) (Figure S8).

```

opsin3-like          -----MLNATAACYIILLKVKKKEITHLFIISLINMMLESIVGFI 41
blue-sensitive opsin MVLVALYTTYIVVLIALSTSLNLIICVVIIRKIKAEIPEHLPILSISISDIIVHTVVGLV 60
long-wave sensitive opsin -----MRDIIIMSLAICDGGVECTLGYP 23
                        : .:.*:*::: : :. :.*

opsin3-like          PDILTSDG-S-LINRTPLCISSGFTVFGCAITSIHTHIVLSFIRTLVIKYPFFYHKTCCK 99
blue-sensitive opsin SEVCVLHK-VTSLKNSYISVGASFLTYSISVSNIMQVIMISAIRVVALRKPMPFFKNCCK 119
long-wave sensitive opsin VELYGYANIDSPSQNEYLCKTNGFIVMYLAL TALTHLVFLCVHRYLVI VHPMKVQKFFTD 83
                        ::
                        :. . . .* . . : : : : . . * : : * : * .

opsin3-like          MW-VKATLIAMCYLYGFSWATFPLIGWSKYE-LDLDKKRCSLDWKL TQSDASASYFLTILI 157
blue-sensitive opsin VK-YKMASLCCCYFYGLLWASFPLLGWSKYE-EDLDKKRCSLDWNLTKNFSLMFAPI 177
long-wave sensitive opsin TKTCALYFIIPSWIYGLFWSITPLIGWSEIVREKEDTHRCTNMPDDLKRSYLALTL 143
                        : .:.*:*: * : **:*:*: . * .:*:*: : . . ** :

opsin3-like          FCNLLPAIVISTTLYTSRKIIS-KRN-----AREDCQNHQASLDILENDYLVNCLLSTGT 211
blue-sensitive opsin FCYKLP TLLI WALRVKHQT VDEHRR-----FRE--NRPNQQIEILEKAYLKVLLCSAIA 230
long-wave sensitive opsin FCYFLPAAILIYCI TKVH FELRNMLKCKQISGEDAAITRATYKLERQNFVLSVLS-IITS 202
                        ** *:* : : : : : : : * : : . : : : * * *

opsin3-like          FFFIWTYPYAVIGFLTILKIVIPTQLVTASAI FAKLSTITNVIINCFIVKSFKNQLLELRL 271
blue-sensitive opsin YFIVWTPYSVVVLLSIFKVKIPSIIFTFCALFAKLSAVLNALVNCYINKSPQAHLDRL 290
long-wave sensitive opsin FFLIWTPTYTCVCYLILGRELPGVILTYSA LFAKSSITLNP IYICIMYKFRQTVRSKV- 261
                        :*:*:*:*: * : * : * . * : * * * : * : * : * : * :

opsin3-like          IQYIRNINNKNS-AVHPCDDSKI---NYS 296
blue-sensitive opsin FQCFLKGKRIEHNISWAEETQVAETGFT 319
long-wave sensitive opsin RKLFRG-----PTVAPITE----- 275
                        : :
                        : :
  
```

Figure S8. Alignment of the predicted protein sequences representative of different classes of Hydra opsins. Predicted protein sequences encoding for blue-sensitive opsin-like (XP_004208212.1), opsin3-like (XP_012560869.1), and long wave-sensitive opsin1-like (XP_002163209.2) genes were aligned using the online tool COBALT ^[40] (available at www.ncbi.nlm.nih.gov/tools/cobalt/cobalt.cgi). The conserved residues of the chromophore-binding transmembrane domain (shown in fig. S7) are boxed (in red). K296 is highlighted in yellow. The alignment of selected Hydra opsin protein shows conservation of key residues involved in the phototransduction pathway, and suggests a functional role for opsin-like-3 gene in light transduction pathway.

REFERENCES

- [1] K. Deisseroth, *Nat. Neurosci.*, **2015**, 18, 1213–1225.
- [2] J. D. Spikes, *Photochem. Photobiol.*, **1991**, 54, 1079–1092.
- [3] N. Chalazonitis, *Photochem. Photobiol.* **1964**, 3, 539–559.
- [4] G. A. Kerkut, *Prog. Neurobiol.*, **1980**, 14, 1–23.
- [5] ^{a)}R. Chen, G. Romero, M. G. Christiansen, A. Mohr, P. Anikeeva, *Science*, **2015**, 347, 1477–1480. ^{b)} H. Huang, S. Delikanli, H. Zeng, D. M. Ferkey, A. Pralle, *Nat. Nanotechnol.*, **2010**, 5, 602–606.
- [6] ^{a)}L. Feng, C. Zhu, H. Yuan, L. Liu, F. Lv, S. Wang, *Chem. Soc. Rev.*, **2013**, 42, 6620–6633. ^{b)} L. Feng, L. Liu, F. Lv, G. C. Bazan, S. Wang, *Adv. Mat.*, **2014**, 26, 3926–3930. ^{c)} E. Miyako, J. Russier, M. Mauro, C. Cebrian, H. Yawo, C. Ménard-Moyon, J. A. Hutchison, M. Yudasaka, S. Iijima, L. De Cola, A. Bianco, *Angew Chem.* **2014**, 53, 13121–13125. ^{d)} M. Peters, N. Zaquen, L. D’Oliessaer, H. Bové, D. Vanderzande, N. Hellings, T. Junkers, A. Ethirajan, *Biomacromolecules*, **2016**, 17, 2562–2571. ^{e)} J. Pennakalathil, A. Özgün, I. Durmaz, R. Cetin-Atalay, D. Tuncel, *J. Polym. Sci. A Polym. Chem.*, **2015**, 53, 114–122.
- [7] E. Colombo, P. Feyen, M. R. Antognazza, G. Lanzani, F. Benfenati, *Front. Neurosci.*, **2016**, 10, 105.
- [8] ^{a)} Y. Takano, T. Numata, K. Fujishima, K. Miyake, K. Nakao, W. D. Grove, R. Inoue, M. Kengaku, S. Sakaki, Y. Mori, T. Murakamia, H. Imahori, *Chem. Sci.*, **2016**, 7, 3331–3337. ^{b)} Y. Lyu, C. Xie, S. A. Chechetka, E. Miyako, K. Pu, *J. Am. Chem. Soc.*, **2016**, 138, 9049–9052. ^{c)} W. Li, R. Luo, X. Lin, A. D. Jadhav, Z. Zhang, L. Yan, C. Y. Chan, X. Chen, J. He, C. H. Chen, P. Shi, *Biomaterials*, **2015**, 65, 76–85. ^{d)} F. Ye, C. Wu, Y. Jin, Y.-H. Chan, X. Zhang, D. T. Chiu, *J. Am. Chem. Soc.*, **2011**, 133, 8146–8149.
- [9] 1) U. Technau, R. E. Steele, *Development*, **2011**, 138, 1447–1458
- [10] K.-J. Baeg, M. Binda, D. Natali, M. Caironi, Y.-Y. Noh, *Adv. Mater.* **2013**, 25, 4267–4295. ^{b)} C. J. Brabec, S. Gowrisanker, J. J. Halls, D. Laird, S. Jia, S. P. Williams, *Adv. Mater.*, **2010**, 22, 3839–3856.
- [11] ^{a)} D. Ghezzi, M. R. Antognazza, M. Dal Maschio, E. Lanzarini, F. Benfenati, G. Lanzani, *Nat. Commun.*, **2011**, 2, 166. ^{b)} V. Benfenati, N. Martino, M. R. Antognazza, A. Pistone, S. Toffanin, S. Ferroni, G. Lanzani, M. Muccini, *Adv. Healthc. Mater.*, **2014**, 3, 392–399.
- [12] ^{a)} D. Ghezzi, M.R. Antognazza, R. Maccarone, S. Bellani, E. Lanzarini, N. Martino, M. Mete, G. Pertile, S. Bisti, G. Lanzani, F. Benfenati, *Nat. Photonics*, **2013**, 7, 400–406 (2013). ^{b)} M. R. Antognazza, M. Di Paolo, D. Ghezzi, M. Mete, S. Di Marco, J. F. Maya-Vetencourt, R. Maccarone, A. Desii, F. Di Fonzo, M. Bramini, A. Russo, L. Laudato, I. Donelli, M. Cilli, G. Freddi, G. Pertile, G. Lanzani, S. Bisti, F. Benfenati, *Adv. Healthc. Mater.*, **2016**, 5, 2271–2282.

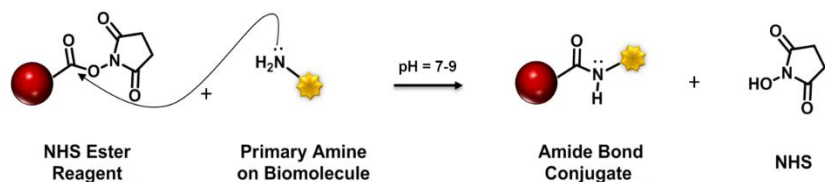
- [13] ^{a)} C. Tortiglione, in *Biomedical Engineering: From Theory to Application*, R. Fazel-Rezai, Ed. (InTech, **2011**), pp. 225–252. ^{b)} A. Ambrosone, C. Tortiglione, *Toxicol. Mech. Methods*, **2013**, 23, 207–216.
- [14] ^{a)} A. Ambrosone, L. Mattera, V. Marchesano, A. Quarta, A. S. Susha, A. Tino, A. L. Rogach, C. Tortiglione, *Biomaterials*, **2012**, 33, 1991–2000. ^{b)} A. Ambrosone, V. Marchesano, J. Bartelmess, F. Strisciante, A. Tino, L. Echegoyen, C. Tortiglione, S. Giordani, *Nanomaterials*, **2015**, 5, 1331–1350. ^{c)} A. Ambrosone, M. R. Scotto di Vettimo, M. A. Malvindi, M. Roopin, O. Levy, V. Marchesano, P. P. Pompa, C. Tortiglione, A. Tino, *Front. Bioeng. Biotechnol.*, **2014**, 2, 37.
- [15] ^{a)} M. A. Malvindi, L. Carbone, A. Quarta, A. Tino, L. Manna, T. Pellegrino, C. Tortiglione, *Small*, **2008**, 4, 1747–1755. ^{b)} J. Conde, A. Ambrosone, V. Sanz, Y. Hernandez, V. Marchesano, F. Tian, H. Child, C. C. Berry, M. R. Ibarra, P. V. Baptista, C. Tortiglione, J. M. de la Fuente, *ACS Nano*, **2012**, 6, 8316–8324. ^{c)} A. Ambrosone, V. Marchesano, S. Carregal-Romero, D. Intartaglia, W. J. Parak, C. Tortiglione, *ACS Nano*, **2016**, 10, 4828–4834.
- [16] ^{a)} D. C. Plachetzki, B. M. Degnan, T. H. Oakley, *PLOS ONE*, **2007**, 2, e1054. ^{b)} D. C. Plachetzki, C. R. Fong, T. H. Oakley, *Proc. Biol. Sci.*, **2010**, 277, 1963–1969. ^{c)} A. Terakita, E. Kawano-Yamashita, M. Koyanagi, *Wiley Interdiscip. Rev. Membr. Transp. Signal.*, **2012**, 1, 104–111. ^{d)} M. L. Porter, J. R. Blasic, M. J. Bok, E. G. Cameron, T. Pringle, T. W. Cronin, P. R. Robinson, *Proc. Biol. Sci.*, **2012**, 279, 3–14.
- [17] O. Wilby, J. M. Tesh, *Toxicol. In Vitro*, **1990**, 4, 582–583.
- [18] T. C. G. Bosch, C. N. David, *Dev. Biol.*, **1984**, 104, 161–171.
- [19] C. Tortiglione, A. Quarta, M. A. Malvindi, A. Tino, T. Pellegrino, *PLOS ONE* **4**, **2009**, e7698.
- [20] ^{a)} V. Marchesano, Y. Hernandez, W. Salvenmoser, A. Ambrosone, A. Tino, B. Hobmayer, J. M. de la Fuente, C. Tortiglione, *ACS Nano*, **2013**, 7, 2431–2442. ^{b)} A. Ambrosone, P. del Pino, V. Marchesano, W. J. Parak, J. M. de la Fuente, C. Tortiglione, *Nanomedicine*, **2014**, 9, 1913–1922.
- [21] M. Moros, A. Ambrosone, G. Stepien, F. Fabozzi, V. Marchesano, A. Castaldi, A. Tino, J. M. de la Fuente, C. Tortiglione, *Nanomedicine*, **2015**, 10, 2167–2183.
- [22] ^{a)} L. M. Passano, C. B. McCullough, *Proc. Natl. Acad. Sci. U.S.A.*, **1962**, 48, 1376–1382. ^{b)} L. M. Passano, C. B. McCullough, *J. Exp. Biol.*, **1964**, 41, 643–644.
- [23] ^{a)} C. Taddei-Ferretti, C. Musio, *J. Photochem. Photobiol. B*, **2000**, 55, 88–101. ^{b)} S. Guertin, G. Kass-Simon, *Comp. Biochem. Physiol. A Mol. Integr. Physiol.*, **2015**, 184, 163–170.
- [24] K. Gellner, G. Praetzel, T. C. G. Bosch, *Eur. J. Biochem.*, **1992**, 210, 683–691.
- [25] V. Malafoglia, L. Traversetti, F. Del Grosso, M. Scalici, F. Lauro, V. Russo, T. Persichini, D. Salvemini, V. Mollace, M. Fini, W. Raffaeli, C. Muscoli, M. Colasanti, *PLOS ONE*, **2016**, 11, e0151386.
- [26] S. Woo, A. Lee, H. Won, J. C. Ryu, S. Yum, *Biochem. Physiol.*, **2012**, 156, 37–41.

- [27] ^{a)} J. A. Westfall, J. C. Kinnamon, D. E. Sims, *J. Neurocytol.*, **1980**, 9, 725–732. ^{b)} Y. Takaku, J. S. Hwang, A. Wolf, A. Böttger, H. Shimizu, C. N. David, T. Gojobori, *Sci. Rep.*, **2014**, 4, 3573.
- [28] A. Terakita, *Biol.*, **2005**, 6, 213.
- [29] M. Koyanagi, E. Takada, T. Nagata, H. Tsukamoto, A. Terakita, *Proc. Natl. Acad. Sci. U.S.A.*, **2013**, 110, 4998–5003.
- [30] B. Wang, H. Yuan, C. Zhu, Q. Yang, F. Lv, L. Liu, S. Wang, *Sci. Rep.*, **2012**, 2, 766–773.
- [31] J. Liu, T.-M. Fu, Z. Cheng, G. Hong, T. Zhou, L. Jin, M. Duvvuri, Z. Jiang, P. Kruskal, C. Xie, Z. Suo, Y. Fang, C. M. Lieber, *Nat. Nanotechnol.*, **2015**, 10, 629–636.
- [32] J. Pecher, S. Mecking, *Chem. Rev.*, **2010**, 110, 6260–6279.
- [33] W. F. Loomis, H. M. Lenhoff, *J. Exp. Zool.*, **1956**, 132, 555–573.
- [34] K. J. Livak, T. D. Schmittgen, *Methods*, **2001**, 25, 402–408.
- [35] P. R. Senthilan, D. Piepenbrock, G. Ovezmyradov, B. Nadrowski, S. Bechstedt, S. Pauls, M. Winkler, W. Mobius, J. Howard, M. C. Göpfert, *Cell*, **2012**, 150, 1042–1054.
- [36] W. L. Shen, Y. Kwon, A. A. Adegbola, J. Luo, A. Chess, C. Montell, *Science*, **2011**, 331, 1333–1336.
- [37] E. Pennisi, *Science*, **2013**, 339, 754–755.
- [38] T. W. Holstein, *BMC Biol.*, **2012**, 10, 18.
- [39] D. C. Plachetzki, C. R. Fong, T. H. Oakley, *BMC Biol.*, **2012**, 10, 17.
- [40] J. S. Papadopoulos, R. Agarwala, *Bioinformatics*, **2007**, 23, 1073–1079.

Part III: Engineering thiophene-based nanoparticles to induce phototransduction in live cells under illumination

I. INTRODUCTION

Over the last few years a wide range of conjugated polymer nanoparticles have been described for application in (opto)electronics, biomedical photonics, theranostics, biosensing, drug delivery and bioimaging ^[1]. Polymer dots for live cell staining and in vivo imaging with narrow emission ranges and fluorescence quantum yields superior to those of commercial inorganic quantum dots have been reported ^[2]. Biocompatible nanoparticles having their surface modified with functional groups for specific targeting have been designed, the functionalization being generally carried out after the formation of the nanoparticles ^[3]. Here we aim at investigating conjugated polymer nanoparticles as phototransducers in living cells that allow controlling with light cell properties such as the membrane potential hence eventually cell's excitation/inhibition. To this purpose we are interested in the mechanism of light–biomatter interaction and more specifically we explore the nanoparticle localization within a cell culture and how this affects the nanoparticle ability to elicit a bioelectrical signal upon illumination. This approach is inspired by previous experiments where cells have been coupled to conjugated polymer films ^[4]. Since the interaction with cells is mediated by the particle surface we are interested in developing chemical strategies allowing the modulation of the interaction of the nanoparticles with live cells through the presence of specific functional groups on their surface. A possible way to deal with this problem is to prepare nanoparticles from preformed, properly functionalized, conjugated polythiophenes, owing to their easy functionalization by organic synthesis and the wide tunability of their functional properties. Nanoparticle water suspensions of poly(3-hexyl)thiophene (NPs-P3HT) have already been investigated for the preparation of active layers in photovoltaic cells and field-effect transistors as a viable alternative to thin films deposited from organic solvents ^[5]. More recently, NPs-P3HT have been tested in live cells and found to leave cell viability and reproducibility unaltered ^[6]. Herein, we report the synthesis of unprecedented poly(3-octylthiophenes) functionalized with the amine-reactive N-hydroxysuccinimidyl ester group (NHS) at the terminal position of the side alkyl chains and the preparation of the corresponding nanoparticles by the reprecipitation method ^[7] in the absence of surfactants. It is known that the NHS group binds covalently (and specifically) to primary amine groups present in amino acids, peptides or proteins, eliminating N-hydroxysuccinimide as the leaving group and forming a covalent amide bond (Scheme 1) at physiological pH in an aqueous environment, the reaction being faster under basic conditions. Thiophene fluorophores containing N-succinimidyl ester groups attached to alpha carbons are known to form amide bonds with the primary amine groups of monoclonal antibodies ^[8] and oligonucleotides ^[9].



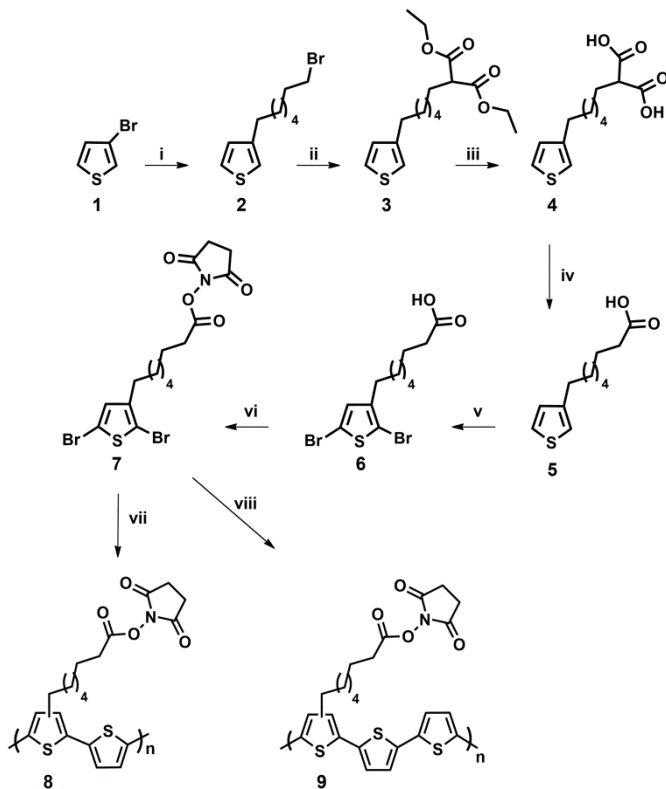
Scheme 1. Reaction of the N-succinimidyl ester group with a primary amine for the formation of an amide bond.

To prove that the external shell of NPs-NHS contains, as expected, amine-reactive NHS groups, and to optimize the reaction conditions, the nanoparticles were reacted with the *D* and *L* enantiomers of tryptophan, an amino acid containing a NH_2 group next to a chiral carbon. The formation of the nanoparticle-tryptophan amidic bond was monitored by circular dichroism (CD) since the presence of tryptophan in the external shell makes the nanoparticles chiral. Afterwards the NPs-NHS were administered to live HEK-293 cells and the cells-nanoparticles interaction was monitored by laser scanning confocal microscopy (LSCM). For comparison, the cells were also treated with NPs-P3HT of comparable size in the same experimental condition. We show that while NPs-P3HT are rapidly internalized by the cells, NPs-NHS remain docked on cell membrane. By means of whole-cell current clamp technique under light illumination, we show that light irradiation of NPs-NHS anchored to cell surface causes polarization of cell membrane while this is not the case of NPs-P3HT. Our results are the proof of principle that nanoparticles prepared from appropriately functionalized polythiophenes can acquire phototransduction properties under illumination.

II. RESULTS AND DISCUSSION

2.1 Synthesis and characterization of polymers and nanoparticles. The synthetic pattern for the preparation of polythiophenes alternating unsubstituted and 3-(2,5-dioxopyrrolidin-1-yl-8-octanoate) substituted thiophene units is shown in Scheme 2. Compounds **3-6** were obtained in very good yields (85-95%). In particular, acid **5** was obtained under vacuum in the absence of solvent, while its dibromination reaction was autocatalytic, i.e. it did not require addition of acid to the NBS solution as needed, for example, in the bromination of 3-hexylthiophene. To go from **2** to **5** we have preferred an alternative although longer way to that already reported for the preparation of the N-succinimidyl derivative^[10], in order to avoid the use of KCN. Once obtained the dibrominated N-succinimidyl ester **7**, there are numerous polymers alternating unsubstituted and 3-(2,5-dioxopyrrolidin-1-yl-8-octanoate) substituted thiophene units that could be prepared by reacting the latter with unsubstituted or substituted thienyl distannanes in the presence of palladium(0) catalysts (Stille reaction). Scheme 1 shows two of these possibilities with the units containing the NHS moiety alternating with one (polymer **8**) or two (polymer **9**) unsubstituted thiophenes. The detailed synthesis, characterization and physical properties of polymers **8** and **9**

are reported in Experimental Section. Note that as indicated in Scheme 2, polymers **8** and **9** are not regioregular, as the side chains can be located on one or the other of the β -positions of the substituted thiophene units. However, this is assumed to scarcely affect the characteristics of the corresponding NPs (see Figure 1) as well as the reactivity of the NHS functionality eight bonds away.



Scheme 2. Synthesis of 2,5-dioxopyrrolidin-1-yl 8-(2,5-dibromothiophen-3-yl)octanoate **7** and of the corresponding polymers **8**, **9**. *i*) *n*-BuLi, THF, -40°C , 1,6-dibromohexane; *ii*) Na_{Et} , EtOH, Diethyl Malonate, THF, 0°C ; *iii*) $\text{KOH}_{\text{(aq)}}$ 20%, reflux, $\text{HCl}_{\text{(aq)}}$ 6N; *iv*) 160°C , vacuum; *v*) NBS, THF, 0°C ; *vi*) NHS, DMAP, DCC, THF, room T; *vii*) 2,5-bis(tributylstannyl)thiophene, $\text{Pd}(\text{PPh}_3)_4$, Toluene, reflux; *viii*) 5,5'-bis(tributylstannyl)-2,2'-bithiophene, $\text{Pd}(\text{PPh}_3)_4$, Toluene, reflux.

For the formation of NPs-NHS nanoparticles, polymers **8** and **9**, which owing to the octyl chains display good solubility in organic solvents, were dissolved in THF (solvent) at room T. The solution was subsequently added to H_2O (non-solvent) under magnetic stirring. For details see SI. Scanning Electron Microscopy (SEM) images, Dynamic Light Scattering (DLS) data (mean size, polydispersity and Z potential) of NPs-NHS, are

reported in Figure 1 together with the normalized absorption and photoluminescence spectra of the nanoparticles dispersion in water suspension, compared to those of the corresponding polymers in CHCl_3 . The figure shows that both polymers afford nanoparticles with spherical morphology, similar diameter and polydispersity. The Z potential is -33 and -41 mV, indicating good stability of the colloidal nanoparticles. The features of absorption and emission signals of both polymers are very similar, as well as the shifts observed on passing from the polymers in chloroform to the nanoparticles in water, similar in turn to those already observed for NPs-P3HT [6]. For comparison SEM and DLS data of NPs-P3HT of comparable size are reported in SI.

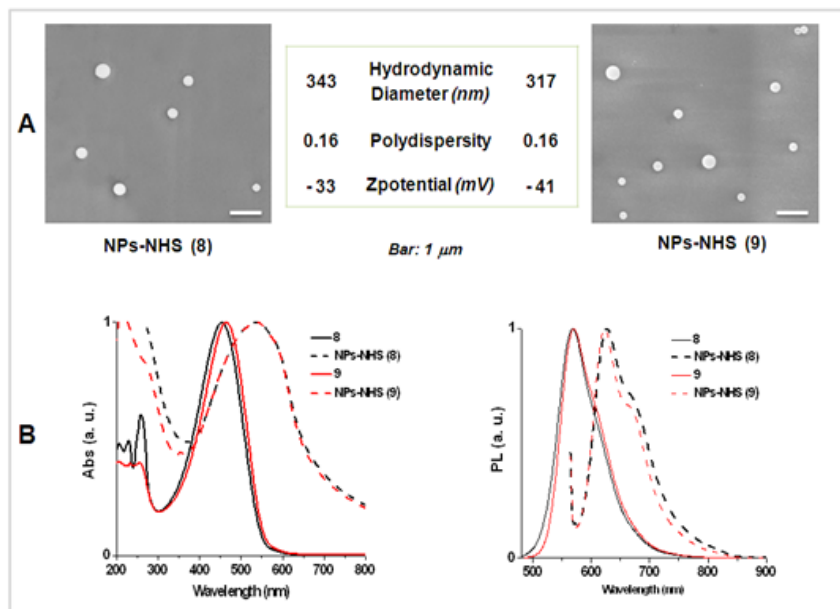


Figure 1. A) Scanning Electron Microscopy (SEM) images and DLS characterization of nanoparticles from polymers **8** and **9**. Z-potential ± 2.5 and ± 1.9 mV, respectively. B) Absorption and photoluminescence spectra of polymers **8**, **9** in CHCl_3 and of the corresponding nanoparticles in water suspension.

To get information on the stability in water of the N-hydroxysuccinimidyl head of the NPs-NHS, proton NMR experiments were carried out. The proton NMR spectrum of NPs-NHS from polymer **8** is shown in Figure 2. In order to analyze the NPs-NHS water suspension by proton NMR, the nanoparticles were prepared using THF-*d*8 as the solvent and D_2O as the non-solvent. The proton signals are much broader than those of the spectrum of **8** in chloroform (Figure S7) but cover roughly the same spectral regions: 0.5-2 ppm for the alkyl groups of the side chains, around 2.5 ppm for the methylene protons of the NHS groups. At $t=0$ (arbitrarily taken at the beginning of the registration of the

NMR spectrum after the preparation of the nanoparticles, Figure 2A), no sharp signal is observed in the region around 2.5 ppm. Instead, after 2h (Figure 2B) a sharp signal is present at 2.7 ppm that we assign to the presence of free N-hydroxysuccinimide due to hydrolysis of the NHS group.

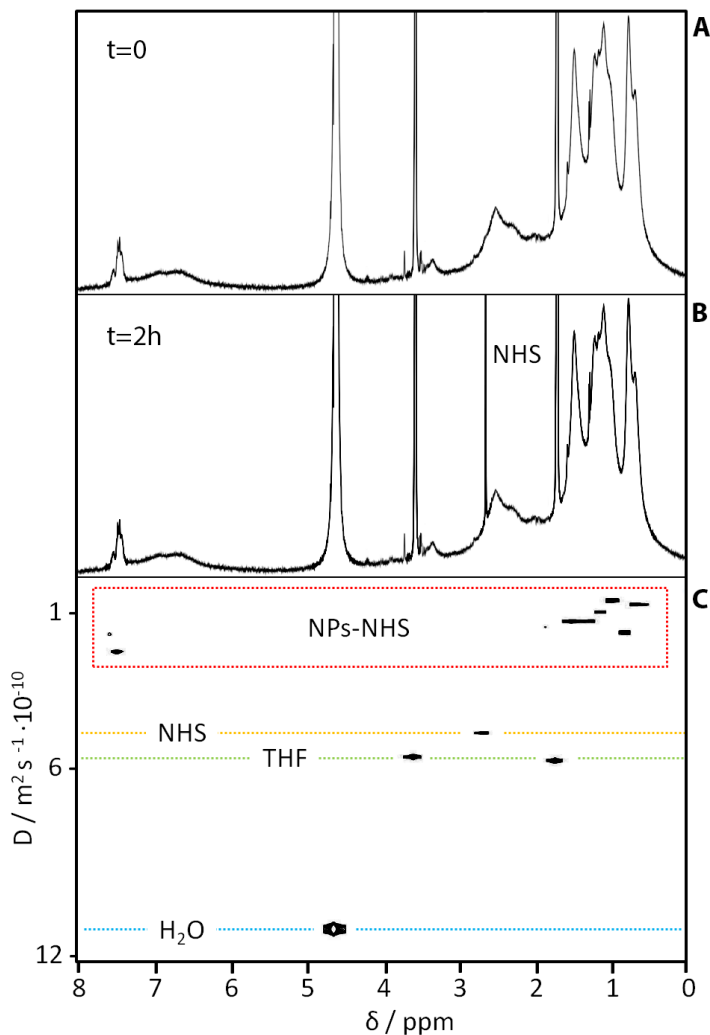


Figure 2. Proton NMR spectra of NPs-NHS obtained from polymer **8** in D₂O dispersion: A) just after preparation (t=0), B) after 2 hours (t=2h) and C) DOSY NMR spectrum of the sample at t=2h showing the formation of free NHS.

Clearly, after two hours the hydrolysis degree is still very limited. The broad multiplet in the region 6.2-7.5 ppm arises from the aromatic protons of the polymer backbone. The most intriguing feature of this region of the spectrum is the much better resolved and narrower multiplet centered at 7.5 ppm. The features of this multiplet are very similar to those of the aromatic region of the spectrum of polymer **8**. To make sure that this part of the spectrum belongs to the nanoparticles we carried out a DOSY NMR experiment, which is reported in Figure 2C. Diffusion Ordered Spectroscopy (DOSY) allows to resolve spectroscopically different components of a mixture on the basis of their diffusion coefficients, which depend on shape and size of the compounds [11]. In this experiment the radiofrequency pulses used in routine NMR are combined with magnetic field gradients encoding spatial information, i.e. the position of the different components along the NMR tube. The distance covered by a nanoparticle is in general around one order of magnitude less than that covered by a molecule. In the DOSY spectrum of Figure 2C the horizontal and vertical axis report the proton chemical shifts and the diffusion coefficients, respectively. The small molecules present in solution – THF, N-hydroxysuccinimide and H₂O – show high diffusion coefficients while the NPs display much lower values, from three to ten times lower than those of the small molecules. More importantly, from our point of view, the more resolved multiplet at 7.5 ppm displays a diffusion coefficients in the range of the NPs-NHS. In other words, this signal is not due to impurities but unambiguously belongs to the NPs-NHS. Nanoparticles are complex systems and the outer layer chains of polymer may have different conformation from the inner layers. Our hypothesis is that these signals are due to nanoparticles with looser segmental packing of the external chains arising from differences in local polymer-solvent interactions induced by the hydrophilic heads of the side chains. This hypothesis is in agreement with the fact that similar signals are not observed in the proton NMR spectrum of nanoparticles prepared from poly(3-hexylthiophene) in D₂O/THF-*d*8 (Figure S11).

2.2 Reaction of NPs-NHS towards primary amine groups of *D* and *L*-tryptophan. The newly synthesized nanoparticles with hydrophilic N-succinimidyl ester heads were tested for their reactivity towards primary amine groups employing *D* and *L* enantiomers of tryptophan. *L*-tryptophan - namely (S)-2-amino-3-(3-indolyl)propionic acid - is commonly found in animal and plant proteins and is essential for the functioning of many organs in the body where it is converted by successive steps to serotonin, the hormone transmitting signals between nerve cells [12]. A sketch of the post-functionalization of NPs-NHS with tryptophan is shown on top of Figure 3. Tryptophan is characterized by large optical activity and blue fluorescence, see Figure S15. To optimize the conditions for the reaction of NPs-NHS with tryptophan, a terthiophene containing one inner 3-(2,5-dioxopyrrolidin-1-yl-8-octanoate) substituted thiophene ring was synthesized, reacted with tryptophan and the corresponding conjugate **11** separated and analysed by NMR and mass spectroscopy. The details are given in SI (Scheme S3, Scheme S4, Figure S9, Figure S10, Figure S12, Figure S13, Figure S14).

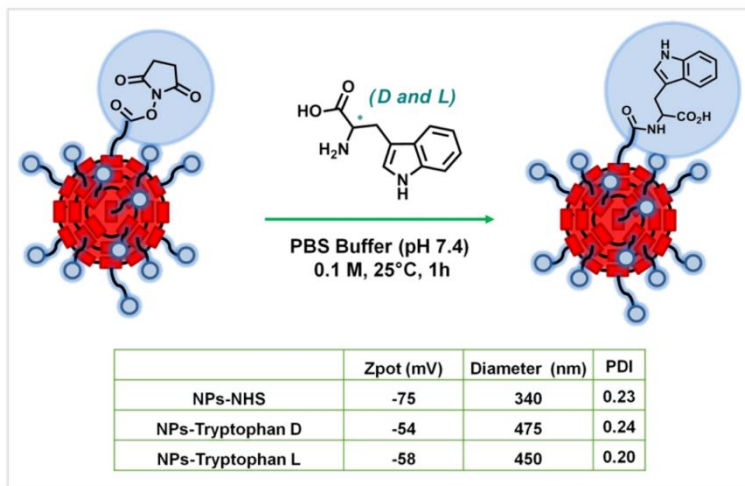


Figure 3. Sketch of the reaction of NPS-NHS with tryptophan (*D* and *L*) and DLS data of the corresponding nanoparticles. Z-potential ± 1.9 , ± 0.4 and ± 0.4 mV, respectively.

Using the optimized conditions (PBS buffer pH 7.4, 0.1 M concentration, 25°C and 1 h time) the NPs-NHS were incubated with *D* and *L* tryptophan (details in experimental section). The reaction product was chromatographed using a Sephadex G-50 column to separate the conjugate from unreacted tryptophan. Figure 3 shows the DLS characteristics of the resulting nanoparticles. The conjugated nanoparticles display a Z potential value indicating still remarkable stability, low polydispersity and sizeably increased diameter (of more than 100 nm). Figure 4A shows the UV and CD spectra of the nanoparticles conjugated with *D* and *L* tryptophan. For comparison, Figure 4B shows the UV and CD spectra of *D* and *L* tryptophan in water. The nanoparticles conjugated with *D* and *L*-tryptophan display identical absorption spectra but opposite circular dichroism values, due to the opposite chirality sign of the chiral shell formed upon reaction of the NHS groups on the surface of the nanoparticles with the primary amine groups of tryptophan. Interestingly, the CD spectra show also a signal - opposite for *D* and *L*-tryptophan - in the region 500-600 nm, i.e. in the absorption region of polythiophene. This indicates that there is chirality transfer from the chiral shell to the covalently bound polythiophene. Chirality transfer has already been observed in nanoparticles obtained from organic polymers ^[13].

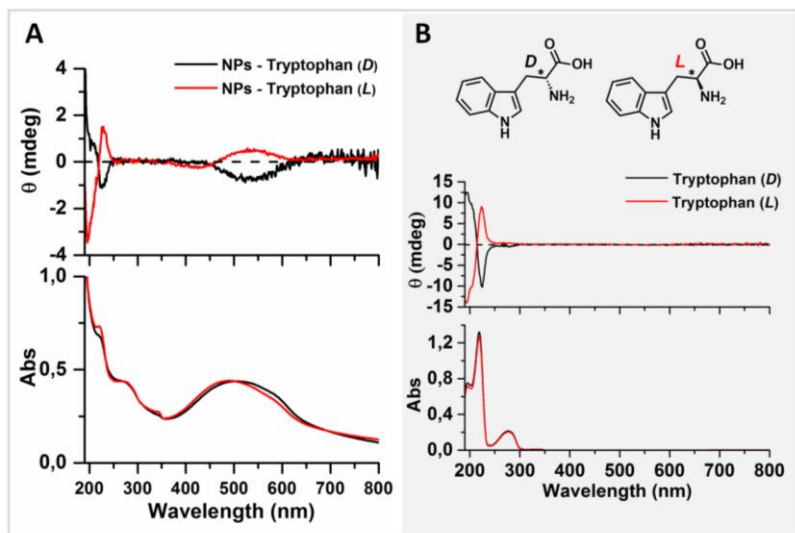


Figure 4. Absorption and circular dichroism spectra of NPs-Tryptophan *D* and NPs-Tryptophan *L* (A) and absorption and circular dichroism spectra of tryptophan *D* and *L* for comparison (B).

Chirality transfer has different origins depending on the system observed and its environment (see, for example, reference [14]). In the present specific case the phenomenon of induced chirality is probably related to polythiophene geometry and conformation changes stimulated by the adjacent chiral carbons of tryptophan and made possible by the geometric adaptability of the thiophene ring to the environment [15].

2.3 A comparative study of live HEK-293 cells treated with NPs-NHS and NPs-P3HT. Human embryonic kidney HEK-293 cells are extensively used in cell biology and pharmacological research for their easy growth and transfection. NPs-NHS obtained from polymer **9** and prepared in sterile conditions were incubated with HEK-293 cells and the outcome compared to that obtained using sterile NPs-P3HT [6]. Table S1 compares mean size, polydispersity and Z-potential of NPs-NHS and NPs-P3HT used for incubation with the cells. HEK-293 cells were plated at a concentration of 3×10^4 cells/wall and after 24 hours were incubated for 30 min at 37 °C with NPs in PBS buffer suspension (pH 7.4) at a concentration to give optical density value of 0.2. MTT viability assays on HEK-293 cells treated with NPs-NHS and NPs-P3HT are reported in SI (Figure S20). In both cases cell proliferation is increased as the incubation time increases. However, cells treated with NPs-NHS display much lower cell activity [16] than those exposed to NPs-P3HT, indicating that further refinement of nanoparticles structure is required to fully prevent cytotoxicity. Work is in progress in this direction.

Figure 5 shows a set of laser scanning confocal (LSCM) images at different depths of cell cultures treated with NPs-NHS for 30 m (Figure 5A) and 24 h (Figure 5B). Corresponding images for NPs-P3HT are shown in Figure S19.

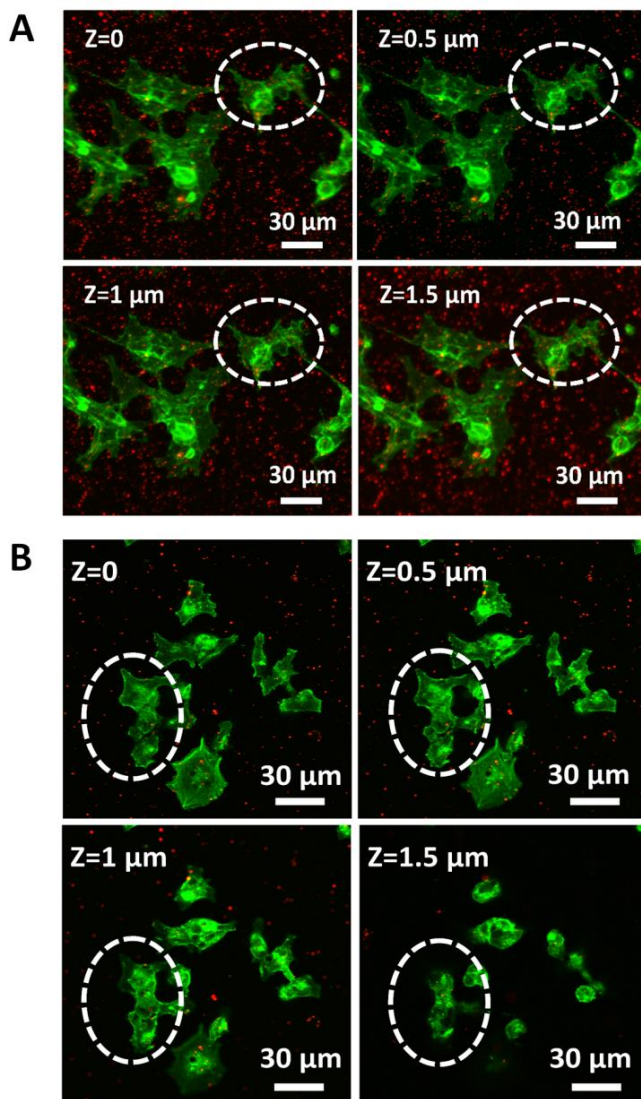


Figure 5. LSCM images of successive slices of HEK-293 cells incubated for 30 m (A) and 24 h (B) with NPs-NHS. Cells cytoskeleton was stained with phalloidin (in green), while the nanoparticles are seen in red channel. Scale bar 30 μm.

After treatment, cell cultures were fixed and the cytoskeleton was stained with phalloidin (visible in green), while the nanoparticles are visible as red spots. Fluorescence confocal images were acquired by scanning the entire specimen from bottom to top and incrementing the focal plane of few hundreds of nm for each step. Additional data are reported in SI (Figure S21, Figure S22, Figure S23 and videos S1.gif, S2.gif and S3.gif). Confocal images indicate that NPs-NHS remain on cell membrane, while P3HT are completely internalized after 30 minutes incubation, in agreement with what we had already observed ^[6]. Figure 5 shows that in the images situated on successive focal planes (z-stacks) the red fluorescence of NPs-NHS progressively comes into focus and describes the border of the cell. By contrast NPs-P3HT show a different behavior, red fluorescent spots being present at any focal plane, indicating full internalization of the nanoparticles (see again Figure S22 and videos S1.gif, S2.gif and S3.gif). The inability of NPs-NHS to cross the cell membrane is mainly ascribed to the reaction of the NHS group with primary amine groups of membrane proteins and formation of an amidic bond docking the nanoparticles on cell membrane. It cannot be excluded that some NPs-NHS could react with amine groups belonging to the numerous molecules present in the culture medium. In this case a ‘hard corona’ would be formed around the nanoparticles which could affect the mechanism of NPs internalization ^[17]. A pictorial illustration of the different behavior of NPs-NHS and NPs-P3HT with respect to the cells is given in Figure 6. The docking of the nanoparticles on cell membrane should facilitate their interaction with the cells through modification of the membrane potential upon an external stimulus.



Figure 6. Pictorial illustration of NPs-NHS docking on surface membrane of cells and forming 2D aggregates (A) and NPs-P3HT that cannot be retained by the membrane and are internalized by the cells (B).

Here we aim at using light for affecting the cell membrane resting potential, thus mimicking a very fundamental mechanism in biological signaling. We apply the whole-cell current clamp technique under light illumination. Cell cultures were shone with 20 ms and 200 ms light pulses ($\lambda=550$ nm, Intensity= 207 mW/mm²) and membrane potential variation was recorded during and after illumination (more details in SI). In Figure 7a and 7b, representative traces of membrane potential variation are shown for cell cultures treated with NPs-NHS (in red), with NPs-P3HT (in blue) and untreated samples as controls (in black). The green box represents the light exposure time interval (20 and 200 ms). In case of cell cultures treated with NPs-NHS, a slow transient depolarization peak arises at the beginning of the light stimulus represented by the green box. At the end of the illumination the membrane potential recovers its original resting value after the

hyperpolarization. Instead, no evident signal is observed in the case of cell cultures treated with NPs-P3HT and control samples (cells without NPs). Similarly, by shining light for 200 ms, the functionalized NPs-NHS were able to excite an initial depolarization and major hyperpolarization during the light pulse, while NPs-P3HT and untreated sample gave no statistically different answers. Electrophysiology shows that at same experimental conditions (particle size, concentration, incubation time, light intensity, cell plating) NPs-NHS display a photoinduced change in the membrane potential of cultured HEK-293 cells, while NPs-P3HT do not. The observed patch clamp signal upon illumination with a radiation wavelength resonant with P3HT absorption peak is a membrane potential depolarization ($\Delta V > 0$) followed by an hyperpolarization ($\Delta V < 0$). These results recall what was recently detected by using the same techniques for measuring HEK-293 cells plated onto a P3HT polymer film [4a, 5a]. In that case authors conclude that the origin of the photoinduced signal is a light induced enhancement of the temperature causing the increase of the membrane capacitance on a faster time scale and a change in the transmembrane potential on a slower timescale, respectively appearing as depolarization and hyperpolarization.

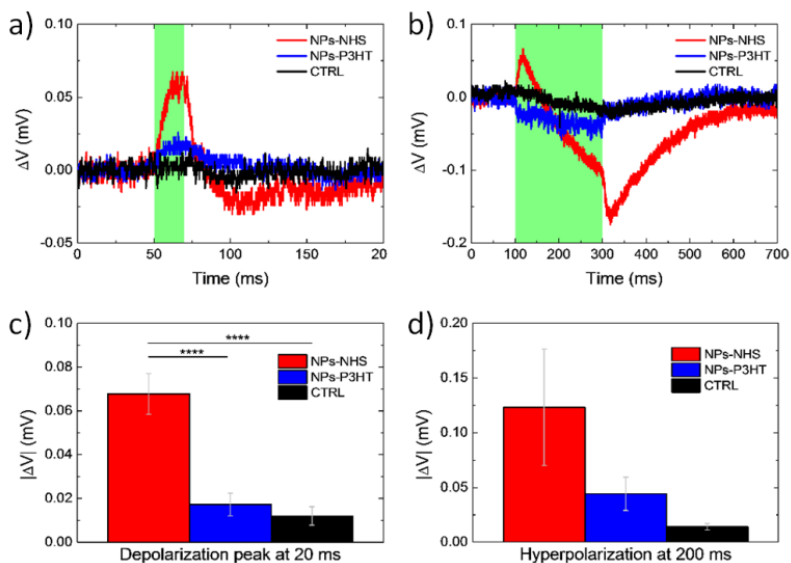


Figure 7. Representative membrane potential variation traces for in vitro samples treated with NPs-NHS (in red), NPs-P3HT (in blue) and untreated cells (in black) and illuminated for 20 ms (a) and 200 ms (b). Average values of depolarizing peak during 20 ms light stimulus (c) and hyperpolarization during 200 ms light stimulus (d) obtained by averaging over the last 50 ms of light stimulus (n=10 cells, Student's t-test).

As we argue in detail in experimental section, in order to ascribe the photoinduced mechanisms active with our NPs-NHS to the same thermal effect, we should consider NPs-NHS aggregation. In particular, due to the peculiar docking of the single NPs-NHS on cell membrane, a quasi 2D aggregation could be envisaged, where the NPs coagulate in a surface patch of more than 1 μm radius on top of the cell (Figure S24 and Table S2). This local modification of the cell outskirts could result into a photoactive site able to absorb visible light and convert it into local heating, thus affecting the membrane potential. This explanation is fully consistent with the thermal-like response of the cell, but it is difficult to be experimentally tested as imaging does not provide enough resolution. Alternatively, single particles or small aggregates sitting on cell membrane could induce a change in the membrane potential by other means but thermal, like electrical polarization or electron transfer reactions. Both mechanisms are plausible, however further experiments are required before a clear-cut answer can be given.

III. CONCLUSIONS

We describe an innovative approach to confer phototransduction capability on polythiophene based nanoparticles in live cells. Our approach is based on the synthesis of polythiophene nanoparticles (NPs-NHS) having on the surface amine-reactive N-succinimidyl ester functionalities starting from novel, appropriately functionalized, polythiophenes. In PBS buffer (pH 7.4) the nanoparticles form an amidic bond with biomolecules having available primary amine groups and give rise to nanoparticle-biomolecule conjugates. In the presence of live HEK cells NPs-NHS are not internalized but are docked on cell membrane, a behavior opposite to that of NPs-P3HT which are rapidly internalized. We show that in the former case light irradiation affects the cell membrane potential whereas in the latter it does not. Thus the nanoparticles docked to cell membrane become a photoactive site capable to absorb visible light and convert it to an electrical signal. Our results suggest a crucial role of bioconjugation in bestowing the photo-transducing function to the nanoparticles. It is worth mentioning that although this is not the focus of this work, the nanoparticles having NHS groups on the surface are very reactive and can easily be grafted to any surface containing primary amine groups. Moreover, post-functionalization with a chiral molecule containing a primary amine group confers on the nanoparticles chiroptical properties whose sign depends on ligand chirality, as we demonstrate in the case of the amino acid tryptophan.

IV. METHODS

4.1 Synthesis and characterization. All synthetic details are given in Experimental Section. Chemicals: 3-Bromothiophene, *n*-butyllithium 2.5 M in hexane, 1,6-dibromohexane, Sodium $\geq 99\%$ pieces, diethyl malonate, N-bromosuccinimide (NBS), N-hydroxysuccinimide (NHS), 4-(dimethylamino)pyridine (DMAP), N,N'-dicyclohexyl-

carbodiimide (DCC), bis(tributylstannyl) thiophene, tetrakis(triphenylphosphine)palladium(0) and 5-5'-bis (tributylstannyl)-2,2'-bithiophene were purchased from Sigma-Aldrich Co. Hydrochloric acid 37% RPE, potassium hydroxide pellets RPE and sodium bicarbonate RPE were purchased from Carlo Erba Reagents. All reagents and solvents were used as received. Characterizations: ^1H NMR and ^{13}C NMR spectra were recorded on a Varian Mercury-400 spectrometer equipped with a 5-mm probe. Chemical shifts were calibrated using the internal CDCl_3 resonance which was referenced to TMS. Mass spectra were collected on a Thermo Scientific TRACE 1300 gas chromatograph. UV-Vis spectra were recorded using a Agilent Technologies CARY 100 UV-Vis spectrophotometer. Photoluminescence spectra were collected on a Perkin Elmer LS50 spectrofluorometer. More details are given in Experimental Section.

4.2 Cell culture. HEK-293 cells were grown in DMEM with 10% FBS supplemented with 2 mL-glutamine, 100 $\mu\text{g}/\text{ml}$ streptomycin, 100 U/ml penicillin, cells were kept in T75 culture flasks and maintained in incubators at 37 °C in a humidified atmosphere with 5% CO_2 . After reaching 80%-90% of confluence, cells were detached by incubation with 0.5% trypsin/0.2% EDTA and plated for further expansion and experiments.

4.3 Immunofluorescence analysis. Cells grown on fibronectin-coated glass coverslips were washed twice with PBS and fixed for 20 min at RT in 4% paraformaldehyde and 4% sucrose in 0.12 M sodium phosphate buffer, pH 7.4. Fixed cells were pre-incubated for 20 min in gelatin dilution buffer (GDB: 0.02 M sodium phosphate buffer, pH 7.4, 0.45 M NaCl, 0.2% (w/v) gelatin) containing 0.3% (v/v) Triton X-100, and subsequently incubated with Phalloidin Alexa Fluor 488 conjugated in GDB for 1h at RT and finally washed with PBS, and incubated for 5 min with 1 μM DAPI in PBS. The confocal images were acquired with Fluoview FV10i Olympus with 60x objective.

4.4 Electrophysiology. Intracellular recordings were performed with a patch-clamp setup (Axopatch 200B, Axon Instruments). HEK-293 cells were measured at 1 DIV in whole-cell configuration with freshly pulled glass pipettes (3-6 M Ω), filled with the following intracellular solution [mM]: 12 KCl, 125 K-Gluconate, 1 MgCl₂, 0.1 CaCl₂, 10 EGTA, 10 HEPES, 10 ATP-Na₂. The extracellular solution contained [mM]: 135 NaCl, 5.4 KCl, 5 HEPES, 10 Glucose, 1.8 CaCl₂, 1 MgCl₂. Only single HEK-293 cells were selected for recordings. All measurements were performed at room temperature. Acquisition was performed with pClamp 10 software suite (Axon Instruments) and all data were elaborated with Origin 8.0.

V. EXPERIMENTAL SECTION

5.1 Synthesis. Organic solvents were dried by standard procedures. Thin-layer chromatographies (TLCs) were carried out on 0.2-mm thick plates of silica gel 60 F₂₅₄ (Merck). Visualization was accomplished by UV light or phosphomolybdic acid solution. Silicagel chromatographies were performed on glass columns of different sizes hand packed with silica gel 60 (particle sizes 0.040-0.063 mm, Merck). Unless otherwise noted, all reactions were carried out under a dry, oxygen-free nitrogen atmosphere.

¹H NMR and ¹³C NMR spectra were recorded on a Varian Mercury-400 spectrometer equipped with a 5-mm probe. Chemical shifts were calibrated using the internal CDCl₃ resonance which was referenced to TMS. Mass spectra were collected on a Thermo Scientific TRACE 1300 gas chromatograph. UV-Vis spectra were recorded using a Agilent Technologies CARY 100 UV-Vis spectrophotometer. Photoluminescence spectra were collected on a Perkin Elmer LS50 spectrofluorometer. Fluorescence measurements were performed using an excitation wavelength corresponding to the maximum absorption wavelength. Dynamic light scattering (DLS) measurements were performed with a Nanobrook Omni Particle Size Analyzer, with a wavelength of 659 nm in backscattering mode. Nanoparticles were dispersed in deionized water during analysis and measurements were taken at 25°C. Zeta potential measurements were performed using Smoluchowski equation. Circular Dichroism (CD) spectra were recorded using a spectropolarimeter JASCO J-715 in water under ambient conditions. Scanning Electron Microscopy (SEM) images were collected with a SEM-FEG Zeiss LEO 1530 operating at V_{acc} = 5 keV. The nanoparticles were drop casted onto Si/SiO₂ wafers and dried under vacuum with no further treatment.

3-(6-bromohexyl)thiophene (2) → A 100 mL two-necked round-bottom flask equipped with a stirrer bar was charged with 3-bromothiophene (4 g, 0.024 mol) and distilled hexane (30 mL) under N₂ atmosphere. The flask was cooled to -40°C and the solution was stirred for 15 min. *n*-BuLi (10.8 mL, 0.027 mol) was added dropwise *via* syringe over 10 min. The mixture was stirred for 15 min, and anhydrous THF (3.5 mL) was added dropwise over 5 min. The solution was stirred for 1 h, the cooling bath was replaced with an ice-salt bath, and then the mixture was warmed to -10 °C. 1,6-Dibromohexane (15.1 mL, 0.098 mol) was added in one portion, and then the solution is left to return to room temperature and stirred 24 h. The mixture was concentrated under vacuum and extracted three times with CH₂Cl₂/H₂O. The resulting crude product was purified under vacuum distillation at 150°C for 1 h, to remove the starting material in excess (1,6-dibromohexane) and then filtered through silica gel (cyclohexane) to provide 2.10 g of product. Colorless oil; yield 50%. EI-MS *m/z* 248 (M⁺). ¹H NMR (400 MHz, CDCl₃, TMS/ppm): δ 7.23 (dd ³J=5.2 Hz, ³J=3.2, 1H), 6.93 (m, 2H), 3.40 (t, 2H), 2.65 (t, 2H), 1.91-1.84 (m, 2H), 1.67-1.62 (m, 2H), 1.52-1.48 (m, 2H), 1.47-1.36 (m, 2H). ¹³C NMR (400 MHz, CDCl₃) δ 142.8, 128.2, 125.2, 119.9, 33.9, 32.7, 30.3, 30.1, 28.4, 27.9.

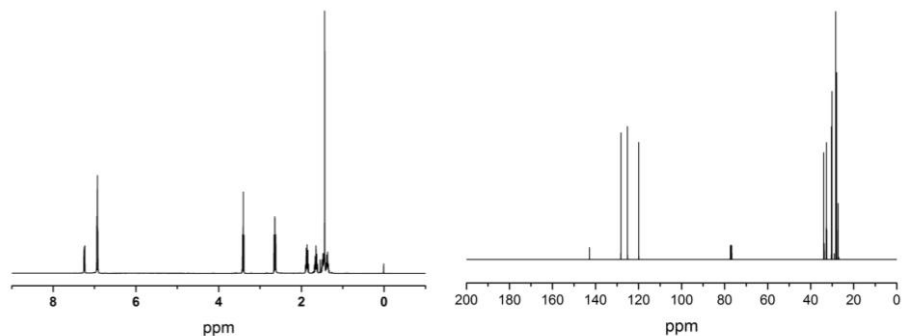


Figure S1. ^1H and ^{13}C NMR spectra of compound **2**.

Diethyl 2-(6-(thiophen-3-yl)hexyl)malonate (3) → A 100 mL two-necked round bottom flask was cooled to $-10\text{ }^\circ\text{C}$, charged with sodium (0.237 g, 0.0103 mol) and anhydrous ethanol (40 mL) under N_2 atmosphere. The solution was stirred until the complete dissolution of sodium (20 min) and then diethyl malonate (2.2 g, 0.0138 mol) was added dropwise over 15 min. After 30 min 3-bromohexylthiophene (1.7 g, 0.0069 mol) was added dropwise and the solution was stirred for 48 h. The reaction was quenched with HCl aqueous solution (3N, 10 mL) and extracted three times with $\text{CH}_2\text{Cl}_2/\text{H}_2\text{O}$. The crude product was purified by flash chromatography (Cyclohexane/ CH_2Cl_2 80/20) to provide 1.9 g of product. Colorless oil; yield 85%. EI-MS m/z 327 (M^+). ^1H NMR (400 MHz, CDCl_3 , TMS/ppm): δ 7.23 (dd $^3J=4.8$ Hz, $^3J=2.8$, 1H), 6.92 (m, 2H), 4.22-4.16 (m, 4H), 3.30 (t, 1H), 2.63 (t, 2H), 1.91-1.85 (m, 2H), 1.63-1.59 (m, 2H), 1.34-1.30 (m, 6H), 1.26 (t, 6H). ^{13}C NMR (400 MHz, CDCl_3) δ 169.5, 143.0, 128.2, 125.1, 119.8, 61.2, 52.0, 30.4, 30.2, 29.0, 28.9, 28.7, 27.2, 14.1.

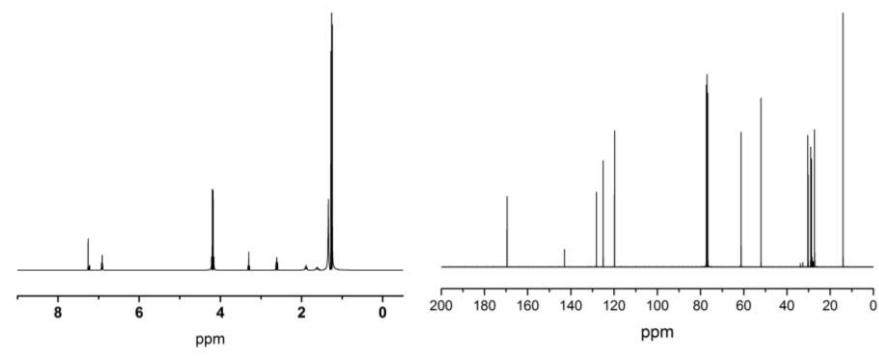


Figure S2. ^1H and ^{13}C NMR spectra of compound **3**.

2-(6-(thiophen-3-yl)hexyl)malonic acid (4) → Diethyl 2-(6-(thiophen-3-yl)hexyl)malonate (1.82 g, 0.0056 mol) was dissolved in a 20 % KOH aqueous solution (4g, 0.071 mol, in 20mL H₂O) and refluxed at 100 °C for 6 h. The reaction mixture was returned to room temperature and then HCl solution (6 N, 10 mL) was added in one portion. The resulting solution was extracted three times with (Et)₂O/H₂O, concentrated under reduce pressure and purified by gel permeation chromatography (CHCl₃), to provide 1.29 g of product. White powder; yield 90%. EI-MS m/z 270 (M⁺). ¹H NMR (400 MHz, CDCl₃, TMS/ppm): δ 7.23 (dd ³J=4.8 Hz, ³J=2.8, 1H), 6.92 (m, 2H), 3.43 (t, 1H), 3.61 (t, 2H), 1.96-1.92 (m, 2H), 1.63-1.59 (m, 2H), 1.42-1.30 (m, 6H). ¹³C NMR (400 MHz, CDCl₃) δ 173.8, 142.9, 128.2, 125.1, 119.8, 51.0, 30.3, 30.1, 28.9, 28.8, 27.1.

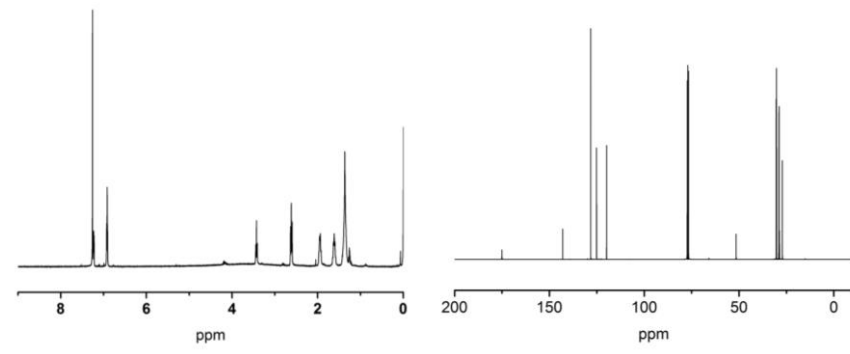


Figure S3. ¹H and ¹³C NMR spectra of compound **4**.

8-(thiophen-3-yl)octanoic acid (5) → 2-(6-(thiophen-3-yl)hexyl)malonic acid (1.287 g, 0.0048 mol) was heated at 130-140 °C for 1 h, until evolution of carbon dioxide had practically ceased; then heated quickly to 170 °C and cooled. The crude product was extracted three times with (Et)₂O/H₂O, dried on Na₂SO₄ and purified by gel permeation chromatography (CHCl₃) to provide 1.05 g of product. Yellow oil; yield 95%. EI-MS m/z 228 (M⁺). ¹H NMR (400 MHz, CDCl₃, TMS/ppm): δ 7.23 (dd ³J=4.8 Hz, ³J=2.8, 1H), 6.92 (m, 2H), 2.63 (t, 2H), 2.35 (t, 2H), 1.66-1.60 (m, 4H), 1.38-1.31 (m, 6H). ¹³C NMR (400 MHz, CDCl₃) δ 180.7, 143.1, 128.3, 125.1, 119.9, 34.2, 30.5, 30.3, 29.13, 29.10, 29.0, 24.7.

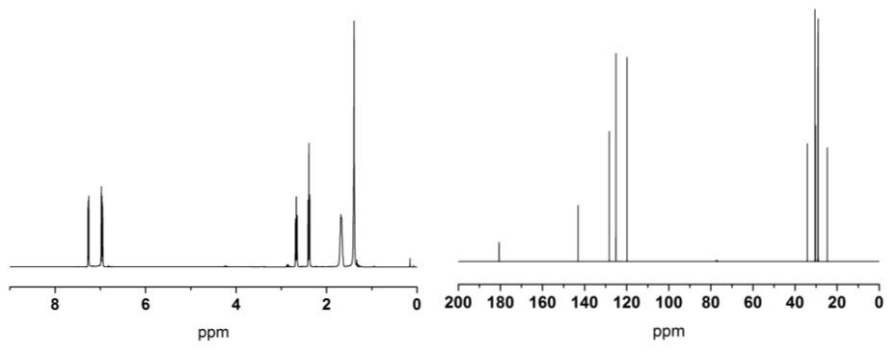


Figure S4. ^1H and ^{13}C NMR spectra of compound **5**.

8-(2,5-dibromothiophen-3-yl)octanoic acid (6) → To a solution of 8-(thiophen-3-yl)octanoic acid (1 g, 0.0044) dissolved in THF (30 mL) at 0 °C small portions of NBS (1.9 g, 0.0101) were added. The reaction mixture was stirred overnight. The resulting product was filtered on silica gel and purified by gel permeation chromatography (CHCl_3), to provide 1.160g of product. White solid; yield 85 %. EI-MS m/z 386 (M^+). ^1H NMR (400 MHz, CDCl_3 , TMS/ppm): δ 6.77 (s, 1H), 2.50 (t, 2H), 2.35 (t, 2H), 1.65-1.61 (m, 2H), 1.56-1.51 (m, 2H), 1.34-1.32 (m, 6H). ^{13}C NMR (400 MHz, CDCl_3) δ 180.5, 142.8, 130.9, 110.3, 107.9, 34.1, 29.5, 29.4, 28.96, 28.91, 28.8, 24.6.

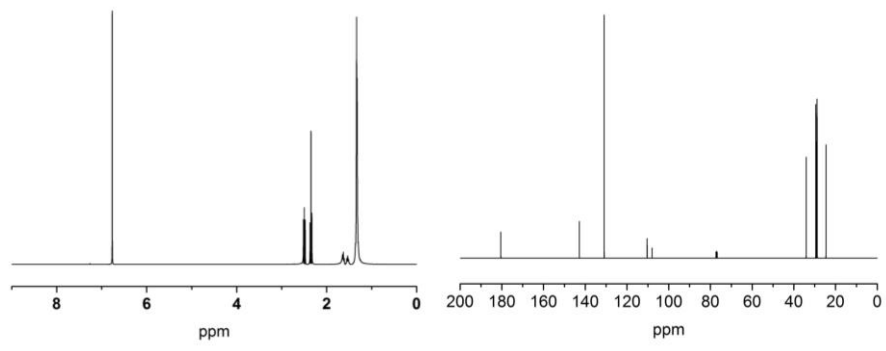


Figure S5. ^1H and ^{13}C NMR spectra of compound **6**.

2,5-dioxopyrrolidin-1-yl-8-(2,5-dibromothiophen-3-yl)octanoate (7) → A two-necked flask equipped with magnetic stirrer was charged with 8-(2,5-dibromothiophen-3-yl)octanoic acid (0.44 g, 0.0011 mol), anhydrous THF (10 mL), NHS (0.395 g, 0.0034 mol) and DMAP (0.110 g, 0.0009 mol). The solution was stirred and cooled in an ice bath to 0°C and then DCC (0.250 g, 0.0013 mol) was added over a 10 min period. After 30 min at 0°C the ice bath is removed and

the reaction mixture was stirred overnight. The crude product was extracted three times in CH₂Cl₂ and NaHCO₃ aqueous solution (PH = 8), concentrated under vacuum and purified by flash chromatography (cyclohexane/CH₂Cl₂ 5/95), to provide 0.520 g of product. Colorless oil; yield >90 %. EI-MS m/z 480 (M⁺). ¹H NMR (400 MHz, CDCl₃, TMS/ppm): δ 6.76 (s, 1H), 2.81 (s broad, 4H), 2.58 (t, 2H), 2.49 (t, 2H), 1.76-1.69 (m, 2H), 1.57-1.50 (m, 2H), 1.39-1.32 (m, 6H). ¹³C NMR (400 MHz, CDCl₃) δ 169.2, 168.6, 142.8, 130.9, 110.3, 107.9, 30.9, 29.4, 29.3, 28.76, 28.74, 28.6, 25.6, 24.5.

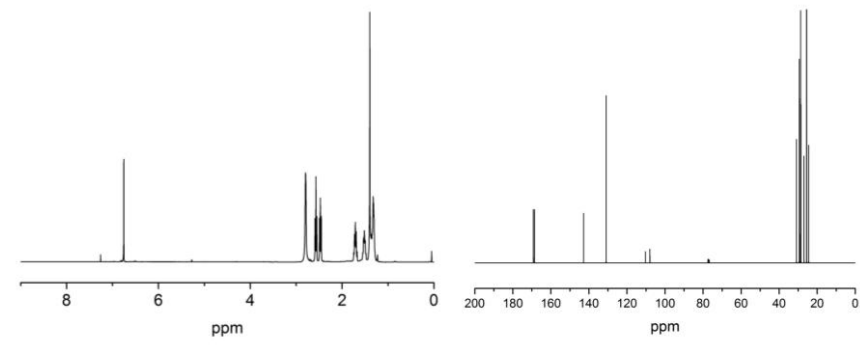


Figure S6. ¹H and ¹³C NMR spectra of compound **7**.

Poly[3-(2,5-dioxopyrrolidin-1-yl 8-octanoate)-2,2'-bithiophene] (**8**) → A mixture of **7** (0.14 g, 0.29 mmol), 2-5-Bis(tributylstannyl)thiophene (0.192 g, 0.29 mmol) and tetrakis(triphenylphosphine)palladium(0) (0.025 g, 0.023 mmol) in toluene (10 mL) was refluxed for 12 h. The crude product was extracted three times in CHCl₃/H₂O, filtered to remove the insoluble fraction and then precipitated for three times by addition of methanol to a solution of the polymers in chloroform to provide 72 mg of product. Dark red solid, mp 103-105°C. Yield 61%. ¹H NMR (400 MHz, CDCl₃, TMS/ppm): δ 7.12-7.01 (m), 2.80 (s, broad), 2.62-2.58 (m), 1.76-1.58 (m), 1.41-1.27 (m), 1.39-1.32 (m), 0.93-0.89 (m). GPC: Mw 4227 Mn 2810, PDI = 1.50. UV/Vis: λ_{max} 454 nm, λ_{em} 568 in CHCl₃.

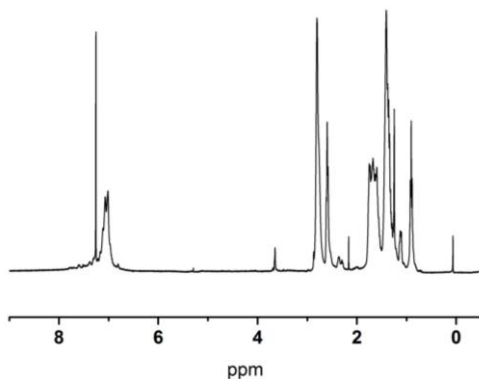


Figure S7. ^1H NMR spectrum of compound **8**.

Poly[3-(2,5-dioxopyrrolidin-1-yl 8-octanoate)-2,2'-5'-2''-terthiophene] (**9**) \rightarrow A mixture of **7** (0.15 g, 0.311 mmol), 5-5'-bis(tributylstannyl)-2,2'-bithiophene (0.231 g, 0.311 mmol) and tetrakis (triphenylphosphine) palladium(0) (0.029 g, 0.025 mmol) in toluene (10 mL) was refluxed for 12 h. The crude product was extracted three times in $\text{CHCl}_3/\text{H}_2\text{O}$, filtered to remove the insoluble fraction and then precipitated for three times by addition of methanol to a solution of the polymers in chloroform to provide 98 mg of product. Dark red solid, mp 213-215°C. Yield 65%. ^1H NMR (400 MHz, CDCl_3 , TMS/ppm): δ 7.07-7.00 (m), 2.81 (s, broad), 2.63-2.59 (m), 2.38-2.36 (m), 1.76-1.61 (m), 1.42-1.28 (m), 1.39-1.32 (m, 6H), 0.94-0.89 (m). GPC: Mw 3634 Mn 2570, PDI = 1.41. UV/Vis: λ_{max} 466 nm, λ_{em} 570 in CHCl_3 .

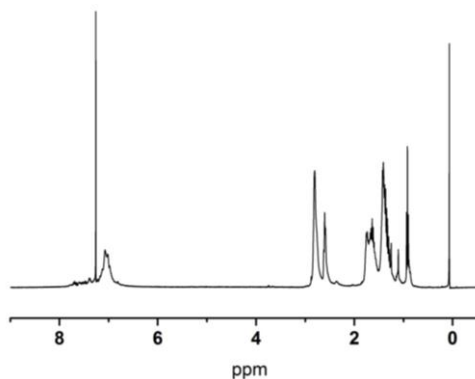


Figure S8. ^1H NMR spectrum of compound **9**.

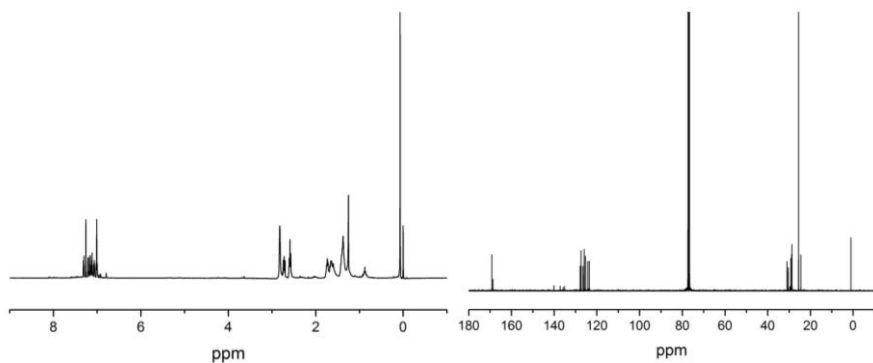


Figure S9. ^1H and ^{13}C NMR spectra of compound **10**.

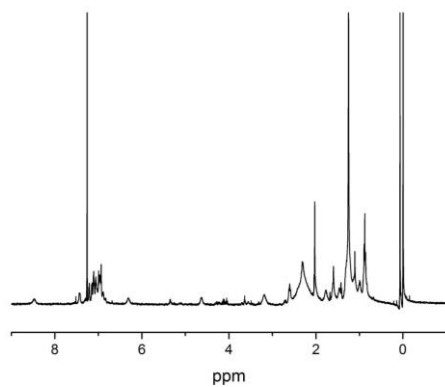


Figure S10. ^1H NMR spectrum of compound **11**.

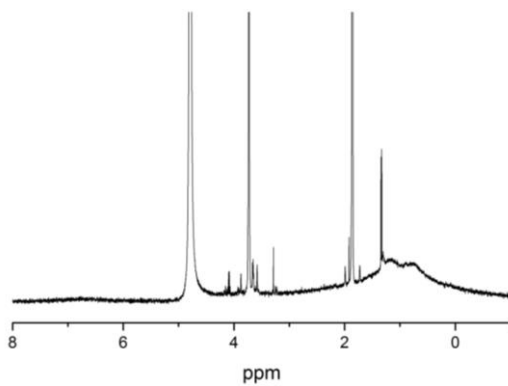


Figure S11. ^1H NMR spectrum of poly(3-hexylthiophene) nanoparticles in $\text{D}_2\text{O}/\text{THF-}d_8$.

5.2 Optical Properties.

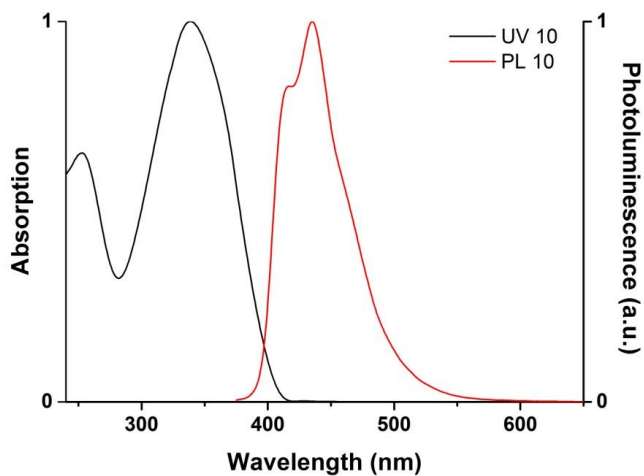


Figure S12. Absorption and emission spectra of compound **10** in CH_2Cl_2 .

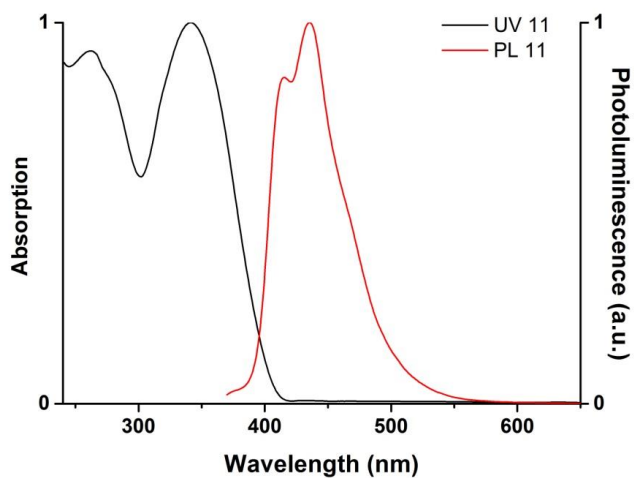


Figure S13. Absorption and emission spectra of compound **11** in CH_2Cl_2 .

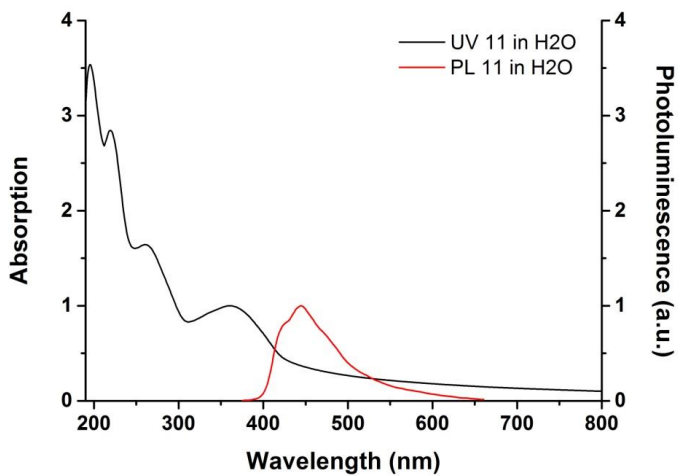


Figure S14. Absorption and emission spectra of compound 11 in H₂O.

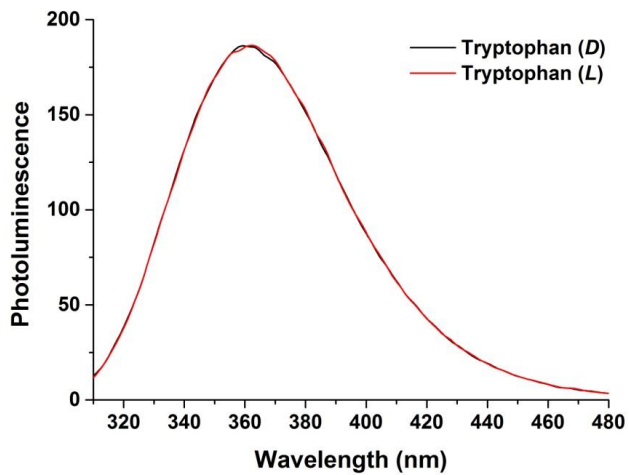


Figure S15. Emission spectra of *D* and *L* tryptophan in H₂O.

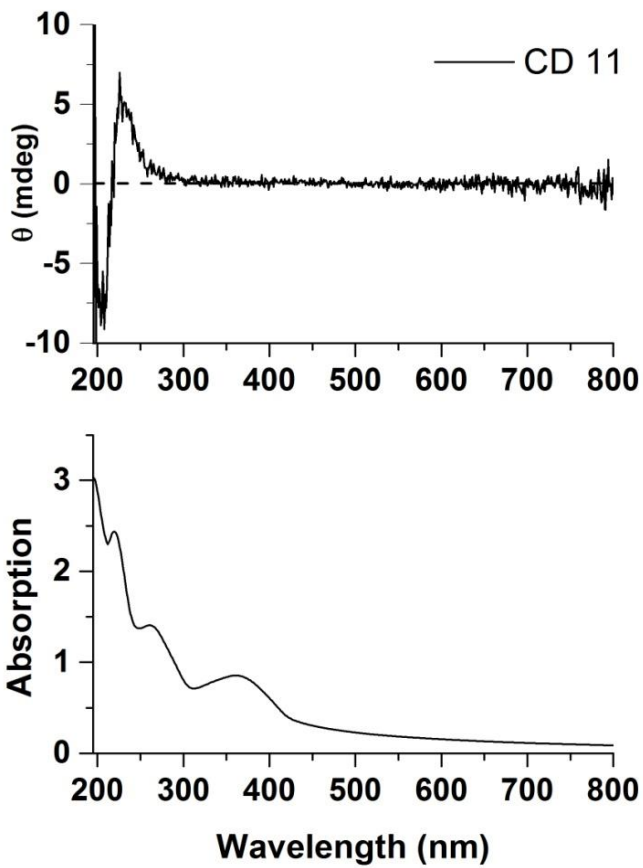


Figure S16. Circular Dichroism spectrum of compound **11** and the corresponding absorption spectrum in H₂O.

5.3 Scanning Electron Microscopy of NPs-NHS.

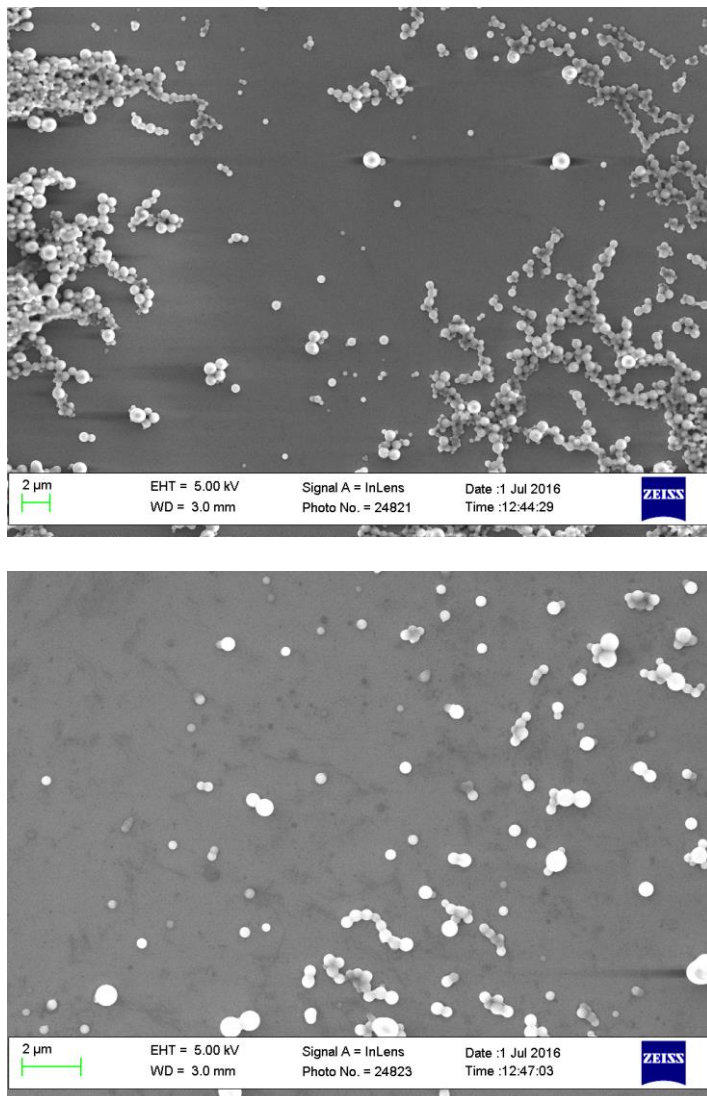


Figure S17. SEM images of NPs-NHS obtained from polymer 8.

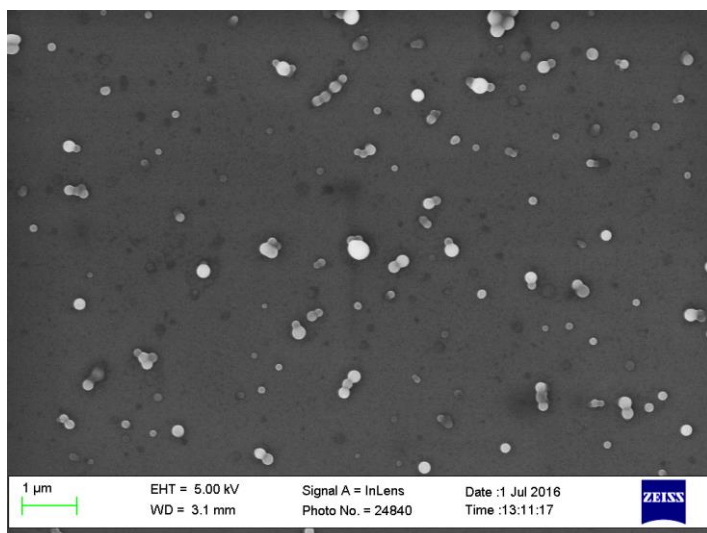
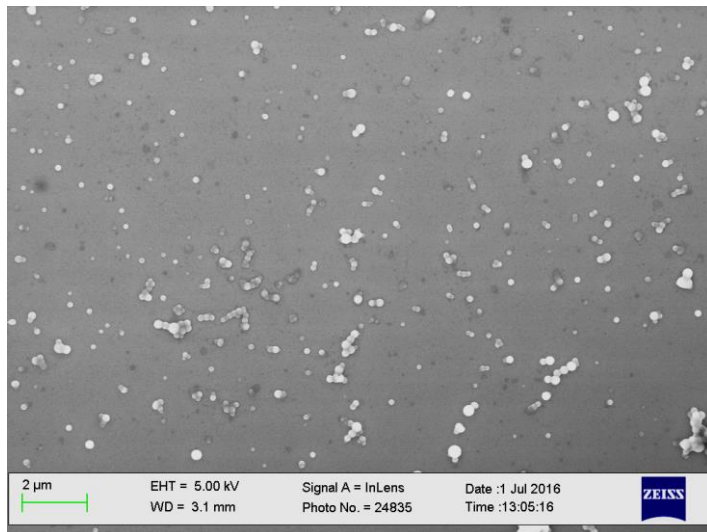


Figure S18. SEM images of NPs-NHS obtained from polymer **9**.

5.4 MTT assay of HEK-293 cells treated with NPs-NHS.

Cytotoxicity of NPs was evaluated by MTT assay [3-(4,5-dimethylthiazol-2-yl)-2,5-diphenyltetrazolium bromide] (Sigma Aldrich) on HEK-293 cells. Basically, this assay exploits the metabolism of living cells to transform a water-soluble tetrazolium salt into a purple colored formazan compound. Absorbance of the purple product is directly related to the proliferation of cells. Cells with a healthy metabolic activity are proliferating cells hence display higher absorbance values. Cells were seeded in 48 well plates at a density of 2×10^4 cells/well, NPs were added directly during the plating phase with a dilution in order to work with a fixed optical density of 0.2. Cell proliferation was evaluated after 6 hours, 1 day, 2 days and 3 days of incubation with NPs. For each time point, the growing medium was replaced with RPMI without phenol red containing 0.5 mg/mL of MTT. The samples were incubated again for 2 h at 37 °C in dark. Formazan salt produced by cells through reduction of MTT was then solubilised with 200 μ L of ethanol and the absorbance was read at 560 nm and 690 nm. The proliferation cell rate was calculated as the difference in absorbed intensity at 560 nm and 690 nm. Figure S19 shows a viability assay conducted for cell cultures incubated with NPs-NHS, NPs-P3HT and untreated samples (N=8 for each condition). As expected, cell proliferation is in general increased as the incubation time increases. Cells treated with NPs-P3HT display good cell activity, while it is evident that exposure to NPs-NHS leads to decreased proliferation properties (J. Pecher, S. Mecking, *Chem. Rev.* **2010**, *110*, 6260-6279).

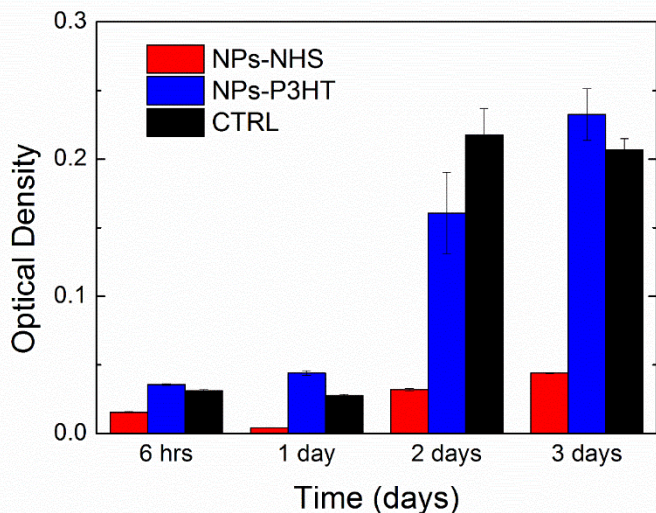


Figure S19. Normalized absorbance of MTT assay in vitro at four different time points for different NPs treatment and control cell samples. Data are reported as average over N=8 samples \pm SEM (standard error mean).

5.5 Laser Scanning Confocal Microscopy images.

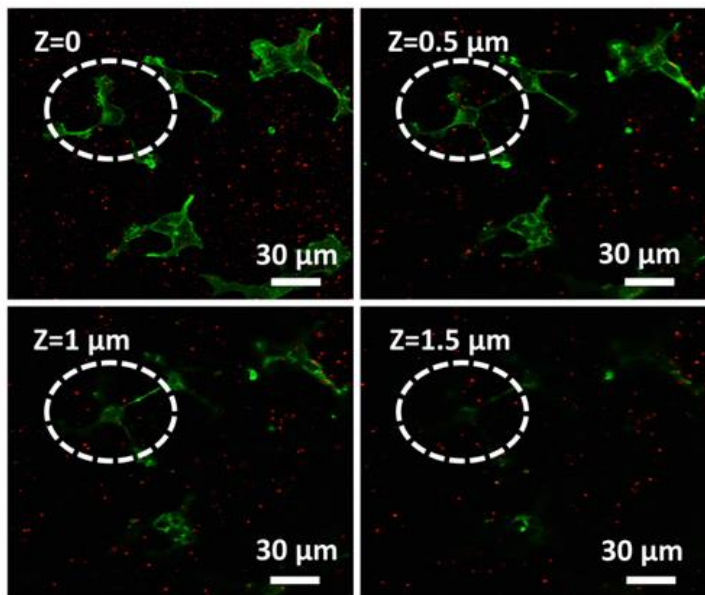
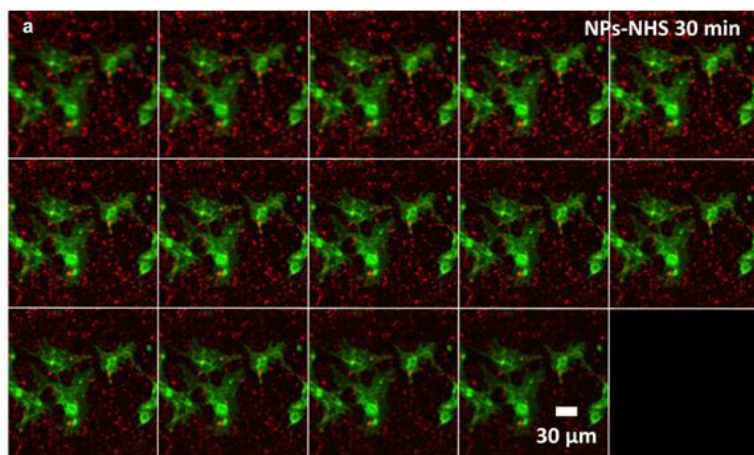


Figure S20. LSCM images of successive slices of HEK-293 cells incubated for 30 min with NPs-P3HT. Cells cytoskeleton was stained with phalloidin (in green), while the nanoparticles are seen in red channel.



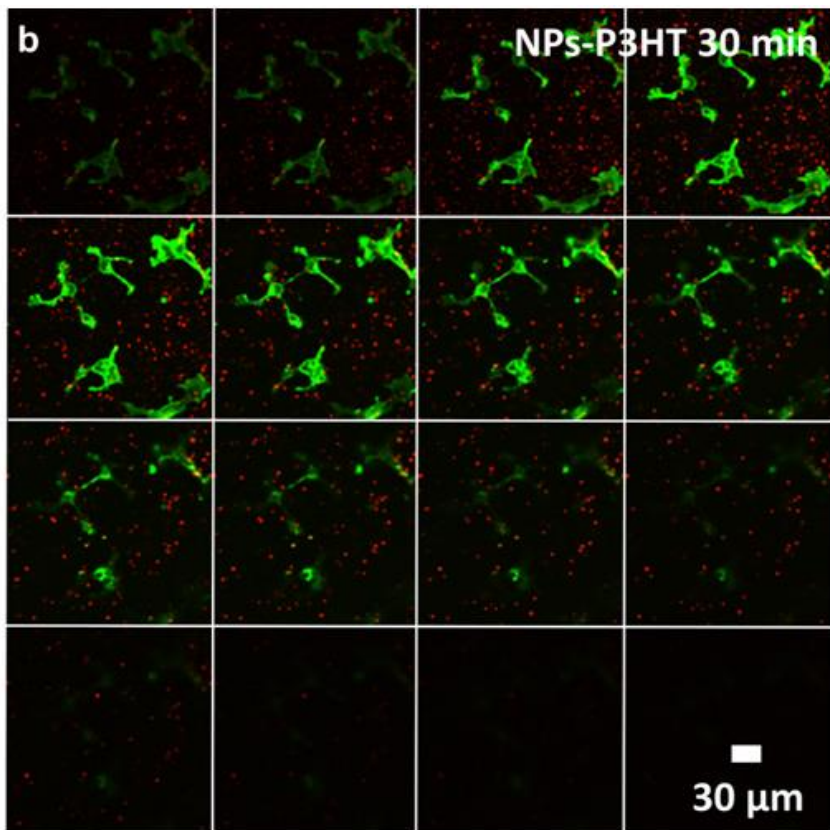


Figure S21. Confocal optical sections of cells loaded with NPs-NHS (panels a) and NPs-P3HT (panels b), stained with phalloidin (green, actin). Emission from NPs is visible in the red channel.

5.6 Images taken with inverted microscope used for electrophysiology and area of NPs aggregates from particle analysis over single cells.

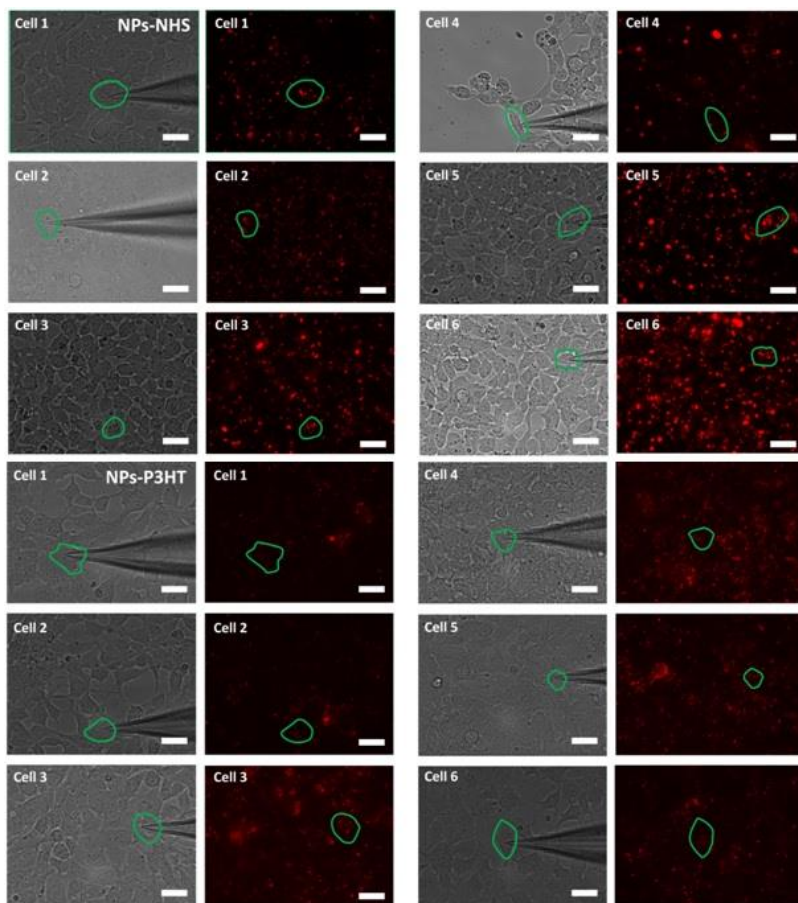


Figure S22. Brightfield and fluorescence images taken with inverted microscope used for electrophysiology experiments with a 40x objective. Cell cultures were treated with NPs-NHS (upper panel) and NPs-P3HT (lower panel). Single cells analysed with ImageJ are outlined in green. Scale bar, 30 μm .

Table S1. Area of the aggregate with the maximum dimension obtained from particle analysis carried out over single cells outlined in Figure S22.

	AREA MAXIMUM AGGREGATE NPS-NHS (μm^2)	AREA MAXIMUM AGGREGATE NPS-P3HT (μm^2)
CELL 1	11.38	4.98
CELL 2	3.93	2.88
CELL 3	8.44	6.4
CELL 4	12.9	1.47
CELL 5	7.03	3.15
CELL 6	4.98	3.25
AVERAGE	8.11	6.69
STANDARD DEVIATION	3.52	1.74

Typically, it can be observed that the biggest aggregates formation prevails in case of samples treated with NPs-NHS (the maximum area of aggregates has an average of $8.11 \mu\text{m}^2$), against the case of NPs-P3HT, whose maximum aggregates cover on average $6.69 \mu\text{m}^2$ of cells. In order to check the possibility that the photoinduced signal upon illumination (Figure 7) is due to a thermal effect, we need to estimate what is the required change in temperature. Depolarization of the membrane potential due to a change in membrane capacitance is described by equation 1:⁽¹⁴⁾ $\Delta V \cong -\frac{\Delta C_m}{C_m}(V_r - V_\sigma) = \alpha_c(V_r - V_\sigma)\Delta T$. From the statistical analysis of the depolarization peaks observed with NPs-NHS, we obtain an average value of $\Delta V \sim 0.07 \text{ mV}$. Considering typical values $V_r = -30 \text{ mV}$, $V_\sigma = 120 \text{ mV}$ and $\alpha_c = 0.0031 \text{ K}^{-1}$, as obtained for HEK-293 cells grown on flat substrate, we then work out a required increase in temperature of $\Delta T \sim 0.16 \text{ K}$. The temperature gradient with respect to the background (here considered unchanged) in a single nanoparticle after light exposure is given by equation 2^[18]: $\Delta T = \frac{I_0 \pi R_{np}^2}{4\pi K r}$ where I_0 is the intensity of the light (200 mW/mm^2), R_{np} is the NP's radius (we adopt the average value $R_{np} = 175 \text{ nm}$), K is the thermal conductivity of water (0.6 W/mK) and r is the distance from the nanoparticle centre. At the particle surface, $r = R_{np}$ the expected ΔT is thus $\sim 0.015 \text{ K}$. Note that according to equation 2 this value is linearly dependent on the particle radius. This is one order of magnitude smaller than required for supporting the thermal mechanism. We have here two possible ways out. One is to consider aggregation. A large cluster can absorb more energy and give rise to a larger temperature gradient according to a simple linear law with the radius. In order to reach the temperature range required the radius should be one order of magnitude larger. This, in terms of a 3D spherical cluster, corresponds to a rather unlucky configuration where a thousand particles are connected. However, due to the peculiar docking of the single NPs-NHS onto the cell membrane, a quasi 2D aggregation could be envisaged, where the NPs coagulate in a surface patch of more than $1 \mu\text{m}$ radius on top of the cell (Figure S22 and Table S1). This local modification of the cell outskirt could result into a photoactive site able to absorb visible light and convert it into local heating, thus affecting the membrane potential. This explanation is fully consistent with the thermal-like response of the cell, but it is difficult to be tested as imaging does not provide enough resolution.

REFERENCES

- [1] ^{a)} L. Feng, C. Zhu, H. Yuan, L. Liu, F. Lva and S. Wang, *Chem. Soc. Rev.*, **2013**, 42, 6620. ^{b)} K. K. Ng and G. Zheng, *Chem. Rev.*, **2015**, 115, 11012. ^{c)} J. Pecher and S. Mecking, *Chem. Rev.*, **2010**, 110, 6260. ^{d)} L. Feng, L. Liu, F. Lv, G. C. Bazan and S. Wang, *Adv. Mater.* 2014, **26**, 3926. ^{e)} T. M. Liu, J. Yu, C. A. Chang, A. Chiou, H. K. Chiang, Y. C. Chuang, C. H. Wu, C. H. Hsu, P. A. Chen and C. C. Huang, *Sci. Reports*, **2014**, 4, 5593. ^{f)} I. Fischer, K. Petkau-Milroy, Y. L. Dorland, A. P. H. J. Schenning and L. Brunsveld, *Chem. Eur. J.*, **2013**, 19, 16646.
- [2] ^{a)} C. Wu, S. J. Hansen, Q. Hou, J. Yu, M. Zeigler, Y. Jin, D. R. Burnham, J. D. McNeill, J. M. Olson and D. T. Chiu, *Angew. Chem. Int. Ed.*, **2011**, 50, 3430. ^{b)} C. Wu and D. T. Chiu, *Angew. Chem. Int. Ed.*, **2013**, 52, 3086.
- [3] F. Ye, C. Wu, Y. Jin, Y. H. Chan, X. Zhang and D. T. Chiu, *J. Am. Chem. Soc.*, **2011**, 133, 8146. J. Wang, X. Xu, Y. Zhao, C. Zheng and L. Li, *J. Mater. Chem.*, **2011**, 21, 18696
- [4] ^{a)} D. Ghezzi, M. R. Antognazza, M. Dal Maschio, E. Lanzarini, F. Benfenati and G. Lanzani, *Nat. Commun.*, **2011**, 2, 166. ^{b)} D. Ghezzi, M. R. Antognazza, R. Maccarone, S. Bellani, E. Lanzarini, N. Martino, M. Mete, G. Pertile, S. Bisti, G. Lanzani, and F. Benfenati, *Nat. Photonics*, **2013**, 7, 400. ^{c)} N. Martino, P. Feyen, M. Porro, C. Bossio, E. Zucchetti, D. Ghezzi, F. Benfenati, G. Lanzani and M. R. Antognazza, *Sci. Rep.*, **2015**, 5, 8911.
- [5] ^{a)} J. E. Millstone, D. F. J. Kavulak, C. H. Woo, T. W. Holcombe, E. J. Westling, A. L. Briseno, M. F. Toney and J.M. J. Frechet, *Langmuir*, **2010**, 26, 13056. ^{b)} M. Bag, T. S. Gehan, D. D. Algaier, F. Liu, G. Nagarjuna, P. M. Lahti, T. P. Russell and D. Venkataraman, *Adv. Mater.*, **2013**, 25, 6411. ^{c)} R. Couto, S. Chambon, C. Aymonier, E. Mignard, B. Pavageau, A. Erriguiblea and S. Marre, *Chem. Commun.*, **2015**, 51, 1008. ^{d)} S. Günes, N. Marjanovic, J. M. Nedeljkovic and N. S. Sariciftci, *Nanotechnology*, **2008**, 19, 424009.
- [6] E. Zucchetti, M. Zangoli, I. Bargigia, C. Bossio, F. Di Maria, G. Barbarella, C. D'Andrea, G. Lanzani and M. R. Antognazza, *J. Mater. Chem. B*, **2017**, 5, 565.
- [7] H. Shimizu, M. Yamada, R. Wada and M. Okabe, *Polym. J.*, **2008**, 40, 33
- [8] M. Zambianchi, F. Di Maria, A. Cazzato, G. Gigli, M. Piacenza, F. Della Sala and G. Barbarella, *J. Am. Chem. Soc.*, 2009, 131, 10892.
- [9] M. L. Capobianco, G. Barbarella and A. Manetto, *Molecules*, **2012**, 17, 910.
- [10] P. Bauerle, M. Hiller, S. Scheib, M. Sokolowski and E. Umbach, *Adv. Mater.*, **1996**, 8, 214.
- [11] L. Avram and Y. Cohen, *Chem. Soc. Rev.*, **2015**, 44, 586.

- [12] A. Slominski, I. Semak, A. Pisarchik, T. Sweatman, A. Szczesniowski and J. Wortsman, *FEBS Lett.*, **2002**, 511, 102.
- [13] ^{a)} J. Lin, H. Huang, M. Wang and Jianping Deng, *Polym. Chem.*, **2016**, 7, 1675.
^{b)} B. Chen, J. Deng, X. Liu and W. Yang, *Macromolecules*, **2010**, 43, 3177.
- [14] E. V. Iski, H. L. Tierney, A. D. Jewell and E. C. H. Sykes, *Chem. Eur. J.*, **2011**, 17, 7205.
- [15] G. Barbarella and F. Di Maria, *Acc. Chem. Res.*, **2015**, 48, 2230.
- [16] J. Pecher, S. Mecking, *Chem. Rev.* **2010**, 110, 6260.
- [17] ^{a)} A. Lesniak, F. Fenaroli, M. P. Monopoli, C. Åberg, K. A. Dawson and A. Salvati, *ACS Nano*, **2012**, 6, 5845. ^{b)} L. Shang, K. Nienhaus and G. U. Nienhaus, *J. Nanobiotechnol.*, **2014**, 12, 5.
- [18] Y. Rabin, *Int. J. Hyperthermia*, **2002**, 18, 194-202.

In this chapter the synthesis of thiophene-based 'hexamers' having the same sulfur-overrich quaterthiophene core is reported.

It is demonstrated that the inner core promotes the spontaneous π -stacking driven self-assembly of the hexamers into 1D crystalline functional microfibers. The fibers were characterized by Scanning Electron Microscopy (SEM), Atomic Force Microscopy (AFM), Circular Dichroism (CD), Cyclic Voltammetry (CV), X-ray diffraction and UV, PL spectroscopies. Density Functional Theory calculations of the conformation and the aggregation modalities of the 'hexamers' are also reported. Currently, electrical characterization of the fibers are under way.

Work in progress.

I. INTRODUCTION

Investigations aimed to the design and synthesis of molecules capable to self-organize into functional supramolecular architectures by means of multiple non-covalent interactions are at the forefront of nanoscience and nanotechnology. In particular, crystalline semiconducting 1D supramolecular structures hierarchically organized across different length scales are of increasing concern in various fields spanning from photovoltaics to supramolecular electronics to nanophotonics^[1]. A great variety of self-assembling functional molecules affording more or less ordered 1D supramolecular structures in different conditions have been synthesized using various chemical strategies, including the preparation of functional nanochains made of organic nanoparticles^[1b]. Most of these self-assembly studies concern organic p-type semiconductors (hole charge carriers). Recently, perylene imide molecules, n-type semiconducting materials (electron carriers), have also been investigated for the formation of 1D supramolecular structures and the relationship between molecular structure, noncovalent interactions, self-assembly conditions and morphology discussed in view of applications in optoelectronics^[1e]. However, further progress is required in design, synthesis, room temperature solution-phase growth, structural analysis and optical and electrical characterization of these materials while work-up simplicity, reproducibility and chemical stability of supramolecular fibers are required for any type of application. Tailoring the electronic properties of 1D self-assembled supramolecular fibers while maintaining control over their crystal structure and morphological habit has not been achieved so far. Contrary to small molecules, oligomers and polymers obtained by means of covalent synthesis for which there is good control on HOMO and LUMO orbital energies, redox and optical properties, a similar control on supramolecular systems has not yet been realized. Moreover, the relevant properties are generally optimized on different molecular structures which self-organize in different manners making difficult to compare their performance.

One important aspect of the investigations in self-assembly is the search for molecular building blocks storing sufficient information in their covalent framework to promote spontaneous self-organization into functional supramolecular structures via particular non-bonded interactions (*specific non covalent interactional algorithms* according to J.M.L. Lehn's definition^[2]). The identification of such molecular building blocks would enable the easy planning of functional supramolecular structures with programmed properties and function.

Here, we report that 3,3',4'',4'''-tetrakis(hexylthio)-2,2':5,2'':5''':2''':5''',2''''-quaterthiophene is one of such building blocks enabling the π -stacking driven formation of a new class of spontaneously self-assembling crystalline 1D structures *via* solvent-vapor diffusion at room temperature. The addition of different terminal groups to the quaterthiophene allowed us for the first time the fine tuning of optical properties, redox potentials, type of prevailing charge carriers and morphology in a series of structurally comparable 1D systems (sexithiophene derivatives **1-5**, Figure 1).

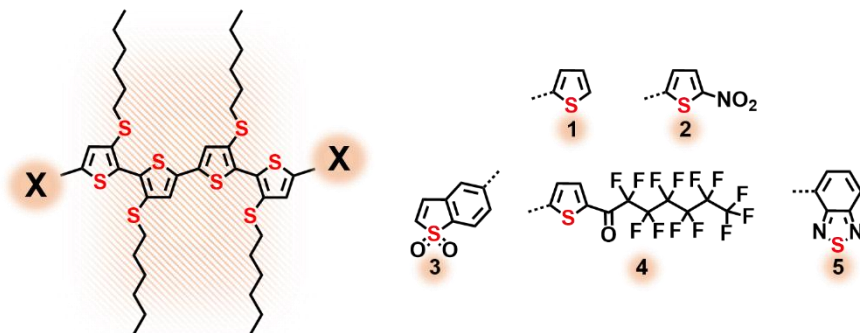


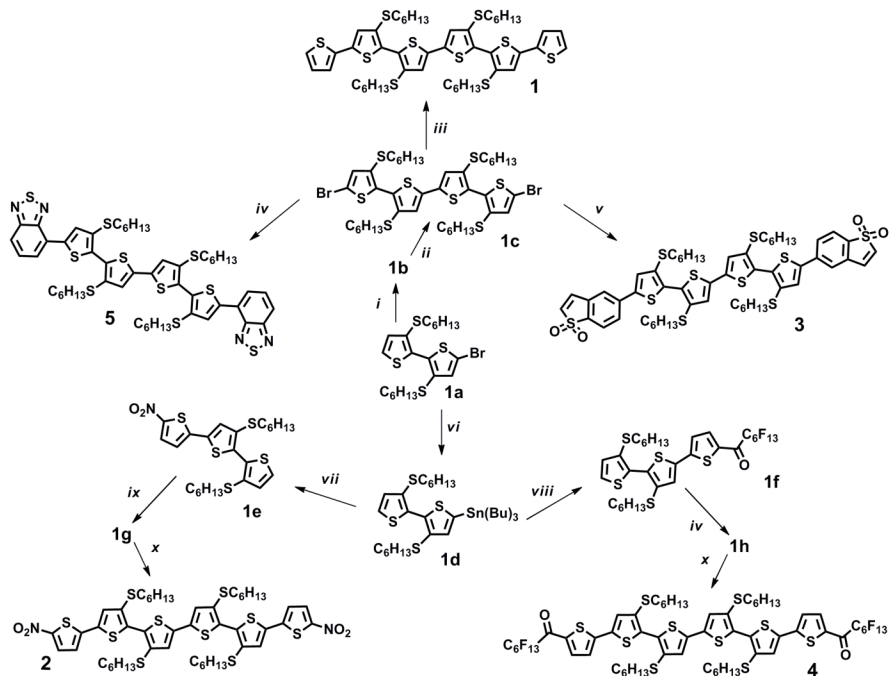
Figure 1. Molecular structure of compounds **1-5**.

Our strategy for the rational tuning of functional properties of 1D oligothiophene supramolecular structure is inspired by our previous work on sulfur overrich octamers (i.e. oligothiophenes containing an extra β -sulfur per ring) and based on the assumption that intra- and intermolecular sulfur-sulfur interactions, which are directional as argued by single crystal studies, would generate anisotropic nanostructured systems ^[3]. A recent paper demonstrating that heteroatom-heteroatom interactions in conjugated molecules are largely contributing to conformation and planarity supports our assumption ^[4].

II. RESULTS

The regiochemistry of substitution and the alkyl chains length of the inner sulfur overrich quaterthiophene of compounds **1-5** (Figure 1) are crucial for promoting the self-assembly of 1D fibers. The synthesis and the characterization of various sulfur overrich quaterthiophenes which are not capable to promote the formation of 1D supramolecular structures have already been described in the master's degree titled "Sintesi, caratterizzazione e comportamento allo stato solido di oligomeri tiofenici diversamente funzionalizzati" from the University of Bologna (October 2013).

2.1 Synthesis of compounds 1-5. Compounds **1-5** were synthesized according to the pattern reported in Scheme 1. All details of preparation and characterization are reported in Experimental Section. All compounds were prepared in high yield starting from the monobromo (**1a**) or the monostannane (**1d**) of 3,3'-bis(hexylthio)-2,2'-bithiophene whose preparation is described in reference ^[3a]. Compounds **1,3** and **5** were obtained from dibromoquaterthiophene **1c**, also described in reference [3a] via Suzuki coupling with the appropriate boranes under microwave (MW) irradiation. Compounds **2** and **4** were ever obtained by Suzuki coupling with MW assistance through the newly synthesized trimers **1e** and **1f** after bromination and subsequent treatment with bis(pinacolato)diboron. For the synthesis of oligothiophenes via Stille and Suzuki coupling with the aid of ultrasound and microwave irradiation see reference ^[5].



Scheme 1. Synthetic pattern for the preparation of compounds **1-5**: *i*) bis(pinacolato)diboron, NaHCO₃, Pd(dppf)Cl₂, MW, THF/H₂O, 80°C; *ii*) NBS, CH₂Cl₂, room T; *iii*) thiophene-2-ylboronic acid, NaHCO₃, Pd(dppf)Cl₂, MW, THF/H₂O, 80°C; *iv*) 4-(4,4,5,5-tetramethyl-1,3,2-dioxaborolan-2-yl)-2,1,3-benzothiadiazole, NaHCO₃, Pd(dppf)Cl₂, MW, THF/H₂O, 80°C; *v*) 5-(4,4,5,5-tetramethyl-1,3,2-dioxaborolan-2-yl)benzo[b]thiophene-1,1-dioxide, NaHCO₃, Pd(dppf)Cl₂, MW, THF/H₂O, 80°C; *vi*) *n*-BuLi, SnBu₃Cl, THF, -78°C; *vii*) 2-bromo-5-nitrothiophene, Pd(tetrakis), toluene, 110°C; *viii*) 1-(5-bromothiophen-2-yl)-2,2,3,3,4,4,5,5,6,6,7,7,7-tridecafluoro-heptan-1-one, Pd(tetrakis), toluene, 110°C; *ix*) NBS, CH₂Cl₂; *x*) bis(pinacolato) diboron, NaHCO₃, Pd(dppf)Cl₂, MW, THF/H₂O, 80°C;

2.2 Self-assembly of **1-5** into 1D Supramolecular Fibers and their Characterization.

Compounds **1-5** spontaneously self-assemble into crystalline 1D nanostructured fibers through solvent-exchange in solution, in which the molecules move from a good solvent (toluene) into a poor solvent (acetonitrile) [3]. Upon about one hour exposition to acetonitrile vapors (see Scheme S6) of a solution of **1-5** in toluene in the range 10⁻³-10⁻⁵ M, the formation of fibers with high aspect ratio and characterized by micrometric length and width and submicrometric thickness was observed (Figure 2). As already reported for sulfur overrich octamers [3a], the formation of the fibers was reproducible and afforded the same results independently of the type of substrate employed (glass, SiO₂, ITO, gold), indicating that thermodynamically stable supramolecular fibers are formed and that the morphologies are mainly determined by the molecular structure. All fibers are crystalline as shown by optical microscopy and X-ray diffraction data (see below).

Figures S37-S41 display the optical microscopy images with cross polars of the fibers obtained from compounds **1-5**, showing birefringence regardless of their morphology. The birefringence extinguishes in four positions every 90° rotation with respect to the polarizers, indicating that the fibers have a high crystalline directional order.

Figure 2 shows representative Scanning Electron Microscopy (SEM) images of the fibers formed by compounds **1-5**. It is seen that compounds **1** and **2** afford tape-like supramolecular fibers whereas compounds **3** and **4** display the presence of helical superstructures at the nano and microscale despite the lack of stereogenic centers in the molecule. Bundles of helices rolled into superhelical structures (coiled coils) are present. Figure 2 also shows that compound **5** leads to the formation of polymorphic fibers, tape-like or helical. While the former could be obtained free of the other polymorph (Figure 2, compound **5**, panel a), we were unable to obtain the latter in isolated form since the helical fibers always grow on top of the tape-like ones as micrometer size ‘fusilli’^[6] (Figure 2, compound **5**, panel b) or as coils wrapped in nanometer size around a micrometer size tape-like fiber (Figure 2, compound **5**, panel c).

Compound **3** forms superhelices (helices of helices) and double helices of superhelices all displaying the same-hand helicity, namely left-handed helicity (*M* type double helices). The inset (Figure 2, compound **3**) shows a larger double helix of superhelices and indicates that the periodicity of the superhelices is size dependent. The SEM images relative to compound **4** show the presence of nice superhelices of nanometer size (see the insets); those in the inset of the a panel displaying opposite handednesses. On the whole the accurate observation of SEM images suggests that π - π stacking of the tetrameric cores (including off-centered stacking, see calculations) and intermolecular hydrogen bonding interactions (see again the results of calculations) lead to the formation of stable single-strand helical assemblies and subsequently to multistrand systems through interstrand interactions.

As shown in Figure 2 all fibers - whether tape-like or helical - are characterized by circular dichroism signals corresponding to the π - π^* transition in the UV-vis spectrum of the corresponding starting compound. Note that compounds **1-5** are centrosymmetric molecules and no CD signal in solution was detectable. The intensity of the CD signal of the fibers ranges from a few mdeg (θ) for **1**, **3**, **5** to 40 mdeg (θ) for **4** to 100 mdeg (θ) for **2**. Noticeably, the most intense CD signal is that afforded by the tape-like fibers of compound **2**. What generates chirality in a centrosymmetric oligomer lacking stereogenic centers are the distortions from planarity caused by the deposition of the molecule on the surface even by a small bias from the molecular plane. In addition, the interactions between two molecules as soon as they come in contact (see calculations below) also contribute to the desymmetrization of the molecule. Then chirality amplification^[7] may take place during the dynamic assembly process. Since the bias from the molecular plane (changes in interring angles ω) can be either in one or the opposite direction ($+\omega$ or $-\omega$) with the same probability of both hand-helicities are expected in different points of the same sample or in two different samples, as already observed for sulfur overrich thiophene octamers^[3a].

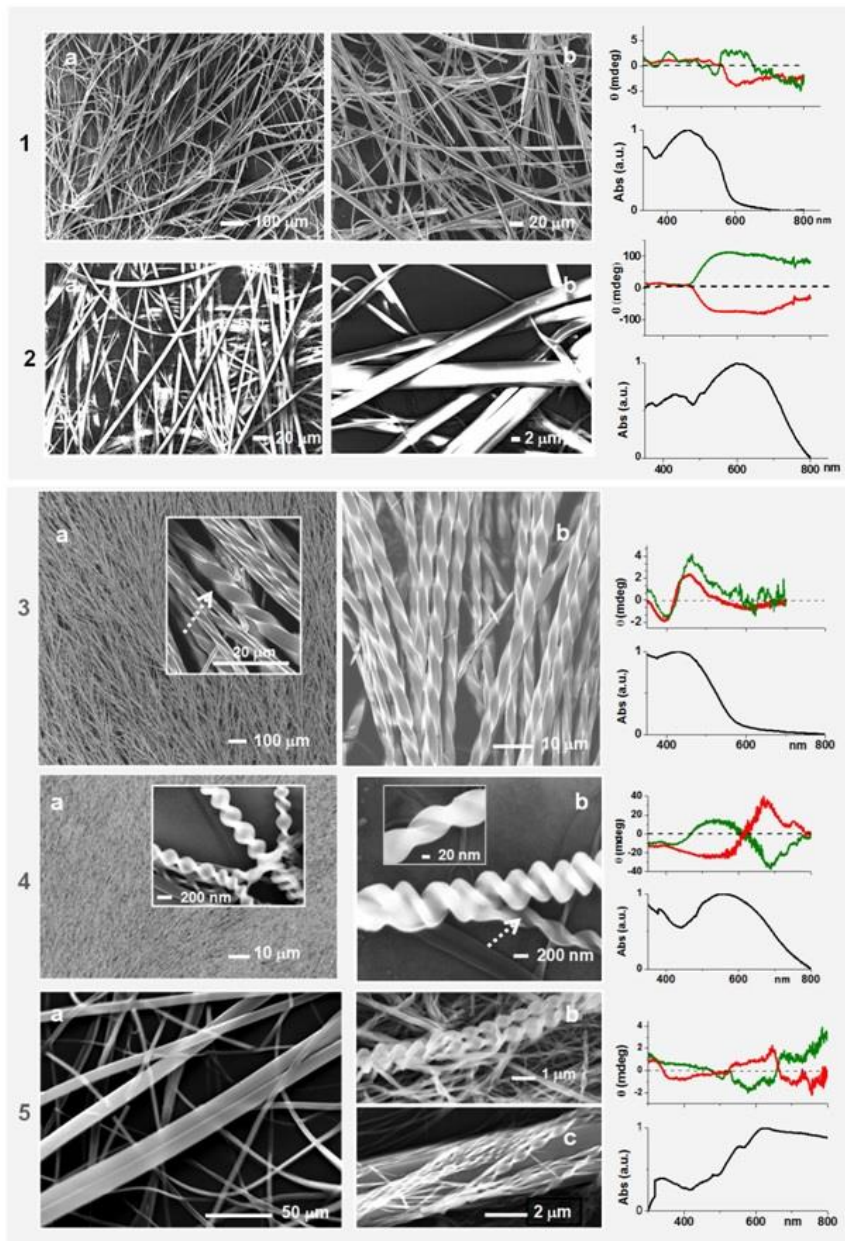


Figure 2. Scanning Electron Microscopy (SEM) images and Circular Dichroism (CD) of 1D fibers grown on glass obtained by compounds **1-5** via the solvent-exchange method.

This results in CD signals with opposite Cotton effect. In agreement with expectations, the CD of all compounds but **3** displayed a Cotton effect of one sign and the opposite sign corresponding to opposite helicity of the aggregates at the initial stage. Indeed, the main source of the CD signal arises from adjacent interacting chromophores giving rise to excitons within a nanometer scale range, thus the signal is related to the supramolecular organization of the aggregate at the initial stage of its formation. The subsequent growth of the aggregate up to the micro- and mesoscale does not necessarily occurs with same modalities^[8].

SEM images of nanoaggregates of opposite helicity are clearly visible in the SEM images of the fibers obtained from **4** (Figure 2, compound **4**, panel a) and **5** (Figure 2, compound **5**, panel c). Accordingly, two opposite CD signals are observed. Although not visible in the SEM images, the presence of nanoscale aggregates of opposite helicity is revealed by the CD spectra of the fibers of compounds **1** and **2**. The fibers formed by **2** give rise to the most intense signal, as outlined before. One of the factors contributing to the intensity of the CD signal is the proximity of the interacting chromophores^[9]. Thus the fact that the intensity of the CD signals for the fibers of **2** is the highest one is in agreement with the fact that the fibers from **2** are the most compact and of the highest quality crystal (see below).

Of all fibers only those pertaining to compound **3** afford a CD signal of one single type. Despite repeated attempts on different samples and on different points of the same sample, we were unable to detect the opposite CD signal. A positive sign of the long-wavelength part of the CD signal indicates the presence of a right handed helix at the nanoscale^[9] while the double helices of superhelices observed in the SEM image are indicative of left-handed helicity (M type) at the microscale. Thus, the right-handed nanostructures self-assemble into left-handed super helices. The spontaneously self-assembled fibers of **1-5** are randomly distributed on the different substrates used (Figure 2). However, well-ordered aligned fibers were obtained making use of the Lithographically Controlled Wetting (LCW)^[10] technique to direct their self-assembly, as already done for sulfur overrich octathiophene fibers^[11]. A few drops of the compound dissolved in toluene was first placed on a silicon wafer, then a polydimethylsiloxane (PDMS) prepatterned stamp was placed on the top and the whole system exposed at r.t. for 24 h to the vapors of the (non-solvent) acetonitrile in a sealed container (see section 4.1 for details). Figure 3 shows well aligned fibers of compounds **2** and **4** grown with the LCW technique. In both cases parallel microfibers of similar dimensions, in particular width (1 μ m) and height (150-300 nm) were obtained. The figure shows that while **2** affords straight tape-like fibers, **4** forms straight fibers made of tightly intertwined helical segments, indicating once again that the morphology of the self-assembled fibers is only dependent on the molecular structure. Note that the possibility to promote self-assembly in a confined space determined by the features of the stamp is crucial if one wants to integrate the fibers into a device.

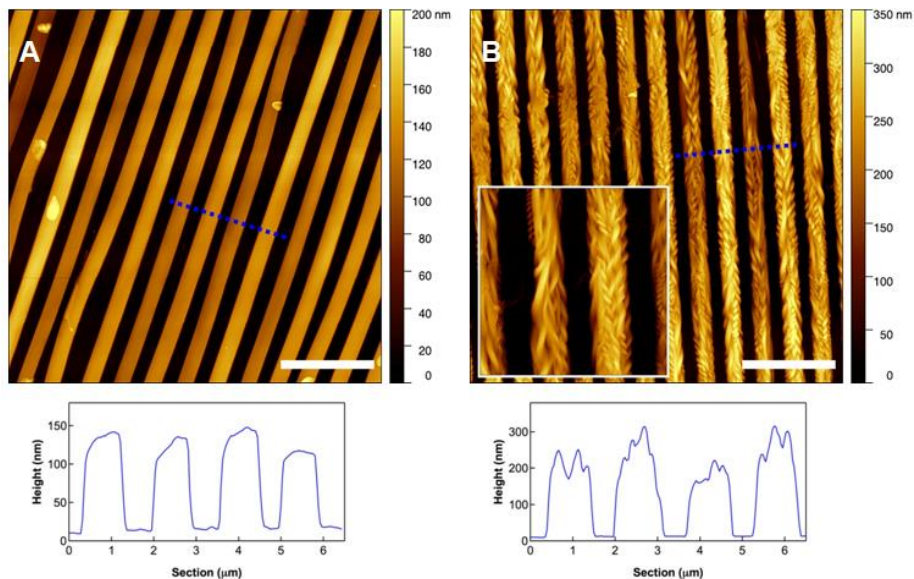


Figure 3. AFM images $20 \times 20 \mu\text{m}^2$ and related height plots of the fibers of **1** (A) and **4** (B) patterned according the Lithographically Controlled Wetting (LCW)^{ref} technique. Scale bars = $5 \mu\text{m}$. Inset image (A): zoom $5 \times 5 \mu\text{m}^2$.

2.3 Optical properties. A comprehensive photophysical analysis of compounds **1-5** in solution and as solid films was carried out. Table 1 reports the maxim absorption and emission values, the molar coefficients and the quantum yields of compounds **1-5** in solution, in cast films and as fibers while Table S1 reports the emission lifetimes in CH_2Cl_2 at r.t.

Table 1. Photophysical data of compounds **1-5**.

Item	Absorption		Emission	
	λ , nm (ϵ , $\text{M}^{-1} \text{cm}^{-1}$) ^[a]	λ_{max} (nm) ^[a] , Φ ^[a,b]	λ_{max} DC (nm) ^[c]	λ_{max} , fib (nm), Φ ^[d]
1	421 (34700)	538, 0.34	552	622, 0.006
2	480 (41300)	657, 0.004	...	840
3	431 (38500)	575, 0.20	626	649, 0.01
4	482 (40200)	667, 0.5	822	828
5	446 (30300)	672, 0.03	674	687

^[a]In CH_2Cl_2 at r.t. on air-equilibrated solutions. ^[b]Determined using $[\text{Ru}(\text{bpy})_3]\text{Cl}_2$ in H_2O ($\Phi=0.04$)^[14].

^[c]Recorded from drop-cast amorphous thin films on glass surfaces. ^[d]Recorded from crystalline fibers grown on glass surfaces.

The corresponding spectra are shown in Figure 4. All compounds show broad absorption bands associated to the lowest energy π - π^* transition of the central thiophenic backbone, with the corresponding maxima shifting to higher wavelengths in the presence of strong electron-withdrawing groups such as $-\text{NO}_2$ and $-\text{COC}_6\text{F}_{13}$ as the outermost substituents.

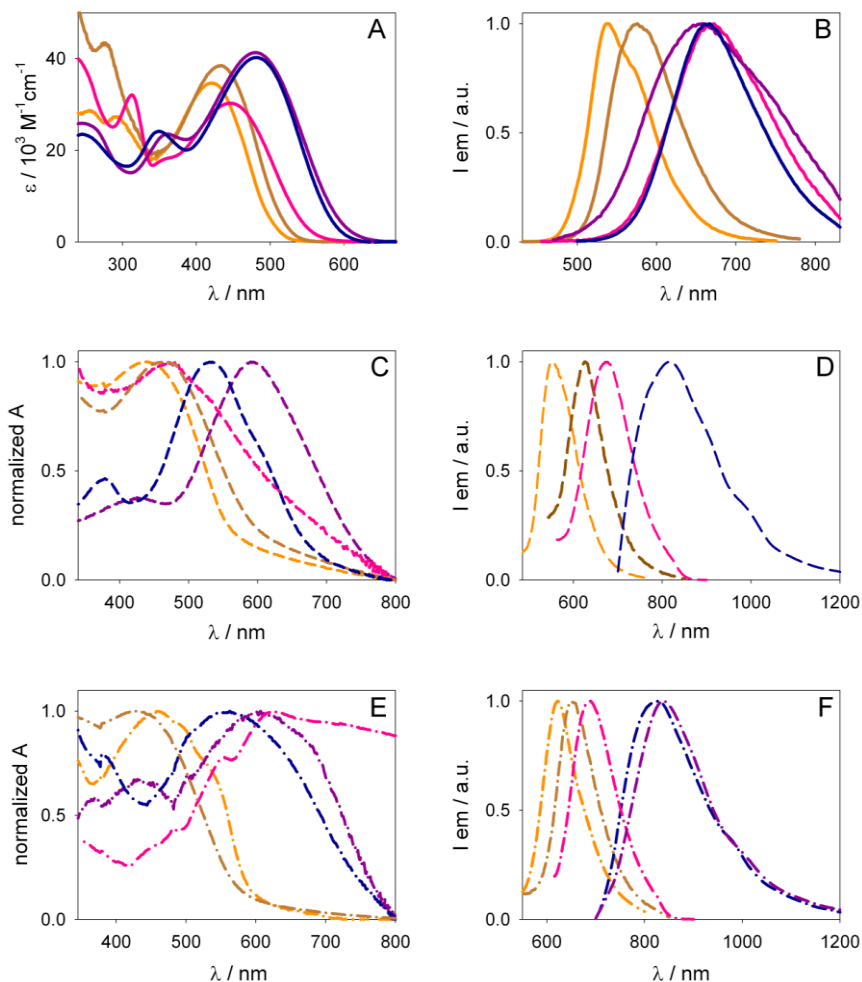


Figure 4. Absorption and emission spectra of **1** (yellow), **3** (brown), **5** (pink), **4** (blue), and **2** (purple) in different conditions. A-B: air equilibrated CH_2Cl_2 at room temperature; C-D: drop-cast films on glass surfaces at room temperature; E-F: as crystalline fibers deposited on glass surfaces at room temperature.

As a consequence, solutions of **1-5** cover a range of colors from yellow (**1**) to wine red (**2**), with extinction coefficients included between *circa* 30000 and 41000 M⁻¹cm⁻¹. Emission spectra in CH₂Cl₂ at r.t. show a similar trend (Figure 4B), with maxima red-shifting in the visible spectrum in a range between 540 and 670 nm, while quantum efficiencies result strongly dependent on the type of substituent, dropping from 0.34 for **1** to 0.004 for **2**. Emission lifetimes (see Table S1), determined in the same conditions, point out singlet excited state deactivations with sub-nanosecond decays; for the majority of the molecules taken in exam, multiexponential decays were evidenced, possibly due to inhomogeneities between the adopted different conformations in solution and in aggregates, as revealed for other thiophene-based oligo- and polymeric structures ^[12]. With the exception of **2**, drop-cast samples from CH₂Cl₂ solutions showed appreciable luminescence signals (with lower quantum yields compared to efficiencies in solution, due to the increased predominance of packing-induced radiationless deactivation pathways ^[13], with **4** displaying a broad emission profile with a maximum in the NIR region (Figure 4D).

Absorption profiles (Figure 4C) are affected to a great extent by the degree of organization of the molecules in the amorphous phase, showing the broadening and the red-shift of the absorption maxima with respect to the signals recorded in solution. This trend is even more evident when molecules organize in crystalline fibers on glass surfaces, which display broader absorptions at lower energies compared to those recorded on drop-cast films (Figure 4E); interestingly, deposited fibers are showing appreciable luminescence ($\Phi \sim 0.01$ for **1** and **3**), ranging from the orange-red of **1** towards the NIR spectrum (Figure 4F). More specifically, **4** and **2** show their fluorescence maximum around 830 and 840 nm, respectively, with a broad emission profile extending up to 1200 nm (~ 1.05 eV).

2.4 Cyclic Voltammetries. Figure 5 shows the CVs of compounds **1-5** in solution, cast films from dimethyl chloride and as fibers, together with the corresponding redox potentials and energy gaps. The compound **1** in solution shows a quasi-reversible oxidation wave but the reduction wave is outside the electrochemical window of the electrolyte. The CVs of compound **2** and of **5** in solution show quasi-reversible oxidation waves, with an absorption pre-peak in the case of **5**, characterized by sharp reverse peaks due to the fast reduction of the radical cation absorbed on the surface of the electrode. The reduction waves appear quasi-reversible with a good symmetry of the direct and reverse waves. Compounds **3** and **4** also show reduction waves within the electrochemical windows but they are not reversible.

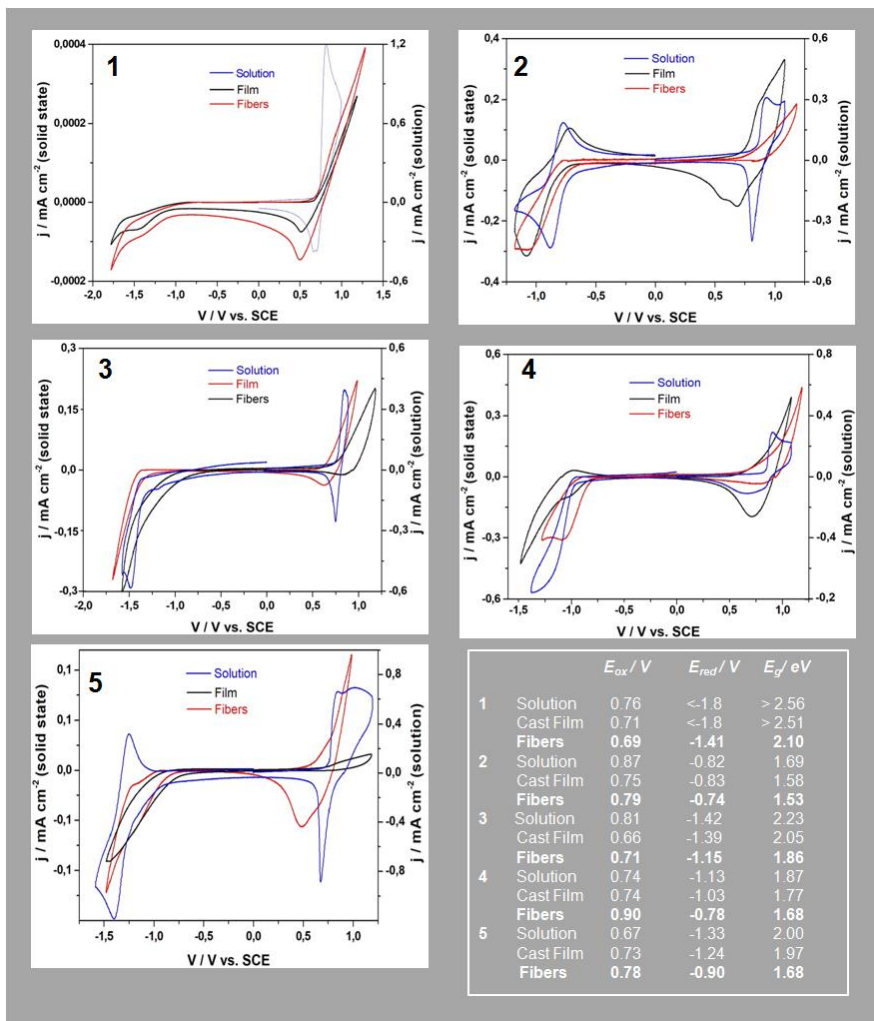


Figure 5. Cyclic voltammograms at 0.1 V s^{-1} of compounds **1-5** in CH_2Cl_2 0.1 mol L^{-1} $(\text{C}_4\text{H}_9)_4\text{NClO}_4$ solution and of the related fibers and thin film grown on ITO and tested in propylenecarbonate 0.1 mol L^{-1} $(\text{C}_2\text{H}_5)_4\text{NBF}_4$. In the table the corresponding redox potentials and energy gaps.

Finally, compound **3** shows an oxidation wave similar to that of compound **2** but 60 mV less positive, whereas compound **4** shows the less positive oxidation wave but also the less symmetric one, due to a broad reverse wave. By comparing the five energy gaps in solution, compound **2** shows the lowest one because of the huge shift of the LUMO related to the strong effect of the nitro-group in stabilizing radical-anions. In general, the compounds **1-5** show smaller energy

gaps when grown in solid state and, in particular, when the order of the solid is driven toward the fibers. So, if the reduction of compound **1** is outside the electrochemical window both in solution and in amorphous film, in the fiber-state the reduction standard potentials became -1.41 V. In the other cases, the energy gaps of the fibers is about 0.2-0.3 eV smaller than that of the cast film, except for compound **2** where it decreases 0.1 eV. The fibers of compound **2** has also the peculiarity of a satisfactory reversibility of the reduction processes. These results confirm the hypothesis that the solid state organization influences the LUMO overlapping especially when the electron withdrawing group is larger, on the other hand, when the reduction potential depends on the solid state assembly, it easier changes with the electrochemical doping-undoping processes.

2.5 DFT calculations. To understand the basic interactions governing the aggregation in fibers of different materials we have studied, using density functional theory (DFT) calculations, the dimers of the various molecules. We have found that in all cases, partially excepting compound **4**, the π - π stacking involving the molecular backbones plays an important role. This is very evident in the dimer of sexithiophene **1**, where the π - π stacking is basically the only force binding the two molecules. Adding side substituents, however, additional effects start to be important. These are related to a significant charge redistribution in the molecules. This is visualized in Figure 6, where we report the electrostatic potential generated by each molecule. In the case of **5**, having terminal benzothiadiazole groups, the net effect is not very large and the molecules in the dimer show only small distortions with respect to the isolated ones. This traces back to the fact that, despite an important charge depletion on the thiadiazole moiety, the charge distribution in the molecular backbone and the side hexyls is not much perturbed. Thus, the main bonding character is still a π - π stacking. On the contrary, in compounds **3** and **2**, the presence of oxygen atoms in the end substituents, induces a stronger polarization, with a charge depletion in the hexyls (and partially in the backbone) and a charge accumulation on the oxygens. As a consequence, when two molecules interact, hydrogen bonds can form. These involve the oxygen atoms and some hydrogens in the hexyls (or, to a less extent, in the backbone). To confirm this effect, we have performed a study using the NCI indicator,^{ref} which can identify hydrogen bonding regions and highlight them in real space.

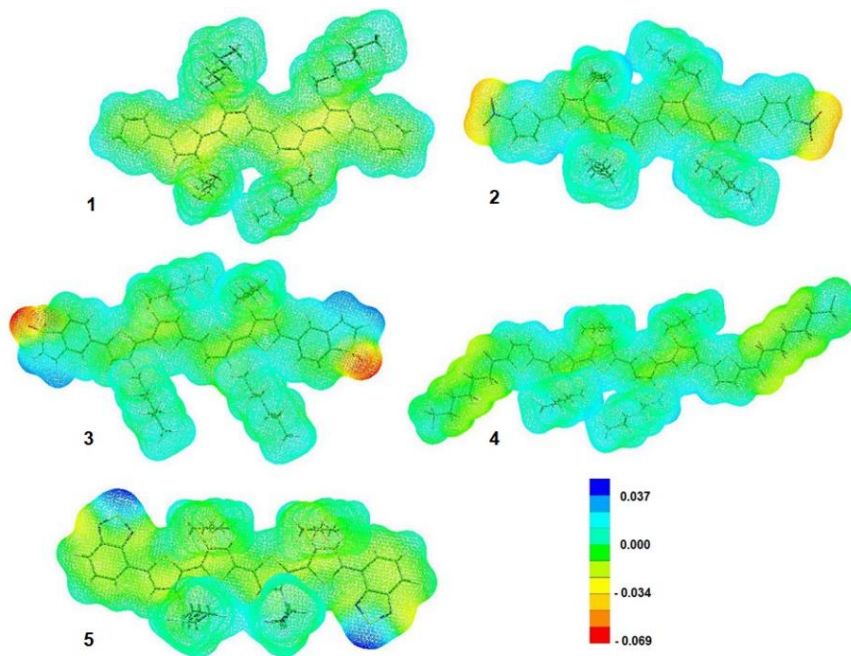


Figure 6. Electrostatic potential (in au) on the van der Waals surface for all the isolated molecules.

The corresponding plot is reported in Figure 7, and shows indeed hydrogen-bond regions between the oxygen atoms and the hydrogens (or the backbone). Nevertheless, because of fine differences between the two molecules and especially due to the different position of the oxygens (out of plane in **3**, in plane in **2**), the final dimers' structure are different in the two cases. For **3**, we observe prominently hydrogen-bond interactions involving the hexyls, thus in the dimer the two molecules tend to twist onto each other, despite the molecular backbone is not strongly distorted. On the other hand, in **2**, the oxygens interact not much with the hydrogens in the hexyls but preferably with the molecular backbone. Consequently, instead of a twisting of the two molecules around each other, we rather observe strong distortion of the backbone of each individual molecule.

Finally, considering compound **4** we see that the presence of many fluorine atoms induces a significant depletion of charge in the π system of the molecular backbone with consequent accumulation on the fluorines. Accordingly, in the dimer we do not observe anymore an important π - π stacking interaction but rather an interaction between the fluorines of one molecule and the backbone of the other molecule.

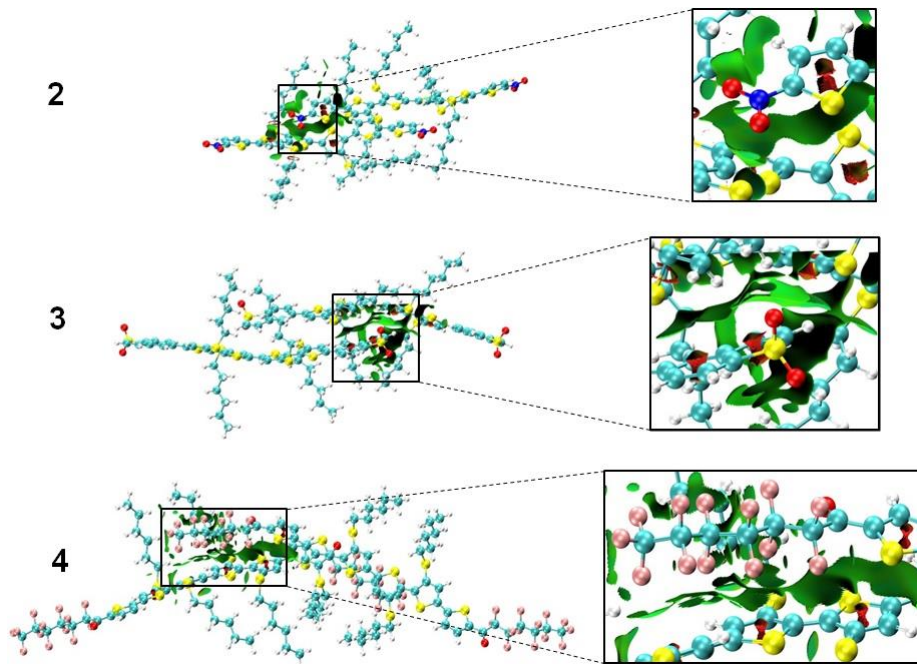


Figure 7. NCI indicator isosurface plots for the dimers of compounds **2-4**. For clarity the isosurfaces were generated only for the regions indicated by the boxes.

2.6 X-ray diffraction. The X-ray diffraction patterns of the microfibers are reported in Figure 8. All the samples show patterns from highly crystalline materials; the large bell shaped background at about 24° (2θ) is due to the glass substrate. The fibers of **5** show different patterns, with peaks at different angular positions and relative intensities, depending on they are collected from a yellow or yellow/black sample. This is a clear evidence the two colors are due to different polymorphs. All the patterns show the second order reflection of some peaks: it is a further indication microfibers have a high degree of crystal orientation. The peaks registered at the lowest angular values correspond to a 2.4-2.5 nm for the **3**, **4** and **5** molecules, to slightly smaller distance, 2.2 nm, for the **2** one and to 1.6 nm for the unsubstituted **1**. Taking into consideration the molecular lengths as obtained from theoretical calculations and the interplanar distances, we can roughly suppose the packing of the unit cell with molecules differently inclined respect to main crystallographic axes. A hypothetical sketch is shown in the Figure 10.

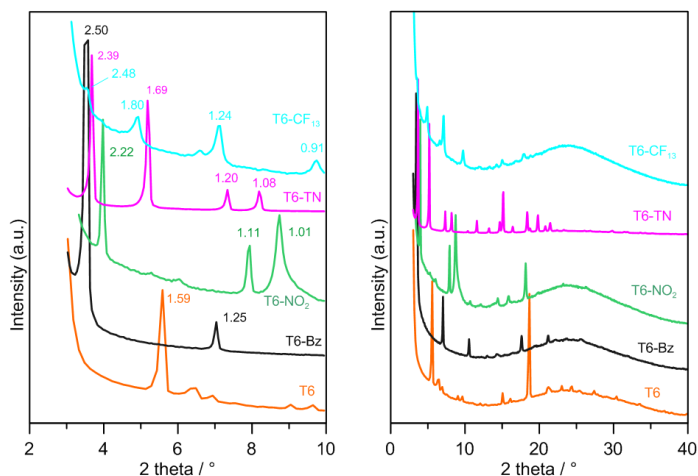


Figure 8. X-ray diffraction plots of microfibrils grown from toluene solution by slow diffusion of CH_3CN vapors. Left side: expansion of the 2-theta interval $2\text{-}10^\circ$. The values reported are interlayer distances in nm. For T6-Bz is reported the pattern of yellow fibers.

Respect to the other samples, fibers of **4** show an overall decrease of the diffracted intensity and a full width at half-maximum (FWHM) of the most intense peak ($\sim 0.23^\circ$), almost double respect to the others fibers ($\sim 0.11^\circ$).

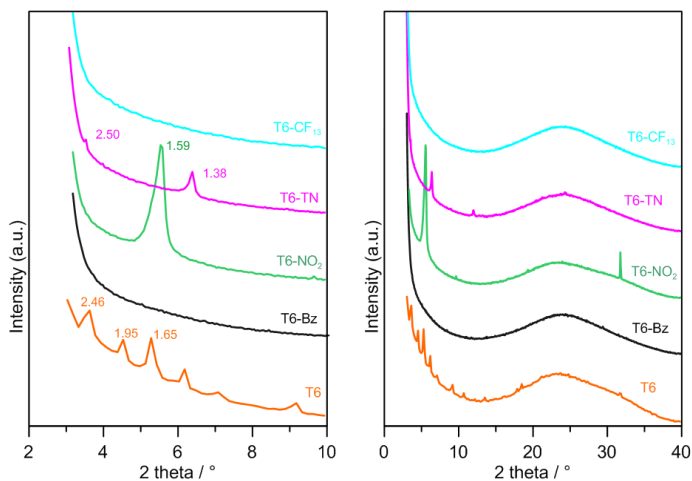
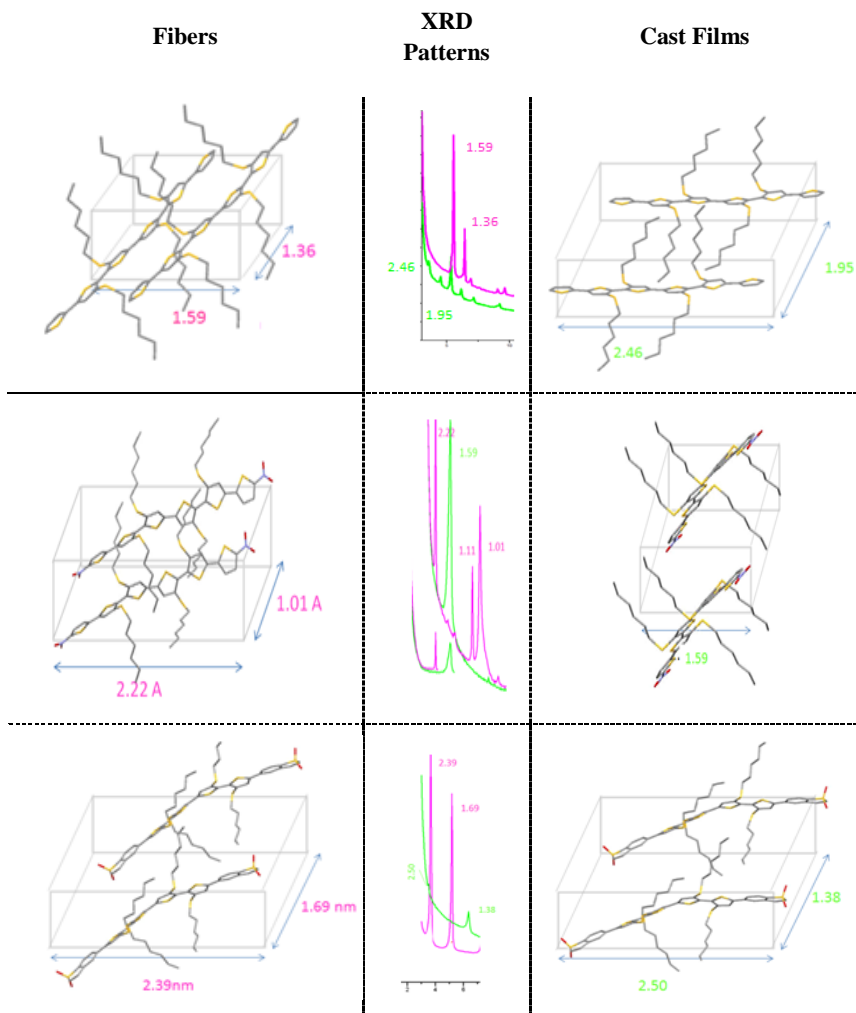


Figure 9. X-ray diffraction plots of cast films. Left side: expansion of the 2-theta interval $2\text{-}10^\circ$. The values reported are interlayer distances in nm.

This is a proof that in the experimental conditions used of **4** crystals are less perfect and with shorter coherent domains. The low tendency of **4** to give good crystals could be related to the presence of the alkyl fluorinated terminal residue that assume disordered conformations.

The patterns of the cast films are reported in Figure 9. Only the **1**, **2** and **3** fibers show peaks due to crystalline order. Respect to the fiber patterns they show a worse overall quality: few or no peaks and bigger peak widths highlight less order and smaller crystal domains. The position of the peaks at different angular values for all the crystalline film samples evidence a different solid state aggregation respect to its own fibers.



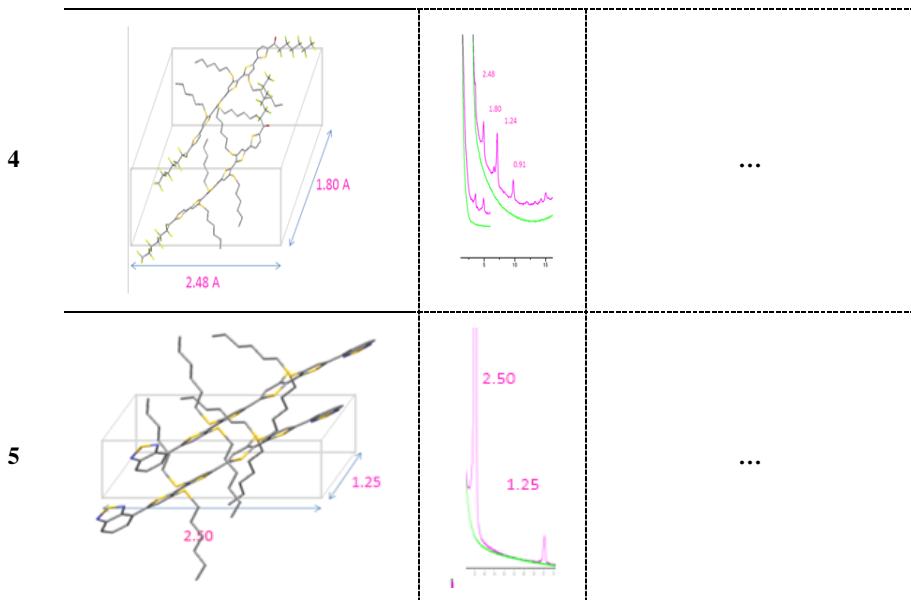


Figure 10. Sketch of the possible molecular structure of fiber nanocrystal (left) or cast film (right). The drawings were done on the hypothesis the main reflections correspond to crystallographic main axes. In the center are reported for each species the XRD patterns of the fiber (magenta) or the film (green). The interlayer distances of the peaks considered are reported in nm.

III. METHODS

3.1 Morphology measurements.

Scanning electron microscopy: SEM images were obtained with a SEM-FEG Zeiss LEO 1530 instrument operating at $V_{acc} = 5$ keV.

Atomic Force Microscopy: AFM images were collected in air on a Multimode8 microscope operated in PeakForce mode and equipped with a type J scanner (Bruker Nano Inc. GmbH, Berlin, Germany) and SNL-A probes with a nominal spring constant of 0.35 N/m (Bruker AFM Probes, Camarillo, CA). Background interpolation and surface roughness parameter calculations were performed with Gwyddion 2.48 (<http://gwyddion.net/>).

Stamp preparation: the elastomeric polydimethylsiloxane (PDMS, Sylgard 184 Dow Corning) stamps were prepared by replica molding of a of an aluminium master. The stamp motifs consist of parallel lines 600 nm wide, 230 ± 15 nm deep and 1.5 μm periodicity. The curing conditions were; temperature 50 °C curing time 12 hours. After curing, PDMS stamps were peeled off, cleaned by sonication in ethanol for 10 min, and dry in nitrogen in order remove the un-cured material.

Material: Sylgard 184 (polydimethylsiloxane) silicone elastomer base and curing agent were purchased from Dow Corning.

Non-solvent vapor-induced crystallization by LCW: 5 μL of 1 g/L toluene solution of compounds were drop cast on the substrate (silicon wafer $1 \times 1 \mu\text{m}^2$), then a PDMS stamp was placed on the top, paying attention to the stripes orientation, and exposed to saturated acetonitrile (non-solvent) vapor atmosphere at room temperature for 24 h in an airtight container. Afterwards, the stamp was removed and, before characterization, the sample was aged in atmospheric conditions for 2 hours.

3.2 Photophysical characterization. Absorption spectra were recorded on air equilibrated solutions at room temperature with a Agilent Cary 100 UV-Vis spectrophotometer, using quartz cells with path length of 1.0 cm. Absorption spectra of films on glass (drop-cast and fibers) were recorded in transmission mode at room temperature with a Perkin Elmer Lambda 650 spectrophotometer. Emission spectra of solutions and films on glass were recorded on a Perkin Elmer LS50B fluorescence spectrofluorometer. Circular Dichroism. CD spectra on films were recorded using a spectropolarimeter JASCO J-715 under ambient conditions. Emission lifetime measurements were performed on a Edinburgh FLS920 spectrofluorimeter equipped with a TCC900 card for data acquisition in time-correlated single-photon counting experiments (0.5 ns time resolution) with a LDH-P-C-405 pulsed diode laser. Longer lifetimes were measured by the PerkinElmer LS-50. Emission quantum yields were measured following the method of Demas and Crosby ^[15] (standard used: $[\text{Ru}(\text{bpy})_3]^{2+}$ in aqueous solution, $\Phi=0.04$) ^[16]. For solid samples, emission quantum yield was calculated from corrected emission spectra registered by an Edinburgh FLS920 spectrofluorimeter equipped with a LabSphere barium sulfate coated integrating sphere (4 in.), a 450W Xe lamp (excitation wavelength tunable by a monochromator supplied with the instrument) as light source, and a R928 photomultiplier tube, following the procedure described by De Mello *et al* ^[17]. The estimated experimental errors are 2 nm on the band maximum, 5% on the molar absorption coefficient and luminescence lifetime, 10% on the emission quantum yield in solution, and 20% on the emission quantum yield in solid.

3.3 Cyclic Voltammetry. The electrochemical measurements were performed with an AMEL electrochemical system model 5000 controlled by the software Corrware 2.9 for Windows using a home-made three-compartments cell at room temperature under Ar pressure. The working electrode was a platinum disk (\varnothing 1 mm), for the experiments in solution, and indium-tin-oxide/glass modified electrodes [ITO, Balzers, 23 ohm/square, area (12 x 12) mm^2] for the experiments on the fibers or amorphous films. The auxiliary electrode was a Pt wire and the reference electrode was an aqueous KCl Saturated Calomel Electrode (SCE) connected to the working compartment with a liquid bridge. The supporting electrolytes were CH_2Cl_2 (Aldrich HPLC grade., distilled on P_2O_5 and stored under Ar pressure) 0.1 mol L^{-1} $(\text{C}_4\text{H}_9)_4\text{NClO}_4$ (Aldrich, puriss. vacuum dried) and propylene carbonate (Aldrich anhydrous, stored under Ar pressure) 0.1 mol L^{-1} $(\text{C}_2\text{H}_5)_4\text{NBF}_4$ (Aldrich, puriss. vacuum dried). The solutions were purged with Ar before the measurements.

3.4 DFT calculations. Ground-state calculations and geometry optimizations have been performed with the TURBOMOLE program package ^[18] using the BLOC exchange-correlation

^[19] functional and the multipole accelerated resolution of identity approximation ^[20]. For isolated molecules a def2-TZVP basis set ^[21] was employed. For the dimers, the optimal structures have been identified performing a preliminary screening, via geometry optimizations at the BLOC/de2-SV(P) level of theory ^[19, 22], on a large number (about 100) of guess structures generated by random displacements of two monomers. Subsequently, the 20 best candidates have been optimized at the BLOC/def2-TZVP level to identify the most stable configuration. The NCI indicator ^[23] investigation has been carried out using the NCI PLOT program ^[24].

3.5 X-ray diffractions analysis. The X-ray diffractions measurements were carried out by means of a PANalytical X'Pert diffractometer equipped with a copper anode (λ mean = 0.15418 nm) and a fast X'Celerator detector. Films grown on glass cover slips were directly investigated.

IV. EXPERIMENTAL SECTION

4.1 Synthesis. *General:* TLC was carried out with 0.2-mm thick of silica gel 60 F₂₅₄ (Sigma). Preparative column chromatographies were carried out on glass columns with silica gel 60 (particle sizes 0.040-0.063 mm, Sigma). 3-bromothiophene, 2-thienylboronic acid, 2-bromo-5-nitrothiophene, 4-bromo-2,1,3-benzothiadiazole, 2-thiophenecarboxaldehyde, 2-bromo-5-nitrothiophene, 5-bromo-1-benzothiophene, *N*-bromosuccinimide, Manganese(IV) oxide, bromine, sodium bicarbonate, *n*-butyllithium 2.5 M solution in hexane, potassium tert-butoxide, 1-bromohexane 98%, palladium(II)chloride dichloromethane complex (PdCl₂dppf), 1,1'-bis(diphenylphosphino)ferrocene, 3-Chloroperbenzoic acid, were purchased from Sigma-Aldrich Co; sulfur sublimed washed winnowed 99.5% from Carlo Erba; 2-isopropoxy-4,4,5,5-tetramethyl-1,3,2-dioxaborolane, Bis(pinacolato)diboron from Alfa Aesar GmbH & Co KG. All reagents and solvents were used as received. Organic solvents were dried by standard procedures. Microwave experiments were carried out in a CEM Discover SP-Microwave Synthesizer reactor in a closed vessel (230W, fixed temperature at 80°C, air, high stirring rate). Reactions with ultrasound were performed in a FALC LBS1 50KHz Ultrasonic bath at room temperature. *Melting* points were determined on *Kofler bank* apparatus and are uncorrected. All ¹H NMR and ¹³C NMR spectra were recorded on a Varian Mercury-400/500 spectrometer equipped with a 5-mm probe. Chemical shifts were calibrated using the internal CDCl₃ resonance which were referenced to TMS. Mass spectra were collected on a Thermo Scientific TRACE 1300 gas chromatograph.

General synthesis of compounds 1,3,5: A mixture of **1c** (1 mmol), thienylboronic ester or **5c** or 4-(4,4,5,5-tetramethyl-1,3,2-dioxaborolan-2-yl)benzo[c][1,2,5]thiadiazole (6 mmol), PdCl₂dppf (0.1 mmol), NaHCO₃ (4 mmol) in THF/water 2:1 (3 mL) was irradiated with microwaves at 80°C for 15 min. The reaction mixture was brought to room temperature and the solvent was evaporated under reduced pressure. All compounds were purified by flash chromatography. **3''',3''''',4',4''''-tetrakis(hexylthio)-2,2':5',2''':5'',2''''':5''''',2''''''':5''''''-sexithiophene (1)** → The residue was isolated by flash chromatography (Cyclohexane/CH₂Cl₂, 80:20). Yield 80%.

Orange solid; mp=54–56°C. ¹H NMR (400 MHz, CDCl₃, TMS/ppm): δ 7.37 (d, ³J = 3.6 Hz, ⁴J = 1.2 Hz, 2H), 7.34 (d, ³J = 5.2 Hz, ³J = 1.2 Hz, 2H), 7.14 (s, 2H), 7.13 (s, 2H), 7.06 (dd, ³J = 3.6 Hz, ³J = 5.2 Hz, 2H), 2.90–2.85 (m, 8H), 1.65–1.59 (m, 8H), 1.41–1.38 (m, 8H), 1.30–1.25 (m, 16H), 0.88–0.85 (m, 12H); ¹³C NMR (400 MHz, CDCl₃): δ 137.2, 136.5, 136.1, 132.5, 132.46, 132.0, 131.2, 127.9, 127.4, 127.0, 125.0, 124.2, 43.5, 36.4, 36.3, 31.4, 30.2, 29.7, 29.5, 28.4, 22.6, 14.0. UV/Vis: λ_{max} 421 nm (ε 34700 cm⁻¹M⁻¹), λ_{em} 538 nm in CH₂Cl₂.

5,5'-(3,3',3''',4''-tetrakis(hexylthio)-[2,2':5',2'':5'',2''''-quaterthiophene]-5,5''''-diyl)bis(benzo[b]thiophene 1,1-dioxide) (3) → The residue was isolated by flash chromatography (Cyclohexane/CH₂Cl₂/AcOEt, 70:25:5). Yield 95%. Dark orange solid. ¹H NMR (500 MHz, CD₂Cl₂, TMS/ppm): δ 7.80 (d, *J*=8 Hz, 2H), 7.75 (d, *J*=8 Hz, 2H), 7.65 (s, 2H), 7.48 (s, 2H), 7.32 (d, *J*=7 Hz, 2H) 7.28 (s, 2H) 6.82 (d, *J*=7 Hz, 2H), 2.93 (t, 8H), 1.68–1.61 (m, 8H), 1.45–1.38 (m, 8H), 1.33–1.28 (m, 16H), 0.90–0.86 (m, 12H); ¹³C NMR (400 MHz, CDCl₃): δ 140.8, 139.0, 136.4, 135.2, 134.1, 133.2, 133.18, 132.4, 131.8, 131.6, 131.4, 128.9, 127.4, 127.3, 122.1, 122.0, 36.4, 36.37, 31.3, 29.4, 28.4, 22.5, 14.0. UV/Vis: λ_{max} 431 nm (ε 38500 cm⁻¹M⁻¹), λ_{em} 575 nm in CH₂Cl₂.

4,4'-(3,3',3''',4''-tetrakis(hexylthio)-[2,2':5',2'':5'',2''''-quaterthiophene]-5,5''''-diyl)bis(benzo[c][1,2,5]thiadiazole) (5) → The residue was isolated by flash chromatography (Cyclohexane/CH₂Cl₂/AcOEt, 80:18:2). Yield 75%. Dark red solid; mp=124–126°C. ¹H NMR (500 MHz, CDCl₃, TMS/ppm): δ 8.20 (s, 2H), 7.95 (d, ³J = 8.4 Hz, 2H), 7.87 (d, ³J = 7.2 Hz, 2H), 7.64 (dd, ³J = 6.8 Hz, ³J = 8.4 Hz, 2H), 7.23 (s, 2H), 2.97–2.89 (m, 8H), 1.68–1.62 (m, 8H), 1.45–1.26 (m, 24H), 0.88–0.83 (m, 12H); ¹³C NMR (500 MHz, CDCl₃): δ 155.5, 152.0, 138.8, 136.6, 133.5, 132.9, 132.8, 131.9, 131.6, 129.6, 127.5, 126.7, 125.3, 120.5, 36.4, 31.4, 31.39, 29.56, 29.51, 28.5, 28.4, 22.6, 22.57, 14.1, 14.0.

General synthesis of compounds 2, 4: A mixture of 5-bromo-3,3'-bis(hexylthio)-5''-nitro-2,2':5',2''-terthiophene (**1e**) or 1-(5''-bromo-3'',4''-bis(hexylthio)-[2,2':5',2''-terthiophen]-5-yl)-2,2,3,3,4,4,5,5,6,6,7,7,7-tridecafluoroheptan-1-one (**1f**) (1 mmol), bis(pinacolato)diboron (0.6 mmol), PdCl₂dppf (0.05 mmol), NaHCO₃ (2 mmol) in THF/water 2:1 (3 mL) was irradiated with microwaves at 80°C for 30 min. The reaction mixture was brought to room temperature and the solvent was evaporated under reduced pressure. All compounds were purified by flash chromatography.

3'',3''''',4',4''''-tetrakis(hexylthio)-5,5''''-dinitro-2,2':5',2'':5'',2''''-5''''',2''''':5''''',2''''''-sexithiophene (2) → The residue was isolated by flash chromatography (Cyclohexane/CH₂Cl₂, 80:20). Yield 80%. Dark blue solid; mp=147–149°C. ¹H NMR (500 MHz, CDCl₃, TMS/ppm): δ 7.88 (d, *J*=4 Hz, 2H), 7.33 (s, 2H), 7.22 (s, 2H), 7.14 (d, *J*=4 Hz, 2H), 2.92–2.88 (m, 8H), 1.66–1.60 (m, 8H), 1.44–1.40 (m, 8H), 1.30–1.28 (m, 16H), 0.90–0.87 (m, 12H); ¹³C NMR (500 MHz, CDCl₃): δ 149.7, 144.0, 136.5, 134.8, 134.2, 133.5, 133.4, 131.4, 129.8, 129.7, 127.7, 122.7, 36.5, 36.48, 31.3, 29.5, 29.4, 28.4, 22.5, 14.0. UV/Vis: λ_{max} 480 nm (ε 41300 cm⁻¹M⁻¹), λ_{em} 657 nm in CH₂Cl₂.

1,1'-(3''',3''''',4',4''''-tetrakis(hexylthio)-[2,2':5',2'':5'',2''''-5''''',2''''':5''''',2''''''-sexithiophene] - 5,5'''''-diyl)bis(2,2,3,3,4,4,5,5,6,6,7,7,7-tridecafluoroheptan-1-one) (4) → The residue was

isolated by flash chromatography (Cyclohexane/CH₂Cl₂, 80:20). Yield 60%. Dark purple solid; mp=136-138°C. ¹H NMR (500 MHz, CDCl₃, TMS/ppm): δ 7.91 (d, *J*=4 Hz, 2H), 7.40 (s, 2H), 7.31 (d, *J*=4 Hz, 2H), 7.22 (s, 2H), 2.92–2.89 (m, 8H), 1.64–1.58 (m, 8H), 1.42–1.41 (m, 8H), 1.29–1.27 (m, 16H), 0.89–0.87 (m, 12H); ¹³C NMR (500 MHz, CDCl₃): δ 174.9, 149.4, 137.8, 136.5, 135.9, 135.0, 134.4, 133.5, 133.4, 131.4, 130.3, 127.7, 125.3, 36.5, 36.4, 31.3, 29.7, 29.5, 29.4, 28.4, 22.7, 22.6, 14.03, 14.01. UV/Vis: λ_{max} 482nm (ε 40200 cm⁻¹M⁻¹), λ_{em}. 667 nm in CH₂Cl₂.

General synthesis of compounds 1e, 1f: A mixture of 1-(5-bromothiophen-2-yl)-2,2,3,3,4,4,5,5,6,6,7,7,7-tridecafluoroheptan-1-one prepared according to ref. (1) or 2-bromo-5-nitrothiophene (1 mmol), (3,3'-bis(hexylthio)-[2,2'-bithiophen]-5-yl)tributylstannane (**1d**) (1 mmol), Pd(PPh₃)₄ (0.05 mmol) in Toluene (10 mL) was refluxed for 24 h. The reaction mixture was brought to room temperature and the solvent was evaporated under reduced pressure. The title compound was isolated by flash chromatography on silica gel.

3,3'-bis(hexylthio)-5''-nitro-2,2':5',2''-terthiophene (1e) → The residue was isolated by flash chromatography (Cyclohexane/CH₂Cl₂, 80:20). Yield 60%. Red solid. EI-MS *m/z* 290 (M⁺). ¹H NMR (500 MHz, CDCl₃, TMS/ppm): δ 7.87 (d, *J*=5 Hz, 1H), 7.43 (d, *J*=5 Hz, 1H), 7.32 (s, 1H), 7.11 (d, *J*=5 Hz, 2H), 2.86–2.82 (m, 4H), 1.62–1.55 (m, 4H), 1.39–1.23 (m, 12H), 0.89–0.85 (m, 6H); ¹³C NMR (500 MHz, CDCl₃): δ 149.6, 144.2, 135.0, 134.1, 133.5, 132.8, 131.2, 130.7, 129.7, 129.6, 126.7, 122.6, 36.2, 36.1, 31.35, 31.32, 29.5, 29.4, 28.4, 28.3, 22.55, 22.52, 14.01.

1-(3'',4'-bis(hexylthio)-[2,2':5',2''-terthiophen]-5-yl)-2,2,3,3,4,4,5,5,6,6,7,7,7-tridecafluoroheptan-1-one (1f) → The residue was isolated by flash chromatography (Cyclohexane/CH₂Cl₂, 80:20). Yield 62%. Orange oil. EI-MS *m/z* 592 (M⁺). ¹H NMR (500 MHz, CDCl₃, TMS/ppm): δ 7.89 (d, *J*=5 Hz, 1H), 7.42 (d, *J*=5 Hz, 1H), 7.39 (s, 1H), 7.29 (d, *J*=5 Hz, 1H), 7.12 (d, *J*=5 Hz, 1H), 2.86–2.83 (m, 4H), 1.62–1.55 (m, 4H), 1.40–1.26 (m, 12H), 0.89–0.85 (m, 6H); ¹³C NMR (500 MHz, CDCl₃): δ 174.8, 149.6, 137.7, 135.8, 135.3, 134.4, 133.6, 132.8, 131.3, 130.7, 130.6, 130.1, 126.4, 125.9, 125.2, 36.2, 36.1, 35.8, 31.4, 29.53, 28.4, 22.5, 13.929.

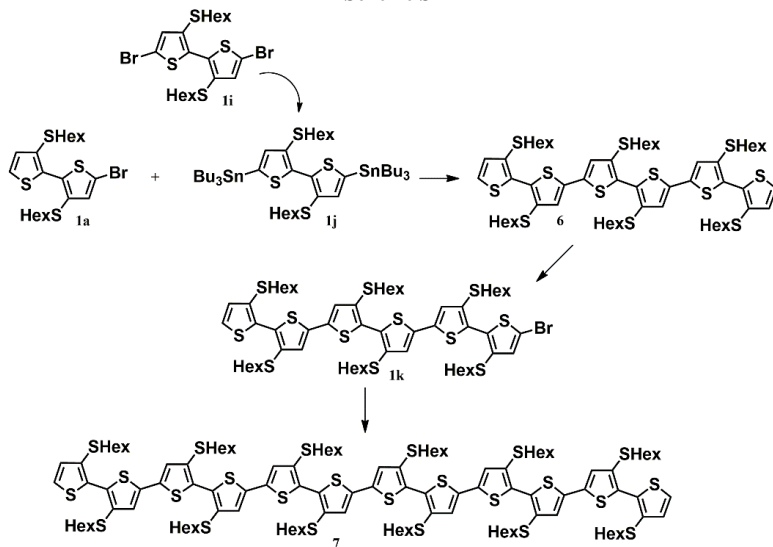
General synthesis of compounds 1g, 1h: To a solution of **1e**, **1f** (1 mmol) in CH₂Cl₂, 1 mmol of NBS were added. The reaction mixture was sonicated for 15 min at room temperature. The solvent was removed and the products were purified by flash chromatography.

5-bromo-3,3'-bis(hexylthio)-5''-nitro-2,2':5',2''-terthiophene (1g) → The residue was isolated by flash chromatography (Cyclohexane/CH₂Cl₂, 80:20). Yield 90%. Dark red oil. EI-MS *m/z* 370 (M⁺). ¹H NMR (500 MHz, CDCl₃, TMS/ppm): δ 7.86 (d, *J*=4 Hz, 1H), 7.29 (s, 1H), 7.11 (d, *J*=4 Hz, 1H), 7.06 (s, 1H), 2.86–2.82 (m, 4H), 1.62–1.56 (m, 4H), 1.39–1.26 (m, 12H), 0.90–0.87 (m, 6H); ¹³C NMR (500 MHz, CDCl₃): δ 149.8, 143.9, 134.5, 134.2, 133.4, 133.1, 132.9, 132.8, 129.8, 129.6, 122.7, 114.1, 36.5, 31.3, 29.44, 29.41, 28.4, 28.3, 22.5, 14.02, 14.01.

1-(5''-bromo-3'',4'-bis(hexylthio)-[2,2':5',2''-terthiophen]-5-yl)-2,2,3,3,4,4,5,5,6,6,7,7,7-tridecafluoroheptan-1-one (1h) → The residue was isolated by flash chromatography (Cyclohexane/CH₂Cl₂, 80:20). Yield 99%. Dark red oil. EI-MS *m/z* 670 (M⁺). ¹H NMR (500 MHz, CDCl₃, TMS/ppm): δ 7.89 (d, *J*=4 Hz, 1H), 7.36 (s, 1H), 7.29 (d, *J*=4 Hz, 1H), 7.06 (s, 1H), 2.87–2.83 (m, 4H), 1.63–1.56 (m, 4H), 1.42–1.24 (m, 12H), 0.90–0.85 (m, 6H); ¹³C NMR

(500 MHz, CDCl₃): δ 175.0, 149.3, 137.7, 136.0, 134.7, 134.5, 133.4, 133.1, 132.9, 132.8, 130.3, 125.4, 114.0, 36.4, 31.3, 29.43, 29.40, 28.3, 26.9, 22.5, 14.0, 13.9.

Scheme S1



3,3',3''',3''''',4'',4''''-hexakis(hexylthio)-2,2':5,2'':5''':5''''-2''''':5''''',2''''':5''''',2''''':5'''''-sexithiophene

(6) → The compound was prepared following the procedure used for compound 1e starting from **1a**² (2 mmol) and **(1j)** (1 mmol). The residue was isolated by flash chromatography (Cyclohexane/CH₂Cl₂, 90:10). Yield 60%. Orange oil. ¹H NMR (400 MHz, CD₂Cl₂, TMS/ppm): δ 7.45 (d, *J*=4.4 Hz, 2H), 7.25 (s, 2H), 7.24 (s, 2H), 7.14 (d, *J*=4.4 Hz, 2H), 2.91–2.85 (m, 12H), 1.62–1.59 (m, 12H), 1.41–1.27 (m, 36H), 0.91–0.87 (m, 18H); ¹³C NMR (400 MHz, CD₂Cl₂): δ 136.2, 136.1, 133.2, 132.9, 132.5, 131.7, 130.6, 127.3, 127.1, 126.2, 36.3, 35.99, 35.94, 31.4, 31.3, 29.55, 29.51, 28.37, 28.36, 28.34, 22.55, 22.53, 13.8. UV/Vis: λ_{max} 417 nm (ε 29900 cm⁻¹M⁻¹), λ_{em}. 540 nm (φ=0.29) in CH₂Cl₂.

5-bromo-3,3',3''',3''''',4'',4''''-hexakis(hexylthio)-2,2':5,2'':5''':5''''-2''''':5''''',2''''':5'''''-sexithiophene (1k)

→ The compound was prepared following the procedure used for compound 1e starting from **6**. The residue was isolated by flash chromatography (Cyclohexane/CH₂Cl₂, 90:10). Yield 50%. Dark orange oil. ¹H NMR (400 MHz, CDCl₃, TMS/ppm): δ 7.39 (d, *J*=4.4 Hz, 1H), 7.19 (s, 1H), 7.18 (s, 2H), 7.14 (s, 1H), 7.10 (d, *J*=4.4 Hz, 1H), 7.05 (s, 1H), 2.88–2.81 (m, 12H), 1.63–1.56 (m, 12H), 1.41–1.24 (m, 36H), 0.90–0.86 (m, 18H); ¹³C NMR (400 MHz, CD₂Cl₂): δ 136.4, 136.3, 136.1, 136.0, 133.9, 132.9, 132.8, 132.6, 132.2, 132.1, 132.0, 131.7, 130.7, 127.6, 127.4, 127.35, 127.31, 126.1, 113.1, 36.3, 36.1, 31.4, 31.35, 31.34, 27.7, 29.5, 29.4, 28.4, 28.3, 22.55, 22.53, 14.0.

Dodecamer (7) → The compound was prepared following the procedure used for compound **2** starting from **1k**. The residue was isolated by flash chromatography (Cyclohexane/CH₂Cl₂ 80:20). Yield 85%. Dark red solid; mp=104-106°C. ¹H NMR (400 MHz, CDCl₃, TMS/ppm): δ 7.40 (d, *J*=4.4 Hz, 2H), 7.20 (s, 6H), 7.19 (s, 2H), 7.18 (s, 2H), 7.11 (d, *J*=4.4 Hz, 2H), 2.90–2.81 (m, 24H), 1.65–1.56 (m, 24H), 1.43–1.24 (m, 72H), 0.89–0.86 (m, 36H); ¹³C NMR (400 MHz, CD₂Cl₂): δ 136.3, 136.2, 136.1, 132.8, 132.65, 132.62, 132.61, 132.1, 132.0, 131.99, 131.95, 131.91, 131.7, 130.7, 127.5, 127.4, 127.3, 126.1, 36.4, 36.1, 31.9, 31.4, 31.3, 29.7, 29.5, 29.48, 29.4, 28.3, 22.6, 22.5, 14.1. UV/Vis: λ_{max} 452 nm (ε 66600 cm⁻¹M⁻¹), λ_{em}. 584 nm (φ=0.28) in CH₂Cl₂.

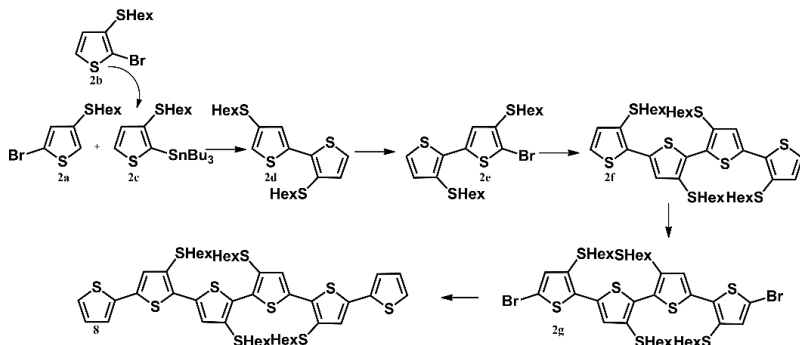
General synthesis of tributyl stannane derivatives: To a solution of brominated derivative (5-bromo-3,3'-bis(hexylthio)-2,2'-bithiophene (**1a**), 5,5'-dibromo-3,3'-bis(hexylthio)-2,2'-bithiophene² (**1i**) or 2-bromo-3-(hexylthio)thiophene² (**2b**) (1 mmol) in anhydrous THF (5 mL) at room temperature, n-BuLi (1 mmol or 2 mmol) was added. After 1.5h, Bu₃SnCl (1mmol or 2 mmol) was added and the reaction was stirred for 12h at room temperature. The mixture was extracted with water and then the organic phase was evaporated under reduced pressure.

(3,3'-bis(hexylthio)-[2,2'-bithiophen]-5-yl)tributylstannane (1d) → Yield 60%. Yellow oil. ¹H NMR (400 MHz, CDCl₃, TMS/ppm): δ 7.33 (d, *J*=5.2 Hz, 1H), 7.08 (s, 1H), 7.06 (d, *J*=5.2 Hz, 1H), 2.79–2.74 (m, 4H), 1.62–1.49 (m, 12H), 1.37–1.09 (m, 22H), 0.93–0.83 (m, 15H)

(3,3'-bis(hexylthio)-[2,2'-bithiophene]-5,5'-diyl)bis(tributylstannane) (1j) → Yield 70%. Yellow oil. ¹H NMR (400 MHz, CDCl₃, TMS/ppm): δ 7.08 (s, 2H), 2.78–2.74 (m, 4H), 1.62–1.49 (m, 16H), 1.37–1.09 (m, 36H), 0.92–0.83 (m, 24H).

Tributyl(3-(hexylthio)thiophen-2-yl)stannane (2c) → Yield 80%. Brown oil. ¹H NMR (400 MHz, CDCl₃, TMS/ppm): δ 7.58 (d, *J*=5.2 Hz, 1H), 7.21 (d, *J*=5.2 Hz, 1H), 2.77–2.74 (m, 2H), 1.68–1.51 (m, 8H), 1.40–1.14 (m, 18H), 0.94–0.86 (m, 12H).

Scheme S2



Synthesis of 2-bromo-4-(hexylthio)thiophene (2a) → To a stirred solution of 3-(hexylthio)thiophene² (1.5 mmol) in anhydrous THF (10 mL) at -78°C, 1.5 mmol of *n*-BuLi (2.5 M in hexane) was slowly added in 1h. After 1 h at -78°C, bromine (1.57 mmol) was added in 10min by a syringe. The resulting mixture was allowed to warm to room temperature and stirred for 20min before quenching with water. The product was extracted with CH₂Cl₂ (2x25 mL). The combined organic layers were dried over anhydrous sodium sulphate and the solvent was removed under reduced pressure. The product was isolated by flash chromatography (Cyclohexane, 100%). → Yield 51%. Yellow oil. ¹H NMR (400 MHz, CDCl₃, TMS/ppm): δ 7.01 (d, ³J=1.2, 1H), 6.96 (d, ³J=1.2, 1H), 2.81 (t, 2H), 1.61–1.57 (m, 2H), 1.42–1.27 (m, 6H), 0.88 (t, 3H).

3,4'-bis(hexylthio)-2,2'-bithiophene (2d) → The compound was prepared following the procedure used for compound 1e, starting from 2a and 2c. The residue was isolated by flash chromatography (Cyclohexane/CH₂Cl₂, 95:5). Yield 85%. Pale yellow oil. EI-MS *m/z* 398(M⁺). ¹H NMR (400 MHz, CDCl₃, TMS/ppm): δ 7.27 (d, ⁴J= 1.6 Hz, 1H), 7.18 (d, ³J = 4.8 Hz, 1H), 7.08 (d, ⁴J= 1.6 Hz, 1H), 7.02 (d, ³J = 4.8 Hz, 1H), 2.88–2.81 (m, 4H), 1.69–1.54 (m, 4H), 1.43–1.23 (m, 12H), 0.91–0.87 (m, 6H).

5'-bromo-3,4'-bis(hexylthio)-2,2'-bithiophene (2e) → The compound was prepared following the procedure used for compound 1g, starting from 2d. The residue was isolated by flash chromatography (Cyclohexane/CH₂Cl₂, 95:5). Yellow oil. Yield 86%. EI-MS *m/z* 476(M⁺). ¹H NMR (400 MHz, CDCl₃, TMS/ppm): δ 7.19 (d, ³J = 5.2 Hz, 1H), 7.14 (s, 1H), 7.01 (d, ³J = 5.2 Hz, 1H), 2.89–2.80 (m, 4H), 1.64–1.58 (m, 4H), 1.43–1.25 (m, 12H), 0.90–0.87 (m, 6H).

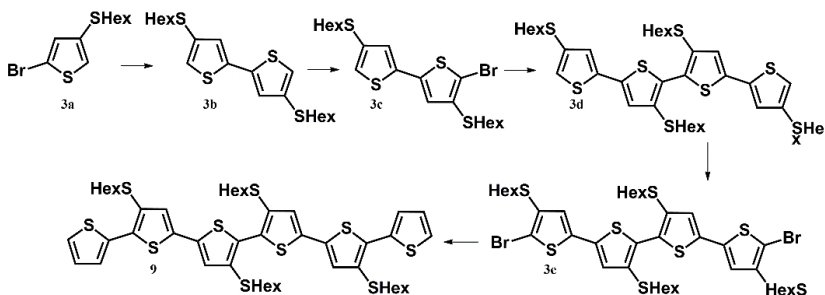
3,3'',3''',4'-tetrakis(hexylthio)-2,2':5',2'':5'',2'''-quaterthiophene (2f) → The compound was prepared following the procedure used for compound 2, starting from 2e. The residue was isolated by flash chromatography (Cyclohexane/CH₂Cl₂, 85:15). Yellow oil. Yield 85%. EI-MS *m/z* 796(M⁺). ¹H NMR (400 MHz, CDCl₃, TMS/ppm): δ 7.36 (s, 2H), 7.2 (d, ³J = 5.2 Hz, 2H), 7.04 (d, ³J = 5.2 Hz, 2H), 2.87–2.84 (m, 8H), 1.64–1.56 (m, 8H), 1.42–1.37 (m, 8H), 1.27–1.24 (m, 16H), 0.91–0.88 (m, 12H).

5,5'''-dibromo-3,3'',3''',4'-tetrakis(hexylthio)-2,2':5',2'':5'',2'''-quaterthiophene (2g) → The compound was prepared following the procedure used for compound 1g, starting from 2f using 2.2 mmol of NBS. The residue was isolated by flash chromatography

(Cyclohexane/CH₂Cl₂, 90:10). Brown yellow oil. Yield 99%. ¹H NMR (400 MHz, CDCl₃, TMS/ppm): δ 7.26 (s, 2H) 6.99 (s, 2H), 2.86–2.77 (m, 8H), 1.63–1.57 (m, 8H), 1.40–1.24 (m, 24H), 0.90–0.86(m, 12H).

3''',3''''',4',4''-tetrakis(hexylthio)-2,2':5',2'':5'',2''':5''',2''''':5''''''-sexithiophene (8) → The compound was prepared following the procedure used for compound 1 starting from **2g** and 2-thienylboronic acid. The residue was isolated by flash chromatography (Cyclohexane/CH₂Cl₂, 90:10). Dark orange oil. Yield 60%. ¹H NMR (400 MHz, CDCl₃, TMS/ppm): δ 7.37 (s, 2H), 7.26 (d, ³J = 5.2 Hz, ⁴J = 1.2 Hz, 2H), 7.19 (d, ³J = 5.2 Hz, ⁴J = 1.2 Hz, 2H), 7.11 (s, 2H), 7.04 (dd, ³J = 3.6 Hz, ³J = 5.2 Hz, 2H), 2.92–2.85 (m, 8H), 1.66–1.60 (m, 8H), 1.43–1.38 (m, 8H), 1.29–1.25(m, 16H) 0.91–0.88 (m, 12H); ¹³C NMR (400 MHz, CDCl₃): δ 137.2, 136.5, 136.1, 132.50, 132.46, 132.0, 131.2, 128.0, 127.4, 127.0, 125.0, 124.2, 36.33, 36.29, 31.4, 30.2, 29.49, 29.48, 28.4, 27.0, 26.89, 22.5, 14.03, 14.01. UV/Vis: λ_{max} 420 nm (ε 31100 cm⁻¹M⁻¹), λ_{em}. 545 nm in CH₂Cl₂.

Scheme S3



4,4'-bis(hexylthio)-2,2'-bithiophene (3b) → The compound was prepared following the procedure used for compound 2 starting from **3a** prepared. The residue was isolated by flash chromatography (Cyclohexane/CH₂Cl₂, 90:10). Yellow powder. Yield 77%. EI-MS *m/z* 398(M⁺). ¹H NMR (400 MHz, CDCl₃, TMS/ppm): δ 7.06 (d, ⁴J = 1.2 Hz, 2H), 6.98 (d, ⁴J = 1.2 Hz, 2H), 2.88–2.83 (m, 4H), 1.66–1.61 (m, 4H), 1.45–1.39 (m, 4H), 1.31–1.28 (m, 8H), 0.90–0.87 (m, 6H).

5-bromo-4,4'-bis(hexylthio)-2,2'-bithiophene (3c) → The compound was prepared following the procedure used for compound 1e starting from **3b**. The residue was isolated by flash chromatography (Cyclohexane/CH₂Cl₂, 90:10). Yellow oil. Yield 60%. EI-MS *m/z* 476(M⁺). ¹H NMR (400 MHz, CDCl₃, TMS/ppm): δ 7.01 (d, ⁴J = 1.6 Hz, 1H), 6.99 (d, ⁴J = 1.6 Hz, 1H), 6.95 (s, 1H), 2.89–2.83 (m, 4H), 1.67–1.59 (m, 4H), 1.46–1.38 (m, 4H), 1.34–1.25 (m, 8H), 0.90–0.87 (m, 6H).

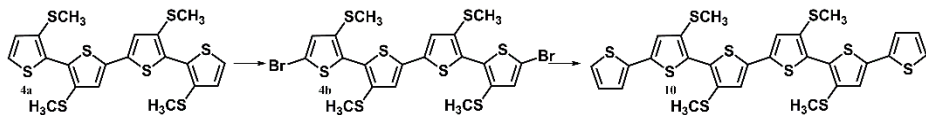
3,3'',3''',4'-tetrakis(hexylthio)-2,2':5',2'':5'',2'''-quaterthiophene (3d) → The compound was prepared following the procedure used for compound 1 starting from **3c**. The residue was isolated by flash chromatography (Cyclohexane/CH₂Cl₂, 85:15). Yellow powder. EI-MS *m/z* 796(M⁺). Yield 55%. ¹H NMR (400 MHz, CDCl₃, TMS/ppm): δ 7.13 (s, 2H), 7.11 (d, ⁴J = 1.2 Hz, 2H),

7.02 (d, $^4J = 1.2$ Hz, 2H), 2.89–2.83 (m, 8H), 1.67–1.59 (m, 4H), 1.46–1.25 (m, 12H), 0.90–0.87 (m, 6H).

5,5'''-dibromo-3,3',3''',4'-tetrakis(hexylthio)-2,2':5',2'':5'',2'''-quaterthiophene (3e) → The compound was prepared following the procedure used for compound 1e starting from **3d** using 2mmol of NBS. The residue was isolated by flash chromatography (Cyclohexane/CH₂Cl₂, 90:10). Brown yellow oil. Yield 99%. ¹H NMR (400 MHz, CDCl₃, TMS/ppm): δ 7.07 (s, 2H), 7.00 (s, 2H), 2.90–2.84 (m, 8H), 1.62–1.59 (m, 8H), 1.45–1.24 (m, 24H), 0.90–0.84 (m, 12H).

3''',3''''',4',4'''-tetrakis(hexylthio)-2,2':5',2'':5'',2''':5''',2''''':5''''',2''''''-sexithiophene (9) → The compound was prepared following the procedure used for compound 1 and starting from **3d** and 2-thienylboronic acid. The residue was isolated by flash chromatography (Cyclohexane/CH₂Cl₂, 90:10). Red powder. Yield 65%. ¹H NMR (400 MHz, CDCl₃, TMS/ppm): δ 7.37 (d, $^3J = 3.6$ Hz, $^4J = 1.2$ Hz, 2H), 7.34 (d, $^3J = 5.2$ Hz, $^3J = 1.2$ Hz, 2H), 7.14 (s, 2H), 7.13 (s, 2H), 7.06 (dd, $^3J = 3.6$ Hz, $^3J = 5.2$ Hz, 2H), 2.90–2.85 (m, 8H), 1.65–1.59 (m, 8H), 1.41–1.38 (m, 8H), 1.30–1.25 (m, 16H), 0.88–0.85 (m, 12H); ¹³C NMR (400 MHz, CDCl₃): δ 136.1, 135.2, 135.18, 133.4, 132.6, 131.6, 128.8, 128.6, 127.2, 127.0, 126.3, 126.27, 36.3, 36.2, 31.4, 31.3, 29.7, 29.5, 28.42, 28.38, 22.6, 22.5, 14.03, 14.01. UV/Vis: λ_{max} 420 nm (ε 27850 cm⁻¹M⁻¹), λ_{em} 540 nm in CH₂Cl₂.

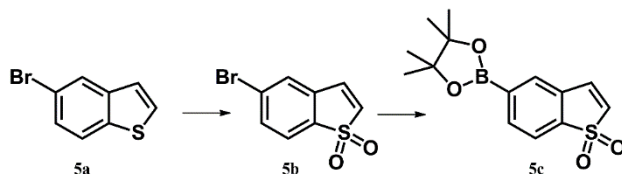
Scheme S4



5,5'''-dibromo-3,3',3''',4'-tetrakis(methylthio)-2,2':5',2'':5'',2'''-quaterthiophene (4b) → The compound was prepared following the procedure used for compound 1e starting from **4a**³ using 2mmol of NBS. The residue was isolated by flash chromatography (Cyclohexane/CH₂Cl₂, 85:15). Orange powder. Yield 99%. ¹H NMR (400 MHz, CDCl₃, TMS/ppm): δ 7.14 (s, 2H), 7.04 (s, 2H), 2.45 (s, 6H), 2.43 (s, 6H).

3''',3''''',4',4'''-tetrakis(methylthio)-2,2':5',2'':5'',2''':5''',2''''':5''''',2''''''-sexithiophene (10) → The compound was prepared following the procedure used for compound 1 starting from **4b** and 2-thienylboronic acid. The residue was isolated by flash chromatography (Cyclohexane/CH₂Cl₂, 80:20). Red powder. Yield 65%. ¹H NMR (400 MHz, CDCl₃, TMS/ppm): δ 7.26 (d, $^3J = 4.8$ Hz, 2H), 7.22 (d, $^3J = 4.8$ Hz, 2H), 7.17 (s, 2H), 7.15 (s, 2H), 7.04 (dd, $^3J = 3.6$ Hz, $^3J = 5.2$ Hz, 2H), 2.50 (s, 12H); ¹³C NMR (400 MHz, CDCl₃): δ 137.8, 136.5, 136.4, 134.23, 134.16, 129.2, 127.9, 126.2, 125.9, 125.2, 124.4, 18.8. UV/Vis: λ_{max} 420 nm (ε 23200 cm⁻¹M⁻¹), λ_{em} 550 nm in CH₂Cl₂.

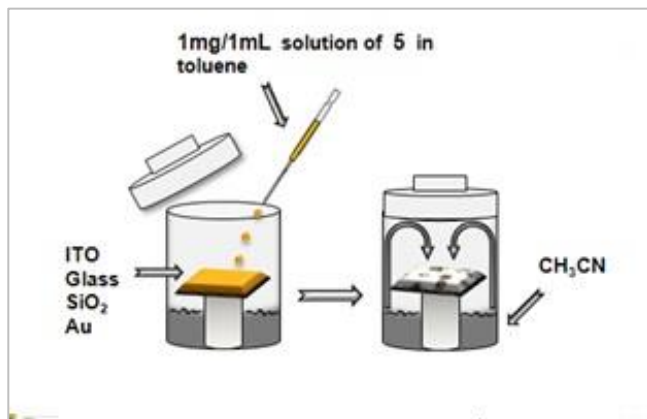
Scheme S5



Synthesis of 5-bromobenzo[b]thiophene 1,1-dioxide (5b) \rightarrow To a solution of **5a** (1 mmol) in CH_2Cl_2 , 3 mmol of meta-chloroperoxybenzoic acid (mCPBA) were added. The reaction mixture was sonicated in an ultrasonic bath. The solvent was removed and the product was purified by flash chromatography (Cyclohexane/ CH_2Cl_2 /AcOEt, 70:25:5). \rightarrow Yield 95%. White solid; EI-MS m/z 245(M^+). ^1H NMR (400 MHz, CDCl_3 , TMS/ppm): δ 7.66 (d, $J=8$ Hz, 1H), 7.59 (d, $J=8$ Hz, 1H), 7.51 (s, 1H), 7.20 (d, $J=6.8$ Hz, 1H), 6.77 (d, $J=6.8$ Hz, 1H); ^{13}C NMR (400 MHz, CDCl_3): 135.4, 133.6, 133.1, 132.0, 131.3, 128.6, 128.1, 122.6.

Synthesis of 5-(4,4,5,5-tetramethyl-1,3,2-dioxaborolan-2-yl)benzo[b]thiophene 1,1-dioxide(5c) \rightarrow A solution of **5b** (1mmol.), Bis(pinacolato)diboron (1.2 mmol), CH_3COOK (3 mmol.) in anhydrous dioxane (3 mL) was first purged with nitrogen for 20 min and then, after addition of $\text{Pd}(\text{dppf})\text{Cl}_2$, refluxed at 110°C for 20 h. The cooled mixture was extracted with CH_2Cl_2 . The combined organic layers were dried over anhydrous sodium sulphate and the solvent was removed under reduced pressure. The crude product was purified by distillation under vacuum (1.5 mmHg) collecting the fraction boiling at 120°C . Yield 96%. Pale yellow solid; EI-MS m/z 292(M^+); ^1H NMR (400 MHz, CDCl_3 , TMS/ppm): δ 7.90 (d, $J=7.2$ Hz, 1H), 7.23 (s, 1H), 7.65 (d, $J=7.2$ Hz, 1H), 7.18 (d, $J=6.8$ Hz, 1H), 6.67 (d, $J=6.8$ Hz, 1H), 1.36 (s, 12H); ^{13}C NMR (400 MHz, CDCl_3): 138.7, 137.4, 132.7, 131.3, 130.4, 130.3, 120.5, 84.6, 25.0, 24.9, 24.6.

Scheme S6



Fibers formation: "vapour diffusion method"

4.2 ^1H and ^{13}C NMR spectra.

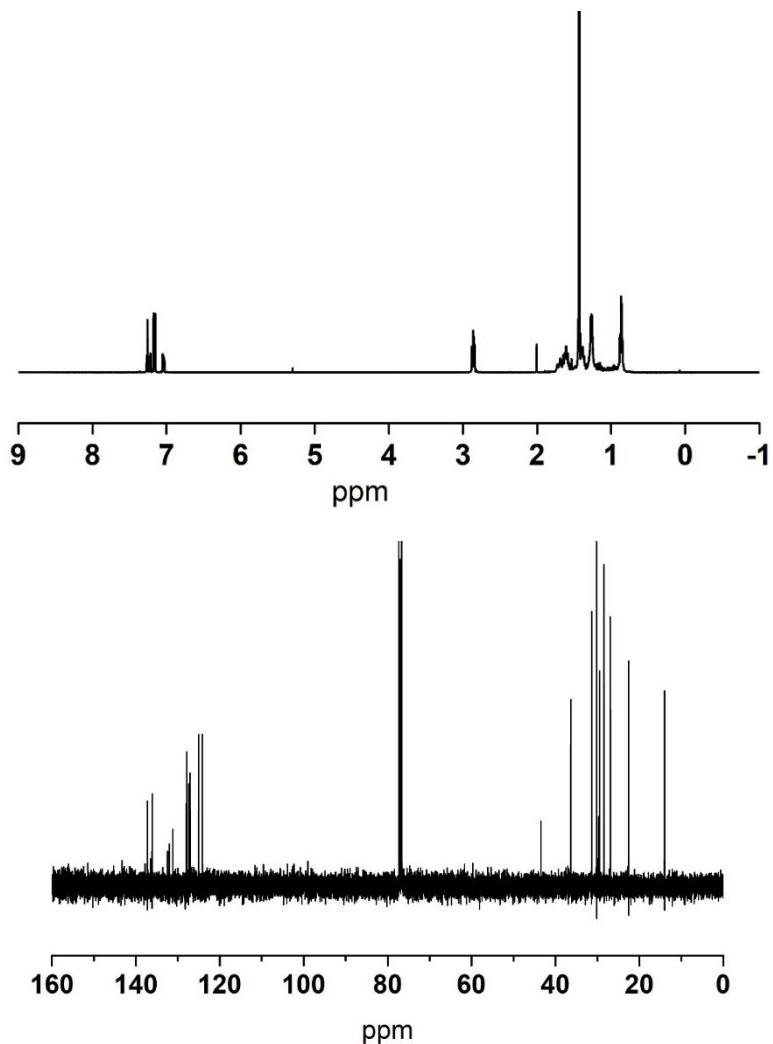
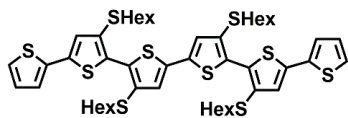


Figure S1. ^1H and ^{13}C NMR spectra of compound **1**.

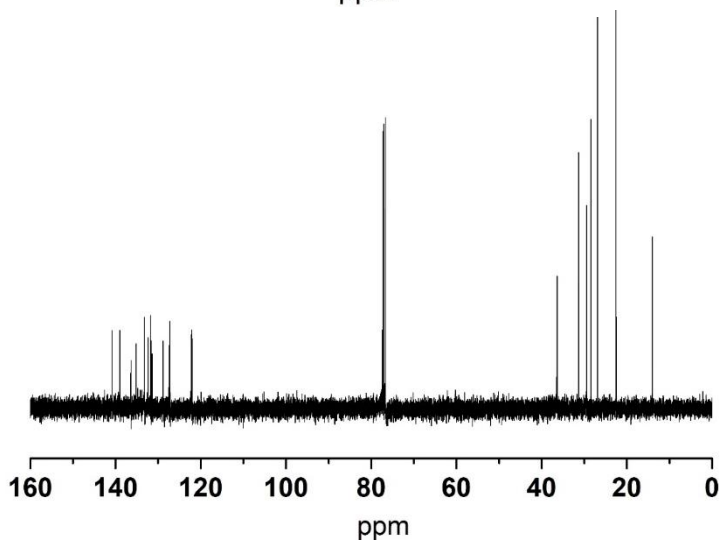
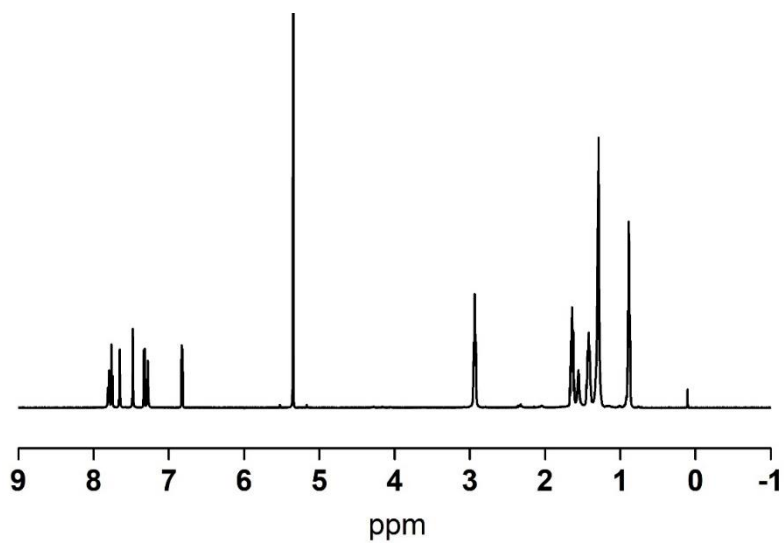
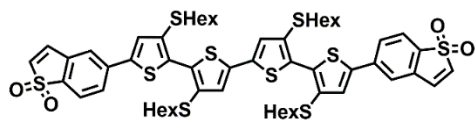


Figure S3. ^1H and ^{13}C NMR spectra of compound 3.

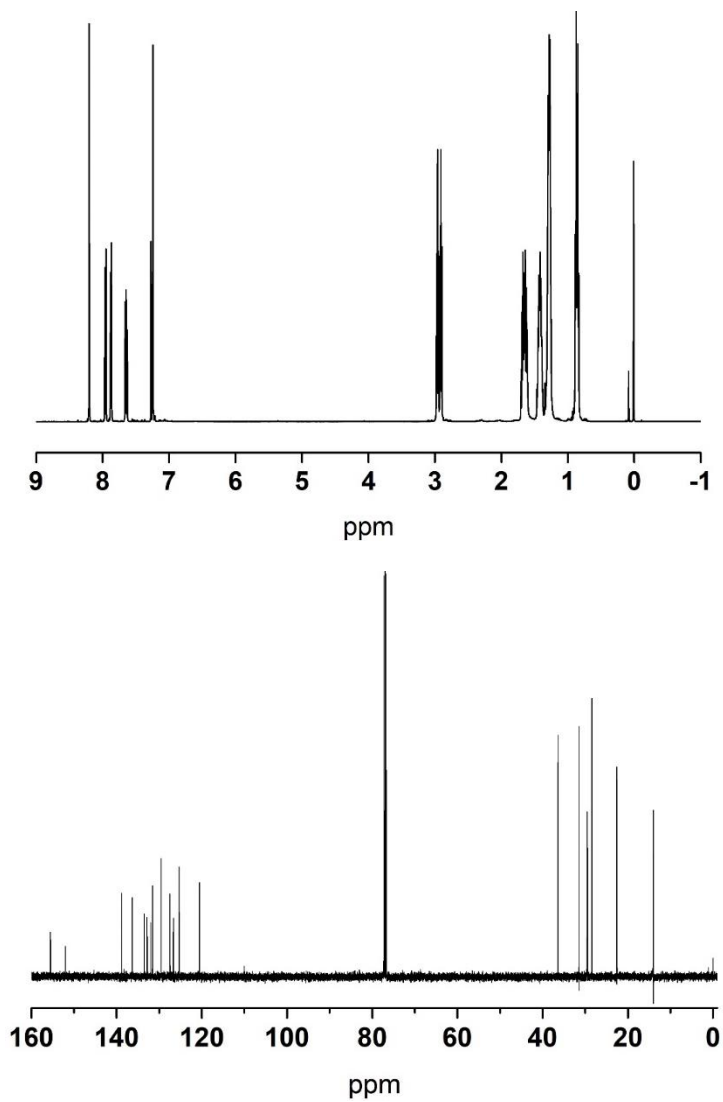
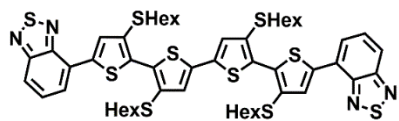


Figure S5. ^1H and ^{13}C NMR spectra of compound 5.

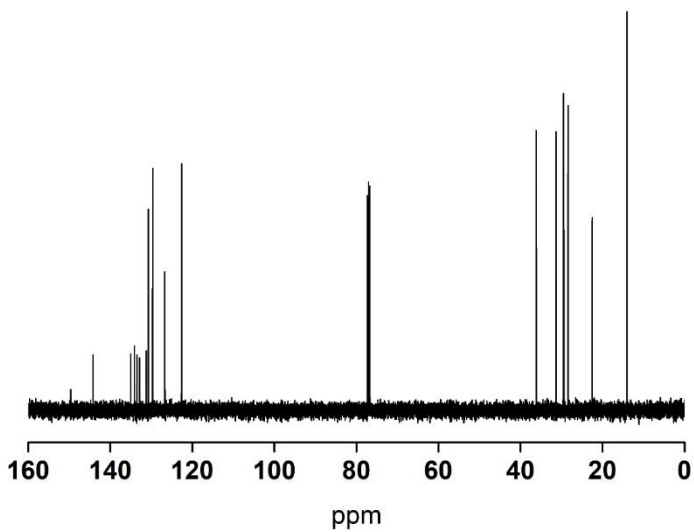
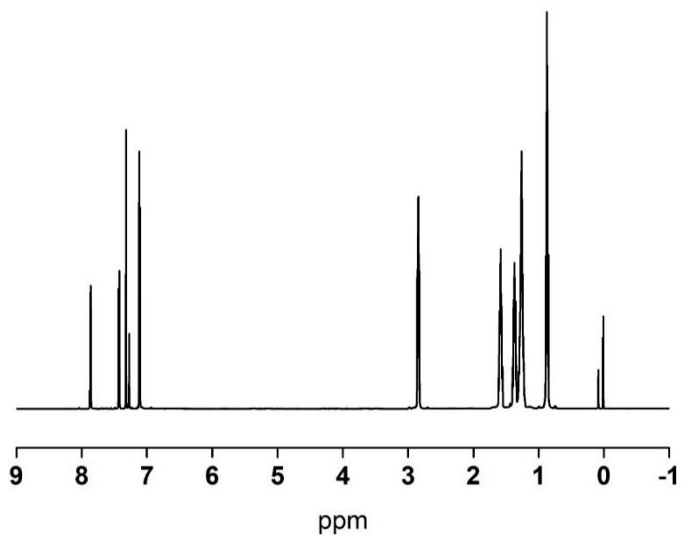
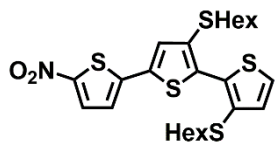


Figure S6. ^1H and ^{13}C NMR spectra of compound **1e**.

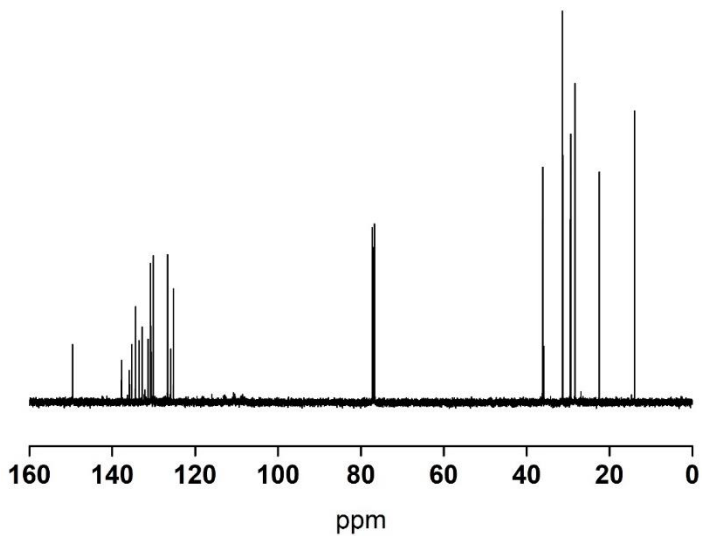
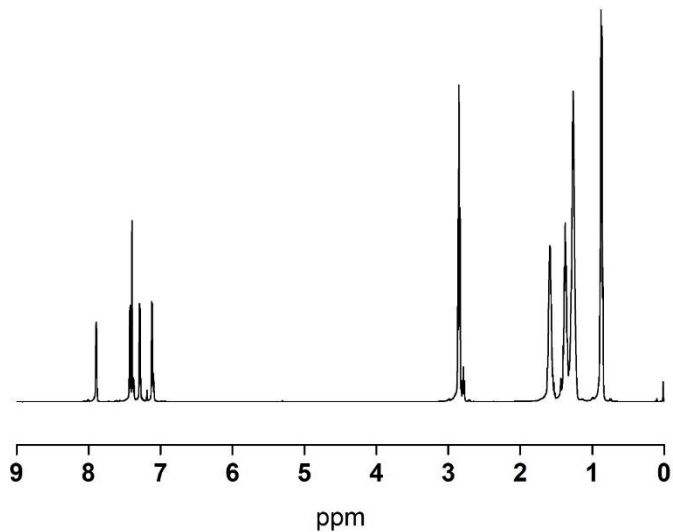
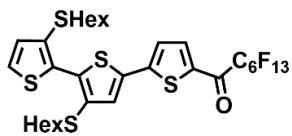


Figure S7. ¹H and ¹³C NMR spectra of compound 1f.
248

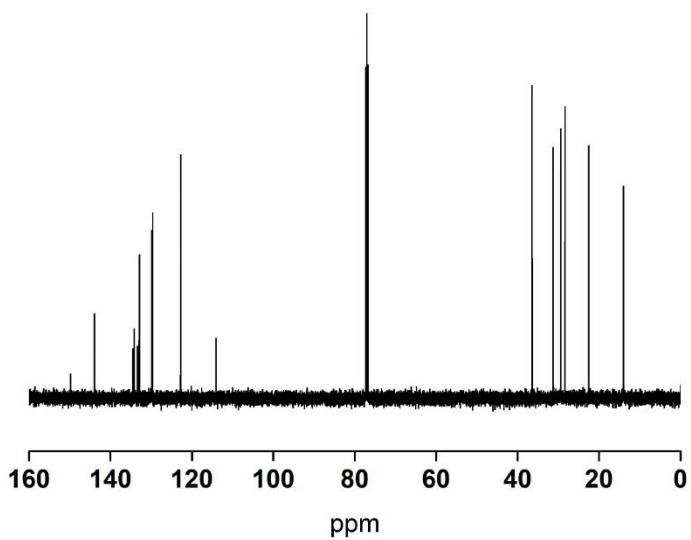
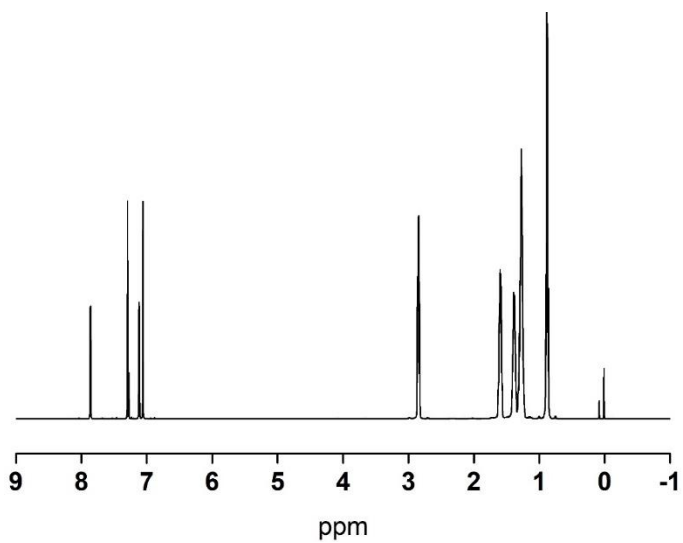
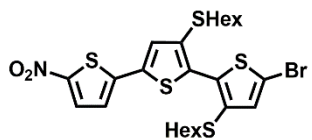


Figure S8. ¹H and ¹³C NMR spectra of compound **1g**.

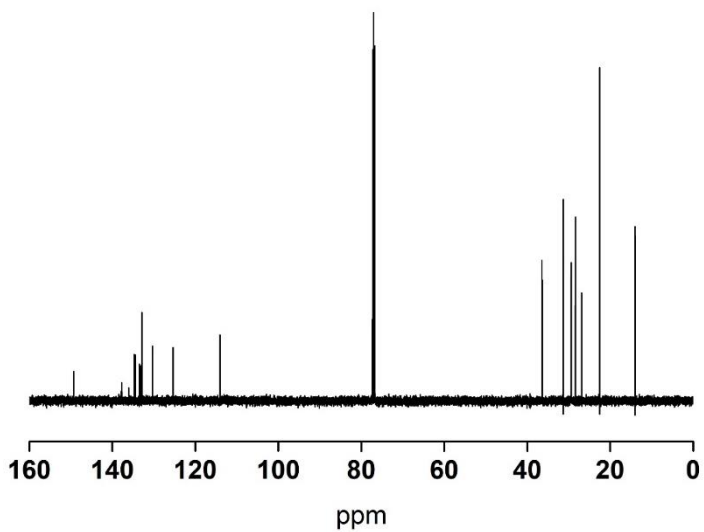
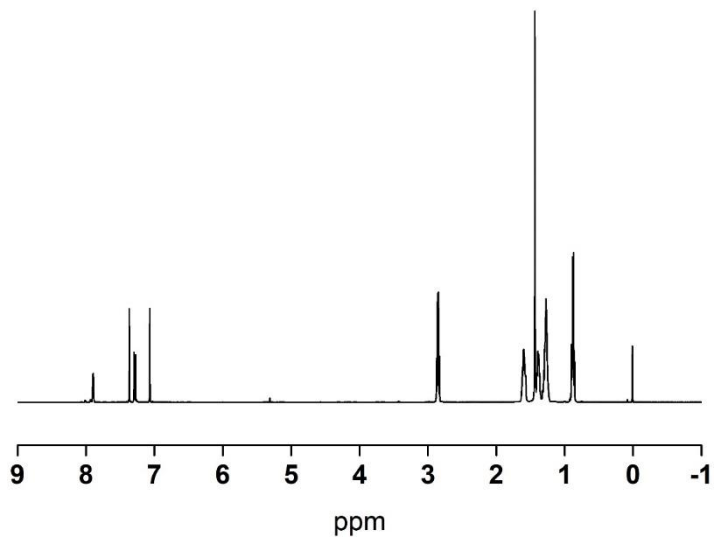
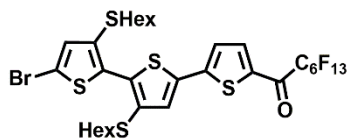


Figure S9. ¹H and ¹³C NMR spectra of compound **1h**.

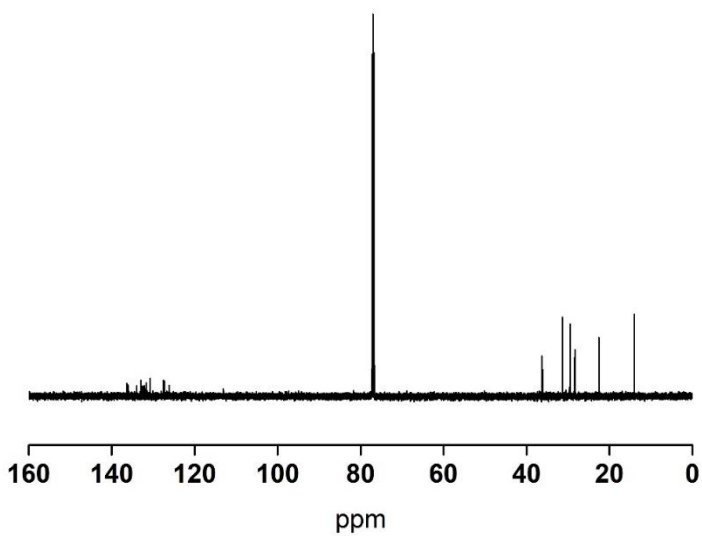
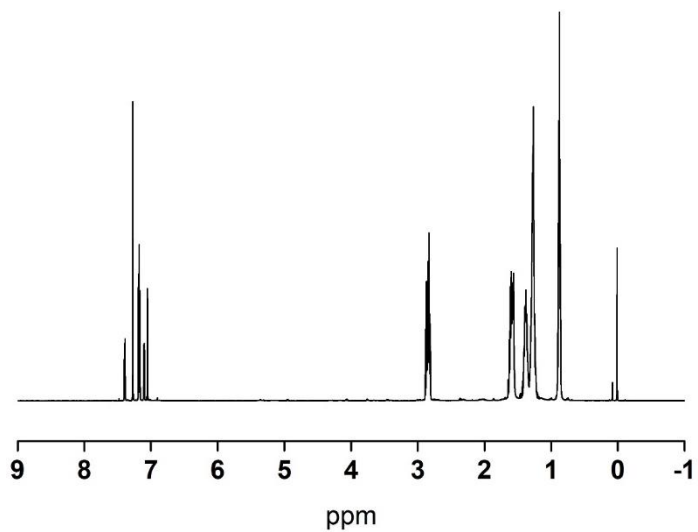
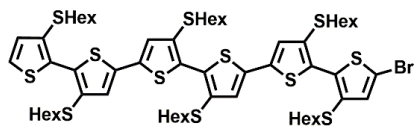


Figure S11. ^1H and ^{13}C NMR spectra of compound **1k**.

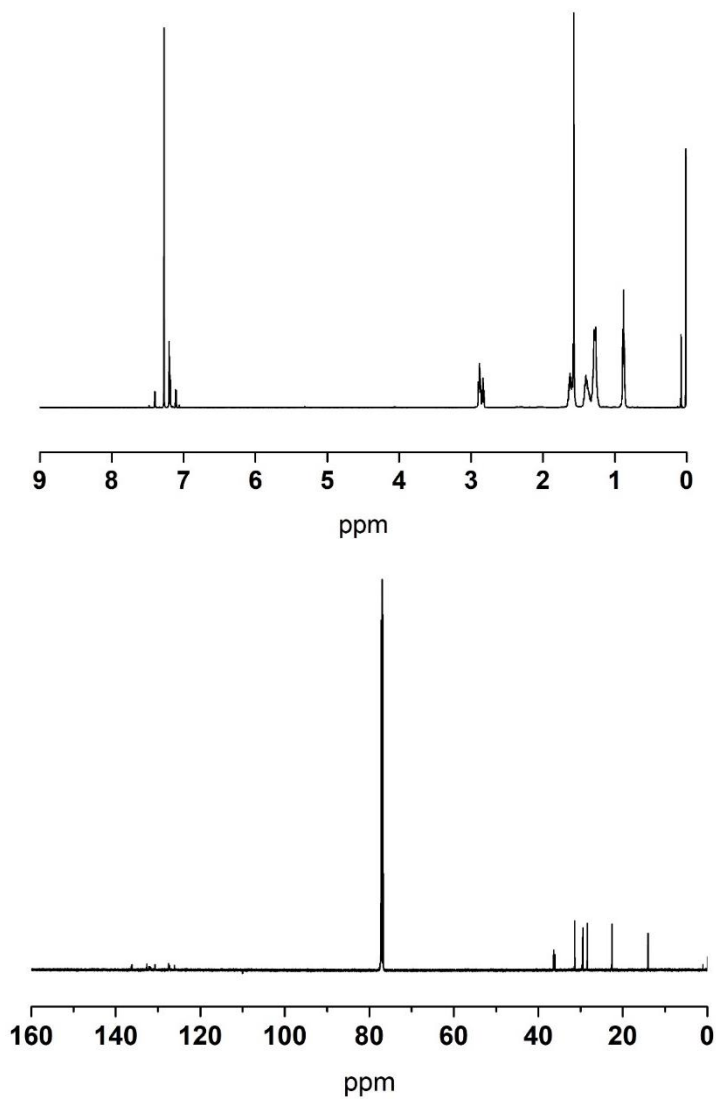
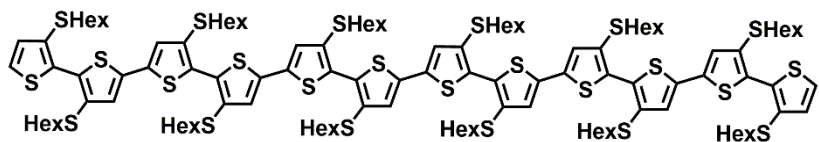


Figure S12. ^1H and ^{13}C NMR spectra of compound 7.

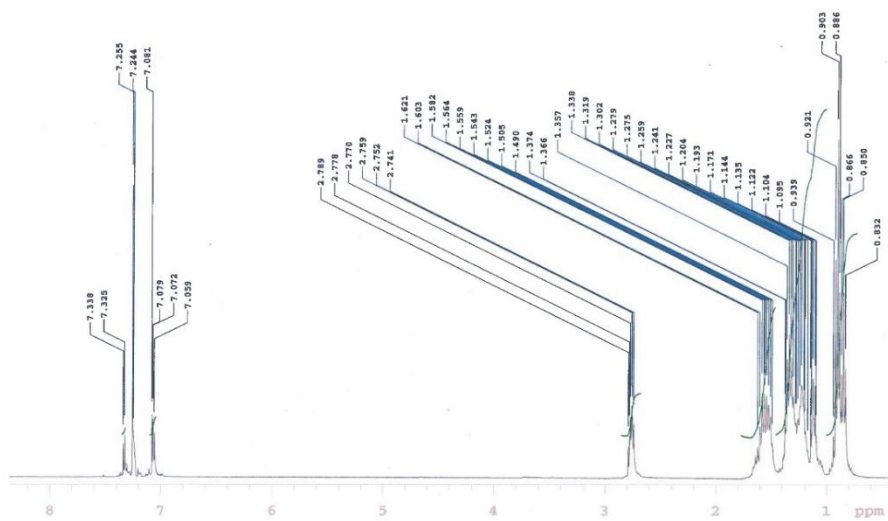
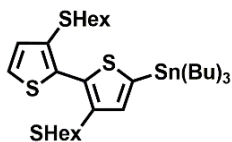


Figure S13. ¹H NMR spectrum of compound 1d.

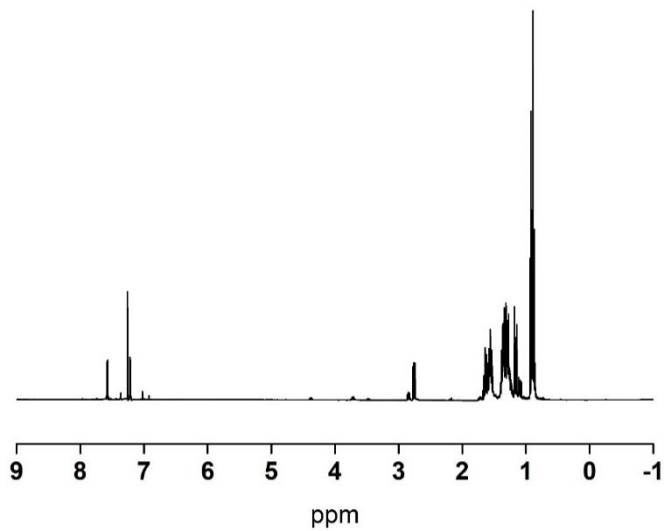
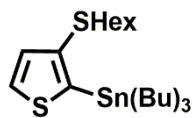


Figure S15. ¹H NMR spectrum of compound 2c.

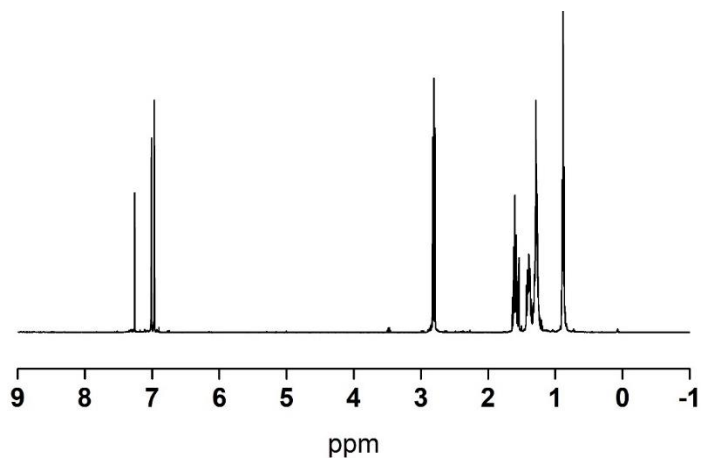
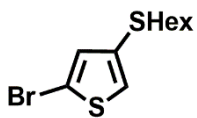


Figure S16. ^1H NMR spectrum of compound 2a.

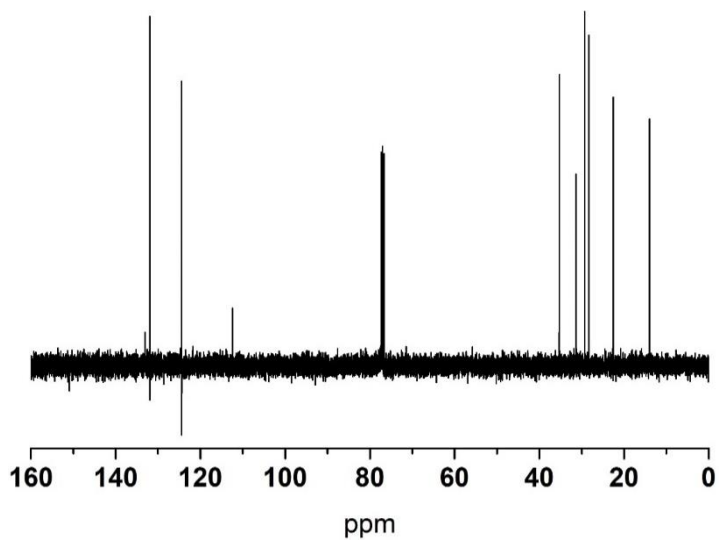


Figure S17. ^{13}C NMR spectrum of compound 2a.

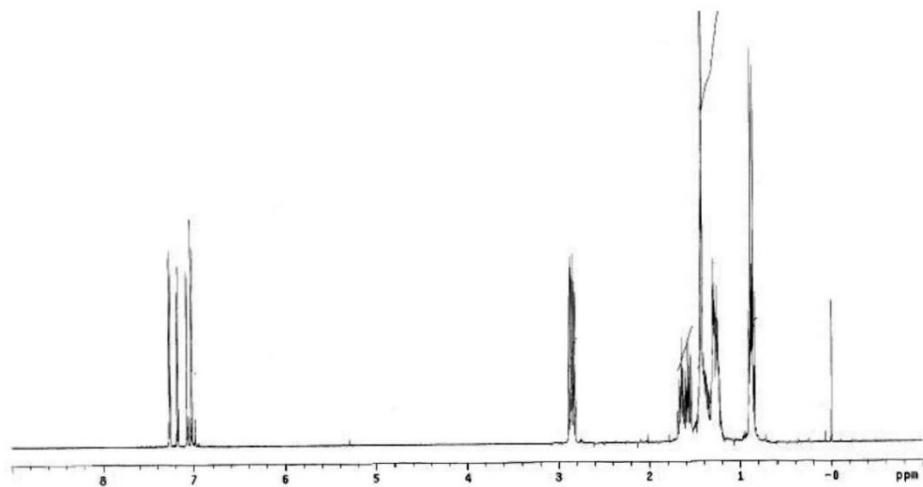
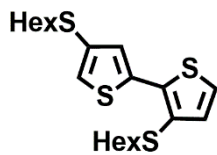


Figure S18. ¹H NMR spectrum of compound 2d.

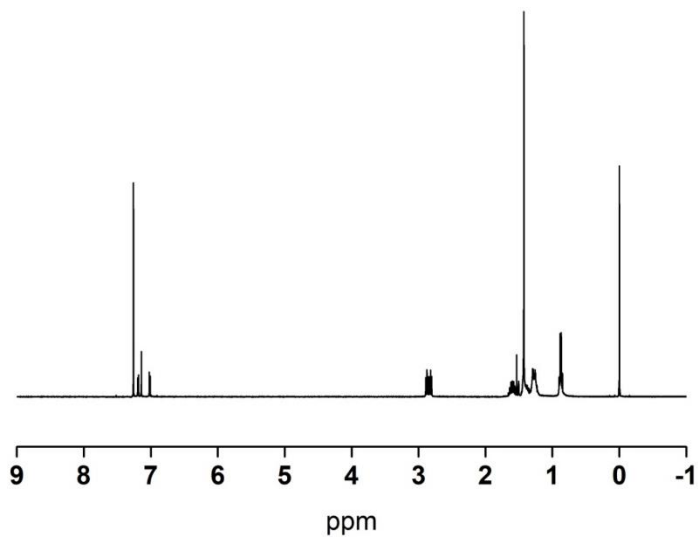
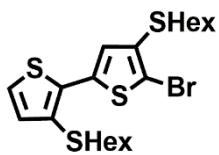


Figure S19. ¹H NMR spectrum of compound 2e.

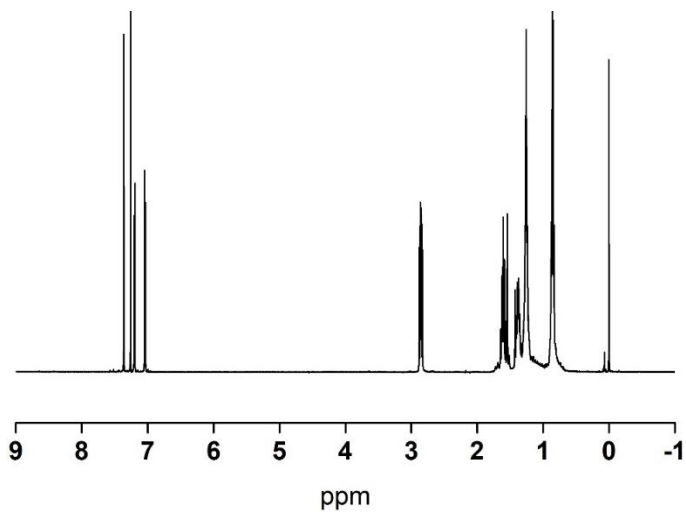
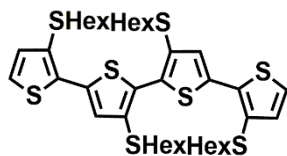


Figure S20. ^1H NMR spectrum of compound 2f.

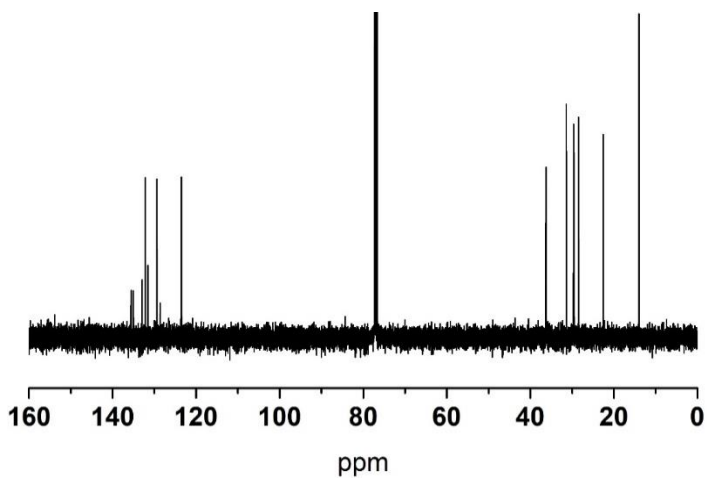


Figure S21. ^{13}C NMR spectrum of compound 2f.

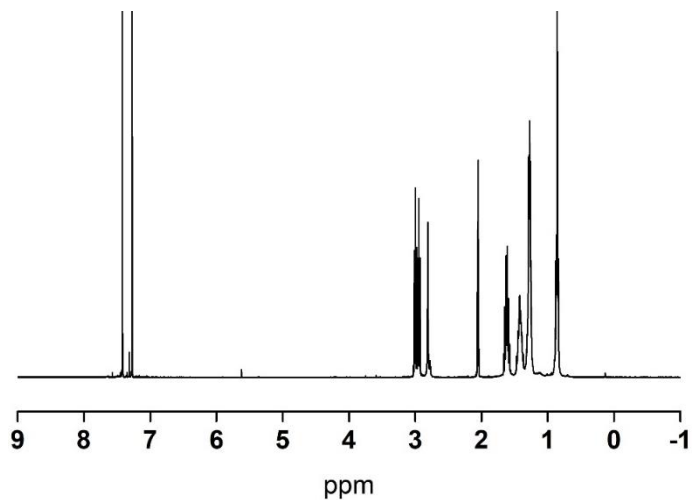
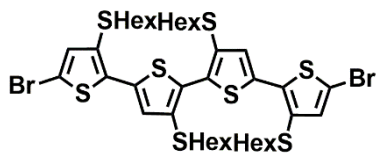


Figure S22. ¹H NMR spectrum of compound 2g.

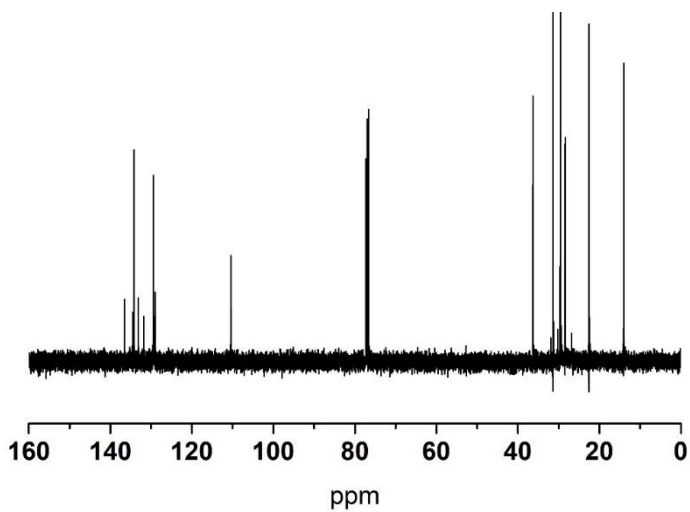


Figure S23. ¹³C NMR spectrum of compound 2g.

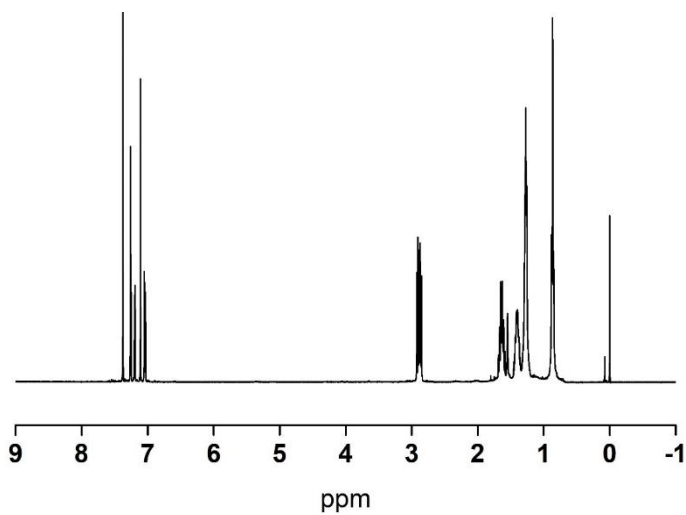
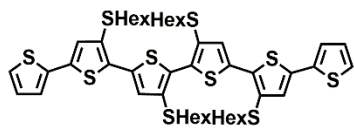


Figure S24. ^1H NMR spectrum of compound 8.

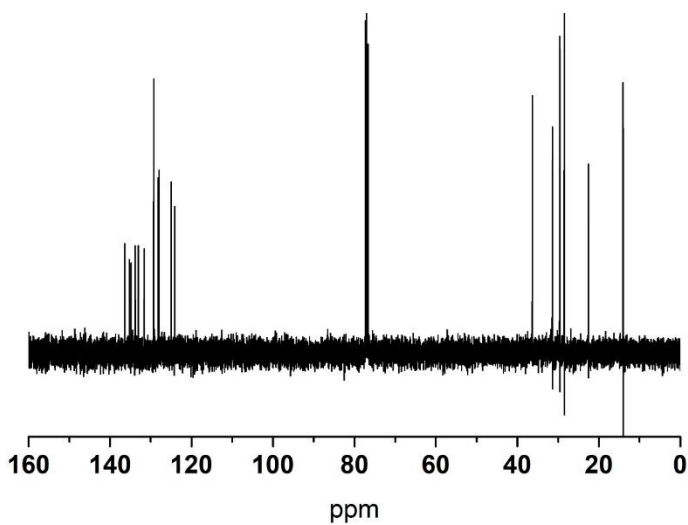


Figure S25. ^{13}C NMR spectrum of compound 8.

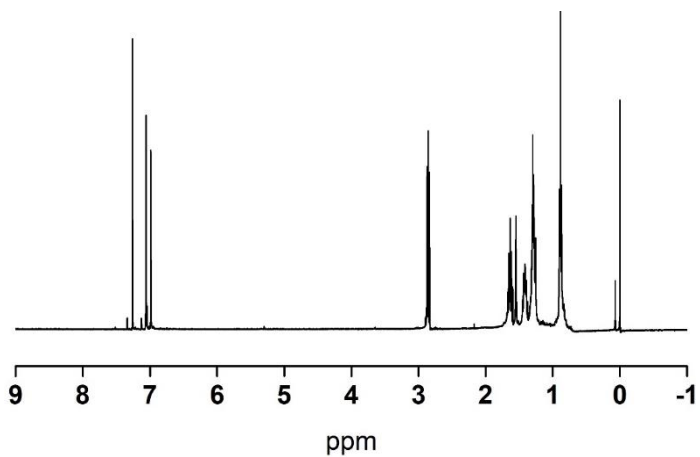
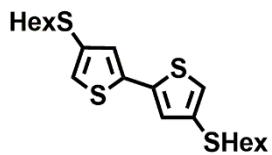


Figure S26. ¹H NMR spectrum of compound 3b.

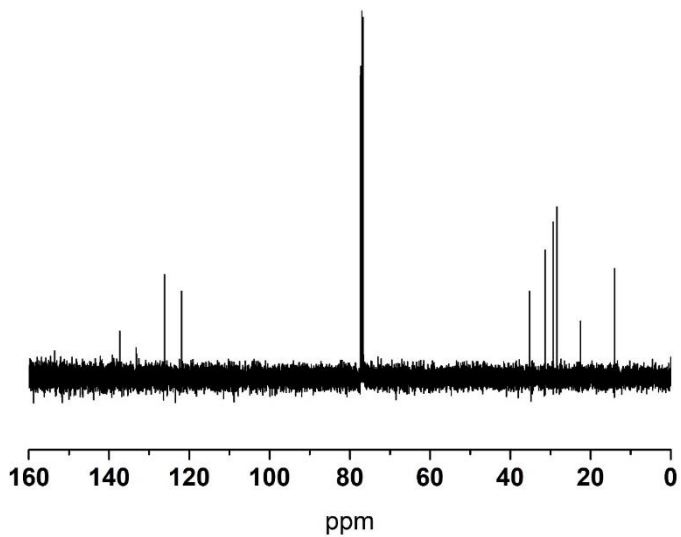


Figure S27. ¹³C NMR spectrum of compound 3b.

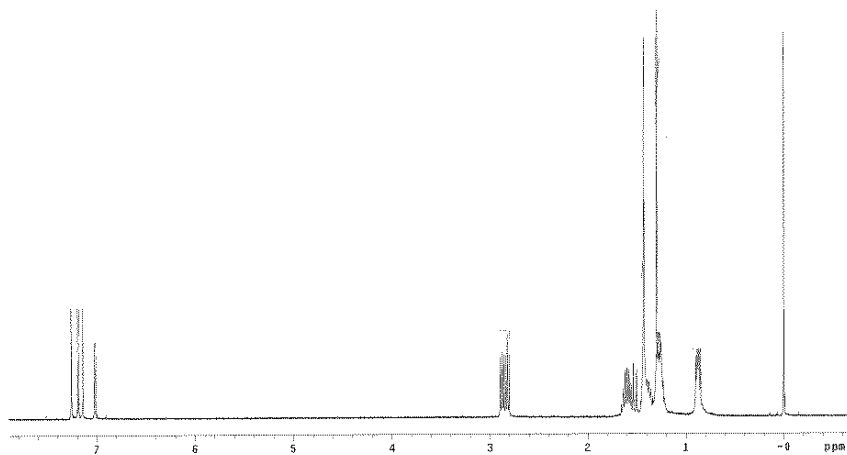
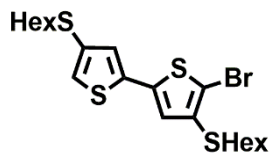


Figure S28. ¹H NMR spectrum of compound 3c.

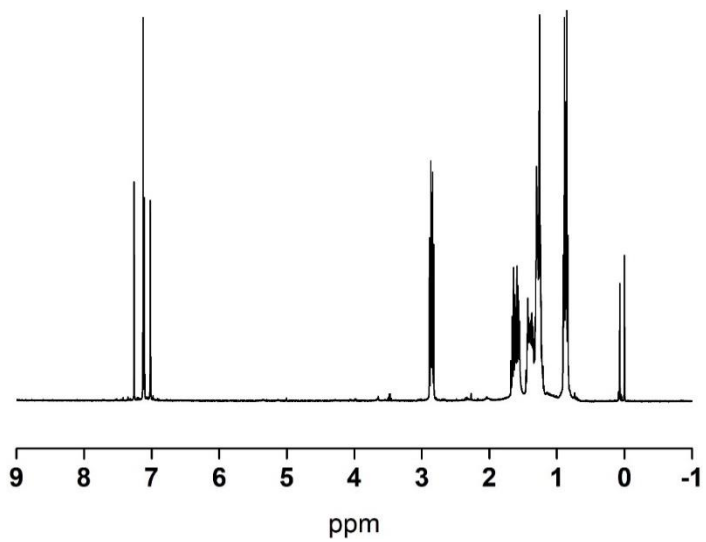
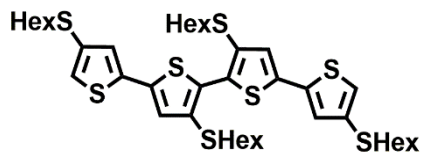


Figure S29. ¹H NMR spectrum of compound 3d.

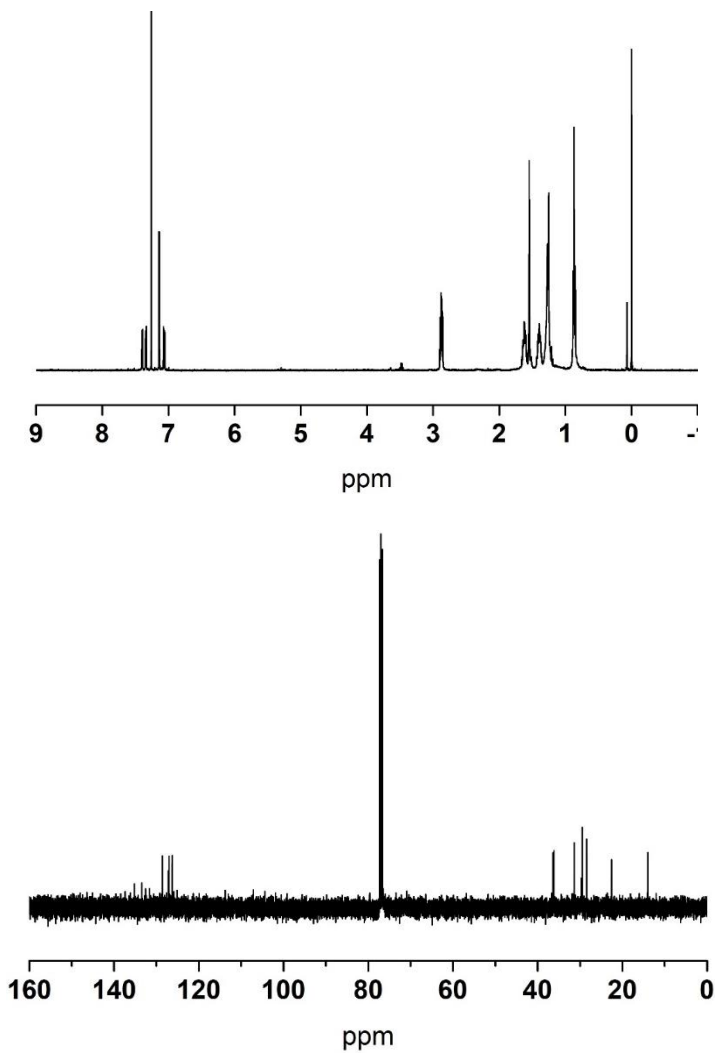
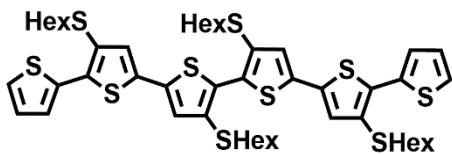


Figure S31. ^1H and ^{13}C NMR spectra of compound 9.

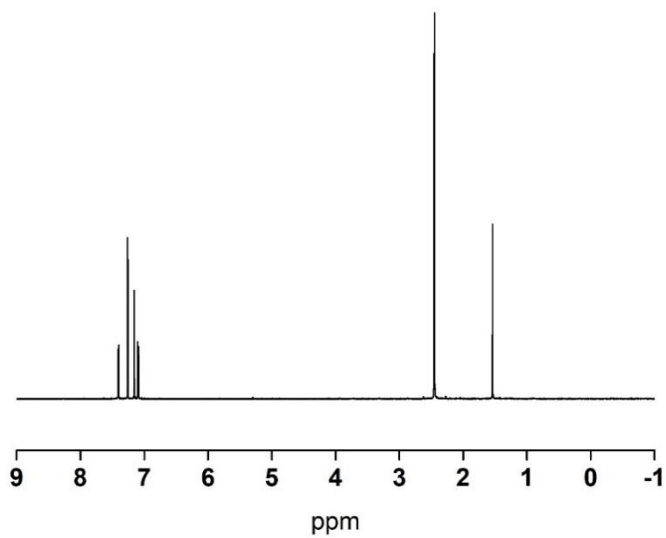
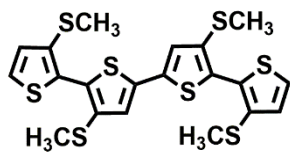


Figure S32. ¹H NMR spectrum of compound 4a.

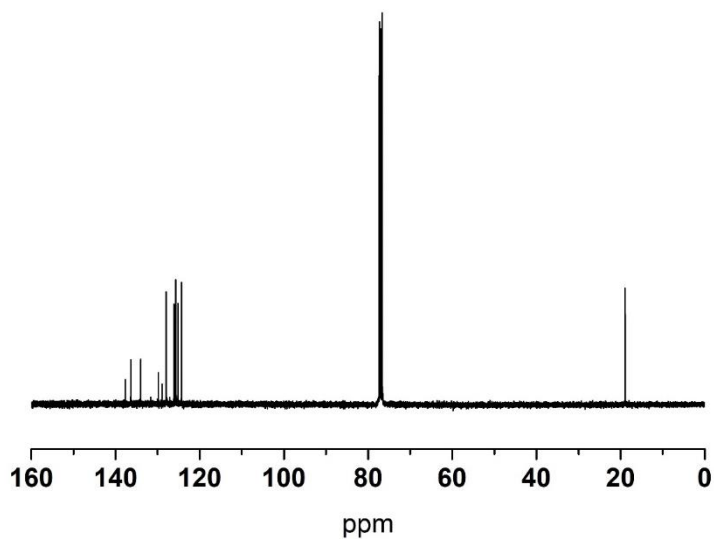
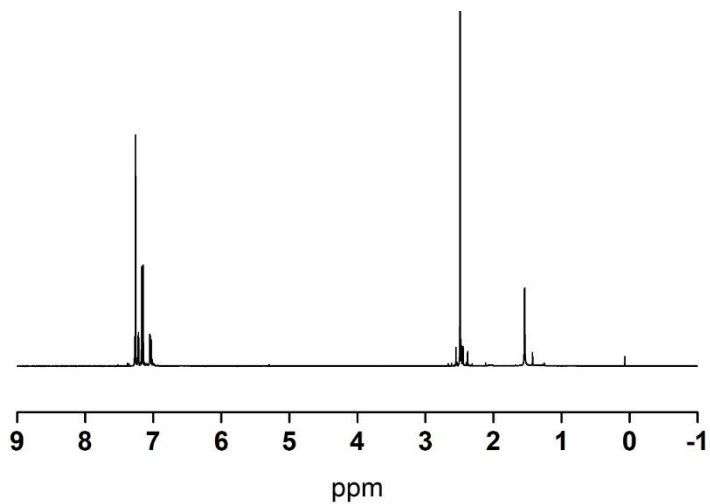
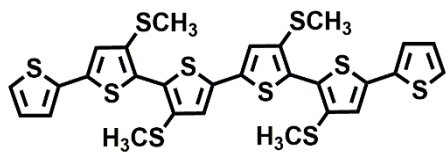


Figure S34. ¹H and ¹³C NMR spectra of compound 10.

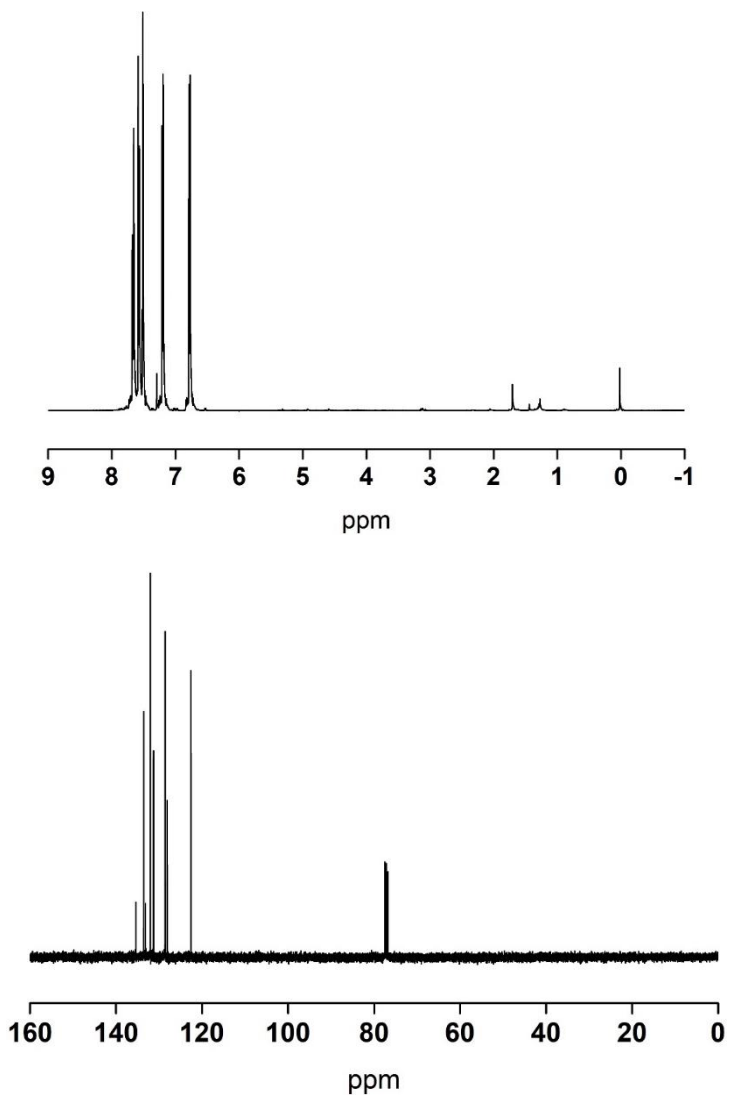
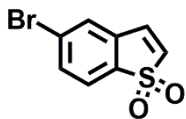


Figure S35. ^1H and ^{13}C NMR spectra of compound 5b.

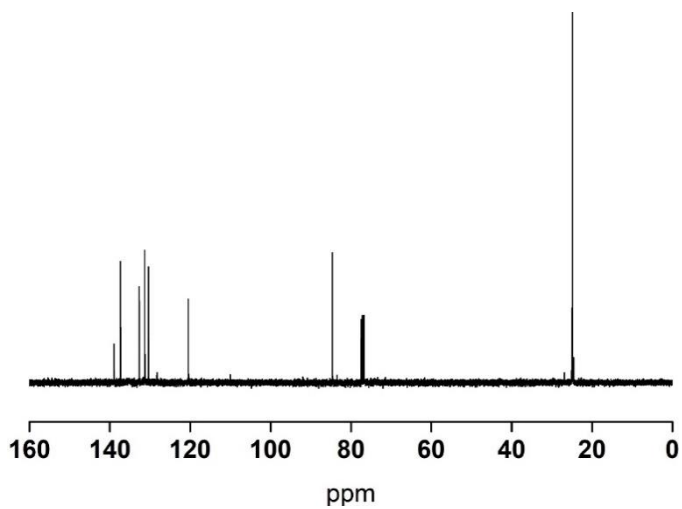
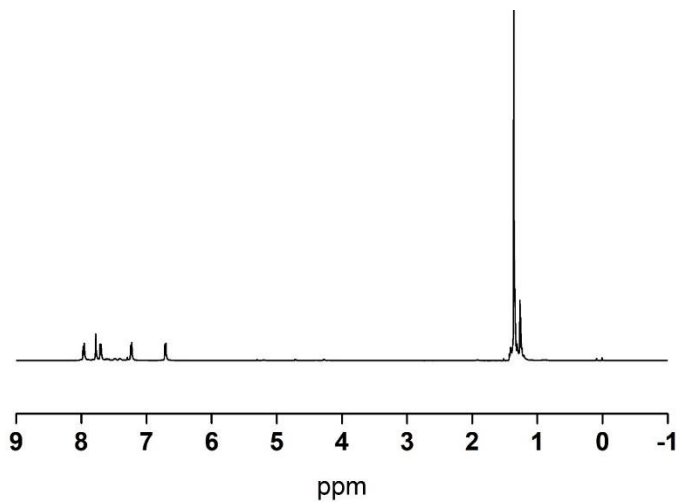
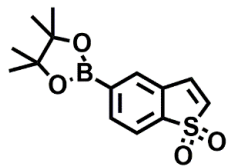


Figure S36. ¹H and ¹³C NMR spectra of compound 5c.

4.3 Lifetime characterization

Table S1. Emission lifetimes in CH₂Cl₂ r.t. ^a

	τ_1 (ns) / %	τ_2 (ns) / %	χ^2
1^b	0.3, 53%	1.1, 47%	0.853
2^c	0.1, 53%	2.3, 47%	1.440
3^d	0.6, 77%	1.0, 23%	0.974
4^e	0.4, 50%	1.0, 50%	2.138
5^f	1.1	-	1.166

^a λ_{ex} =405 nm. ^b λ_{em} =540 nm. ^c λ_{em} =660 nm. ^d λ_{em} =575 nm. ^e λ_{em} =670 nm. ^f λ_{em} =670 nm

4.4 Optical microscopy.

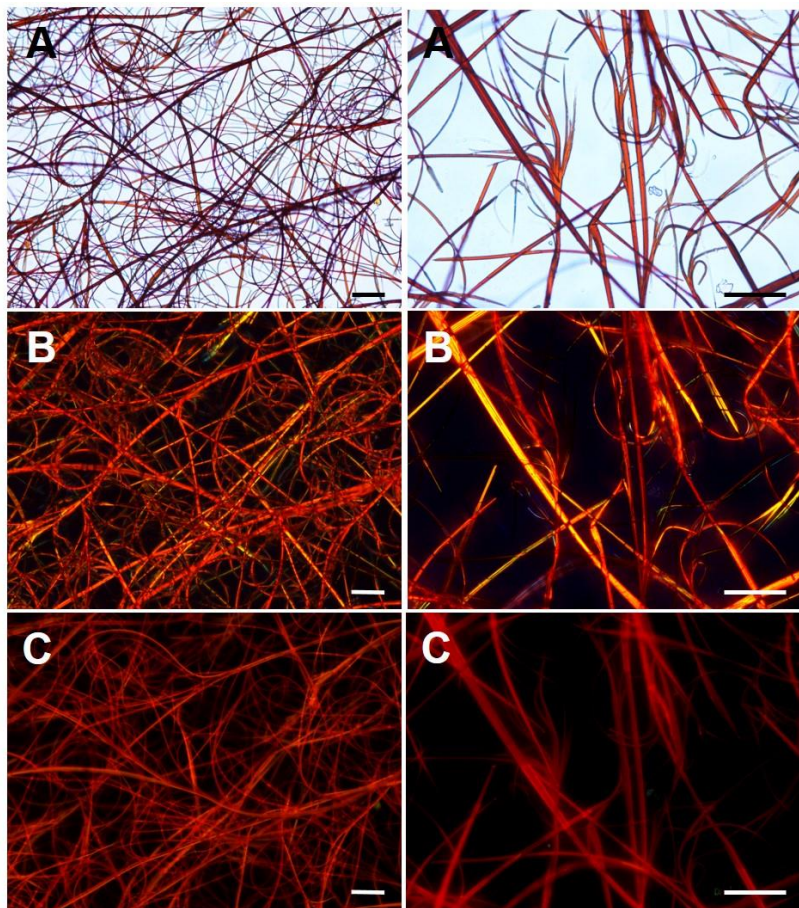


Figure S37. A) Light transmission optical microscopy, B) optical microscopy with cross polars, C) fluorescence microscopy images of compound **1** (scale bar 50nm).

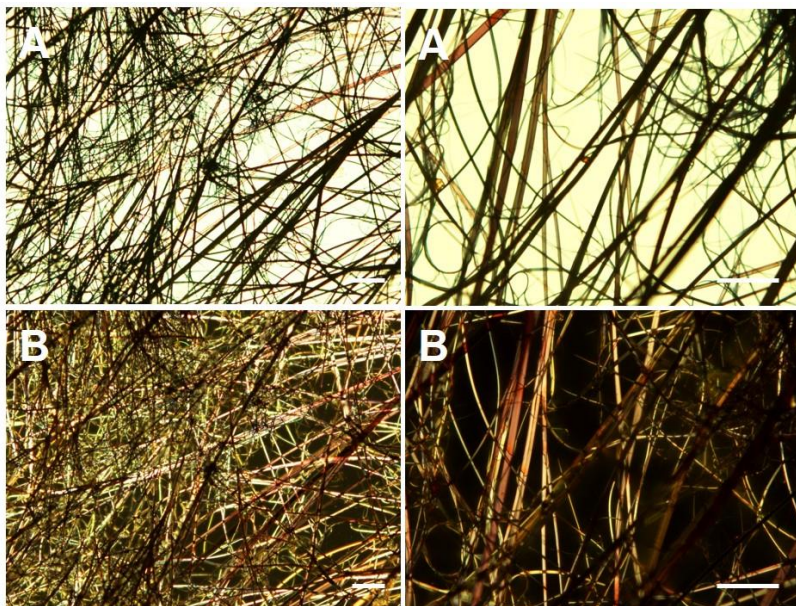


Figure S38. A) Light transmission optical microscopy, B) optical microscopy with cross polars, images of compound **2** (scale bar 50nm).

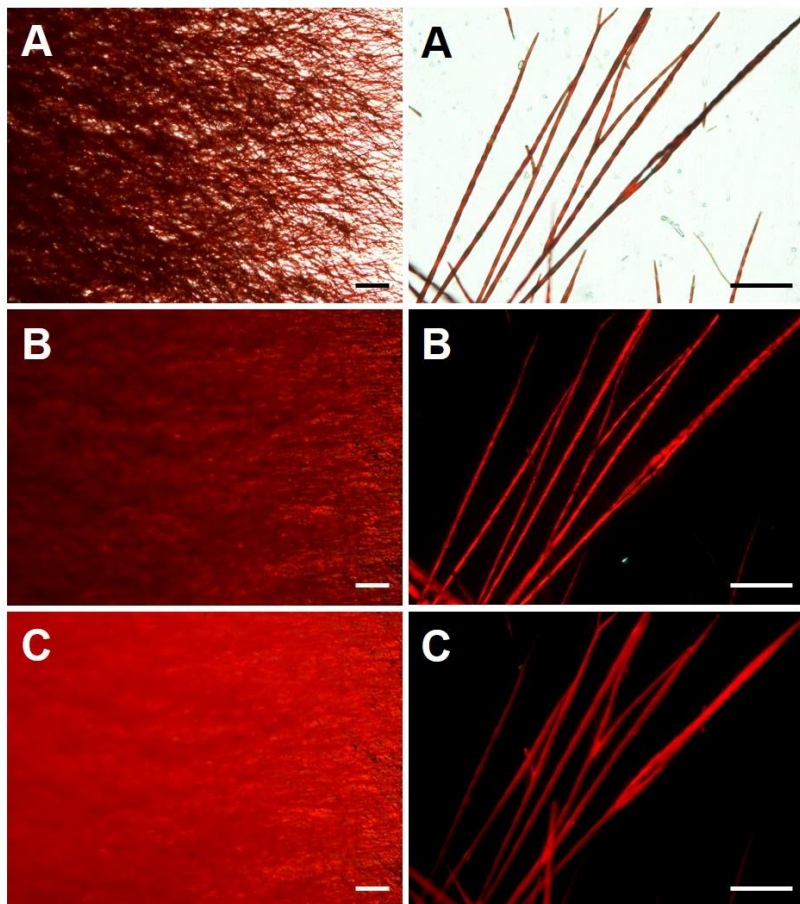


Figure S39. A) Light transmission optical microscopy, B) optical microscopy with cross polars, C) fluorescence microscopy images of compound **3** (scale bar 50nm).

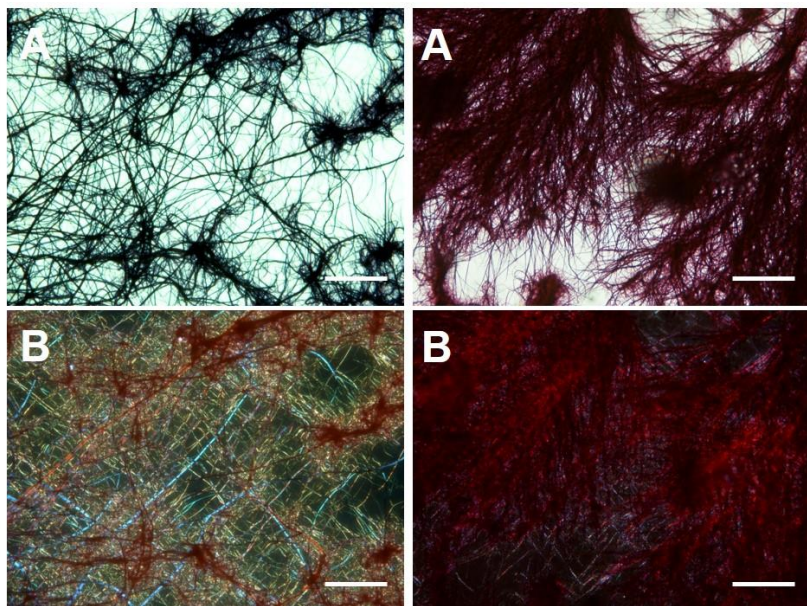


Figure S40. A) Light transmission optical microscopy, B) optical microscopy with cross polars, images of compound **4** (scale bar 50nm).

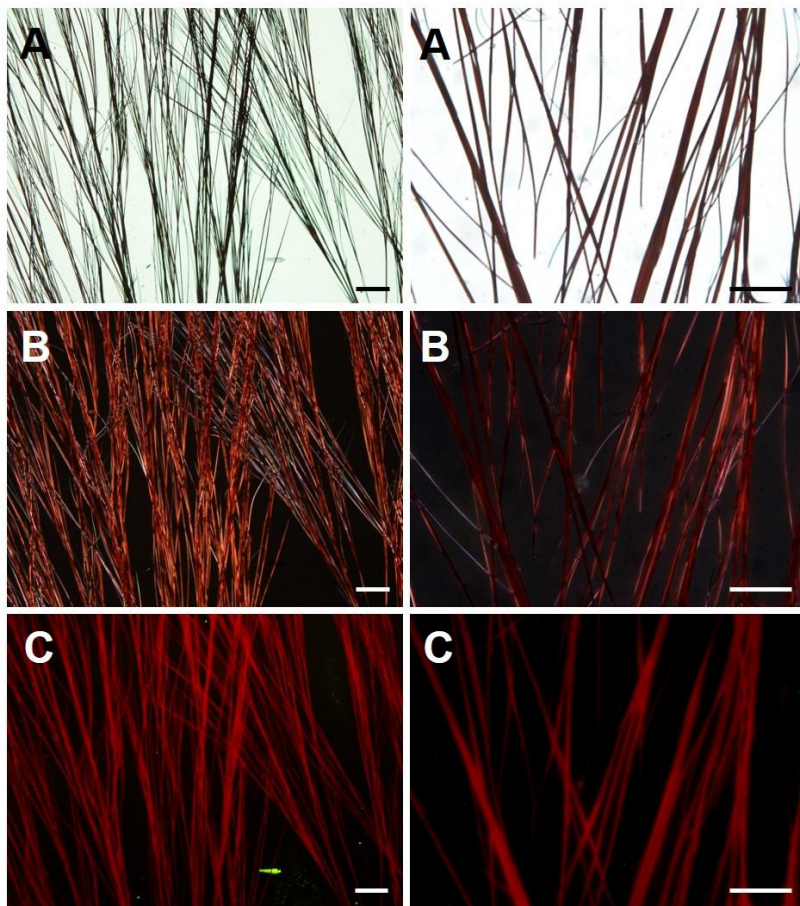


Figure S41. A) Light transmission optical microscopy, B) optical microscopy with cross polars, C) fluorescence microscopy images of compound **5** (scale bar 50nm).

REFERENCES

- [1] ^{a)} Y. Guo, L. Xu, H. Liu, Y. Li, C. M. Che, Y. Li, *Adv. Mater.*, **2015**, 27, 985-1013. ^{b)} Y. Gong, Q. Hu, N. Cheng, Y. Bi, W. Xuac; L. Yu, *RSC Adv.*, **2015**, 5, 32435-32440. ^{c)} F. S. Kim, G. Ren, S. A. Jenekhe, *Chem. Mater.*, **2011**, 23, 682-732. ^{d)} Y. Yamamoto, *Sci. Technol. Adv. Mater.*, **2012**, 13, 033001 (15pp). ^{e)} S. Chen, P. Slattum, C. Wang, L. Zang, *Chem. Rev.*, **2015**, 115, 11967-11998. ^{f)} E. Moulin, J. J. Cid, N. Giuseppone, *Adv. Mater.*, **2013**, 25, 477-487.
- [2] J-M. Lehn, *Angew. Chem. Int. Ed.* **2015**, 54, 3276-3289.
- [3] ^{a)} F. Di Maria, P. Olivelli, M. Gazzano, A. Zanelli, M. Biasiucci, G. Gigli, D. Gentili, P. D'Angelo, M. Cavallini, G. Barbarella, *J. Am. Chem. Soc.*, **2011**, 133, 8654-8661. ^{b)} F. Di Maria, E. Fabiano, D. Gentili, M. Biasiucci, T. Salzillo, G. Bergamini, M. Gazzano, A. Zanelli, A. Brillante, M. Cavallini, F. Della Sala, G. Gigli, G. Barbarella, *Adv. Funct. Mater.*, **2014**, 24, 4943-4951.
- [4] G. Conboy, H. J. Spencer, E. Angioni, A. L. Kanibolotsky, N. J. Findlay, S. J. Coles, C. Wilson, M. B. Pitak, C. Risko, V. Coropceanu, J-L. Brédas, P. J. Skabara, *Mater. Horiz.*, **2016**, 3, 333-339.
- [5] G. Barbarella, M. Zangoli, F. Di Maria, Book Series: Advances in Heterocyclic Chemistry, Volume: 123, E.F.V. Scriven, C. A. Ramsden, Eds., 105-167, **2017**.
- [6] V. Schaller, A. R. Bausch, *Nature*, **2012**, 481, 268-269.
- [7] A. R. A. Palmans, E. W. Meijer, *Angew. Chem. Int. Ed.*, **2007**, 46, 8948-8968
- [8] M. Hifsudheen, R. K. Mishra, B. Vedhanarayanan, V. K. Praveen, A. Ajayaghosh, *Angew. Chem. Int. Ed.*, **2017**, 56, 12634-12638.
- [9] Circular Dichroism: Principles and Applications, 2nd Edition, N. Berova, K. Nakanishi, R. W. Woody, *Wiley*, **2000**.
- [10] M. Cavallini, F. Biscarini, *Nano Letters*, **2003**, 3, 1268-1271.
- [11] D. Gentili, F. Di Maria, F. Liscio, L. Ferlauto, F. Leonardi, L. Maini, M. Gazzano, S. Milita, G. Barbarella, M. Cavallini, *J. Mater. Chem.*, **2012**, 22, 20852-20856.
- [12] ^{a)} H. Chosrovian, S. Rentsch, D. Grebner, D. U. Dahm, E. Birckner, H. Naarmann, *Synth. Met.*, **1993**, 60 (1), 23. ^{b)} M. Theander, O. Inganäs, W. Mammo, T. Olinga, M. Svensson, M. R. Andersson, *J. Phys. Chem. B*, **1999**, 103 (37), 7771.
- [13] ^{a)} A. Yang, M. Kuroda, Y. Shiraishi, T. Kobayashi, *J. Chem. Phys.*, **1998**, 109 (19), 8442. ^{b)} L. Antolini, E. Tedesco, G. Barbarella, L. Favaretto, G. Sotgiu, M. Zambianchi, D. Casarini, G. Gigli, R. Cingolani, *J. Am. Chem. Soc.*, **2000**, 122 (37), 9006.
- [14] K. Suzuki, A. Kobayashi, S. Kaneko, K. Takehira, T. Yoshihara, H. Ishida, Y. Shiina, S. Oishi, S. Tobita, *Phys. Chem. Chem. Phys.*, **2009**, 11 (42), 9850.
- [15] G. Crosby, J. Demas, *J. Phys. Chem.*, **1971**, 75 (8), 991.
- [16] K. Suzuki, A. Kobayashi, S. Kaneko, K. Takehira, T. Yoshihara, H. Ishida, Y. Shiina, S. Oishi, S. Tobita, *Phys. Chem. Chem. Phys.*, **2009**, 11 (42), 9850.
- [17] J. C. de Mello, H. F. Wittmann, R. H. Friend, *Adv. Mater.*, **1997**, 9 (3), 230.

- [18] ^{a)} TURBOMOLE, V7.1; TURBOMOLE GmbH: Karlsruhe, Germany, 2011. <http://www.turbomole.com>. ^{b)} F. Furche F, R. Ahlrichs, C. Hättig, W. Klopper, M. Sierka, F. Weigend, *Wiley Interdiscip. Rev. Comput. Mol. Sci.*, **2014**, 4, 91.
- [19] ^{a)} L. A. Constantin, E. Fabiano, F. Della Sala, *J. Chem. Theory Comput.*, **2013**, 9, 2256. ^{b)} L. A. Constantin, E. Fabiano, F. Della Sala, *Phys. Rev. B*, **2012**, 86, 035130. ^{c)} L. A. Constantin, E. Fabiano, F. Della Sala, *Phys. Rev. B*, **2013**, 88, 125112.
- [20] M. Sierka, A. Hogekamp and R. Ahlrichs, *J. Chem. Phys.*, **2003**, 118, 9136.
- [21] F. Weigend, M. Haser, H. Patzelt, R. Ahlrichs, *Chem. Phys. Lett.*, 1998, 294, p. 143.
- [22] A. Schäfer, H. Horn, R. Ahlrichs, *J. Chem. Phys.*, **1992**, 97, 2571.
- [23] ^{a)} E. R. Johnson, S. Keinan, P. Mori-Sanchez, J. Contreras-Garcia, A. J. Cohen, W. Yang, *J. Am. Chem. Soc.*, **2010**, 132, 6498. ^{b)} J. Contreras-García, W. Yang, E. R. Johnson, *J. Phys. Chem. A*, **2011**, 115, 12983.
- [24] J. Contreras-García, E. R. Johnson, S. Keinan, R. Chaudret, J.-P. Piquemal, D. N. Beratan, W. Yang, *J. Chem. Theory Comput.*, **2011**, 7, 625.

This Dissertation describes:

1) the preparation of a series of fluorescent and semiconducting thiophene-based oligomers and polymers, most of them never prepared before. The syntheses were carried out by taking advantage of enabling technologies such as ultrasound and microwave irradiation. Moreover, in most cases green solvents (H₂O, H₂O/EtOH, H₂O/THF) were employed. The newly synthesized compounds were tested for application in organic electronics and bioimaging.

2) the preparation of 0D (nanospheres) supramolecular structures based on poly(3-hexylthiophene) and the newly synthesized poly(2:2'-bithiophene-*alt*-(3-(2,5-dioxopyrrolidin-1-yl-8-(thiophen-3-yl)octanoate))). The nanoparticles were not toxic and were used as phototransducers under light illumination in live cells (HEK-293) and live organisms (*Hydra vulgaris*)

3) the preparation of 1D (fibers) supramolecular structures based on variously terminated sulfur overrich 3,3',4'',4''''-tetrakis(hexylthio)-2,2':5',2'':5'',2''':5''',2''''-quaterthiophene. The addition of different terminal groups to the quaterthiophene allowed us for the first time to obtain a structurally homogeneous class of 1D supramolecular fibers where the progressive tuning of light emission from visible to near IR and the progressive increase in electron affinity can be obtained while the morphological habit changes from rod-like to helical (in the absence of chiral centers).